



**HAL**  
open science

# Evolution de la microstructure lors du frittage de capacités céramiques multicouches : nanotomographie et simulations discrètes.

Zilin Yan

► **To cite this version:**

Zilin Yan. Evolution de la microstructure lors du frittage de capacités céramiques multicouches : nanotomographie et simulations discrètes.. Autre. Université de Grenoble; Technische Universität (Darmstadt, Allemagne), 2013. Français. NNT : 2013GRENI054 . tel-01070456

**HAL Id: tel-01070456**

**<https://theses.hal.science/tel-01070456>**

Submitted on 1 Oct 2014

**HAL** is a multi-disciplinary open access archive for the deposit and dissemination of scientific research documents, whether they are published or not. The documents may come from teaching and research institutions in France or abroad, or from public or private research centers.

L'archive ouverte pluridisciplinaire **HAL**, est destinée au dépôt et à la diffusion de documents scientifiques de niveau recherche, publiés ou non, émanant des établissements d'enseignement et de recherche français ou étrangers, des laboratoires publics ou privés.

**THÈSE**

Pour obtenir le grade de

**DOCTEUR DE L'UNIVERSITÉ DE GRENOBLE**

Spécialité : **Matériaux, Mécanique, Génie Civil, Electrochimie**

Arrêté ministériel : 1 Octobre, 2010

Et de **DOCTEUR DE TECHNISCHE UNIVERSITÄT DARMSTADT**

Présentée par

**Zilin YAN**

Thèse dirigée par **Christophe L. MARTIN (Université de Grenoble)** et codirigée par **Olivier GUILLON (TU Darmstadt)**

préparée au sein du **Laboratoire SIMaP** dans l'école Doctorale **I-MEP2** et de **Material- und Geowissenschaften, Technische Universität Darmstadt**

**Évolution de la microstructure lors du frittage de capacités céramiques multicouches: nano-tomographie et simulations discrètes**

Thèse soutenue publiquement le **17 Octobre 2013**

devant le jury composé de :

**M. Clive A. RANDALL**

Professeur à Penn State University, Rapporteur

**M. Dominique BERNARD**

Directeur de Recherche à ICMCB-Bordeaux-CNRS, Président, Rapporteur

**M. Christophe L. MARTIN**

Directeur de Recherche à Grenoble INP-CNRS, Directeur de thèse

**M. Olivier GUILLON**

Professeur à L'université d'Iéna, Co-directeur de thèse

**M. Didier BOUVARD**

Professeur à Grenoble INP, invité

**M. Jürgen RÖDEL**

Professeur à L'université de technologie de Darmstadt, invité

**M. Hans-Joachim KLEEBE**

Professeur à L'université de technologie de Darmstadt, invité

**M. Yongqi WANG**

Professeur à L'université de technologie de Darmstadt, invité



## *Acknowledgements*

---

# **Acknowledgements**

I gratefully thank my supervisors Profs. Christophe L. Martin, Olivier Guillon and Didier Bouvard for introducing me into the community of constrained sintering, and their seasoned guidance, continuous supports and patience throughout my PhD study. I highly appreciate their insightful discussions and comments on my monthly project reviews such that I am in a precise and correct track to the end of this dissertation. They not only guide me, a tourist in sciences, to some altitudes, but also cultivate my scientific attitudes. Also, I appreciate very much their offering me a plenty of academic exchanges and professional travels that benefit the development of my career.

I sincerely express my gratitude to the European Commission for the ERASMUS MUNDUS PhD fellowship to cover my three-year stay in France and Germany. I also thank the administrative board of the IDS-FUNMAT program for their well organised training program as well as my PhD colleagues' teamwork that enhance my transferrable skills.

Thanks to the Laboratoire SIMaP/GPM2, Université de Grenoble - CNRS providing a pleasant atmosphere to work in. Thanks to Dr. Luc Salvo and Dr. Pierre Lhuissier for their helpful discussions when I performed the 3D imaging processing. Thank Claire, Claude for taking good care of my employment case, professional trips and other administrative stuff such that I can concentrate on my scientific topic. Thanks to postdocs in the lab: Dr. Xiaoxing Liu, Dr. Patrick Pizette, Dr. David Jauffres, Dr. Hao Wang and senior PhD students Magali, Iottifi, Jean-Marie, Thiboult, Audrey, Mathilde for their assistances in helping me get integrated with my PhD study while enjoying my life in France. Thanks to the birthday croissant and cakes, and joyful chatting which help me to appreciate the French culture little by little. Thanks to Pawel, Edouard, Achraf, Benjamin, Denis, Loinel, Natalia, Mateo, Jérémy for their sharing their stories, point views and exotic natures which make my daily life pleasant.

I would like to thank Prof. Jürgen Rödel, the leader of Ceramics Group, Department of Materials Science, Technischen Universität Darmstadt, for his kind hosting me in his group to carry out the material characterizations. In this dynamic, international group, I have been

## *Acknowledgements*

---

exposed to various topics in ceramics at the group seminars which enlighten me in a subtle way. Thanks to technical specialists Emil, Michael, Gundel and Daniel Isaia for their supports when I carried out my experiments. Thanks to my colleagues: Irene, Christine, Raschid, Jiadong, Sikle, Eva Anton, Eva Sapper, Yohan, Suyan, visiting scientists Prof. Hailong Zhang, Dr. Ke Wang for their instructions to the uses of some key instruments. Thanks to Roswita and Gila for taking care of my administrative case with patience. Thanks to all the Ceramics Group members for their companion at the work lunch, and for the birthday cakes and BBQs which made my sweetest memories of Darmstadt.

Thanks to Prof. Olivier Guillon for hosting me in the Mechanics of Functional Materials Group, Institute of Materials Science & Technology (IMT), Friedrich Schiller University of Jena. Thank Mrs. Anke Partschefeld for her administrative support. Thanks to Mr. Volker Helmig, Susanne for technical assistances. Thanks to Mr. Ralf Wagner (IMT), Mrs. Carmen Voigt (Institute for Solid State Physics, ISSP) for their expertise in sample preparation using FIB milling. Thanks for the companion of Jesus, André, Benjamin, Kaira, Christophe at daily lunch at the Campus Mensa.

Thanks to Dr. Chulseung Lee, senior scientist at the LCR Division of Samsung Electro-Mechanics for his invitation to an on-site visit to the Samsung's Suwon MLCC factory that made me have a good and clear understanding of the procedures for industrial MLCCs production. Thanks for his successive provide of materials and for his professional advices on technical questions.

Thanks go to Beam-line scientist Dr. Steve Wang and beam-line staff, Alex Deriy, Dr. Joan Vila-Comamala at the Sector 32 ID-C (APS synchrotron, Argonne National Laboratory, USA) for their support to set up the in-situ X-ray imaging experiment unit and help with conducting the Transmission X-ray Microscope data acquisition. Without their assistances, the X-ray tomography could not have gone smoothly.

I am indebted to Frederic Charlot at the CMTC, Grenoble for his helpful discussions on the FIB tomography experiments, also for his expertise and efforts in the FIB stack acquisitions.

Thanks to Prof. Gerhard Brey of Frankfurt University for the access to the micro drill to machine the MLCC samples.

Specially, I would like to thank Profs. Clive A. Randall, Jürgen Rödel, Hans-Joachim Kleebe and Dominique Bernard for their time spent reviewing my manuscript. I highly appreciate their perceptive comments and enlightening suggestions.

Last, thanks to my beloved parents, my sisters, my brothers-in-law. Thanks for their persistent love, understanding and support during my pursuit of my academic careers.



*Throughout life, we rely on small groups of people for love, admiration, respect,  
moral support, and help.*

*By Ralph Waldo Emerson*





## Résumé

Les condensateurs multicouches en céramique (Multilayer Ceramic Capacitors, MLCCs) sont des composants passifs clés de l'électronique moderne. Les MLCCs sont constitués d'une alternance d'électrodes métalliques et de couches diélectriques de céramique. Les puces ultraminesces sont composées de mélanges de couches micrométriques métalliques et céramiques et d'additifs de céramique de taille nano (pour retarder le frittage de l'électrode et réduire au minimum les différences de cinétique de frittage). Un certain nombre de défauts tels que des fissures, des délaminations des couches et des discontinuités au sein de l'électrode, peuvent survenir dans la fabrication de ces MLCCs ultraminesces. Les fissures et la délamination se traduisent par un rejet de la puce. Les discontinuités d'électrode (zones non couvertes) et l'hétérogénéité dans l'épaisseur génèrent aussi un certain nombre de problèmes, notamment la perte de capacité, des courts-circuits, un courant de fuite et au final une moins bonne fiabilité.

Il est généralement reconnu que ces défauts sont liés à une inadéquation entre les cinétiques de frittage de l'électrode et de la couche diélectrique au cours du processus de co-frittage des MLCCs. Cependant, quand il s'agit de l'origine de ces défauts et de leur évolution pendant le processus de frittage, peu de connaissances sont disponibles. Les méthodes conventionnelles d'observation post-frittage souffrent de limitations. Dans ce contexte, de l'imagerie in-situ synchrotron par rayons X et des simulations numériques reposant sur la méthode des éléments discrets (DEM) sont utilisées pour explorer l'origine et l'évolution des défauts au cours du processus de co-frittage. L'imagerie par rayons X, y compris de la radiographie 2D et 3D par nano tomodensitométrie (X-ray nCT), permet l'observation in situ non-destructive de l'évolution de la microstructure en 2D et 3D. La DEM, de son côté, peut simuler le frittage de MLCCs en tenant compte de la nature particulière des poudres (granulométrie, empilement, etc).

Un dispositif expérimental à rayons X (TXM, Transmission X-ray Microscope) avec une résolution spatiale de 30 nm au synchrotron APS (Advanced Photon Source, Argonne National Laboratory, USA) a été utilisé pour caractériser un volume cylindrique représentatif de  $\varnothing 20 \mu\text{m} \times 20 \mu\text{m}$  extrait d'une puce 0603 (1,6 mm  $\times$  0,8 mm) au nickel (Ni) + titanate de

baryum ( $\text{BaTiO}_3$ , ou BT) avant et après frittage sous argon hydrogéné (2%). La tomographie 3D de la microstructure montre que les discontinuités de l'électrode finale sont liées à des hétérogénéités initiales dans les couches d'électrodes. La radiographie in-situ aux rayons X pendant le frittage (vitesse de chauffage de  $10\text{ }^\circ\text{C}/\text{mn}$ , température de maintien à  $1200\text{ }^\circ\text{C}$  pendant 1 heure, puis refroidissement à  $15\text{ }^\circ\text{C}/\text{min}$ ) d'un volume représentatif d'électrode au palladium (+ baryum-néodyme-titanate) confirme bien que les discontinuités dans l'électrode proviennent de l'hétérogénéité initiale de la poudre, qui est lié à la nature du compactage d'un matériau particulaire. La discontinuité se produit à l'étape précoce du cycle de frittage. A ce stade, l'électrode métallique commence à fritter tandis que le matériau diélectrique peut être considéré comme un substrat inerte qui contraint le frittage de l'électrode.

Des études corrélatives utilisant un FIB-SEM (Focused Ion Beam Scanning Electron-microscopie) en tomographie à haute résolution ( $5 \times 5 \times 5\text{ nm}^3$ ) ont été effectuées sur des échantillons MLCC à vert et frittés. Elles confirment que la résolution de la nanotomographie X est suffisante pour étudier l'évolution des hétérogénéités. Cependant la tomographie par FIB permet à la nanotomographie X d'être réinterprétée avec plus de précision. D'autre part, le FIB fournit les paramètres des particules pour les simulations DEM.

La méthode des éléments discrets (DEM) a été utilisée pour simuler la microstructure du système multicouche lors du frittage. Ces simulations fonctionnent à l'échelle des particules et permettent donc de reconnaître la nature particulaire des multicouches à un stade précoce de frittage. Tout d'abord, le frittage de la matrice de nickel avec inclusions BT a été simulé en utilisant le code dp3D (développé à SIMaP/GPM2, Université de Grenoble, France). L'effet retardateur des inclusions de BT sur le frittage de la matrice de nickel a été prédit en faisant varier la taille, la quantité et l'homogénéité des inclusions. Nous avons pu montrer que la vitesse de densification de la matrice diminue avec l'augmentation la fraction volumique d'inclusions et avec la diminution de la taille des inclusions. Pour une fraction volumique donnée, et une taille d'inclusions donnée, une meilleure dispersion des inclusions conduit à un retard plus marqué de la densification du frittage de la matrice de nickel.

Le co-frittage de multicouches de BT/Ni/BT a été simulé en tenant compte des informations collectées à partir de la tomographie FIB-SEM à résolution élevée (taille des particules, distribution de taille, hétérogénéités, et pores). Le profil de température aussi été reproduit. On constate que les discontinuités d'électrodes proviennent des hétérogénéités initiales dans le comprimé à vert et se forment au début de frittage sous contrainte. Ces résultats de

simulation sont en bonne correspondance avec les observations expérimentales. Une étude paramétrique indique que les discontinuités d'électrodes peuvent être minimisées par l'homogénéisation de la compacité, par l'augmentation de l'épaisseur des électrodes et par l'utilisation d'un chauffage rapide.

A partir des résultats expérimentaux et des simulations DEM, une conclusion générale peut être avancée: la discontinuité finale provient de l'hétérogénéité initiale dans les couches d'électrodes et survient à un stade précoce de frittage lorsque les couches diélectriques contraignent les couches d'électrodes.

Un mécanisme d'évolution des défauts est proposé: après laminage des couches de BT, il existe des régions inévitablement hétérogènes dans les électrodes. Pour des températures inférieures à 950-1000 °C, la poudre de nickel se densifie sauf dans les zones hétérogènes pour lesquels un phénomène de dé-densification a été observé. Pendant cette étape, les couches de nickel sous traction. La contrainte de traction dans les sections les plus minces induit un flux de matière vers les sections plus épaisses. Ce phénomène intervient jusqu'à la disparition locale des sections les plus minces qui forment ainsi des discontinuités. Lorsque le nickel est complètement dense, les électrodes sont soumises à une contrainte de compression à haute température (1100 °C) en raison de la densification du BT. La contrainte de compression provoque une contraction du nickel dense visqueux, ce qui entraîne un gonflement des électrodes et par conséquent une nouvelle augmentation de la discontinuité de l'électrode. En parallèle, les additifs BT nanométriques sont rejetés en raison de leur non-mouillage par le nickel à haute température. Les additifs agrégés (BT) frittent jusqu'à leur éventuel percolation entre deux couches adjacentes de BT. Ceci conduit à l'amélioration de l'adhérence mécanique entre les couches de Ni et de BT dans les MLCCs.

Mots clés: Frittage; Condensateur céramique multicouche (MLCC); Méthode des éléments discrets; Nano-tomographie



# Abstract

Multi-Layer Ceramic Capacitors (MLCCs) are key passive components in modern electronics. MLCCs consist of alternating metal electrode and ceramic dielectrics layers. In ultrathin MLCC chips, the micrometric layers are composed of submicrometric metal and ceramic powders and nano sized ceramic additives (to retard the sintering of electrode and minimize the sintering mismatch). A number of defects such as cracks, delamination of layers and electrode discontinuity and homogeneity, may arise in the processing of these ultrathin MLCCs. The cracks and delamination result in product rejection. Electrode discontinuities (uncovered areas) and thickness homogeneity generate a number of problems including capacitance loss, electrical short, leakage current and decreased reliability.

It is generally recognized that these defects are linked to the sintering kinetics mismatch between electrode and dielectric materials, during the co-firing (co-sintering) process of MLCCs. However, when it comes to the origin of these defects and to their evolution during the sintering process, little knowledge is available. Conventional post-sintering and 2-dimensional (2D) imaging methods suffer limitations.

In this context, in-situ synchrotron X-ray imaging and Discrete Element Method (DEM) have been carried out to explore the origin and the evolution of defects during the co-sintering process. X-ray imaging including 2D radiography and 3-dimensional (3D) nano computed tomography (X-ray nCT) enable non-destructive in-situ observation of the microstructure change in 2D and 3D. In parallel, DEM can simulate the sintering of MLCCs by taking into account the powders' particulate nature (particle size, packing, etc.)

Synchrotron (Advanced Photon Source, Argonne National Laboratory, IL, USA) X-ray based Transmission X-ray Microscope (TXM) with spatial resolution of 30 nm was used to characterize a representative cylindrical volume of  $\text{Ø } 20 \text{ }\mu\text{m} \times 20 \text{ }\mu\text{m}$  extracted from a 0603 (1.6 mm $\times$ 0.8 mm) case size Nickel (Ni)-electrode Barium Titanate ( $\text{BaTiO}_3$ , or BT)-based MLCC before and after sintering under 2H<sub>2</sub>%+Ar atmosphere. 3D tomographic microstructure imaging shows that the final electrode discontinuity is linked to the initial heterogeneity in the electrode layers. In situ X-ray radiography of sintering (heating ramp of 10 °C, holding at 1200 °C for 1 hour, cooling ramp -15 °C) of a Palladium (Pd) electrode BNT (Barium-neodymium-titanate) based MLCC representative volume was also carried out.

It confirmed that discontinuities in the electrode originate from the initial heterogeneities, which are linked to the very particulate nature of the powder material. The discontinuity occurs at the early stage of the sintering cycle. At this stage, the electrode starts to sinter while the dielectric material may be considered as a constraining substrate.

Correlative studies using Focused Ion Beam - Scanning Electron Microscope (FIB - SEM) tomography were conducted on green and sintered MLCC samples at high resolution ( $5 \times 5 \times 5 \text{ nm}^3$ ). FIB images confirmed that the resolution of the X-ray nCT is sufficient to deal with these heterogeneity evolutions. Still, FIB tomography allows the X-ray nCT to be re-interpreted more accurately. Also, it provides detailed particulate parameters for the DEM simulations.

The DEM was used to simulate the microstructure of a multilayer system during sintering. These simulations operate at the particle length scale and thus recognize the particulate nature of the multilayers at the early stage of sintering. First, the sintering of Nickel matrix with BT inclusions was simulated using the dp3D codes (developed at SIMaP/GPM2, Université de Grenoble, France). The retarding effect of BT inclusions on the sintering of Nickel matrix was predicted by varying the size, the amount and the homogeneity of inclusions. It is found that the densification rate of the matrix decreases with increasing volume fraction of inclusions and with decreasing size of inclusions. For a given volume fraction and size of inclusions, a better dispersion of the inclusions results in a stronger retardation of the densification kinetics of the nickel matrix.

Co-sintering of BT/Ni/BT multilayers was simulated with DEM by taking into account the particulate nature collected from the high resolution FIB nanotomography (FIB-nT) data, such as particle size, size distribution, heterogeneities, pores, and geometry. The temperature profile was also reproduced in these simulations. It is found that the electrode discontinuities originate from the initial heterogeneities in the green compact and form at the early stage of sintering under constraint, in good correspondence to the experimental observations. Parametric studies suggest that electrode discontinuities can be minimized by homogenizing the packing density and thickness of the electrodes and using a fast heating rate.

Based on both experimental and DEM simulation results, a general conclusion is reached: the final discontinuity originates from the initial heterogeneity in the electrode layers and occurs at the early stage of sintering when the dielectric layers constrain the electrode layers.

A defect evolution mechanism is proposed: after the lamination of BT sheets, there exist inevitably heterogeneous regions in the electrodes. Below 950-1000 °C, the nickel powder densifies except in heterogeneous zones for which desintering has been observed. At this stage, the Ni layers are under tensile stress. Tensile stresses in the thinner sections induce matter flow towards the thicker sections until the thinner sections are disrupted and discontinuities form. Once nickel is fully dense, electrodes are subjected to compressive stress at high temperature (1100 °C) due to BT densification. The compressive stress causes contraction of the viscous nickel, resulting in swelling of electrodes and hence a further increase in electrode discontinuity. Meanwhile, the nano-sized BT additives are expelled due to their unwettability with Ni at high temperature. The aggregated BT additives sinter, possibly forming percolation between two adjacent BT layers and enhancing the mechanical adhesion between Ni and BT layers in the MLCCs.

**Key Words:** Sintering; Multilayer Ceramic Capacitor (MLCC); Discrete Element Method; Nanotomography





# Content

<b>Acknowledgements .....</b>	<b>i</b>
<b>Résumé.....</b>	<b>vii</b>
<b>Abstract.....</b>	<b>xi</b>
<b>Contents .....</b>	<b>xv</b>
<b>Table of figure .....</b>	<b>xix</b>
<b>List of abbreviations .....</b>	<b>xxv</b>
<b>List of symbols.....</b>	<b>xxvii</b>
<b>Chapter 1 .....</b>	<b>- 1 -</b>
<b>Introduction.....</b>	<b>- 1 -</b>
1.1 Basics of Multi-Layer Ceramic Capacitors (MLCCs).....	- 4 -
1.1.1 Structure.....	- 4 -
1.1.2 Materials .....	- 4 -
1.1.3 Manufacturing of MLLCs.....	- 9 -
1.1.4 Challenges for miniaturization of MLCCs .....	- 11 -
1.2 Motivation.....	- 13 -
1.3 Objectives and Organization of the Dissertation .....	- 15 -
<b>Chapter 2 .....</b>	<b>- 17 -</b>
<b>Co-firing of Multilayer Ceramic Capacitors.....</b>	<b>- 17 -</b>
2.1 Sintering.....	- 17 -
2. 1.1 Mechanisms of sintering.....	- 18 -
2.1.2 Sintering stages .....	- 19 -
2.2 Constrained sintering .....	- 21 -
2.2.1 Sintering with inclusions (agglomerates).....	- 23 -
2.2.2 Constrained sintering of film and multilayers .....	- 25 -
2.3 Co-firing of MLCCs .....	- 28 -
2.4 Conclusion .....	- 30 -
<b>Chapter 3 .....</b>	<b>- 31 -</b>
<b>Material characterization and sintering behaviour study .....</b>	<b>- 31 -</b>
3.1 Materials .....	- 31 -
3.2 Experiment procedure.....	- 32 -

3.3 Results and discussions.....	- 34 -
3.4 Conclusions.....	- 44 -
<b>Chapter 4 .....</b>	<b>- 45 -</b>
<b>Synchrotron X-ray imaging of the sintering of MLCCs .....</b>	<b>- 45 -</b>
4.1 Introduction.....	- 45 -
4.1.1 X-ray computed tomography .....	- 45 -
4.1.2 Application to sintering.....	- 48 -
4.2 Experiment procedure.....	- 49 -
4.2.1 Set-up: Transmission X-ray Microscope .....	- 49 -
4.2.2 Sample preparation using FIB milling.....	- 50 -
4.2.3 Image acquisition and 3D reconstruction .....	- 52 -
4.3 Results and discussion .....	- 53 -
4.3.1 Ex-situ X-ray CT on Ni-MLCC sample.....	- 53 -
4.3.2 In situ X-ray imaging of Pd-MLCC.....	- 59 -
4.4 Conclusion .....	- 63 -
<b>Chapter 5 .....</b>	<b>- 65 -</b>
<b>Correlative studies using FIB-SEM nanotomography .....</b>	<b>- 65 -</b>
5.1 Introduction.....	- 65 -
5.2 Experiments .....	- 71 -
5.2.1 Experiment setup .....	- 71 -
5.2.2 Materials and procedures .....	- 72 -
5.2.3 Image processing .....	- 74 -
5.3 Comparison of FIB-nT with X-ray nCT .....	- 78 -
5.3.1 Characterization of green microstructures .....	- 78 -
5.3.2 Characterization of sintered microstructures .....	- 79 -
5.3.3 Evaluation of pore size.....	- 80 -
5.4 Particle size distribution (PSD).....	- 82 -
5.4.1 Segmentation.....	- 82 -
5.4.2 3D watershed segmentation .....	- 83 -
5.4.3 Particle size distribution.....	- 84 -
5.4.4 Particle size distribution in 2D and 3D.....	- 89 -
5.5 Heterogeneities in the green electrode.....	- 90 -
5.6 Porosity .....	- 93 -
5.7 Anisotropy.....	- 94 -

5.7.1 Pore orientation in BT layer.....	- 94 -
5.7.2 Density gradient .....	- 98 -
5.8 Microstructure evolution of the electrode.....	- 101 -
5.8.1 Discontinuity of electrode.....	- 101 -
5.8.2 Correlation between discontinuity and capacitance.....	- 103 -
5.9 Conclusion .....	- 104 -
<b>Chapter 6 .....</b>	<b>- 107 -</b>
<b>Discrete element simulations of the sintering of electrode material.....</b>	<b>- 107 -</b>
6.1 Introduction.....	- 107 -
6.1.1 DEM simulation of sintering .....	- 107 -
6.1.2 Principle of DEM.....	- 108 -
6.2 Model description .....	- 113 -
6.3 Simulation procedure .....	- 115 -
6.4 Result and Discussion .....	- 118 -
6.5 Conclusions.....	- 121 -
<b>Chapter 7 .....</b>	<b>- 123 -</b>
<b>DEM simulation of Ni/BaTiO<sub>3</sub> multilayers .....</b>	<b>- 123 -</b>
7.1 Model description .....	- 123 -
7.2 Simulation procedures .....	- 124 -
7.2.1 Sample preparation .....	- 124 -
7.2.2 Sintering conditions .....	- 126 -
7.2.3 Post processing.....	- 127 -
7.3 Free sintering and constrained sintering .....	- 128 -
7.4 Effect of heating ramp .....	- 131 -
7.5 Effect of green density .....	- 133 -
7.6 Effect of contact viscosity.....	- 135 -
7.7 Effect of electrode thickness.....	- 137 -
7.8 Retarding effect of the inclusions .....	- 139 -
7.9 Co-sintering induced anisotropy .....	- 142 -
7.10 Towards more realistic microstructure: coupling with experiments.....	- 145 -
7.11 Conclusions.....	- 148 -
<b>Chapter 8 .....</b>	<b>- 151 -</b>
<b>Conclusion and perspectives .....</b>	<b>- 151 -</b>
8.1 General conclusions .....	- 151 -

## *Content*

---

8.2 Recommendations.....	- 154 -
8.3 Research Perspectives.....	- 154 -
<b>Appendix A.....</b>	<b>- 157 -</b>
<b>Appendix B.....</b>	<b>- 159 -</b>
<b>Appendix C.....</b>	<b>- 161 -</b>
<b>Author's contribution.....</b>	<b>- 163 -</b>
Peer-reviewed articles.....	- 163 -
Conferences.....	- 163 -
<b>References.....</b>	<b>- 165 -</b>

# Table of figures

Figure 1. 1 MLCCs mounted on a graphic card circuit [4]	- 1 -
Figure 1. 2 Case size trend over the year (Murata's road map [8])	- 2 -
Figure 1.3 Cut-away view of a MLCC chip (adapted from Kishi [4])	- 4 -
Figure 1. 4 Perovskite crystal structure of BaTiO <sub>3</sub> (from Perditax [10])	- 7 -
Figure 1. 5 Phase transformation of BaTiO <sub>3</sub> (after Pan [5])	- 7 -
Figure 1. 6 A schematic of the MLCC fabrication process (adapted from Pan [5])	- 9 -
Figure 1. 7 The electrode and dielectric thickness evolution [25]	- 12 -
Figure 1. 8 SEM image of the cross-section of a sintered 0603 type 22 μF MLCC (provided by Samsung Electro-mechanics). Surface was treated with focused ion beam	- 13 -
Figure 2. 1 Six mechanisms for the sintering of crystalline particles([43])	- 19 -
Figure 2. 2 Shrinkage during a typical sintering (after Kang [44])	- 20 -
Figure 2. 3 The three stages of sintering and microstructure (after Tanaka [45])	- 21 -
Figure 2. 4 Schematic illustrations of structures that will undergo differential densification (after Green [47])	- 22 -
Figure 2. 5 Two types of interface flaws produced by the tensile stress when one region (shaded) sinters slower than the other (reproduced after Raj [48])	- 23 -
Figure 2. 6 (a) the composite sphere model; (b) the stress components in a volume element at a distance $r$ in the sintering matrix. The sphere has $v_i$ (volume fraction) of inclusions with radius value $a$ and outer radius $b$ (adapted from [55, 57])	- 24 -
Figure 2. 7 A schematic of defects induced by constrained sintering of layers [75]	- 27 -
Figure 2. 8 An equilibrium configuration diagram for the sintering of a thin film with thickness of $a$ and grain size of $G$ (dihedral angle $\varphi = 120^\circ$ ) ( after Miller [77])	- 28 -
Figure 2. 9 A typical firing cycle for the Ni-MLCCs	- 29 -
Figure 2. 10 FIB treated cross-sections of 0603 size 22 μf Ni-MLCC	- 30 -
Figure 3. 1 A schematic for the Bragg's scattering [80]	- 33 -
Figure 3. 2 TOM-AC optical dilatometer	- 34 -
Figure 3. 3 Particle size distributions	- 35 -
Figure 3. 4 XRD pattern of the starting powder	- 36 -
Figure 3. 5 Linear shrinkage of nickel paste and dielectrics	- 37 -
Figure 3. 6 Linear shrinkage of 1206 type MLCCs	- 38 -

## *Table of figure*

---

Figure 3. 7 Starting powders: (a) X5R type BT powder; (b) debinded nickel paste	- 38 -
Figure 3. 8 Green chips with binders at three different magnifications	- 39 -
Figure 3. 9 SEM images of cross-section of debinded sample	- 40 -
Figure 3. 10 SEM images of the fracture cross-sections	- 40 -
Figure 3. 11 Microstructural evolution of chips sintered with different temperature profiles	- 41 -
Figure 3. 12 Roughness on the surface of an electrode	- 42 -
Figure 3. 1 A schematic of discontinuous electrode	- 43 -
Figure 3. 14 Discontinuity and thickness, roughness of electrodes as a function of time	- 43 -
Figure 4. 1 A schematic diagram of the X-ray image acquisitions [96]	- 46 -
Figure 4. 2 A schematic diagram of tomographic reconstruction using the back-projection method [85].	- 47 -
Figure 4. 3 Spatial resolutions achievable with different lenses: calculated resolutions (open symbols), measured resolutions (filled symbols); synchrotron source (circle symbol) and lab sources (square symbol) (reproduced after withers [94])	- 48 -
Figure 4. 4 A schematic illustration of a TXM imaging system consisting of a condenser lens, objective lens, and detector system. Beamstop and pinhole block out the unfocused X-rays (after Nelson [128])	- 49 -
Figure 4. 5 A schematic for the setup of the TXM at Sector 32-IDC of APS Synchrotron	- 50 -
Figure 4. 6 Photograph of a microscope adapted drill	- 51 -
Figure 4. 7 Two-step preparation of sample for X-ray nCT	- 51 -
Figure 4. 8 (a) MLCC sample for X-ray tomography; (b), (c) 2D projection images before and after sintering, respectively; and (d), (e) reconstructed 3D microstructure before and after sintering, respectively.	- 54 -
Figure 4. 9 BT and Ni absorption edge	- 54 -
Figure 4. 10 Microstructural changes of MLCC samples	- 55 -
Figure 4. 11 Morphology of inner electrode #2	- 56 -
Figure 4. 12 (a) Discontinuity of electrodes; (b) Axial and radial strains in different BT layers, irregular top BT layer (#1) was not considered and (c) relative densities of BT layers (the layers are indexed as in Fig. 4.8(c)).	- 58 -
Figure 4. 13 Microstructural evolutions during sintering. Note that Au particles were used both for image alignment in the reconstruction and for calibrating the temperature in the furnace.	- 59 -

---

Figure 4. 14 3D reconstruction and rendering (top view) of the electrodes in the Pd-MLCC samples	-- 59
-	
Figure 4. 15 Radial and axial strains in dielectric layers, radial strains in electrodes as function of time	- 61 -
Figure 4. 16 A schematic of the defect evolution mechanism during sintering	- 63 -
Figure 5. 1 Resolution of different tomography techniques (after Holzer [135])	- 66 -
Figure 5. 2 Dual beam FIB-SEM system (after Volkert [151])	- 67 -
Figure 5. 3 Schematic for the FIB serial sectioning (after Holzer [135] )	- 68 -
Figure 5. 4 Electron material (SiO <sub>2</sub> ) interaction diagram (adapted from Salh [152])	- 69 -
Figure 5. 5 The schematic of drift correction	- 70 -
Figure 5. 6 Configuration of the nVison 40 FIB/SEM [153]	- 72 -
Figure 5. 7 Serial sectioning on the sample #2	- 73 -
Figure 5. 8 Serial sectioning on the sample # 1-s-ct	- 73 -
Figure 5. 9 Serial sectioning on the sample # 3	- 74 -
Figure 5. 10 Imaging pretreatment flow chat	- 75 -
Figure 5. 11 Removal of noise using 3D median filter	- 76 -
Figure 5. 12 (a) an original slice (b) the gray gradient of the slice, (c) resulting image after subtraction of from the gradient image, (d) histogram of the original image a, (e) histogram of the filtered image c, (f) the pore phase separated from the original image, and (g) the pores in the image after the filtering	- 77 -
Figure 5. 13 3D reconstructed volume for (a) #2, (b) #1-s-ct and (c) #3	- 77 -
Figure 5. 14 Microstructures of the green MLCC with X-ray nCT (column a: sample #1-s) and FIB-nT (column b: sample #2)	- 78 -
Figure 5. 15 X-ray nCT (column a) and FIB tomography (SE mode: column b), (BSE mode: column c) on the final microstructure	- 79 -
Figure 5. 16 Percolation of pores and skeletons: (a) before sintering; (b) after sintering	- 80 -
Figure 5. 17 Pore size distribution in the BT (a) and Ni (b) layer obtained with X-ray -nCT and FIB-nT	- 81 -
Figure 5. 18 (a) an original slice, (b) a zoomed in area of the original image, (c) histogram of the slice, (d) identification of Ni phase, (e) removal of noises from image (d), (f) manual removal of the artifacts, (g) imposition of the electrode on the original image, (h) identification of the BT phase, and (i) the remaining pore phase	- 83 -
Figure 5. 19 Definition of watershed in a watershed segmentation algorithm from [157]	- 84 -



## Table of figure

---

Figure 5. 20 Separation of Ni particles using 3D watershed segmentation (Avizo Fire)	- 85 -
Figure 5. 21 Result of the 3D watershed segmentation of Ni particles in the electrode: (a) 3D view of separated Ni particles, colors are assigned randomly (BT inclusions not considered); (b) PSD measured with FIB-nT and laser scattering.	- 86 -
Figure 5. 22 3D watershed segmentation for the BT particles in a representative dielectric layer	- 87 -
Figure 5. 23 Result of the 3D watershed segmentation of BT particles in the BT layer	- 88 -
Figure 5. 24 Sectioning a sphere randomly produce a distribution of circle sizes, which can be calculated from analytical geometry (after [155])	- 89 -
Figure 5. 25 Correlation between PSDs in 2D and in 3D using the unfolding scheme	<b>ERROR!</b>
<b>BOOKMARK NOT DEFINED.</b>	
Figure 5. 26 (a) 3D rendering of the electrode (the electrode plane is $xz$ ); (b) $xy$ middle plane cross-section; (c) $zy$ middle plane cross-section; (d) $xz$ middle plane cross-section	- 91 -
Figure 5. 27 Density profile in $x$ , $y$ , $z$ direction (1 pixel represents 5 nm)	- 92 -
Figure 5. 28 Coordination number map for the $xz$ plane cross-sections	- 93 -
Figure 5. 29 Pore orientations in the 2D cross-section	- 95 -
Figure 5. 30 Pore orientation in the $xz$ plane before and after sintering	- 96 -
Figure 5. 31 Pore orientation in the $x'y'$ plane before and after sintering	- 97 -
Figure 5. 32 Pore orientation in the $y'z'$ plane before and after sintering	- 98 -
Figure 5. 33 Density profile in the thickness (from the surface to the bottom of the cylinder sample)	- 99 -
Figure 5. 34 Anisotropy in thin film on substrate	- 100 -
Figure 5. 35 A model for the co-sintering of multilayers	- 100 -
Figure 5. 36 An electrode (#2) from the sample #1-s-ct	- 101 -
Figure 5. 37 EDX mapping of the cross-section of the sintered chips (sample #3)	- 102 -
Figure 5. 38 The PSD evolutions of BT inclusion particles entrapped in the electrode (#2) in sample #1-s-ct	- 103 -
Figure 5. 39 Two reconstructed electrodes and a unit capacitor	- 103 -
Figure 6. 1 Two-particle contact model	- 110 -
Figure 6. 2 Schematics of (a) wall conditions and (b) periodic conditions	- 112 -
Figure 6. 3 Contact models: (a) matrix-matrix contact (matrix can be metal or ceramic); and (b) inclusion-matrix contact	- 115 -
Figure 6. 4 Generating of the numerical samples	- 116 -

Figure 6. 5 Numerical microstructure of composites with: 20% of randomly dispersed 300 nm (a), 100 nm (b), and 60 nm (c) inclusions; 10% of randomly dispersed 60 nm inclusions (d); and 10% of agglomerated 60 nm inclusions (agglomerate sizes are ~ 120 nm (e) and ~300 nm (f)). - 117 -

Figure 6. 6 (*mm*) and (*im*) contact numbers in the green packing for various amounts and size of inclusions. - 118 -

Figure 6. 7 Evolution of (*mm*) contacts upon densification: (a) effect of inclusion amount, (b) of inclusion size, and (c) of the inclusions as agglomerates (agg.) or well dispersed (no agg.) - 119 -

Figure 6. 8 Contact size evolution of three types of contacts. - 119 -

Figure 6. 9 Densification rate evolution with relative density: (a) effect of inclusion amount, (b) effect of inclusion size, and (c) of inclusions as agglomerates (agg.) or well dispersed (no agg.). - 120 -

Figure 7. 1 Numerical samples: (a) BT dielectric layer (b) Ni electrode layer without BT additives (c) Ni electrode with 10 vol% BT additives (d) BT/Ni/BT multilayers - 125 -

Figure 7. 2 (a) definition of coble contact radius  $a_c$ ; (b) visualization of two sintered particles after the voxelization procedure. - 128 -

Figure 7. 3 Microstructure evolution of electrode: (a) green microstructure; (b) definition of the inter/intra- agglomerate pores; (c) freely sintered electrode; and (d) constrained sintered electrode - 129 -

Figure 7. 4 The microstructure evolution in the magnified area - 130 -

Figure 7. 5 Electrode discontinuity against the temperature - 131 -

Figure 7. 6 Microstructure of electrode sintered at different heating rates, with the calculated discontinuity. - 132 -

Figure 7. 7 Discontinuity of electrode as functions of heating time - 133 -

Figure 7. 8 Microstructure of electrode with different green density (at 15 °C/min) - 134 -

Figure 7. 9 Discontinuity of electrode as functions of heating time for different values of the viscous parameter. - 136 -

Figure 7. 10 Microstructure of electrode with different viscosities (at 15 °C/min) - 137 -

Figure 7. 11 Green microstructures of different samples with (a) 0.2  $\mu\text{m}$ , (b) 0.4  $\mu\text{m}$  (c), 0.6  $\mu\text{m}$ , and (d) 0.8  $\mu\text{m}$  thick electrode (pure nickel) - 138 -

Figure 7. 12 Electrode discontinuity as functions of heating time - 138 -

Figure 7. 13 Microstructure of electrode with different electrode thickness (at 15 °C/min) - 139 -

## *Table of figure*

---

Figure 7. 14 Green microstructures of pure Ni electrode	- 140 -
Figure 7. 15 Microstructures of the sintered pure Ni electrode (a) and the composite electrode excluding the BT inclusions	- 141 -
Figure 7. 16 Discontinuity as function of sintering time	- 141 -
Figure 7. 17 Crystalline-like packed BT/Ni/BT multilayers	- 142 -
Figure 7. 18 Microstructure and density profile: (a) before sintering; (b) after sintering	- 143 -
Figure 7. 19 Contact size evolution during sintering	- 144 -
Figure 7. 20 Contact size evolution during sintering	- 145 -
Figure 7. 21 (a) cylinder sample extracted from FIB nano tomography; (b) equivalent numerical model; (c) initial microstructures of the nickel electrode; (d) equivalent numerical model	- 146 -
Figure 7. 22 Rearrangement of particles after relaxation process	- 147 -
Figure 7. 23 Microstructures of electrode before and after sintering (nano additives of BT have been removed for clarity)	- 148 -

## **List of abbreviations**

2D	2 Dimension/Dimensional
3D	3 Dimension/Dimensional
BBO	Binder Burn-Out/Binder Bake-Out
BME	Base Metal Electrode
BNT	Barium Neodymium Titanate
BSE	Backscattered Electrons
BT	Barium Titanate
CCD	Charge-Coupled Device
CMOS	Complementary Metal-Oxide-Semiconductor
CT	Computed Tomography
DEM	Discrete/Distinct Element Method/Modeling
EBS	Electron Backscatter Selective Diffraction
EDX(S)	Energy-dispersive X-ray spectroscopy
FIB	Focused Ion Beam
FOV	Field of View
HTCC	High Temperature Co-fired Ceramics
LSA	Laser Scattering Analyzer
LTCC	Low Temperature Co-fired Ceramics
MEMS	Microelectromechanical Systems
MLCC	Multilayer Ceramic Capacitors
NDT	Non-destructive Test
NME	Noble Metal Electrode
OM	Optical Microscope
PC	Personal Computer

*List of abbreviations*

---

PCB	Printed Circuit Board
PSD	Particle/Pore Size Distribution
PVB	Polyvinylbutyral
PVD	Physical Vapor Deposition
ROI	Region of Interest
RVE	Representative Volume Element
SE	Secondary Electrons
SEM	Scanning Electron Microscope
SOFC	Solid Oxide Fuel Cells
TEM	Transmission Electron Microscope
TXM	Transmission X-ray Microscope
XRD	X-ray Diffraction

# List of symbols

Symbol	Unit	Description
$a_{mm}$	m	Matrix-matrix contact radius
$a_{ii}$	m	Inclusion-inclusion contact radius
$a_{im}$	m	Inclusion-matrix contact radius
$A$	$m^2$	Effective electrode overlapping area
$C$	F	Capacitance
$d_0$	Å	Length of the lattice
$d_e$	m	The distance between adjacent electrodes
$D$	-	Relative density
$D_{0b}$	$m^2 \cdot s^{-1}$	Diffusion coefficients for grain boundary
$D_{10}$	m	The size below which lies 10% of the population of particles
$D_{50}$	m	The median diameter of the particle size
$D_{90}$	m	The size below which lies 90% of the population of particles
$E$	eV	Beam energy
$h$	m	Indentation
$I_0$	photons $\cdot$ s <sup>-1</sup>	Intensity of the incidence X-ray
$I$	photons $\cdot$ s <sup>-1</sup>	Intensity of the transmitted X-ray
$K_m$	Pa $\cdot$ s	Bulk viscosities
$M$	Kg	Mass
$M_m$	Kg mol <sup>-1</sup>	Molar mass
$N_e$	N	Number of electrode in a multilayer ceramic capacitor
$N_{ii}$	N	Normal force at the inclusion-inclusion contact
$N_{ij}$	N	Normal force at contact between particle $i$ and particle $j$
$N_{mm}$	J $\cdot$ m <sup>-2</sup>	Normal force at the matrix-matrix contact

## List of symbols

---

$Q_b$	$\text{KJ}\cdot\text{mol}^{-1}$	Sintering activation energy
$R_a$	m	Roughness
$R$	m	Radius of particles
$R_m$	m	Radius of the matrix particle
$R_g$	$\text{JK}^{-1}\text{mol}^{-1}$	Gas constant
$R^*$	m	Reduced radius
$T$	$^{\circ}\text{C}$	Temperature
$T_{mm}$	N	Tangential force at matrix-matrix contact
$T_e$	m	Mean Thickness of electrode
$T_{ij}$	N	Tangential force at contact between particle $i$ and particle $j$
$u$	$\text{m}\cdot\text{s}^{-1}$	Tangential velocity at the contact
$V$	$\text{m}^3$	Volume
$V_{solid}$	$\text{m}^3$	Volume of the solid phase
$V_{envelop}$	$\text{m}^3$	Volume that envelops the material
$V_{mol}$	$\text{m}^3\cdot\text{mol}^{-1}$	Molar volume
$w$	$\text{J}\cdot\text{mol}^{-1}$	Work of adhesion
$Z_{mm}$	-	Average matrix-matrix contact number
$Z_{im}$	-	Average inclusion-matrix contact number
$\alpha$	$^{\circ}\text{C}^{-1}$	Thermal expansion coefficients
$\gamma_s$	$\text{J}\cdot\text{m}^{-2}$	Surface energy
$\delta_b$	m	Thickness of grain boundary
$\Delta t$	s	Time step
$\varepsilon_0$	$\text{F}\cdot\text{m}^{-1}$	Vacuum permittivity
$\varepsilon_r$	-	Relative permittivity
$\varepsilon^r$	-	Radial strain
$\varepsilon^a$	-	Axial strain

$\varepsilon_{ij}$	-	Strain between particle $i$ and $j$
$\dot{\varepsilon}_{ij}$	$s^{-1}$	Strain rate between particle $i$ and particle $j$
$\dot{\varepsilon}_c$	$s^{-1}$	Sintering strain rate of the composites
$\dot{\varepsilon}_m^{free}$	$s^{-1}$	Sintering strain rate of the matrix of composites
$\dot{\varepsilon}_x$	$s^{-1}$	$x$ component strain rate
$\dot{\varepsilon}_y$	$s^{-1}$	$y$ component strain rate
$\dot{\varepsilon}_z$	$s^{-1}$	$z$ component strain rate
$\phi_{porosity}$	-	Porosity
$\emptyset$	m	Diameter of the unit cell
$\lambda$	Å	Wave length of the incidence X-ray
$\nu$	-	Poisson's ratio
$\nu^p$	-	Viscous Poisson's ratio
$\nu_i$	-	Volume fraction of the inclusion phase
$\rho_{appar.}$	$Kg \cdot m^{-3}$	Apparent density
$\rho_{theor.}$	$Kg \cdot m^{-3}$	Theoretical density
$\rho_{BT}^{theor.}$	$Kg \cdot m^{-3}$	Theoretical density of BaTiO <sub>3</sub>
$\sigma_{rm}$	Pa	Radial component stress in the matrix
$\sigma_{\rho m}$	Pa	Polar component stress in the matrix
$\sigma_{\phi m}$	Pa	Angular component stress in the matrix
$\sigma_m$	Pa	Mean stress in the matrix
$\sigma_i$	Pa	Stress in the inclusion
$\sigma_x$	Pa	$x$ component stress
$\sigma_y$	Pa	$y$ component stress
$\sigma_z$	Pa	$z$ component stress
$\Sigma$	Pa	Sintering stress in the matrix
$\eta$	-	Viscosity coefficients



## *List of symbols*

---

$\mu$	$\text{m}^{-1}$	The material's linear attenuation coefficient
$\mu_f$	-	Friction coefficient
$\Omega$	$\text{m}^3$	Atomic volume

# Chapter 1

## Introduction

Capacitors, resistors and inductors are passive components often considered as minor but crucial parts in modern electronics. Capacitors can accomplish in electrical circuits numerous functions including blocking, coupling and decoupling, alternating-direct current separation, filtering and energy storage [1]. In particular, ceramic capacitors are crucial to leading-edge semiconductor devices, which cannot operate properly without them. In 2012 the global capacitor market reached \$17.933 billion USD, including \$8.8 billion USD in ceramic capacitors. Unit shipments of capacitors totalled an estimated 1.594 trillion pieces worldwide [2]. Multi-Layer Ceramic Capacitors (MLCCs), characterized by their high volumetric efficiency, high reliability, and excellent high-frequency features, dominate in the ceramic capacitor market. In 2008, it accounted for ~90% of the capacitor market in part volume [1]. The global MLCC market is forecast to grow at a compound-annual-growth rate of 22.2 % over the period 2010-2014 [3]. One of the key factors contributing to this market growth is the increasing demand for MLCCs in consumer electronics such as cellular phones, digital players and personal computers (PCs). Figure 1.1 shows typical MLCCs mounted on a graphic card circuit.

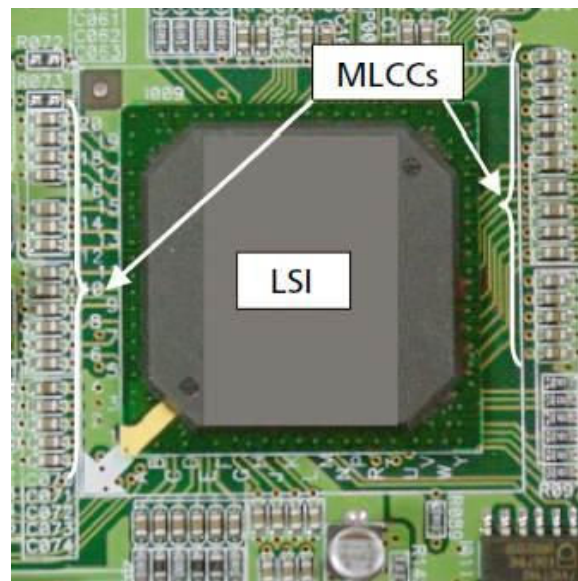


Figure 1. 1 MLCCs mounted on a graphic card circuit [4]

## Introduction

Recently, trends towards miniaturization, higher performance, and lower energy-consumption have driven research and development efforts [4]. Miniaturizations of passive components used in these pieces of equipment have also been accelerated. With hundreds of MLCCs used in typical electronic devices (Table 1.1), trillions of pieces of MLCC are demanded by market each year [5].

Electronic equipment	Typical number of MLCCs
Laptop PC	730
Cellular Phone	230
Smart Phone	500
Digital Camcorder	400
Car Navigation System	1000
Digital TV	1000

Table 1. 1 Number of MLCCs used in electronic devices [6]

Since the first MLCCs were introduced in the early years of World War II there have been two major development trends. One is towards smaller size and higher capacitance, that is towards maximizing volumetric efficiency (capacitance per volume) at a rate that exceeds Moore's Law [7] (Figure 1.2).

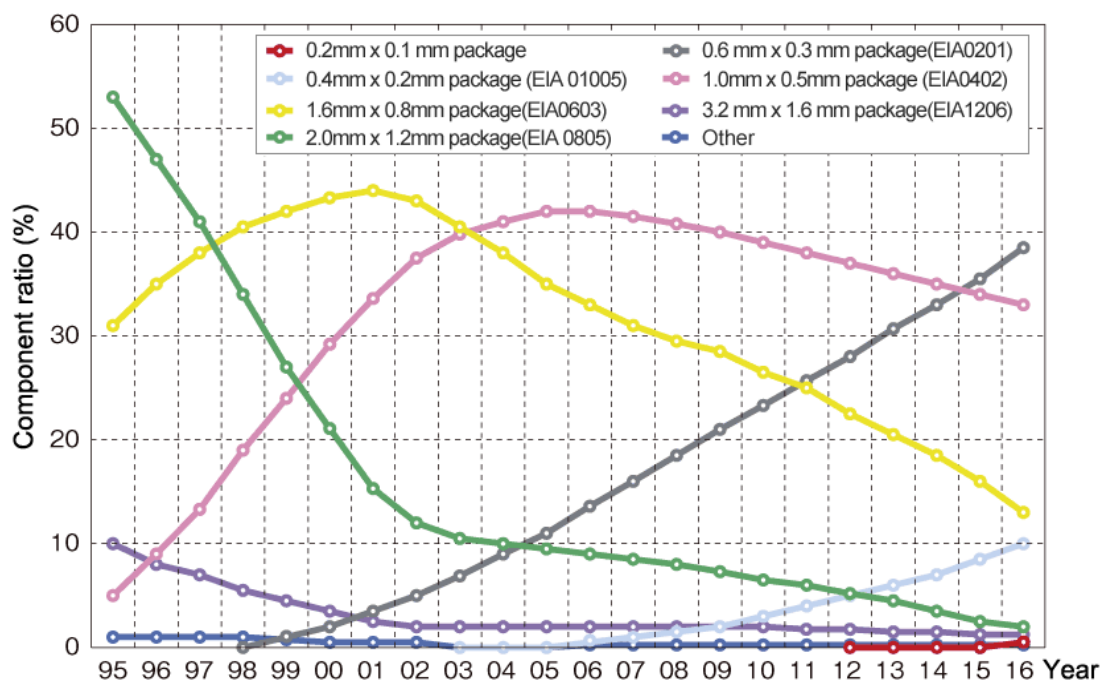
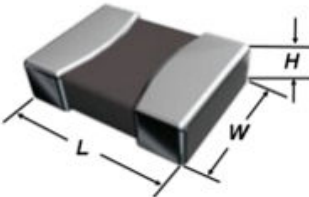


Figure 1. 2 Case size trend over the year (Murata's road map [8])

To keep pace with the miniaturization of modern electronics, the thicknesses of the electrode and dielectric layers are increasingly being downsized to meet the shrinking surface mounting space in the PCBs (Printed Circuit Boards). Presently, EIA<sup>1</sup> case sizes 0603 and 0402 are most common as shown in Figure 1.2. The state-of-the-art case size is EIA01005 (0.4 mm × 0.2 mm). In a EIA 0402 case size 22 μF MLCC, thickness of dielectric layers is approximately 0.3 μm [6]. The smallest available size (0.2 mm × 0.1 mm) of commercial MLCCs by Murata still does not have an EIA definition.

The other important trend is to reduce the production cost. Over the last two decades, the noble metal electrode (NME, mainly, palladium/silver) has been gradually replaced by the base metal electrode (BME, mainly, copper/nickel) due to the high price of Pd and Ag. Nowadays, the BME-MLCCs account for more than 95% of the MLCC market [9].

Drawing	EIA inch code	Dimensions L × W(inch)	IEC/EN metric code	Dimensions L × W(mm)
 <p>Dimensions L×W×H of the multi-layer ceramic chip capacitors</p>	01005	0.016 × 0.0079	0402	0.4 × 0.2
	015015	0.016 × 0.016	0404	0.4 × 0.4
	0201	0.024 × 0.012	0603	0.6 × 0.3
	0202	0.02 × 0.02	0505	0.5 × 0.5
	0302	0.03 × 0.02	0805	0.8 × 0.5
	0303	0.3 × 0.03	0808	0.8 × 0.8
	0504	0.05 × 0.04	1310	1.3 × 1.0
	0402	0.039 × 0.020	1005	1.0 × 0.5
	0603	0.063 × 0.031	1608	1.6 × 0.8
	0805	0.079 × 0.049	2012	2.0 × 1.25
	1008	0.098 × 0.079	2520	2.5 × 2.0
	1111	0.11 × 0.11	2828	2.8 × 2.8
	1206	0.126 × 0.063	3216	6.2 × 1.6
	1210	0.126 × 0.10	3225	6.2 × 2.5
	1410	0.14 × 0.10	3625	3.6 × 2.5
	1515	0.15 × 0.15	3838	3.81 × 3.81
	1806	0.18 × 0.063	4516	6.5 × 1.6
	1808	0.18 × 0.079	4520	6.5 × 2.0
	1812	0.18 × 0.13	4532	6.5 × 6.2
	1825	0.18 × 0.25	4564	6.5 × 6.4
2010	0.20 × 0.098	5025	5.0 × 2.5	
2020	0.20 × 0.20	5050	5.08 × 5.08	

*Table 1. 2 EIA code table*

<sup>1</sup> Metric codes define the dimensions of MLCC chips: 0402 stands for (0.4 mm × 0.2 mm) for example, (0402 is 01005 in inch code), see Table 1.2. The EIA code is used for the MLCCs in this thesis.

## 1.1 Basics of Multi-Layer Ceramic Capacitors (MLCCs)

### 1.1.1 Structure

A MLCC is a monolithic block of ceramic consisting of two sets of offset, interweaved (“interdigitated”) planar electrodes that extend to two opposite surfaces of the ceramic dielectric (Fig. 1.3). The capacitance  $C$  (unit, farad,  $F$ ) of a MLCC is given by:

$$C = \epsilon_r \epsilon_0 \frac{A(N_e - 1)}{d_e} \quad (1.3)$$

Where  $\epsilon_0$  is the vacuum permittivity (unit  $F \cdot m^{-1}$ ),  $\epsilon_r$  the relative permittivity of the dielectrics (dimensionless),  $N_e$  the number of inner electrodes,  $A$  the capacitive area of the electrodes, and  $d_e$  the thickness of the dielectrics.

The area  $A$  is increased by stacking many electrodes in parallel. This construction allows for very thin inter-planar space  $d_e$  between opposing electrodes. For a given case size,  $d_e$  is equal to the chip thickness  $H$  divided by  $N_e$ . Thus the capacitance  $C$  is proportional, for a given chip thickness, to  $N_e^2$ .

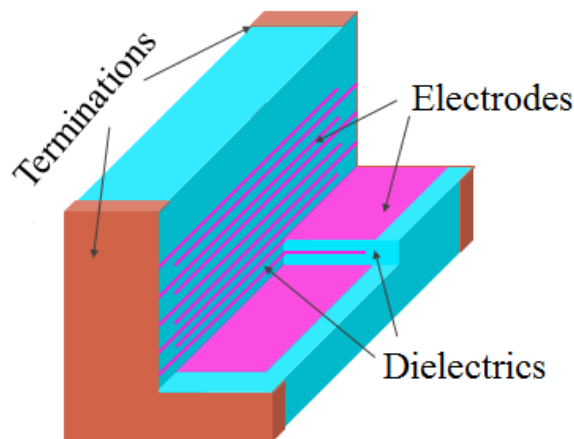


*Figure 1.3 Cut-away view of a MLCC chip (adapted from Kishi [4])*

### 1.1.2 Materials

#### a) Ceramic Dielectric Materials[1]

Ceramic dielectrics cover a broad range of properties, from steatite with an  $\epsilon_r$  value of 6 to complex ferroelectric compositions with  $\epsilon_r$  higher than 20,000. Commercial ceramic dielectrics can be categorized into three classes:

**Class I** dielectrics usually include low- and medium- permittivity ceramics with dissipation factors (loss tangent<sup>2</sup>) < 0.003. Relative permittivity  $\epsilon_r$  covers a range of 15-500 with stable temperature coefficients of permittivity that lies between +100 and -2,000 ppm/°C.

For example, a P3K capacitor has a -1,500 ppm/°C change in capacitance and a tolerance of  $\pm 250$  ppm/°C, and a C0G capacitor has zero temperature coefficient and a  $\pm 30$  ppm/°C tolerance.

Significant figure of temperature coefficient of permittivity (ppm/°C)	Symbol	Multiplier applied to significant figure	Symbol	Tolerance of temperature coefficient (ppm)	Symbol
0	C	-1	0	$\pm 30$	G
0.3	B	-10	1	$\pm 60$	H
0.8	L	-100	2	$\pm 120$	J
0.9	A	-1,000	3	$\pm 250$	K
1.0	M	-10,000	4	$\pm 500$	L
1.5	P	1	5	$\pm 1,000$	M
2.2	R	10	6	$\pm 2,500$	N
6.3	S	100	7		
4.7	T	1,000	8		
5.6	V	10,000	9		
7.5	U				

*Table 1. 3 Class I EIA specification codes for Class I dielectrics*

**Class II/III** dielectrics consist of high-permittivity ceramics based on ferroelectrics. They have  $\epsilon_r$  values between 2,000 and 20,000 and properties that depend more on temperature, field strength and frequency than Class I dielectrics. Their dissipation factors are generally less than 0.03 but may exceed this level in some temperature ranges and in many cases become much higher when high AC fields are applied. Their main importance lies in their high volumetric efficiency (Table 1.4).

<sup>2</sup> The loss tangent is a parameter of a dielectric material that quantifies its inherent dissipation of electromagnetic energy

EIA Code	Temperature range/°C	EIA Code	Capacitance change/%
X5	-55 to +125	D	±6.3
X7	-55 to +150	E	±4.7
X8	-30 to +85	F	±7.5
Y5	+10 to +85	P	±10
Z5		R	±15
		S	±22
		T	+22 to -33
		U	+22 to -56
		V	+22 to -82

*Table 1. 4 Coding for temperature range and capacitance variation for Class II/III Capacitors (codes D-R: Class II; Codes S-V: Class III)*

For instance, a Z5U capacitor will operate from +10 °C to +85 °C with a capacitance change of at most +22% to -56%. An X7R capacitor will operate from -55 °C to +125 °C with a capacitance change of at most ±15%.

**Class IV** dielectrics have a conductive phase that effectively decreases the thickness of dielectric layers in capacitors by at least an order of magnitude. Very simple structures such as small discs and tubes having two parallel electrodes can achieve capacitances of over 1 mF. Their disadvantages are low working voltages in range of 2-25V and high losses. They mainly apply in “barrier layer” capacitors that are now very little used and considered as outdated.

- **Barium Titanate [5]**

Emblematic for class II/III dielectrics, barium titanate ( $\text{BaTiO}_3$ , or BT) was discovered simultaneously in several countries during World War II. Due to the presence of ferroelectricity, BT features high permittivity (maximum  $\epsilon_r > 10,000$ ) that was orders of magnitude greater than other existing dielectrics at that time. The technological importance of BT was recognized immediately, and extensive efforts were devoted to tune its dielectric properties. Nowadays, BT is still the base material for ceramic dielectrics. BT has a perovskite crystal structure as shown in Figure 1.4.

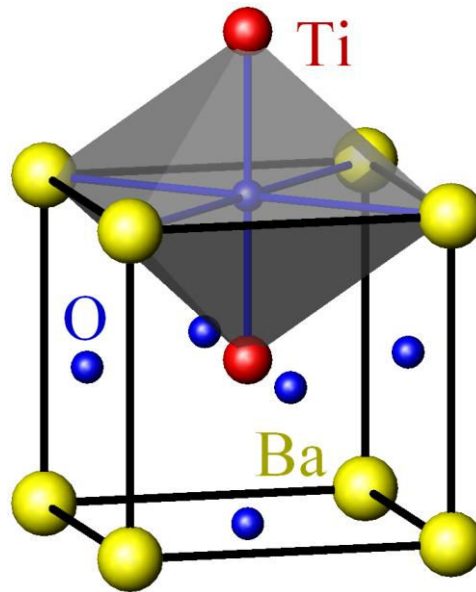


Figure 1. 4 Perovskite crystal structure of  $\text{BaTiO}_3$  (from Perditax [10])

Three phase transitions take place in BT when cooled from high temperature (Fig. 1.5): cubic to tetragonal at  $\sim 120^\circ\text{C}$ , tetragonal to orthorhombic at  $0^\circ\text{C}$ , and orthorhombic to rhombohedral at  $-90^\circ\text{C}$ . The temperature induced phase transitions cause dramatic drifts in dielectric constants. Thus, pure BT cannot be used directly since the dielectric in the capacitors should have little temperature dependency. Manufacturers typically use solid solutions of BT. with dopants based on Sr, Ca, Zr, Sn and rare earths. Dopants broaden the dielectric constant peaks of the doped BT.

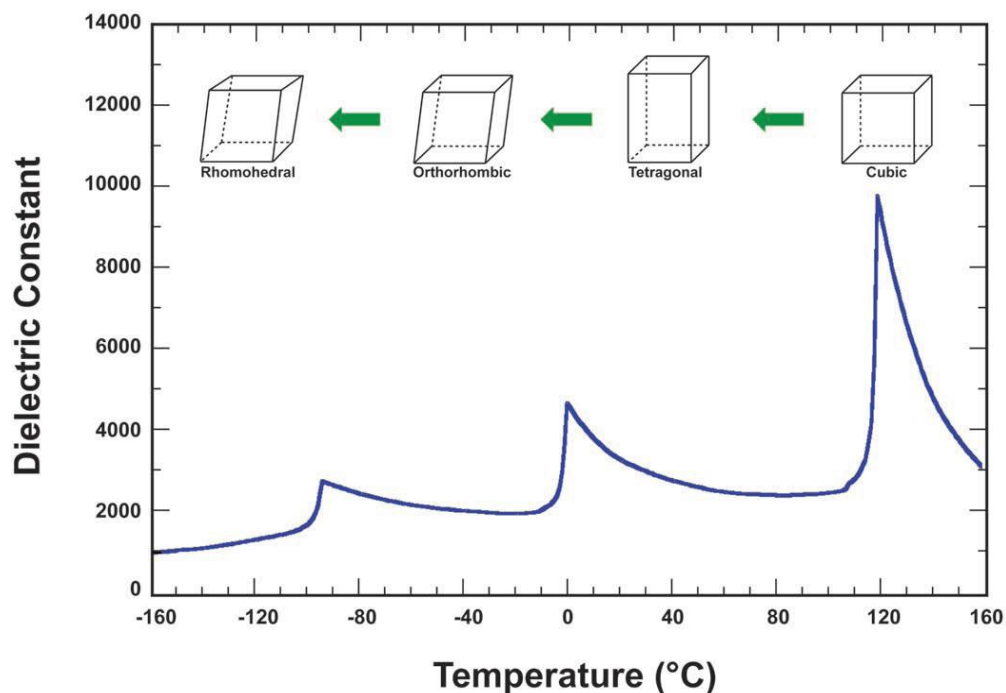


Figure 1. 5 Phase transformation of  $\text{BaTiO}_3$  (after Pan [5])



### b) Electrode metals

The electrode material is supposed to lead to a conductive and continuous film that does not diffuse into, or react with the ceramic dielectric during sintering. This requires the use of non-oxidizing metals or alloys with high melting points. There are two material systems used today to make ceramic capacitors: Noble Metal Electrode (NME) and Base Metal Electrode (BME).

- **NME**

The NME is the older technology and uses Pd/Pd-Ag electrodes, Ag termination, and Ni and Sn plating. Palladium reduces during heating to allow film formation, and its surface oxidizes during cooling (below 870 °C). This causes it to bond to the ceramic. For cost reduction, increasing amounts of silver are added to the electrode alloys to replace palladium. This also allows the melting point of the alloy to be lowered. The development of lower firing formulations allows the use of more silver, which results in electrode cost savings.

- **BME**

The BME is of a newer technology and uses Ni electrode, Ni or Cu termination, and Ni and Sn plating. The use of Ni electrodes reduces further the cost of electrode, but the requirement for a low oxygen partial pressure (to keep the metal from oxidizing) during firing causes significant changes in ceramic composition and processing. Base-metal-electrode MLCCs have accounted for >95% of global MLCC market for their high volumetric efficiency and low cost [9].

Metals	Melting point(°C)	Resistivity(mΩ)	Firing atmosphere	Price ratio
Ag	961	1.62	Air	3
Cu	1080	1.72	Reducing	1
Ni	1453	6.9	Reducing	1
Pd	1552	10.4	Air	80

*Table 1. 5 Physical properties and price ratio of various electrodes [4]*

### 1.1.3 Manufacturing of MLCCs

The processes used in the manufacture of MLCCs require a high degree of sophistication to insure high-yield, large-scale and low-cost production. The typical procedure of MLCCs fabrication is shown in Figure 1.6.

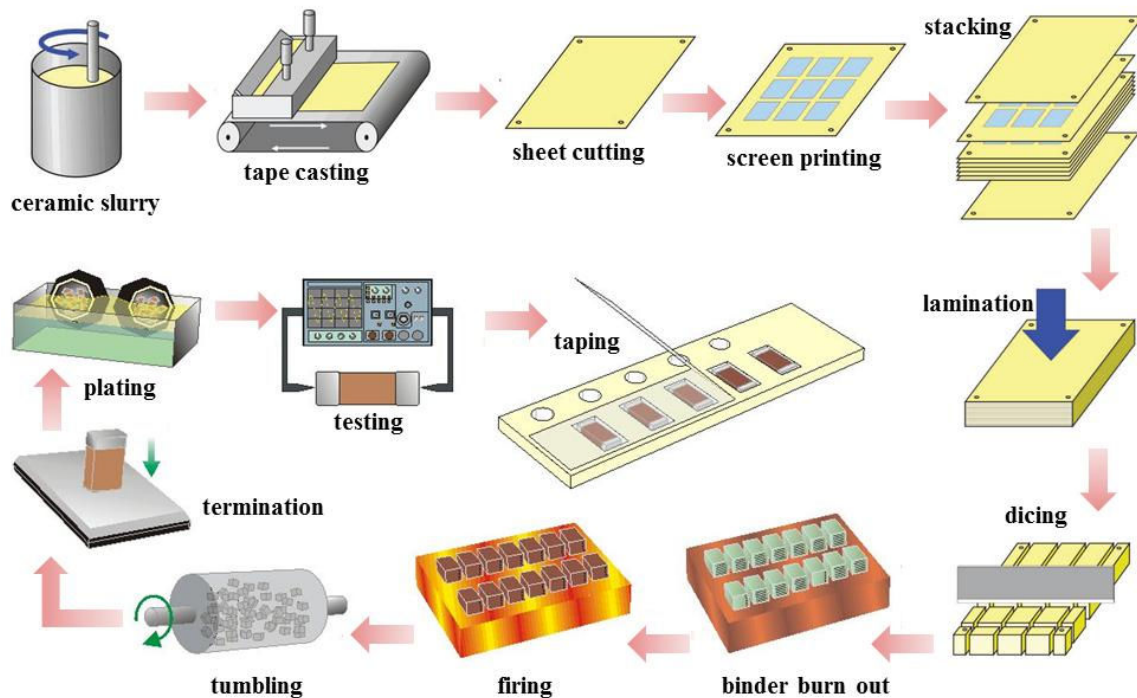


Figure 1. 6 A schematic of the MLCC fabrication process (adapted from Pan [5])

- **Ceramic slurry making [11]**

The ceramic slurry is made by mixing predetermined proportions of powder in a solvent, dispersing agent, binder (polyvinylbutyral, PVB), plasticizer and other additives using dispersing apparatus such as a bead mill, ball mill, attriter, paint shaker or sand mill to yield a homogeneous ceramic slurry.

- **Tape casting**

The slurry is cast on a film carrier by tape casting (doctor blading). The slip is carried by a conveyor belt into a drying oven to produce the dry ceramic tape. This tape is then cut into pieces, so called sheets. A proper dispersion of the powder in the slip is necessary to secure a maximum packing in the dried slip.

- **Screen printing**

The electrode ink is made by mixing a submicron metal powder, solvents and ceramic

additives. The ink is deposited on the green ceramic sheets according to the electrode patterns using a screen printing process. Poor printing quality may cause significant yield loss. Proper dispersion of metal particles helps to provide a homogeneous film. This is required to minimize the amount of metal that gives a continuous fired film.

- **Stacking and lamination**

The patterned sheets are stacked and laminated to form a solid bar. The pressure, temperature and dwelling time are important parameters and have to be optimized in accordance with to the material system.

- **Dicing**

The bar is cut into separate parts (capacitors). The parts are now in a “green” state. In general, the yield decreases with increasing volume of capacitor and depends on the aspect ratio of the component.

- **Binder burn out**

The binder burn-out or bake-out (BBO) process is to remove the organics from the chips before firing. This process usually requires the longest time and often causes a large amount of product rejection. Voids or pores arise when the generation of gaseous products exceeds some critical pressure within the body. The heating profiles need to be adjusted according to specific capacitor geometry and size. This step must be performed gradually since excessive initial heating rates result in rapid gas generation. Therefore, it is necessary to control the heating rates and the atmosphere.

- **Firing**

The firing (sintering) of green parts is conducted in kilns with slowly moving conveyor belts. The temperature profile is crucial to the characteristics of the capacitors. Time dependent changes in firing conditions and variations due to location of the parts in the kiln must be minimized.

- **Wet tumbling**

During this process, sharp corners of MLCCs are rounded to minimize potential breakage during handling. Also, this rounding of corners is helpful to obtain good coverage of termination ink.

- **Termination and curing**

Fired chips are terminated in the electrode pick-up regions with a conductive ink. Then the ink cures in the range of 650-800 °C. The termination provides the external layer with electrical and mechanical connection to the capacitor. The conductive ink is made of metal powder, solvents and glass frit in a mixer.

- **Plating**

The termination is coated with a nickel layer and a tin layer using an electroplating process. The nickel serves as a barrier layer between the tin plating and the termination. The tin is to protect the nickel from oxidizing.

- **Testing**

The parts are tested and sorted according to their correct capacitance tolerances. The parts can be packaged on tape and reel after this process.

#### **1.1.4 Challenges for miniaturization of MLCCs**

As Eq. (1.1) indicates, increase in volumetric efficiency of MLCC can be achieved by increasing the number of dielectric layers and decreasing the layer thickness. Today, a Class II capacitor could have up to 1000 submicrometric layers. The innovative efforts in MLCC technology has resulted in an exponential increase of capacitance in recent years (see Figure 1.7). With the thinning of dielectric layers, tape-casting technology becomes problematic for the development of next generation MLCCs. Conventional processing of tape casting/screen printing has reached its technological limit at 0.8-1.0  $\mu\text{m}$ . MLCC manufacturers tend to reduce the BT grain size in order to pack more grains across the thickness of the dielectric layer. However, due to size effects, smaller grains lead to lower permittivity and thus to lower capacitance [12-15]. Many efforts have gone to the development of novel core-shell ceramic dielectrics with higher dielectric constant and smaller grain size [16-21]. The core-shell grain features a core region, pure tetragonal structure BT surrounded by a pseudocubic shell which contains other additive elements [22-24].

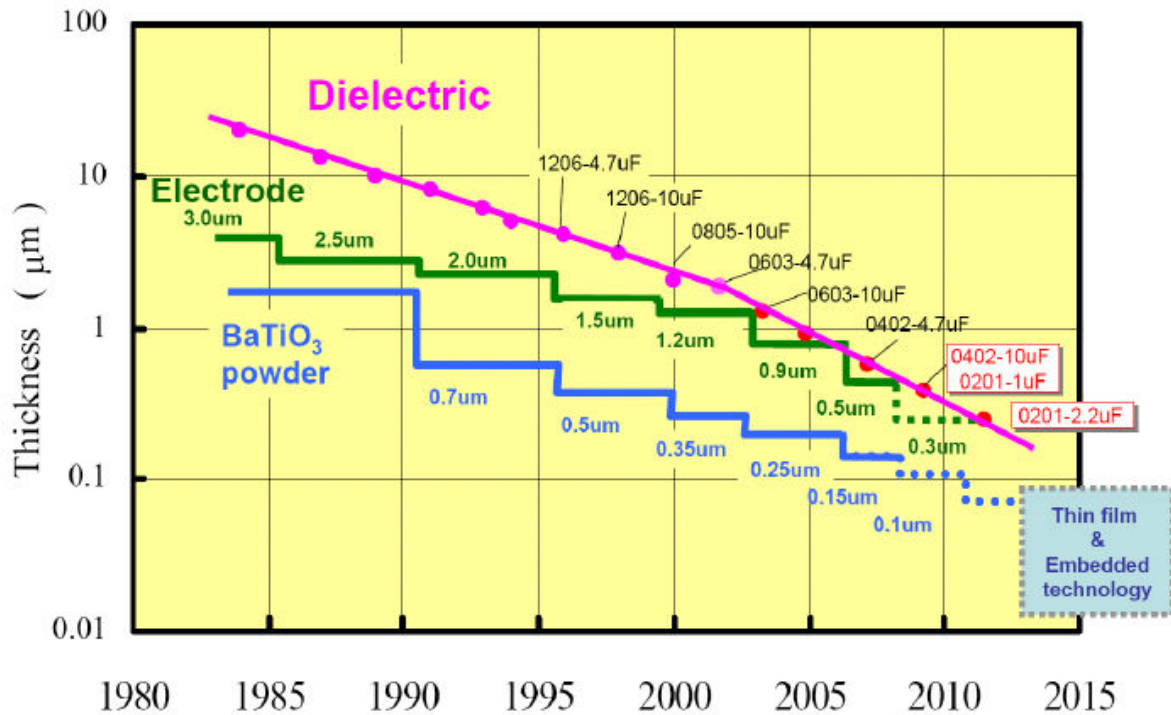


Figure 1. 7.The electrode and dielectric thickness evolution [25]

In the meanwhile, thinning of electrode also goes with the thinning of dielectrics to reduce the case size of the chips and the consumption of electrode materials. However, when the thickness of electrodes approaches  $1.0 \mu\text{m}$  or less, significant discontinuities of electrode build up after the firing process (see Fig. 1.8). The electrode coverage loss results in a direct decrease in the overlapping area ( $A$ ) in Eq.(1.1). An average discontinuity of 15% causes around 20% capacitance loss. Inversely, this means that, for a given capacitance, the volume of MLCC could have further downsized by 20% if one was able to get rid of this discontinuity. Furthermore, the effects of microstructural heterogeneities are much more significant when thinning electrodes. In particular, the local electric field is disturbed at electrode discontinuities and roughness [26-29]. Thus, controlling of the connectivity and smoothness of the electrode in ultrathin MLCC is of much interest to enhance the capacitance, the performance and the reliability of MLCCs.

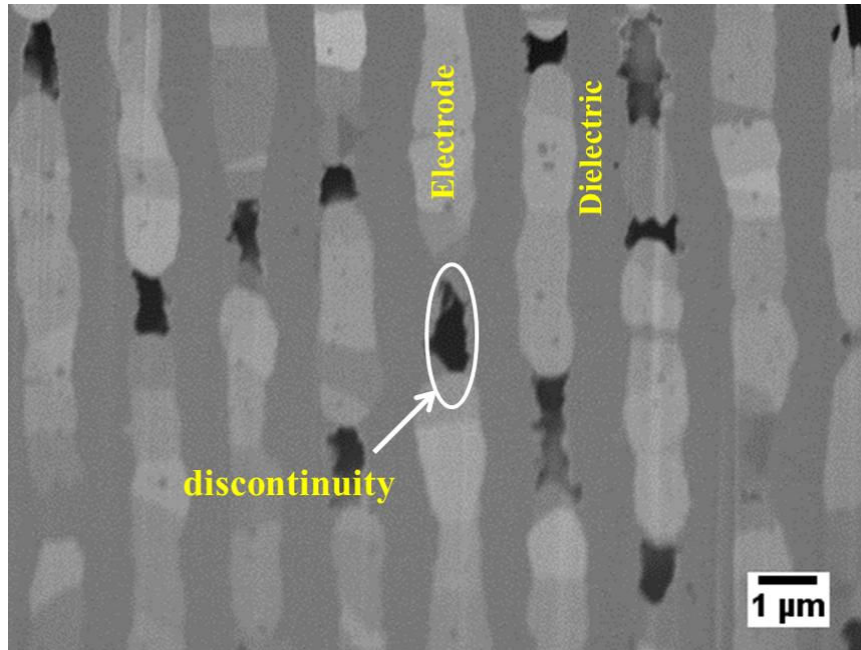


Figure 1. 8 SEM image of the cross-section of a sintered 0603 type 22  $\mu\text{F}$  MLCC (provided by Samsung Electro-Mechanics). Surface was treated with Focused Ion Beam.

## 1.2 Motivation

It has been reported that defects in electrode layers are related to different processing phases. Gas release from inappropriately controlled BBO [30] results in residual pores which act as initial defects. To achieve thinner electrode layers, it is necessary to reduce the electrode paste attachment during the printing process. However, a reduction in the paste attachment results in a decreased coverage rate of the metal electrode following the firing process [31]. Moreover, the sintering shrinkage mismatch [32] between the electrode and dielectric layers also leads to other defects, such as delamination, cracks, and warpage [30, 31, 33-35].

Takahashi [36] and Sugimura [31] et al. found that the addition of BT particles into the Ni paste results in a higher coverage ratio of nickel film on BT sheets due to reduced sintering mismatch. Accordingly, Kang et al. [37] have shown that an additional amount BT particle into the nickel paste decreases the shrinkage of the composite electrode.

Weil et al. [38] studied the sintering of nickel film on BT sheets and found that instabilities of Ni film were formed as a series of interconnected or discrete nickel islands separated by

patches of exposed BT substrate surfaces. This is due to a dewetting effect and becomes significant when the nickel layer thickness is sub-micronmetric.

Polotai et al. [28, 29, 39] proposed that thin (~10 nm) liquid (Ni, Ba, Ti) alloy layer formed at Ni/BT interfaces during sintering of ultrathin MLCCs. The presence of the high-temperature interfacial liquid film modifies the interfacial free energy and provides a fast kinetic pathway for mass transport, which leads to the enhanced Ni grain growth and degradation of the electrode layers. By using a fast heating scheme this liquid alloy could be suppressed and Yoon et al. [26] observed higher linear connectivity (93%) of electrode by using high heating rates of 3600 °C/h. Addition of refractory elements (Cr, Pt) into the nickel paste further limits the formation of interfacial liquid alloy layer and improves the Ni electrode continuity [40]. These authors also suggest that the residual carbon [41] due to incomplete removal of the binder plays a role in the formation of this liquid phase.

To date, the investigations were mainly based on 2-dimensional (2D) information from sectioned surfaces using optical microscopy (OM) or Scanning Electron Microscopy (SEM) [26, 42]. First, the final microstructures cannot reveal correctly the origin and historic evolution of the defects. Second, 2D evaluation such as the linear electrode coverage is sometimes not sufficient to quantify defects and layer thickness shrinkage. Furthermore, inappropriate handling during sample preparation can be problematic and add some artifacts. Samantaray et al. [27] demonstrated Focused Ion Beam - Scanning Electron Microscope (FIB-SEM) based 3-dimensional (3D) tomography characterization on the 3D morphology of electrode in sintered MLCC sample for the first time. To refine the understanding of mechanisms that are responsible for the defects initiation and evolution during the co-firing of the MLCCs, we need some superior, non-destructive, 3D and quantifiable characterization techniques.

In parallel to 3D observations, simulation of the sintering process at the pertinent length scale (particle length scale) should provide information that can relate the defect origin and evolution to structural parameters (particle size, particle packing, layer thickness, temperature profile, etc.)

### **1.3 Objectives and Organization of the Dissertation**

In this thesis, the aim is to better understand the origin of the electrode defects and the defect evolution mechanism during the co-firing process. This understanding will be built on the sintering phenomena at the particle length scale in 3D by using state-of-the-art nanotomography techniques and discrete element simulations. The dissertation is organized as follows:

**Chapter 2:** This chapter presents a background study. The co-firing process of the MLCCs is revisited and the possible scenarios that might result in defects development are considered. Co-sintering or constrained sintering of composites and multilayers is reviewed.

**Chapter 3:** This chapter describes the characteristics of the starting electrode and dielectric powders (Ni and BT, respectively) including their compositions, particle size distribution and sintering kinetics using X-ray diffraction (XRD), SEM and dilatometry.

**Chapter 4:** In this chapter, the application of the state-of-the-art synchrotron based X-ray nano- computed tomography (nCT) is introduced. The microstructure of a Ni-MLCC sample is characterized using X-ray nCT and quantifications of microstructure evolution have been carried out before and after sintering. An in-situ x-ray radiographic observation on sintering of a Pd-MLCC sample is also presented and discussed.

**Chapter 5:** In this chapter, correlative studies on the sintering of Ni-MLCCs have been carried out using high-resolution Focused Ion Beam (FIB)-SEM nanotomography. FIB-SEM reconstruction of Ni-MLCC samples have been conducted to enhance the resolution available in X-ray nanotomography.

**Chapter 6:** In this chapter, the applications of discrete elements method to the sintering is introduced and reviewed. The effect of the ceramic additives on the sintering kinetics of the electrode paste materials is investigated using DEM simulation. Simulation parameters include the size, and the volume fraction and the dispersion degree of the additives.

**Chapter 7:** Free sintering of single electrode and co-sintering sandwiched BT/Ni/BT layers are simulated using DEM. The defects origin and evolution of the electrode are investigated.



Comparison between the experiments and simulation limitations are commented. The effect of microstructure and process parameters, such as the thickness of the electrode layers, the green packing density, the arrangement of the particles, and the heating ramp have been investigated.

**Chapter 8:** This chapter summarizes the findings from the experiments and DEM simulations. A defect evolution mechanism is put forward. Finally, recommendations are proposed to improve the manufacturing of MLCCs with less electrode discontinuity.

## Chapter 2

# Co-firing of Multilayer Ceramic Capacitors

Microstructural control in ultrathin MLCCs is nowadays one of the main challenges for maintaining an increase in volumetric efficiency of capacitance. To help solve this problem, understanding the impact of the firing process on the microstructure of materials (compact of metallic and dielectrics powder) is of the greatest importance. During the firing process of MLCC parts, complex phenomena take place, including chemical reaction, and microstructural evolution. In this chapter, we attempt to understand this firing process by considering the fundamentals of the sintering mechanisms in the firing process. Starting from an introduction to the sintering, the literature on co-sintering of composite and layered systems is revisited to find potential solutions.

### 2.1 Sintering

Generally, the term *firing* has been used when the processes occurring during the heating stage are very complex, as in many traditional ceramics produced from clay-based materials. In less complex cases, the term *sintering* has been used [43]. *Sintering* is a processing technique used to produce dense or density-controlled materials and products from metal and/or ceramic powders by applying thermal energy [44]. This sintering process is associated with a reduction of the free energy of the system. The sources that cause this reduction of the free energy are usually referred to as the driving forces for sintering. There are three possible driving forces: (i) the curvature of the particle surfaces; (ii) an external pressure, and (iii) a chemical reaction.

When an external stress and a chemical reaction are not involved, surface curvature provides the driving force for sintering. Considering one mole of powder consisting of  $N$  spherical particles with a radius  $R$ .

$$N = \frac{3M_m}{4\pi R^3 \rho} = \frac{3V_m}{4\pi R^3} \quad (2.1)$$

Where  $\rho$  is the density of the particles,  $M$  the molecular mass, and  $V_m$  the molar volume. The surface area of the powder is

$$S_A = 4\pi R^2 N = \frac{3V_m}{R} \quad (2.2)$$

If  $\gamma_{sv}$  is the specific surface energy of the particles, then the surface free energy associated with the system of particles is

$$E_s = \gamma_s S_A = \frac{3\gamma_s V_m}{R} \quad (2.3)$$

$E_s$  represents the reduction in surface free energy of the system if a fully dense body were to be achieved finally. It implies powder with high surface energy (as for metals) or fine particle size is prone to sintering more rapidly. External pressure and chemical reaction are not in the scope of current study of sintering of MLCCs and not detailed here (see Ref. [44]).

Sintering of crystalline materials is usually categorized into two types: solid state sintering and liquid phase sintering. Solid state sintering occurs when the powder compact is densified fully in the solid state at the sintering temperature. Liquid phase sintering occurs when the powder compact is densified during sintering in the presence of a liquid phase. Normally, this liquid phase is formed due to the sintering temperature exceeding melting point of one material. If it is not specified, sintering in this thesis refers to solid state sintering.

### ***2. 1.1 Mechanisms of sintering***

Sintering of polycrystalline materials occurs by transport of matter along definite paths (bulk, lattice, grain boundary, and surface) that define the mechanisms of sintering. Matter is transported from higher chemical potential regions (the source) to lower chemical potential regions (the sink). As schematized in Figure 2.1, there are six typical mechanisms of sintering in polycrystalline materials. They all lead to bonding and neck growth ( $a$ ) between particles (with radius of  $R$ ). They can also be generally categorized as *densifying* and *nondensifying* mechanisms.

- a) *Nondensifying* mechanisms include surface diffusion, volume (lattice) diffusion from the particle surfaces to the neck, and vapor transport (mechanisms 1, 2, and 3) which lead to neck coarsening without densification. The nondensifying mechanisms cannot simply be ignored because they reduce the curvature of the neck surface (i.e., sintering potential, activation energy).

- b) *Densifying* mechanisms include grain boundary diffusion and lattice diffusion from the grain boundary to the pore (mechanisms 4 and 5) which permits neck growth as well as densification (common in polycrystalline ceramics) and plastic flow by dislocation motion (mechanism 6, common in the sintering of metal powders).

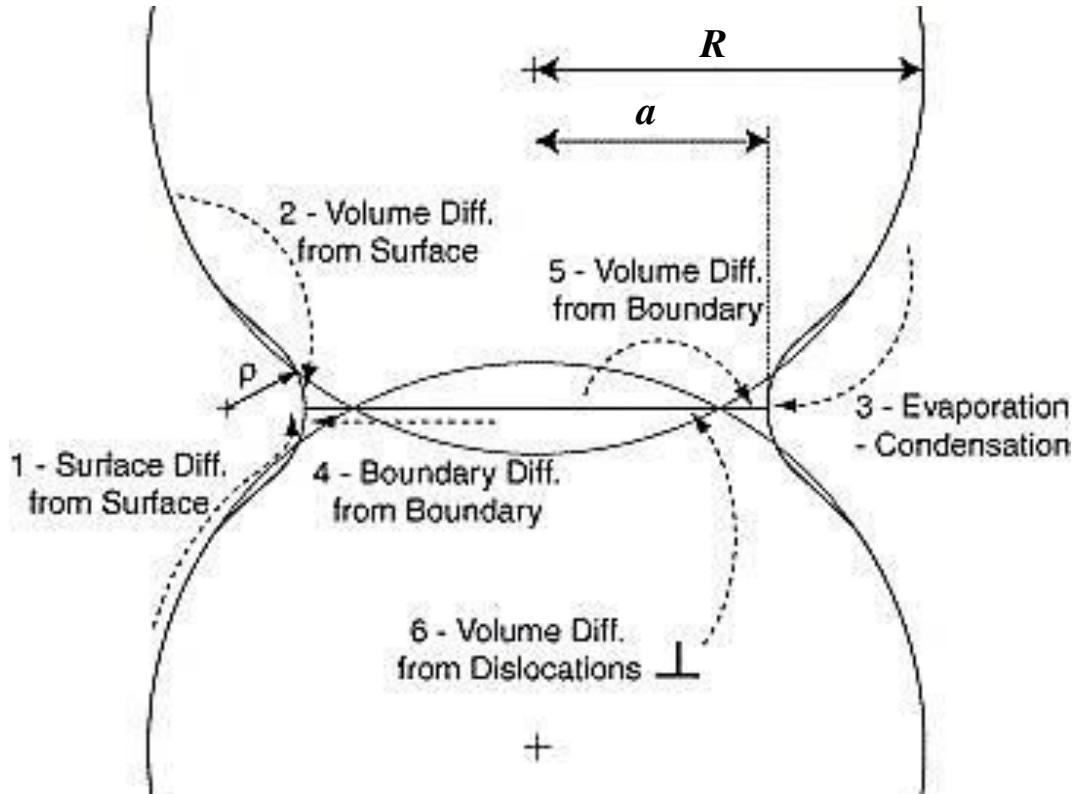


Figure 2. 1 Six mechanisms for the sintering of crystalline particles: (1) surface diffusion, (2) volume diffusion from the surface, (3) evaporation/condensation transport, (4) grain boundary diffusion from the grain boundary, (5) volume diffusion from the grain boundary, and (6) plastic flow by dislocation motion (after Rahaman [43]).

### 2.1.2 Sintering stages

The curves in the Figure 2.2 shows the relative density against the sintering time in a typical sintering. Sintering is usually subdivided into three sequential stages referred to as: (1) the initial stage, (2) the intermediate stage, and (3) the final stage.

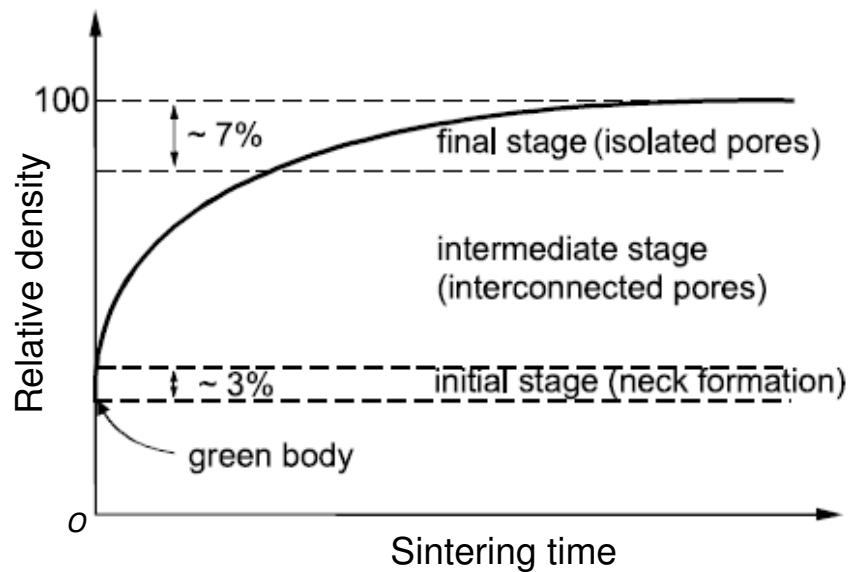


Figure 2. 2 Shrinkage during a typical sintering (after Kang [44].)

- 1) *The initial stage*: this stage features a rapid inter-particle neck growth (Fig. 2.3) by diffusion, vapor transport, plastic flow, or viscous flow. Large initial differences in surface curvature characterize this stage, and densification accompanies neck growth for the densifying mechanisms. It is assumed to last until the normalized neck radius<sup>3</sup> has reached a value of 0.4-0.5. This corresponds to a linear shrinkage of around 3% when the densifying mechanisms dominate, for a packing with an initial green density of 0.5-0.6.
- 2) *The intermediate stage*: this stage begins when pores have reached their equilibrium shapes as governed by the surface and interfacial tensions. Densification is assumed to result from pores simply shrinking to reduce their cross section. Finally, the pores become unstable and pinch off, resulting in isolated pores. The intermediate stage normally covers the major part of the sintering process, and it comes to an end when the density is ~0.9.
- 3) *The final stage*: the final stage begins when the pores pinch off and become isolated at the grain corners. With continuous shrinking of pores, relative density of 0.90-0.95 is achievable. Fully dense final state has been achieved in the sintering of several real powder systems when all the pores vanish (Fig. 2.3).

<sup>3</sup> Defined as the ratio of neck to particle radius

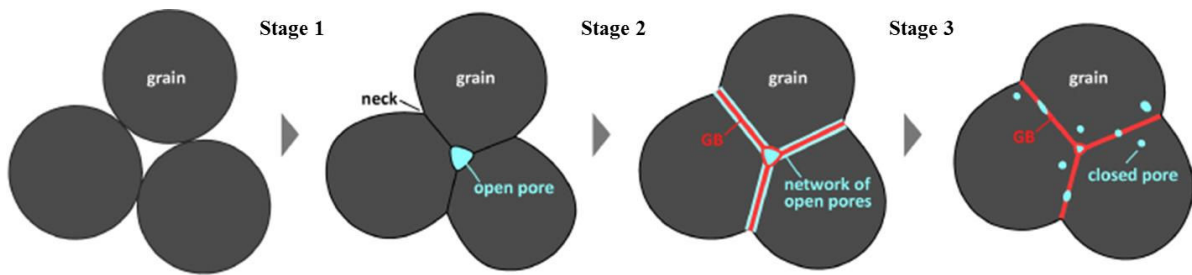


Figure 2. 3 The three stages of sintering and microstructure (after Tanaka [45])

## 2.2 Constrained sintering

The term *constrained sintering* is commonly used to refer to sintering in which a geometrical constraint is present, as shown in Figure 2.4. Conversely, a system in which the constraint is absent is referred to as free or unconstrained system. The constraint may be inherent to the sintering system: for example, a second rigid phase (particles, platelets or whiskers) is incorporated intentionally into the matrix to obtain tunable functionality and improve the mechanical properties. A common feature of such inhomogeneities is that they often lead to different local densification, referred to as *differential densification*. Due to sintering shrinkage mismatch, some regions will be constrained by others. Even in a single-phase material system, the presence of agglomerates or inhomogeneous powder packing in the green bodies also provides constraining conditions (Fig. 2.4(a)). The inhomogeneities can also be density variations (green-density gradients) through a single-phase porous media (Fig. 2.4(b)).

Adherent films/coatings on a rigid substrate are required in some important applications, such as corrosion resistance coating, thermal barrier coating, insulating and optical coatings. Coatings made by deposition of particles, sol-gel or consolidated agglomerates need further densification. When a thin ceramic film is sintered on a rigid substrate, it is placed under biaxial tension and the densification can only occur in vertical direction (thickness direction) (Fig. 2.4(c)).

Multilayered ceramics are widely used and being developed in electronics, information, medical and energy. Excellent examples include Low/High Temperature Co-fired Ceramics, Solid Oxide Fuel Cells, and piezoelectric multilayer actuators. When these multilayered

structures are co-fired, the different layers intend to shrink at different rates and constrain each other, giving rise to internal compatibility stresses (Fig. 2.4(d)).

In the four types of co-sintering, two or more materials with different inherent densification behaviors are in physical contact. The difference in the densification behavior originates from the chemical nature or physical characteristics (e.g., particle size, green density) that control the densification behavior. The internal stresses induced have the potential to hinder densification and lead to defects and/or distortion in the fired bodies.

In this section, focus will be concentrated on sintering with inclusions and co-sintering of multilayers. An example of density-induced constrained sintering can be found in Ref. [46].

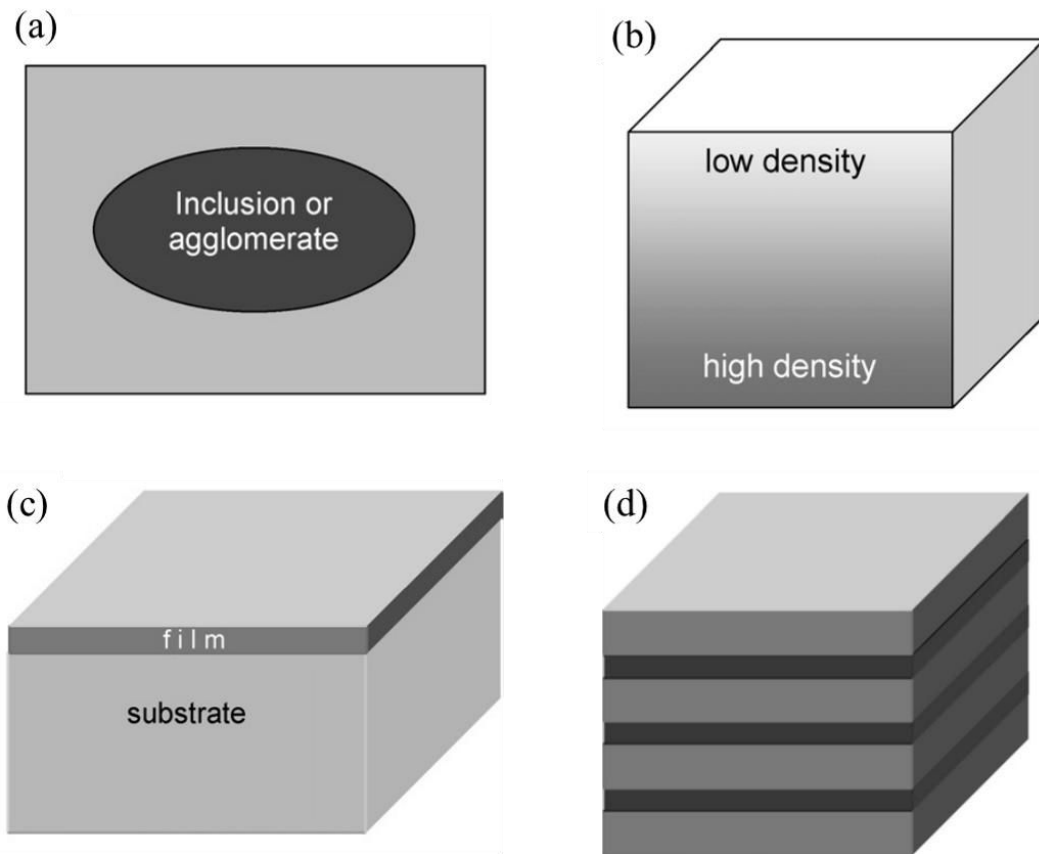


*Figure 2. 4 Schematic illustrations of structures that will undergo differential densification (a) Sintering of composite materials in which a porous matrix densifies around rigid inclusions; (b) a porous material that has a gradient in density; (c) a thin film densifying on a rigid (nondensifying) substrate; (d) Layered structures of two or more types of materials that densify at different rates (after Green [47])*

### 2.2.1 Sintering with inclusions (agglomerates)

The presence of inert and rigid inclusions results in drastic reduction in the densification rates of both polycrystalline ceramic matrix composites [48-51] and metal matrix composites [31, 37, 52, 53]. Hence, due to inhomogeneous or random distribution of the inclusions, differential densification takes place during sintering. This sintering shrinkage mismatch results in stresses concentration at the interfaces. Theoretically, when stresses exceed the strength of the materials, crack, delamination will develop, resulting in detrimental failure or loss of functionality (Fig. 2.5).

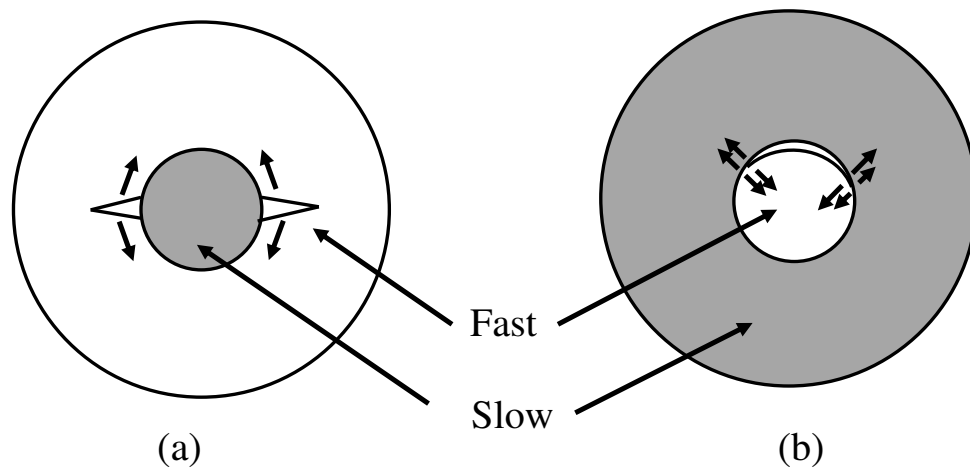


Figure 2. 5 Two types of interface flaws produced by the tensile stress when one region (shaded) sinters slower than the other: (a) radial cracks; (b) circumferential cracks (reproduced after Raj [48])

Different models have been proposed to describe the sintering behavior of such mixtures and have been reviewed by Bordia and Scherer [54-56]. These theoretical models and simulations operate under the following conditions: (i) the matrix is homogeneous and isotropic [57], and may be treated as a continuous linear viscoelastic body [48], (ii) the inclusions are inert rigid spherical particles that are homogeneously distributed in the matrix [58].

- **The Rule of Mixtures**

The rule of mixtures assumes the densification of the composite to be a weighted average of the independent densification rates of the matrix and of the inclusions; that is, it assumes that in the composite, each phase densifies in the same way as it would independently by itself. If, for example, we consider the *linear* densification rate  $\dot{\epsilon}$ , defined as one-third the *volumetric* densification rate  $1/\rho(dp/dt)$ , then according to the rule of mixtures:



$$\dot{\epsilon}_c = \dot{\epsilon}_m^{free} (1 - v_i) + \dot{\epsilon}_i v_i = \dot{\epsilon}_m^{free} (1 - v_i) \quad (2.4)$$

where  $\dot{\epsilon}_c$  is the composite densification rate,  $\dot{\epsilon}_m^{free}$  is the densification rate of the free matrix, and  $\dot{\epsilon}_i$  ( $=0$ ) is the densification rate of the inclusions. According to Eq.(2.4), the ratio  $\dot{\epsilon}_c / \dot{\epsilon}_m^{free}$  varies linearly as  $(1 - v_i)$ .

This model is considered limited and inadequate to describe the sintering behavior of the composites because the assumptions are too simplistic.

- **Scherer's Model [55, 57]**

Scherer proposed the Composite Sphere (CS) model to deal with sintering with well-dispersed inclusions. In the CS model, a core/cladding structure is used to represent the porous matrix in which the core represents the inclusion and the cladding represents the matrix (Fig. 2.6(a)). When the inclusion is much larger than the matrix particle size, justified in most practical composites, the matrix can be considered as a continuum. In doing this, phenomenological constitutive equations can be used for matrix.

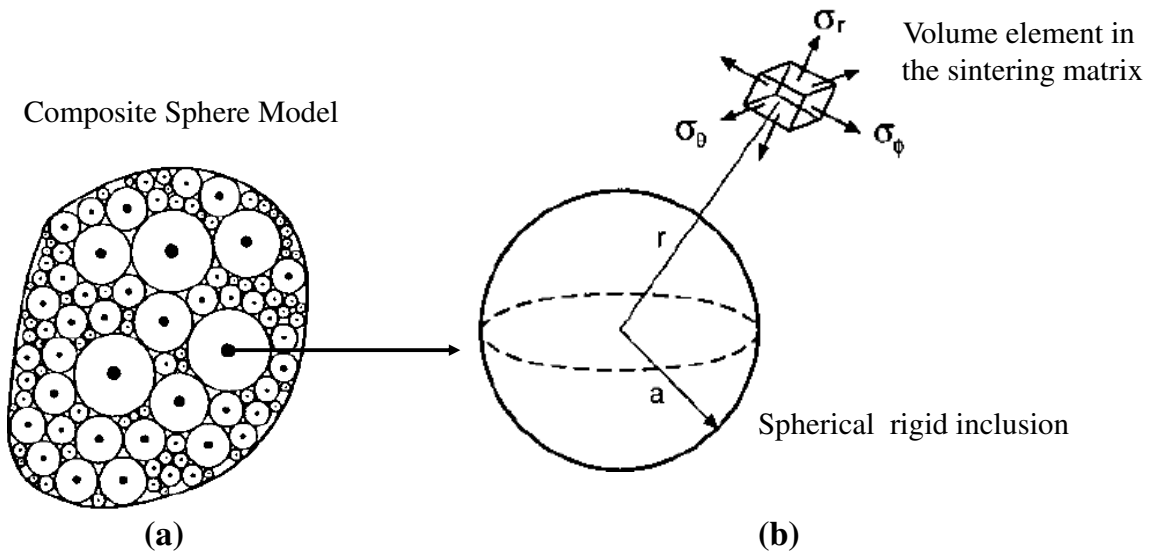


Figure 2. 6 (a) the composite sphere model; (b) the stress components in a volume element at a distance  $r$  in the sintering matrix. The sphere has  $v_i$  (volume fraction) of inclusions with radius value  $a$  and outer radius  $b$  (adapted from [55, 57])

A shrinking cladding (matrix) around a core (inclusion) gives rise to compressive stresses within the core and a compressive radial stress and tangential tensile stresses within the cladding (Fig. 2.6(b)). The mean hydrostatic stress in the matrix is:

$$\sigma_m = \frac{1}{3}(\sigma_m + \sigma_{\theta m} + \sigma_{\phi m}) = -\sigma_i \left( \frac{v_i}{1-v_i} \right) \quad (2.5)$$

According to Eq.(2.5), the mean hydrostatic stress  $\sigma_m$  is uniform in the matrix and it is independent of the radius and shape of the inclusions. Since  $\sigma_i$  is compressive,  $\sigma_m$  is tensile, opposing to the compressive sintering stress.  $\sigma_m$  is often called a backstress.

The linear densification rate in the matrix is given by:

$$\dot{\epsilon}_m = \frac{\Sigma + \sigma_m}{K_m} = \frac{1}{K_m} \left[ \Sigma - \sigma_i \left( \frac{v_i}{1-v_i} \right) \right] \quad (2.6)$$

Where  $\Sigma$  is the sintering potential. It is also the compressive hydrostatic stress that causes densification of an unconstrained sintering material [54].  $K_m$  is the densification or bulk viscosity. The backstress  $\sigma_m$  opposes  $\Sigma$  so it reduces the densification rate of the matrix. The tensile hoop stress  $\sigma_m$  may influence the growth of radial cracks in the matrix.

### **2.2.2 Constrained sintering of film and multilayers**

A common feature in sintering of these coatings and multilayers is that different components densify at different rates. Different stress states develop in the layers in analogy to the thermal expansion mismatch. The stresses in turn interact and modify the densification behavior of different layers. For instance, in-plane tensile stresses develop in the coating due to the constraint imposed from the substrate. This stress lowers the densification rate of the constrained film relative to that of a freely sintered one [59].

- **Sintering of thin films**

Bordia and Raj [60] studied the sintering of thin ceramic films on rigid substrates and presented a model using phenomenological descriptions of the densification and shear properties. Scherer and Garino [61] and Hsueh [62] performed similar analyses. Assuming the densifying film is linear viscous, by analogy with Hooke's law, the sintering rate along the orthogonal  $x$ ,  $y$ , and  $z$  directions can be written as:

$$\begin{aligned}\dot{\varepsilon}_x &= \dot{\varepsilon}_f + \frac{1}{E_p}(\sigma_x - \nu_p[\sigma_y + \sigma_z]) \\ \dot{\varepsilon}_y &= \dot{\varepsilon}_f + \frac{1}{E_p}(\sigma_y - \nu_p[\sigma_x + \sigma_z]) \quad (2.7) \\ \dot{\varepsilon}_z &= \dot{\varepsilon}_f + \frac{1}{E_p}(\sigma_z - \nu_p[\sigma_x + \sigma_y])\end{aligned}$$

If the film is totally constrained in the  $xy$  plane, then  $\dot{\varepsilon}_x = \dot{\varepsilon}_y = 0$  and the film stress,  $\sigma_f$ , is easily derived from Eq.(2.7) as:

$$\sigma_f = -\frac{E_p \dot{\varepsilon}_f}{1 - \nu_p} \quad (2.8)$$

The strain rate in the non-constrained direction,  $\dot{\varepsilon}_z$ , also follows and it depends only on  $\nu_p$  and the unconstrained strain rate:

$$\dot{\varepsilon}_z = \dot{\varepsilon}_f \left( \frac{1 + \nu_p}{1 - \nu_p} \right) \quad (2.9)$$

- **Sintering of laminates**

In absence of external forces, the integrals of forces and bending moments along the thickness direction  $z$  should be equal to zero for a multilayer in mechanical equilibrium. Cai et. al. [63] considered a symmetric laminate consisting of alternating layers of two sintering materials. Applying the infinite plate solution to materials that densify by linear viscous sintering, it was shown that the equi-biaxial stresses that arise in the layers are given by:

$$\begin{aligned}\sigma_1 &= \frac{1}{1 + mn} E_{p1}^i \Delta \dot{\varepsilon} \quad (2.8) \\ m &= \frac{t_1}{t_2}, \quad n = \frac{E_{p1}^i}{E_{p2}^i} \quad (2.9)\end{aligned}$$

Where  $t$  is the layer thickness,  $\Delta \dot{\varepsilon} = \dot{\varepsilon}_1 - \dot{\varepsilon}_2$  the strain rate difference between the layers,  $E_p^i = E_p / (1 - \nu_p)$  for plates and  $E_p^i = E_p$  for beams and the subscripts refer to layer 1 or 2. The above solution is obtained by setting the strain rates in the two layers equal to each other and maintaining a force balance for the compensating tensile and compressive stresses in the two layers.

When the stress is higher than the strength of materials, a variety of defects and shape distortions can be generated, including warpages [64-70], cracks [71] and delamination [72]

as shown in Figure 2.7. Besides, anisotropic pore orientation develops during constrained sintering of layers [73, 74].

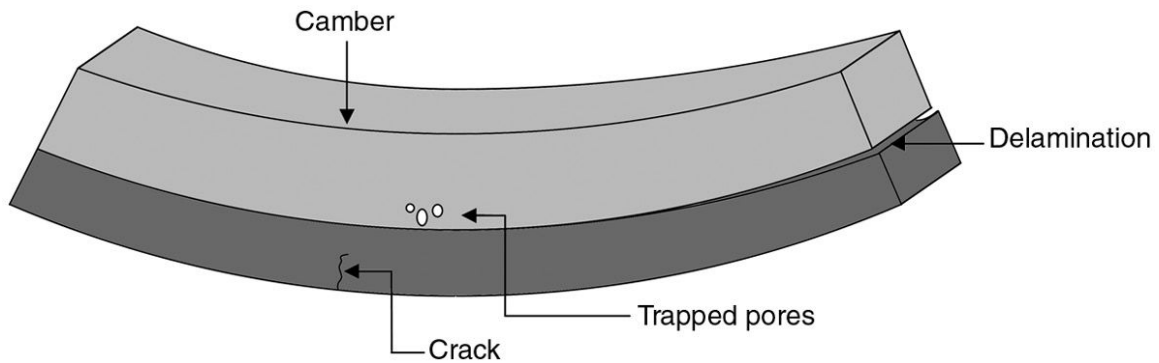


*Figure 2. 7 A schematic of defects induced by constrained sintering of layers [75]*

In addition, when the thickness of polycrystalline film or thin layer is less than the critical value (in which case, the single grains cross the layer), they may become unstable under an interfacial energy equilibrium disturbance [76] and break up into discontinuous islands [38], thereby uncovering the substrate [31]. This instability is driven by capillarity (surface tension) due to the thermodynamic requirement of minimization of the interfacial energy. A necessary condition is that the film/substrate interface has a higher specific energy than the substrate surface. Miller et al. [77] analyzed the breakup phenomena of an  $Y_2O_3$ -stabilized  $ZrO_2$  film (8 mol%  $Y_2O_3$ ) that was prepared by spin coating. By evaluating the total energy of the surfaces and interfaces to determine its minimum value as a function of the configuration of the film, an equilibrium configuration diagram was calculated (Fig. 2.8). The diagram can be divided into three regions, showing the conditions for the completely covered substrate, the uncovered substrate and the partially connected film (with the grain boundary just intercepting the substrate).

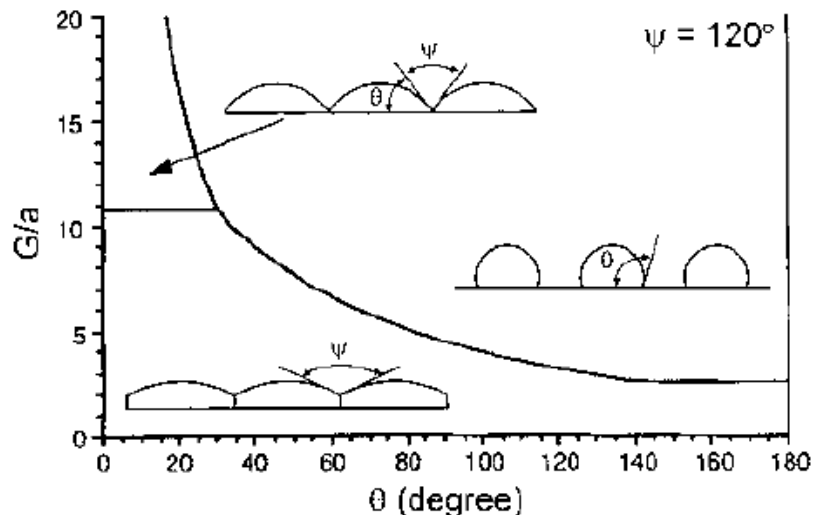


Figure 2. 8 An equilibrium configuration diagram for the sintering of a thin film with thickness of  $a$  and grain size of  $G$  (dihedral angle  $\psi = 120^\circ$ ) ( after Miller [77])

### 2.3 Co-firing of MLCCs

Firing is a key and complex stage in the manufacture of MLCCs. In this stage of the fabrication route, the green chips are loaded into continuous kilns and fired on zirconia slabs. The multilayer capacitors with noble metal electrodes (NME), such as pure Pd, Ag-Pd and pure Ag inner electrodes are fired in air since they exhibit excellent oxidation resistance. Conversely, firing of MLCCs with Ni, Cu electrode is conducted in moist reducing atmosphere (0.1-0.01% $H_2$ /Ar- $H_2O$ ) to control the oxygen partial pressure  $pO_2$  during the firing process. Time dependent changes in firing conditions, as well as variations caused by location of the parts in the kiln, must be minimized. A second binder burn-out (bake-out) (BBO) is applied to completely deplete the organics. After the sintering step the products are re-oxidized at a lower temperature of 1000 °C in a higher  $pO_2$  atmosphere consisting of moist Ar to recover resistivity. Figure 2.9 shows a typical firing profile for Ni-MLCCs.

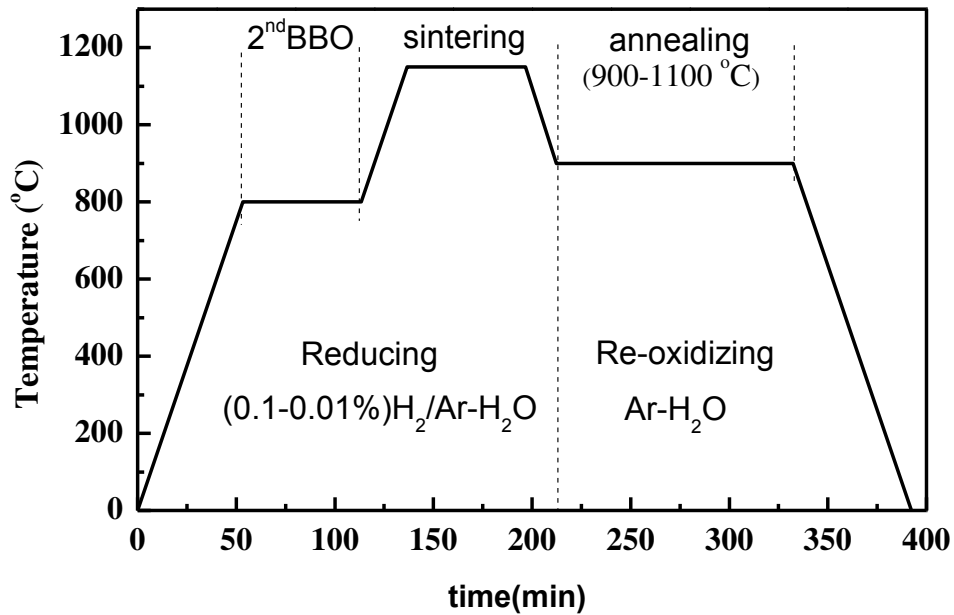
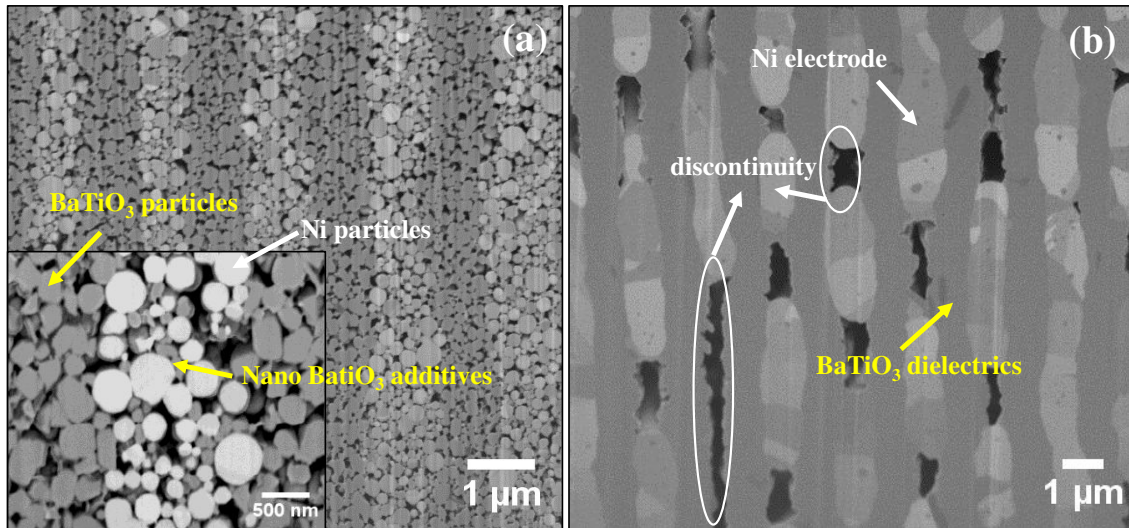


Figure 2. 9 A typical firing cycle for the Ni-MLCCs

Nano-sized BT particles are added to the nickel paste (see Fig. 2.10) to reduce the sintering shrinkage mismatch between nickel and BT layers during the firing process. The onset sintering temperature for Ni electrode material is 400-600 °C, and the onset sintering temperature for BT is 900-1000 °C [29]. Thus, we are expecting the following sintering scenarios:

- I. During the heating ramp and the second BBO, the Ni particles in the electrode sinter while the sintering of BT has not started yet. In presence of BT additive nanoparticles, the sintering kinetics of Ni particles is expected to be modified.
- II. During the early stage of sintering of Ni particles, the particles at the interfaces interact with the BT particles through viscous friction. This interaction should hinder the rearrangement of the Ni particles.
- III. At high temperature (>1000 °C), sintering of Ni and BT co-exists. This has been referred to as co-sintering due to the different sintering strain rates encountered in the different layers. In addition, different stress states develop in the layers. This in-plane stress state plays an important role in the anisotropy development.



*Figure 2. 10 FIB treated cross-sections of 0603 size 22  $\mu$ F Ni-MLCC (Samsung Electro-Mechanics, Inc.) (a) before firing; (b) after firing*

## **2.4 Conclusion**

We have attempted in this chapter to relate the sintering sciences and the practical firing processes employed in the MLCC industry. Based on this review, we conclude that in order to understand defect evolution during the co-firing process of MLCCs, the sintering behavior and the microstructure evolution must be better analyzed. This may be undertaken by studying in more details the co-sintering of Ni/BT composite material and of Ni/BT multilayers.

The general aim of this thesis is to describe the use of novel tools (tomography and numerical simulations) that may help in attaining this goal.

## Chapter 3

# Material characterization and sintering behaviour study

The aim of this chapter is to characterize the materials involved in this work, including the starting Nickel (Ni) powder and the BaTiO<sub>3</sub> (BT) dielectrics powder. The Ni-electrode BT based MLCC chips were also characterized. The microstructures of these materials were characterized using Scanning Electron Microscope (SEM) and their sintering behavior were characterized by dilatometry.

### 3.1 Materials

- *Starting powders*

Ni powder and X5R BT powder were provided by Samsung Electro-mechanics (Suwon, South Korea). Ni powder (Shoei Chemical, Tokyo, Japan) is made using a PVD (Physical vapor deposition) method. X5R type characteristic 99.9% BT powder (NanoAmor, Inc., NM, USA) is made using solid state synthesis as the dielectric material. Nickel paste is made by mixing 55 vol. % of Ni and nano-sized BT powder at a ratio of 100 : 7 by weight with 41 vol. % terpineol (C<sub>10</sub>H<sub>18</sub>O) and 4 vol. % resin.

- *MLCC manufacture*

For Ni-electrodes MLCC chips, EIA 1206 series (3.2 × 1.6 × 1.6 mm<sup>3</sup>), and EIA 0603 series (1.6 × 0.8 × 0.8 mm<sup>3</sup>), were fabricated at Samsung Electro-mechanics (Suwon, South Korea). Dielectric sheets (2.5-μm-thick) were fabricated by tape casting with X5R type BT powder. Electrodes (1.2-μm-thick) were made with deposition of nickel paste on those sheets using screen-printing. Patterned sheets were laminated, isostatically pressed, and finally diced into green chips.

- *Preparation of BT and electrode pellets*

Nickel paste was dried first in an oven at 100 °C for 2 hrs, and then the organic binder was removed in a muffle furnace with a temperature profile: heating 25-120°C at 3°C/min and



120-230 °C at 0.3 °C /min, holding for 2 hrs at 230 °C, and cooling 230-25 °C at 3 °C/min. The debinded bulk Ni paste was ground into powder in a corundum mortar.

Ni and BT powders were compacted in a closed cylindrical die (inner Ø 8mm) under uniaxial pressure of 30 MPa using a P/O/Weber (PW100, Remshalden, Germany) laboratory press.

### 3.2 Experiment procedure

- **Particle size measurement**

A LA-950 high performance Laser diffraction Analyzer (Horiba, Kyoto, Japan) was used to characterize Ni and BT particle size distribution. The LA-950 uses Mie Scattering (laser diffraction) to measure particle size of suspensions or dry powders with a measuring range of 0.01-3000 µm. In practice, a small amount of powder is dropped into water or alcohol, and give the reflective index, and then the size distribution data is gathered [78].

- **Green density**

Green density measurement was conducted by weighting the mass and measuring the volume of cylindrical samples. Some parameters are defined as follows:

$$\text{Density definition: } \rho = \frac{M}{V} \quad (3.1)$$

$$\text{Theoretical or true density: } \rho_{theor.} = \frac{M_m}{V_m} \quad (3.2)$$

$$\text{Apparent density: } \rho_{appar.} = \frac{M}{V_{envelop}} \quad (3.3)$$

$$\text{Relative density: } D = \frac{V_{solid}}{V_{envelop}} = \frac{\rho_{appar.}}{\rho_{theor.}} \quad (3.4)$$

$$\text{Percent porosity: } \phi_{porosity} = 100(1 - D) \quad (3.5)$$

Where  $M$  is the mass (Kg),  $M_m$  the molar mass (Kg·mol<sup>-1</sup>),  $V$  is the volume (m<sup>3</sup>),  $V_m$  the molar volume (m<sup>3</sup>·mol<sup>-1</sup>),  $V_{solid}$  the volume of the solid phase in the porous media, and  $V_{envelop}$  the overall volume including the volume of the solid phase and pore phase in the porous media.

For BT pellet sample, relative density is given as:

$$D_{BT} = \frac{M_{BT} / \rho_{BT}^{theor.}}{\pi\Phi^2 H / 4} \quad (3.6)$$

For composite Ni paste sample, relative density is given as:

$$D_{electrode} = \frac{V_{Ni} + V_{BT}}{V_{envelop}} = \frac{M_{Ni} / \rho_{Ni}^{theor.} + M_{BT} / \rho_{BT}^{theor.}}{\pi\Phi^2 H / 4} \quad (3.7)$$

Where  $\rho_{BT}^{theor.}$ ,  $\rho_{Ni}^{theor.}$  are the theoretical density of the BT and Ni;  $M_{Ni}$ ,  $M_{BT}$  are the mass of the Ni matrix and the BT additives in the electrode, and  $\Phi$ ,  $H$  are the diameter and height of the samples.

- **Phase determination**

Room temperature X-ray powder diffraction (XRD) was applied to determine the phases of starting powders. X-ray diffraction is based on Bragg's law. The general relationship between the wavelength of the incident X-rays, angle of incidence and spacing between the crystal lattice planes of atoms is known as Bragg's Law, expressed as [79]:

$$n\lambda = 2d\sin\theta \quad (3.8)$$

Where  $n$  (an integer) is the "order" of reflection,  $\lambda$  is the wavelength of the incident X-rays,  $d$  is the inter-planar space distance of the crystal and  $\theta$  is the angle of incidence.

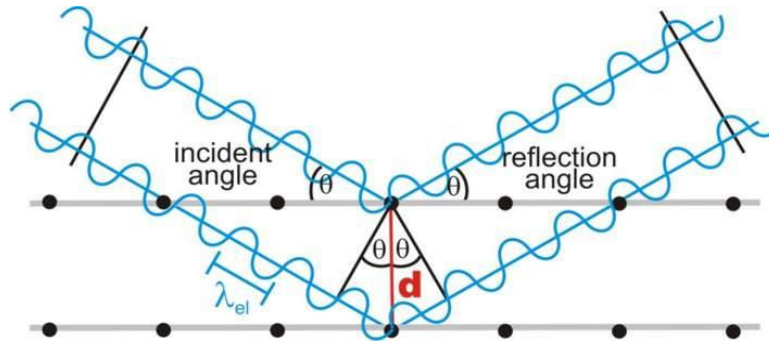


*Figure 3. 2 A schematic for the Bragg's scattering [80]*

Dry BT and Ni paste samples are analyzed using a Bruker D8 X-ray diffractometer (Billerica, MA, USA) with Cu K $\alpha$ 1 X-Ray radiation.

- **Sintering kinetics**

After the removal of binders between 120-230 °C for 30 hrs in air, the samples were sintered in a DIL-402E dilatometer (NETZSCH, Germany) in 2% $H_2$ /Ar atmosphere at 800, 900 and 1150 °C for 1 hr, at heating rate of 15 °C/min and cooling rate of 50 °C/min. To investigate

the effects of dwelling time on the electrode evolution, dwelling time was varied ( $t = 0, 5, 10, 15, 20, 25, 30, 45$  and  $60$  min). The linear shrinkages were measured in real time. Sintering behaviors of pure bulk electrode material and X5R dielectrics were also measured with a TOM-AC optical dilatometer (Fraunhofer ISC, Würzburg, Germany) as reference. The images were taken every 60 s and an average image calculated within the period of the 60 s was saved. Figure 3.2 shows the structure of the TOM-AC optical dilatometer. This optical dilatometry enables measurement with resolution of  $0.4 \mu\text{m}$  [81]

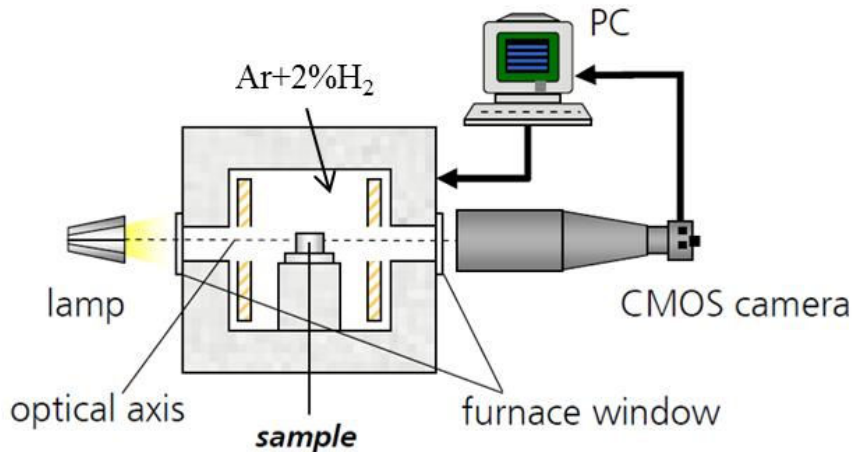


*Figure 3. 3 TOM-AC optical dilatometer (adapted from user manual of the TOM-AC)*

- **Scanning Electron Microscopy**

The starting powder of Ni paste and BT dielectrics, the green MLCC chips, the debinded MLCC chips were characterized using a FEI/Philips XL30 FEG High-resolution scanning electron microscope (HR-SEM) (Hillsboro, Oregon, USA). The cross-sections of green and the other sintered chips were characterized with an AURIGA 60 Focused Ion Beam-Scanning Electron Microscope (FIB-SEM) (Carl Zeiss, Germany). The chips were embedded in cold resin (EpoFix, Struers) then ground using SiC sand papers (#240, #600, #800, and #1200) and polished with diamond aqueous suspension abrasives (diamond particles size from  $6 \mu\text{m}$ ,  $3 \mu\text{m}$ ,  $1 \mu\text{m}$ , and  $0.25 \mu\text{m}$ ). The polished cross-sections of the samples were cleaned with flowing alcohol and dried quickly with compressed air. The powder samples were prepared by dropping a small amount of powder on a conductive tape. Prior to the SEM measurements, the BT power sample, cross-section sample were coated with thin gold thin film in an argon atmosphere using a sputtering coater (SCD 050, BAL-TEC) at a current of 40 mA for 20 s.

### **3.3 Results and discussions**

- **Particle size distribution (PSD)**

Figure 3.3 shows the PSDs of the starting powders (Ni powder and BT powder). Both powders follow a lognormal size distribution function.

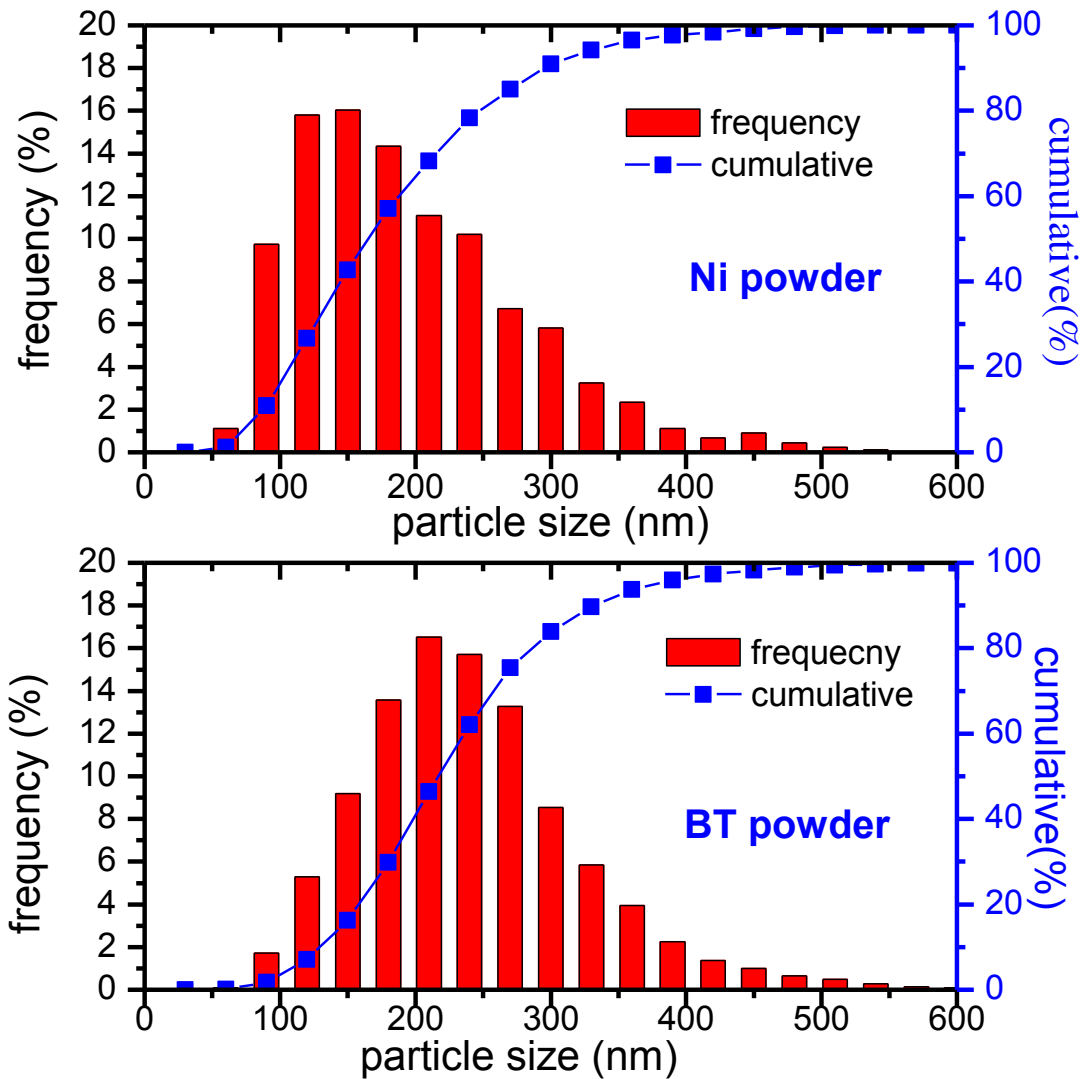


Figure 3. 4 Particle size distributions: (a) Ni powder (b) BT powder

Table 3.1 shows particle size characteristics of both powders. BT powder has a narrower span, defined as  $(D_{90}-D_{10})/D_{50}$ , than Ni powder.

Powder	$D_{mean}$	$D_{10}$	$D_{50}$	$D_{90}$	Span = $(D_{90}-D_{10})/D_{50}$
BT	0.260	0.16	0.23	0.34	0.783
Ni	0.181	0.088	0.164	0.294	1.257

Table 3.1 particle size of the BT and Ni powder

In MLCC industry, nano sized BT additives are added into the Ni powders to make the electrode paste. Ueyama et al. [31] reported that the largest particle size ratio of ceramic (BT) particles/metallic (Ni) particles is 0.155, because it is required that the smaller ceramic

particles enter triple bond spots (three spots) among the Ni particles. In this work, the mean size of the BT additive nanoparticles for the Ni-MLCC chip is 50 nm.

• **Phase determination**

Figure 3.4 shows the XRD patterns of the starting powders. In Figure 3.4(a), only single phase, tetragonal BT (PDF # 05-0626), is detected from BT powder. As shown in Figure 3.4(b), Ni (PDF # 04-0850) as a major phase and additive BT (PDF #05-0626) as a secondary phase are confirmed in the Ni paste.

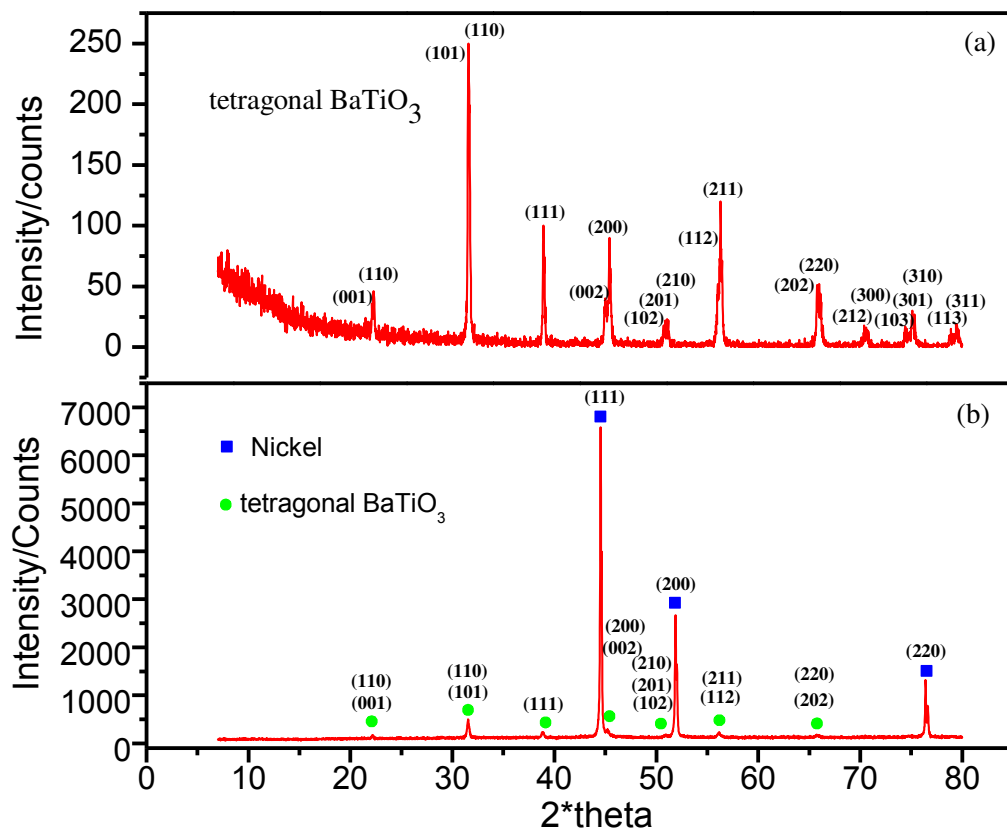


Figure 3. 5 XRD pattern of the starting powders: (a) BT powder; (b) Ni paste (debinded)

• **Green density**

Table 3.2 shows the green density of the compacted pellets of BT sample and Ni paste samples for the sintering curve measurements.

Materials	$M$ (g)	$\rho_{theor.}$ (g/cm <sup>3</sup> )	$\Phi$ (cm)	$H$ (cm)	$V_{envelop}$	$V_{solid}$	$D$
Dielectric BT	0.5285	6.020	7.77	6.14	148.889	87.791	0.590
Electrode Ni	0.6550	8.908				73.529	
(Ni:BT=10:1) BT	0.0655	6.020	7.89	6.22	157.434	10.880	0.536

Table 3.2 Density of BT and Ni pellets for the sintering curve measurements

• **Sintering behavior**

Figure 3.5 shows the shrinkage and densification rate of Ni electrode paste and X5R type dielectrics powders as a function of time. The densification onset temperature of electrode paste was around 450 °C, much sooner than that of the dielectrics, 900-950 °C (Fig. 3.5(a)). It can be seen in Figure 3.5(b) that the maximum densification rate of Ni electrode corresponds to 900 °C. The densification rate decreases as the temperature increases further. The reason for this decrease in densification rate is the coarsening of Ni grains. The densification rate of Ni is almost zero when maximum temperature (1150 °C) is reached. In contrast, the densification rate of BT peaks at 1150 °C and densification ceases after about 25-30 min dwelling time at this maximum temperature.

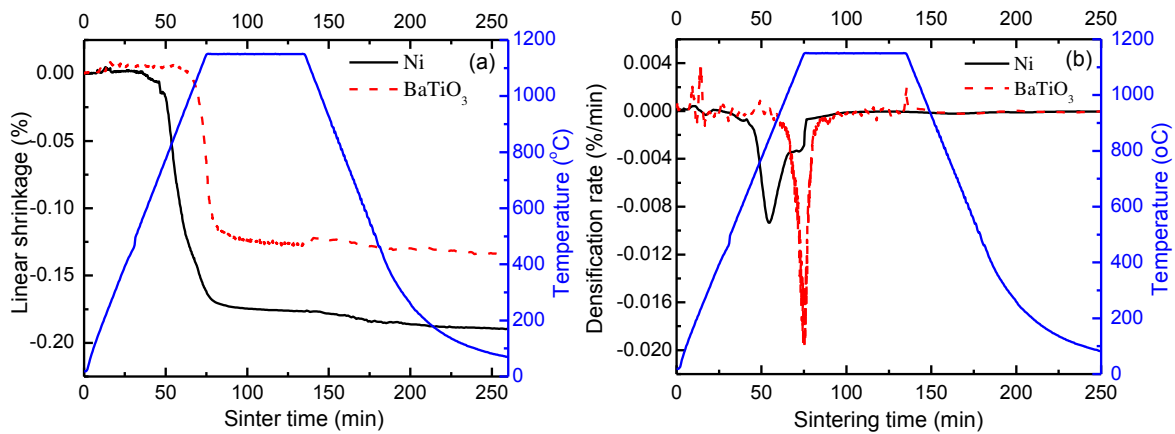


*Figure 3. 6 Linear shrinkage of nickel paste and dielectrics*

Figure 3.6 shows the densification behaviors of Ni-MLCC chips sintered with different temperature profiles. The densification of all the Ni-MLCC chips starts around 900 °C that is the same as the sintering onset temperature of the dielectrics. The densification of the electrode (450-950 °C) does not contribute to the macroscopic densification of the chips until the dielectrics begin to sinter. All the densification curves are identical until the temperature reaches 1150 °C. Sintering in the range of 950-1150 °C accounts for 6-7% shrinkage, that is about half of the final shrinkage. The densification leads to a ~12% linear shrinkage after holding time of 30 min at 1150 °C. Sintering curves for dwelling time  $t = 30-60$  min are identical and longer dwelling times do not contribute to further densification.

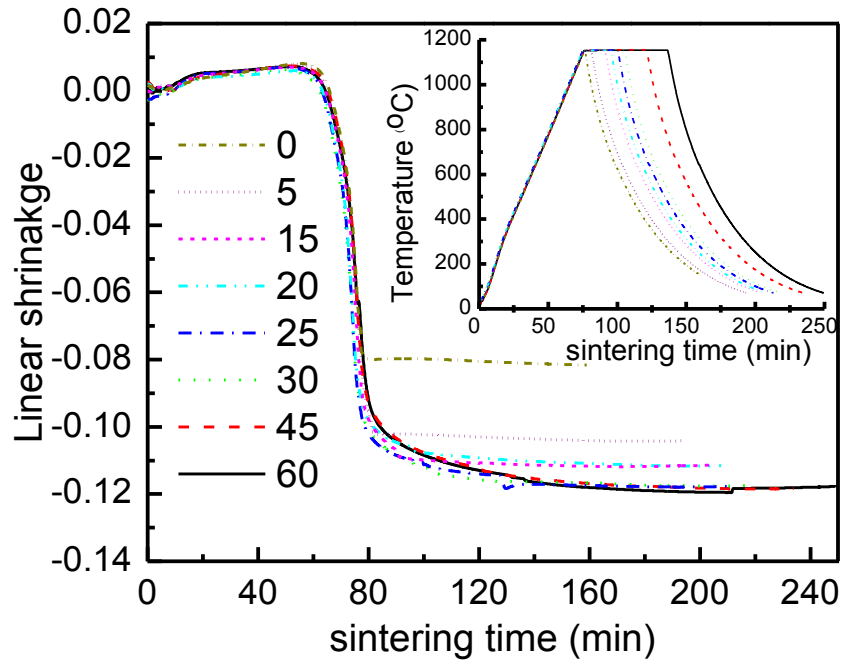


Figure 3. 7 linear shrinkage of 1206 type MLCCs

- **Microstructures**

Figure 3.7 shows the morphology of the starting BT and Ni powders. The BT particles (Fig. 3.7(a)) made using solid synthesis are irregular, while Ni powders made using PVD are almost spherical. As could be seen in the Ni paste, nano scaled BT additives aggregate together.

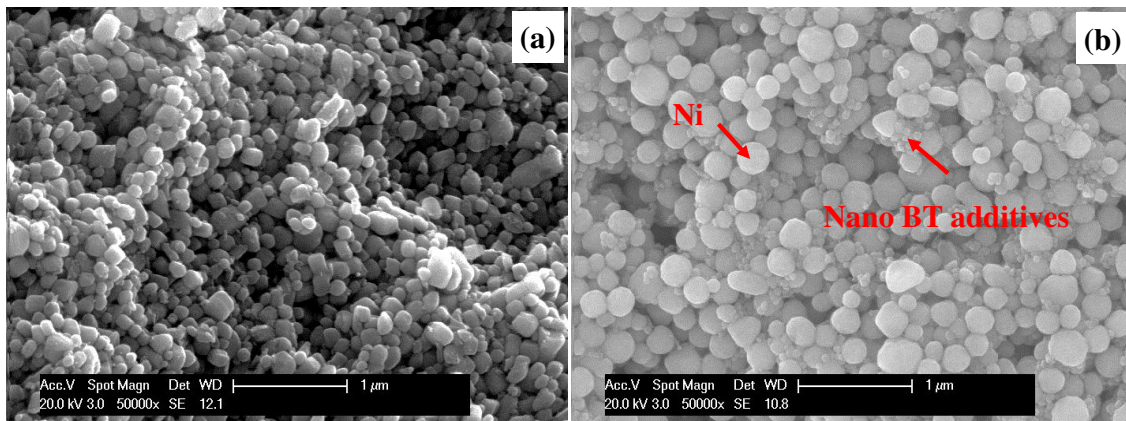
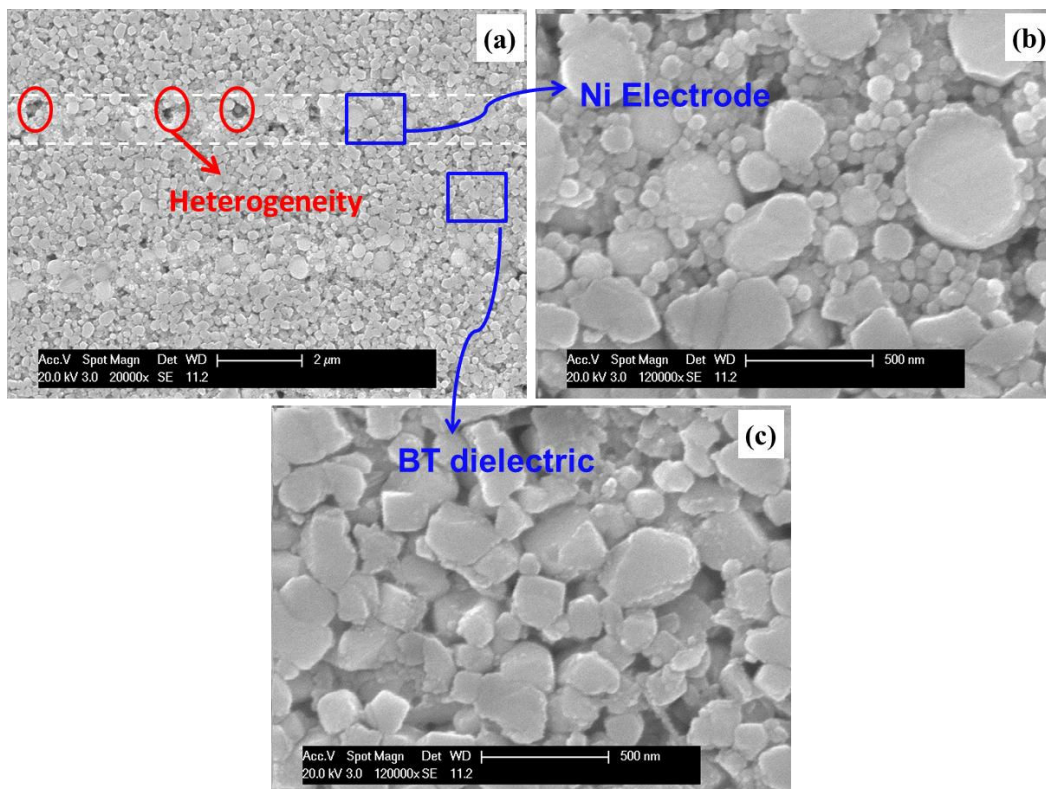


Figure 3. 8 Starting powders: (a) X5R type BT powder; (b) debinded Nickel paste

Figure 3.8 shows the microstructures of the cross-sections of the green chips before the binder burnout (BBO). In the  $\sim 1 \mu\text{m}$ -thick electrode, there are about 4-5 layers of Ni particle packing on the top of each other (Fig. 3.8(a)). Heterogeneities in Ni packing can be observed in the form of pores that are larger than the particles. Particles arrange into well packed

regions (or agglomerates) surrounded by low density regions. In this work, we refer to pores inside these well-packed agglomerates as intra-agglomerate pores and to pores in between agglomerates as inter-agglomerate pores. Some authors use a different wording. Bordia, for example, defines intra and inter- pores as intra and inter- granular pores [82]. Figure 3.8(b) and (c) show the zoomed Ni packing in the electrode and the BT packing in the dielectric layer, respectively. The electrode layer is more porous than the dielectric layer. The heterogeneities and high porosity in the electrode might be due to the addition of a significant amount of organics (40-50 vol.%) which are mixed with powder to enhance the ink rheological property such that it is suitable for the screen printing process. Note that the nano sized BT additive particles in the electrode are aggregated. This agglomeration appears probably during the making and/or the drying of the Ni paste.

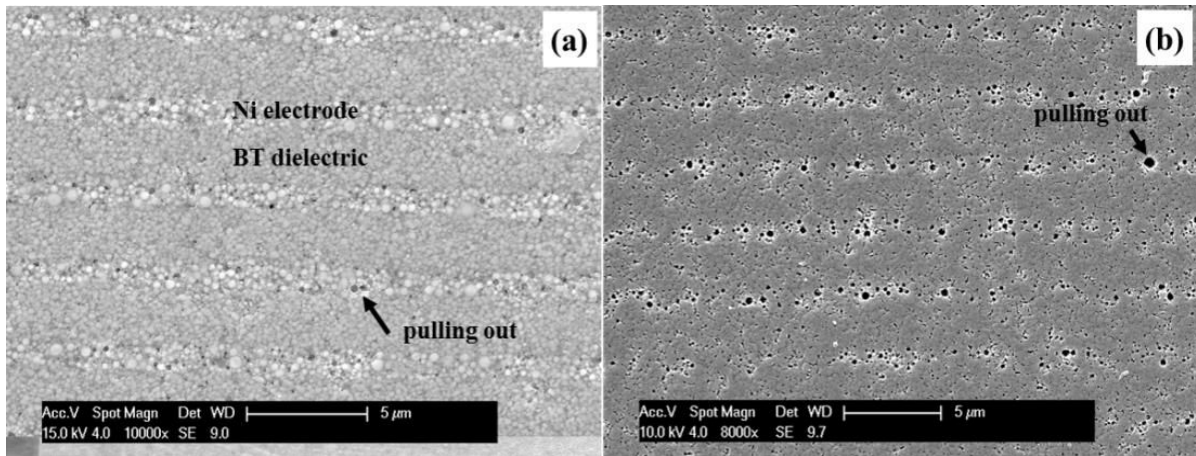


*Figure 3. 9 Green chips with binders at three different magnifications: (a) 20000 ×; (b) 12000 × dielectric layer; (c) 12000 × Ni layer*

Figure 3.9 shows the microstructures of the sample after the first BBO process. The cross-section was prepared using traditional sectioning and polishing. It is observed that a substantial fraction of inter-agglomerate pores remain. This may be due to the pulling out of the particles during the polishing process. After the removal of the polymeric binders,

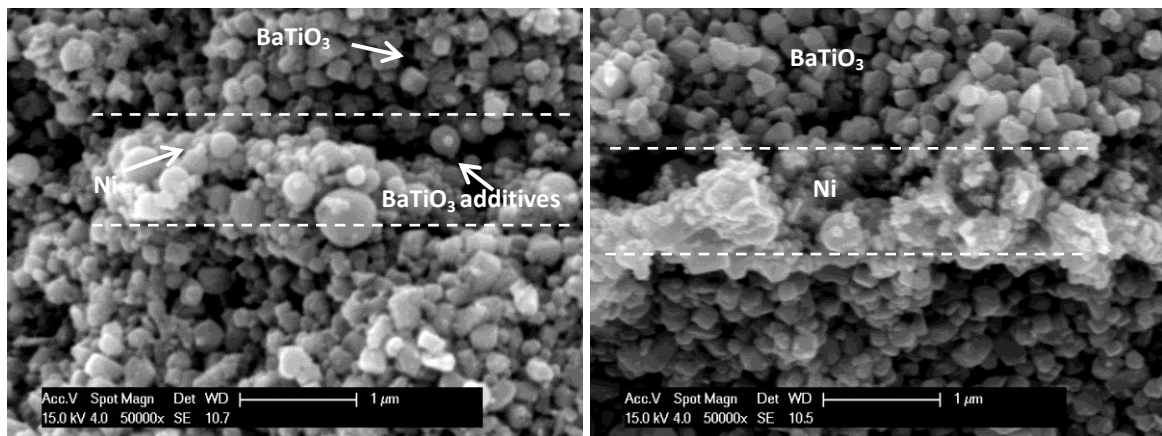


adhesion between nickel particles is degraded. This means that a conventional sectioning method can be problematic in studying the defect formation in the electrode.



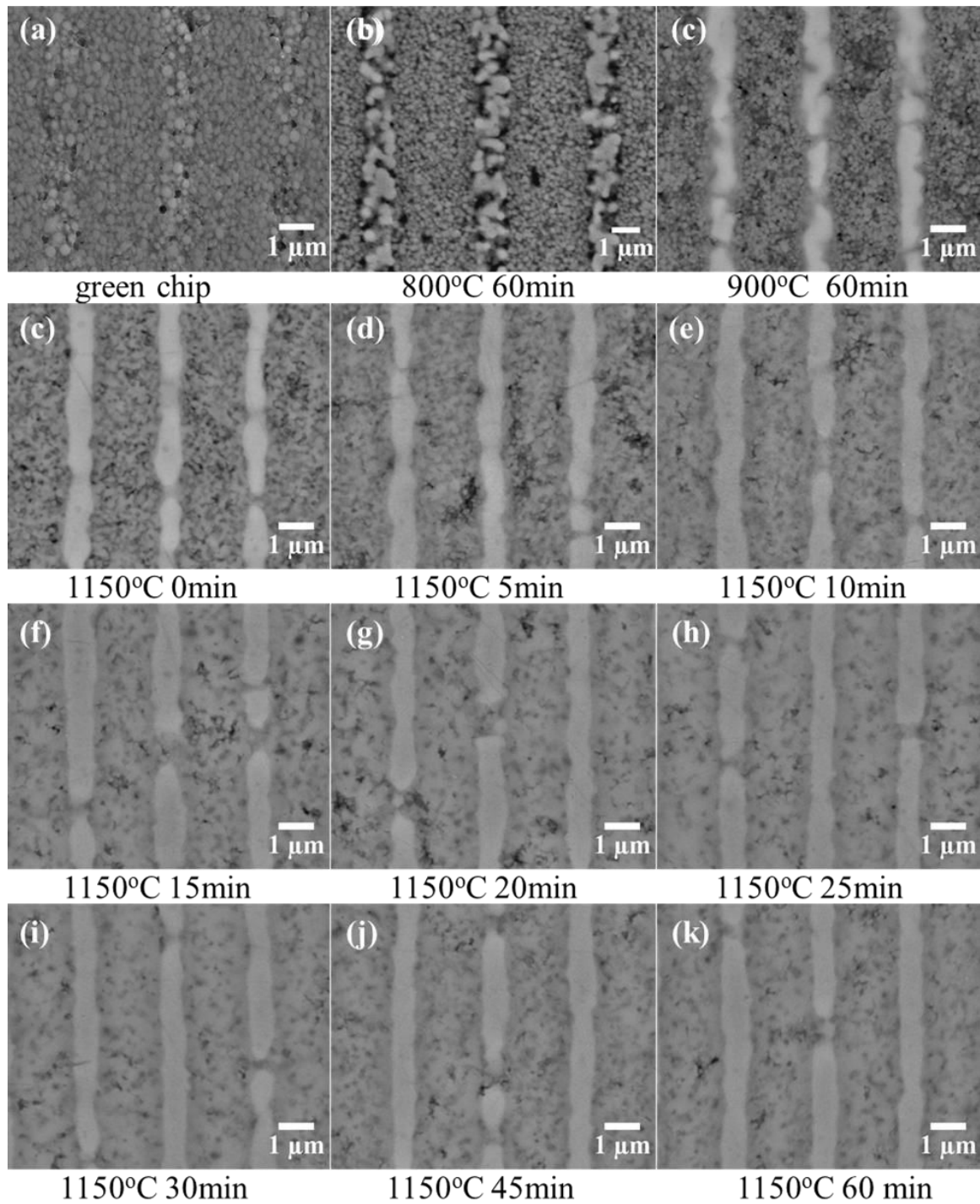
*Figure 3.10 SEM images of cross-section of debinded sample: (a) SE; (b) BSE*

Figure 3.10(a) shows the fracture surfaces of the green chips after the first BBO process (230 °C, 34 hrs). Nanocrystalline BT particles dispersed in the nickel matrix can be noticed. They are used to increase the onset temperature for sintering and reduce the densification rate of electrode layers. After the second BBO (800 °C, 1 hr), which is required to burn-out the organics binders completely, nickel powder sintered already, as shown in Figure 3.10(b). No significant modification can be observed in the BT powder in the dielectrics layers.



*Figure 3.11 SEM images of the fracture cross-sections of (a) green chip and; (b) after bake-out at (800 °C)*

Figure 3.11 shows the microstructural evolution at different sintering stages.



*Figure 3. 12 Microstructural evolution of chips sintered with different temperature profiles*

Figure 3.11(a) and (b) show polished cross-sections of the green chips after the first (230 °C) and second BBO (800 °C). It is very clear that the electrode already densified during the second BBO. Clustering of Ni particles occurred and pores were enlarged. When the temperature reaches 900 °C, as shown in Figure 3.11(c), some discontinuities of electrode form while the particulate nature of BT layers is still recognizable. When the temperature increases to 1150 °C, the densification of BT layers is obvious. By increasing dwelling time

at 1150 °C (Fig. 3.11(d-h)), the densification of both layers continues. It seems that electrodes are fully densified after only 10 min while the densification of BT layer is not completed even after 30 min. Hardly any microstructure changes occur for longer dwelling time as shown in Figure 3.11(i-l), which correlates well with the absence of further shrinkage at the macroscopic scale (Fig. 3.6).

• **Roughness of electrodes**

Roughness is usually measured as a summation of negative and positive deviations from a “mean plane” fit over the surface of interest referencing to the standard DIN EN ISO 4287:1998. Figure 3.12 shows an example of a roughness profile where variations in the y-direction are depicted as a function of x.

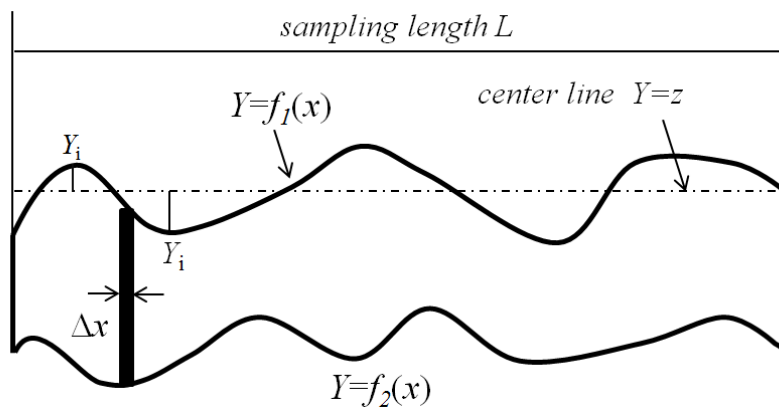


Figure 3.13 Roughness on the surface of an electrode

Roughness of the electrode is defined as below in the following relations:

$$R_a = \frac{\sum_1^L |f(x) - z|}{L/\Delta x} \quad (3.9)$$

Where  $R_a$  is the arithmetic average surface roughness, or average deviation,  $Y$ , of all points from a plane fit to the test surface over sampling length,  $L$ .

Thickness is measured as the arithmetic average thickness of the  $(L/\Delta x)$  segments of electrode, each of which could be treated as a flat electrode when the  $\Delta x \rightarrow 0$ .

$$T_e = \frac{\sum_0^L |f_1(x) - f_2(x)|}{L/\Delta x} = \frac{1}{L} \int_0^L |f_1(x) - f_2(x)| dx = \frac{A}{L} \quad (3.10)$$

The linear, or 1-dimensional (1D) electrode discontinuity is defined as the ratio of summation of the lengths of discontinuous segments to the entire length considered (See Fig. 3.13).

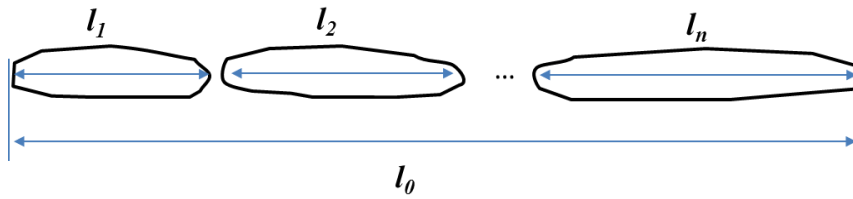


*Figure 3.14 A schematic of discontinuous electrode*

$$Discontinuity_{1D} = \frac{l_1 + l_2 + \dots + l_n}{l_0} \quad (3.11)$$

Figure 3.14 shows the thicknesses and the linear electrode discontinuity change as a function of holding time. It turned out that the thickness of electrode layer decreases with sintering of chips at first (densifying phase), but this trend reversed after the holding temperature last for ~15 min (densification fulfilled). That means swelling of electrodes was observed from this moment.

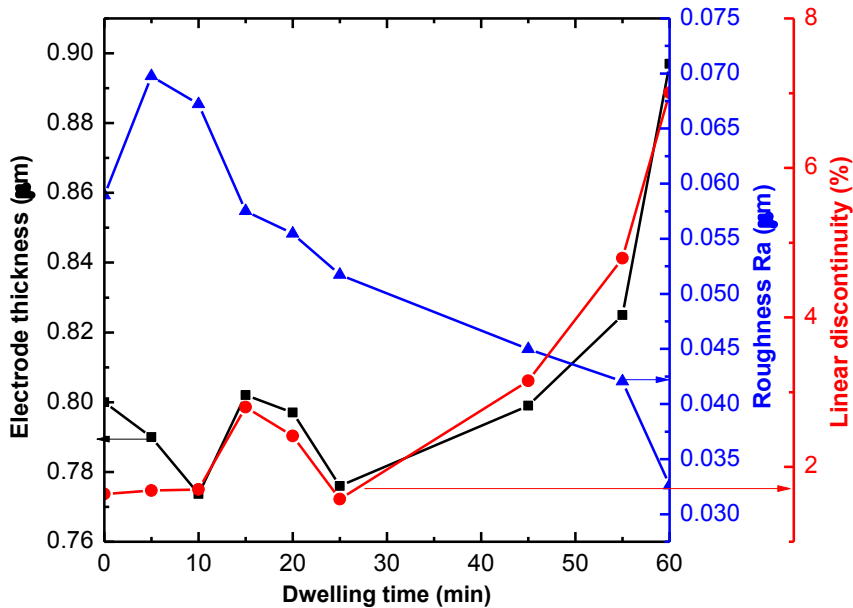


*Figure 3.15 discontinuity and thickness, roughness of electrodes as a function of time*

The thicknesses of electrodes changes as a function of holding time. We observed that the thickness of the electrode layer decreases with sintering of chips at first (densifying phase), but this trend reverses after a holding temperature of ~15 min (densification fulfilled). This corresponds also to a swelling of electrodes. This phenomenon was also found in the work of Polotai et al [29]. However, the swelling of electrodes was not discussed in this paper. The

evolution of discontinuities with dwelling time follows, like the electrode thickness, a non monotonous behavior. A local maximum is observed around 15 min dwelling time. The reason for this non-intuitive behavior may be linked to the compressive stresses in the electrode at high temperature that temporarily facilitate the recovery of the discontinuity of electrode [29]. However, when the densification of BT layers is completed, the compressive stresses are released and this recovery disappears. The further decrease in the coverage of electrode is considered to be due to the creep of nickel at elevated temperature and this is accompanied by swelling and flattening of electrodes. After around 30 min dwelling time, densification of BT ceases (although not fully densified). While the wavy electrode deforms to fit the dielectric layers, which is comparatively flatter. This makes the electrode swell in the thickness direction and the lateral discontinuities become much more severe.

### **3.4 Conclusions**

- (1) It is observed that some initial extrinsic pores exist in the green MLCC chips, especially in the composite electrode layers. However, the presence of these extrinsic pores needs confirmation as they may originate from the sample preparation.
- (2) These artifacts could be problematic in the characterization of the initial defect in the green chips.
- (3) It is found that after the second bake out procedure, some nickel particles have already sintered, and discontinuities form. However, this slight modification does not cause the macroscopic shrinkage, since the BT skeleton does not start to sinter yet.
- (4) Measurement of the thickness of the electrode layers is not accurate, because the cross-section of the MLCCs is not necessarily perpendicular to the layers. This is a motivation to use focused ion beam machining and utilize non-destructive X-ray tomography.

## **Chapter 4**

# **Synchrotron X-ray imaging of the sintering of MLCCs**

Since the discovery of X-rays by W. C. Roentgen in 1895, a wide range of applications has been developed in X-ray imaging techniques. As a non-destructive detective technique (NDT), X-ray imaging, including 2D radiography and 3D tomography, is applied to medicine, geosciences [83, 84], life sciences, mineralogy, archeology, and materials sciences [85-93]. It was commented on Hounsfield's first system for computed X-ray tomography of 1968 that led to a Nobel Prize in Physiology or Medicine in 1979, "It can be no exaggeration to maintain that no other method within X-ray diagnostics has, during such a short period of time, led to such remarkable advances, with regard to research and number of applications, as computer-assisted tomography." This continues to be true today [94]. Thanks to the advances in optics and computer sciences, in-situ and real-time X-ray tomography with nanometric spatial resolution is mature as a NDT routine to image an object.

### **4.1 Introduction**

#### **4.1.1 X-ray computed tomography**

The technique of X-ray Computed Tomography (CT) invented by Godfrey Hounsfield in 1972, is based on x-ray radiography used by doctors when they image tissues in a patient's body. However, rather than taking just one 2D X-ray radiograph, a large number of radiographs are taken at serial spatial angles. The series of 2D radiographs can then be mathematically reconstructed into a 3D image. This 3D image can be resliced into stacks at arbitrary orientation. For interested readers, a history of the X-ray CT can be found in Ref.[95].

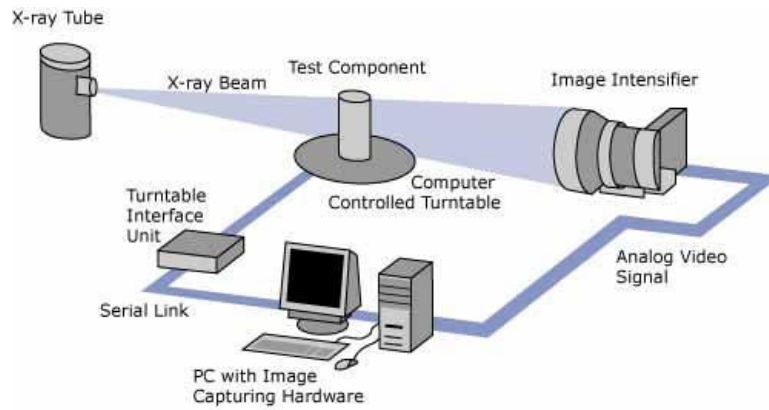


Figure 4. 1 A schematic diagram of the X-ray image acquisitions [96]

The acquisition of a 2D radiograph is based on the Beer's Law. The intensity of a monochromatic X-ray beam travelling through a homogeneous material is:

$$I = I_0 \exp[-\mu x] \quad (4.1)$$

Where  $I_0$  and  $I$  are the incident and transmitted X-ray intensities,  $\mu$  is the material's linear attenuation coefficient (unit  $\text{m}^{-1}$ ) and  $x$  is the length of the X-ray path. A high value of the constant  $\mu$  corresponds to an efficient absorption of X-rays by the considered material, with only a small amount of photons reaching the detector. If there are multiple materials, the equation becomes:

$$I = I_0 \exp\left[\sum_i -\mu_i x_i\right] \quad (4.2)$$

Where  $\mu_i$  is the attenuation coefficient of the  $i^{\text{th}}$  material. In a well-calibrated system using a monochromatic X-ray source (i.e. synchrotron), this equation can be solved directly. If a polychromatic X-ray source is used and as the attenuation coefficient strongly depends on X-ray energy, the complete solution would require solving the equation over the range of the X-ray energy ( $E$ ) spectrum utilized:

$$I = \int I_0(E) \exp\left[\sum_i -\mu_i(E) x_i\right] dE \quad (4.3)$$

There are a number of methods by which the X-ray attenuation data can be converted into an image [97]. The classical approach is called "filtered back projection", in which the linear data acquired at each angular orientation are convolved with a specially designed filter and then back-projected across a pixel field at the same angle. As demonstrated in Figure 4.2, a series of images are recorded at successive tilts (Fig. 4.2(a)), and then these images are back projected in along their original tilt directions into a three-dimensional object space. The

overlap of all of the back-projections will define the reconstructed object (Fig.4.2 (b)). However, the mathematics behind is out of scope in this thesis, and can be found in Ref. [97].

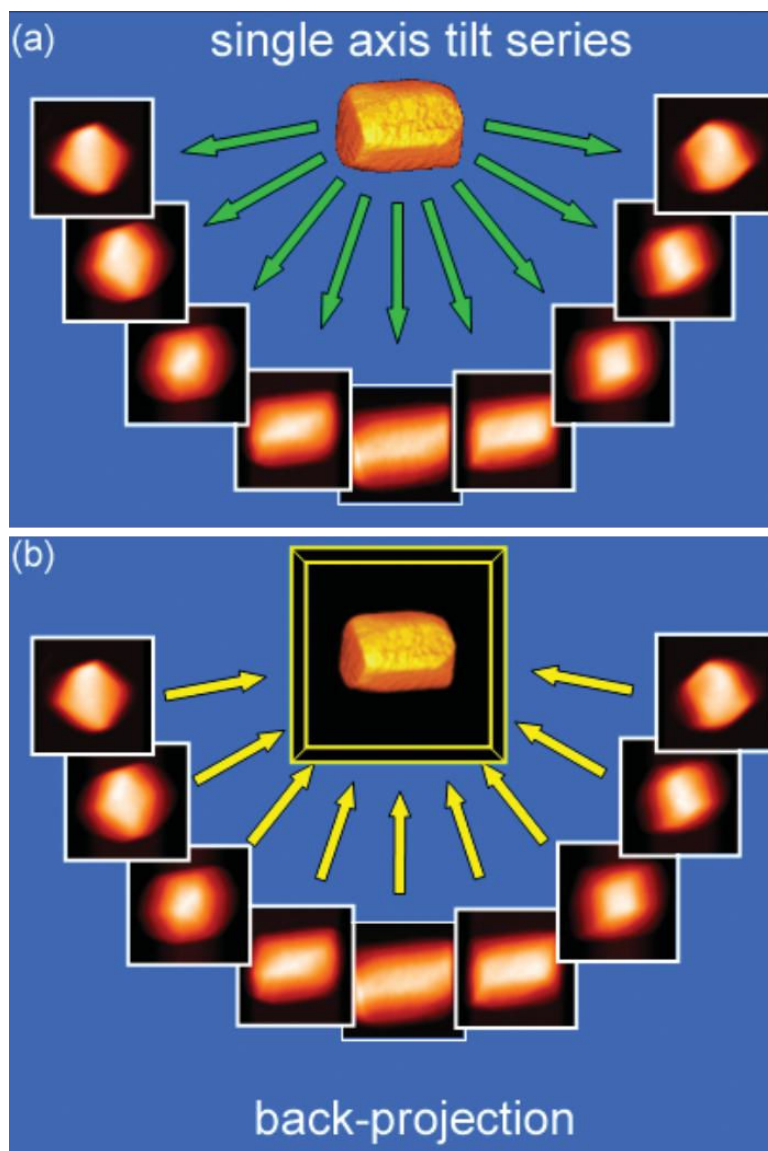


*Figure 4. 2 A schematic diagram of tomographic reconstruction using the back-projection method [85].*

Owing to advances in optics, spatial resolution of 10-50 nm has been achieved recently [98-101]. Withers [94] shows resolution of X-ray tomography techniques as a function of X-ray energy (see Fig. 4.3). Advances in Nano scale X-ray tomography techniques and related applications were recently reviewed by Sakdinawat [102].



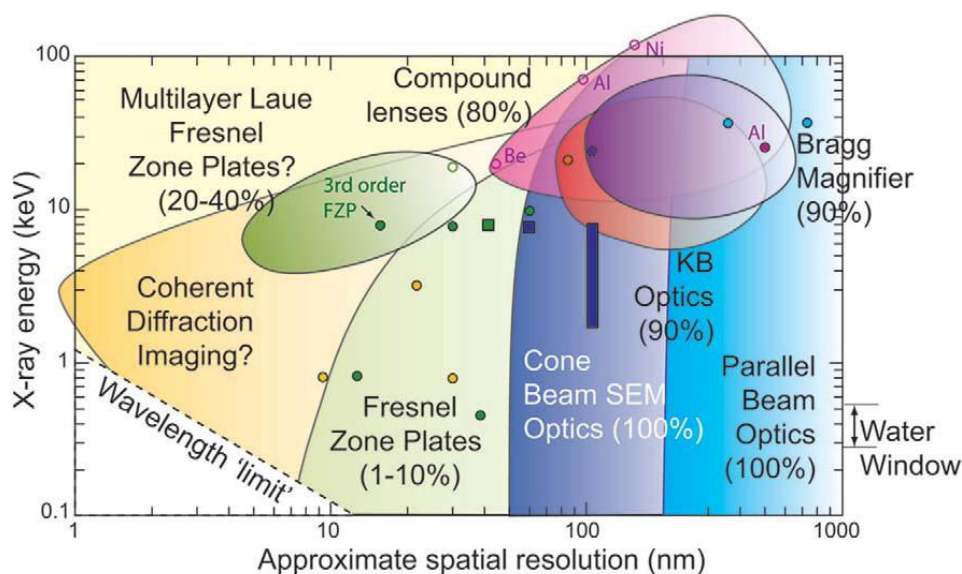


*Figure 4. 3 Spatial resolutions achievable with different lenses: calculated resolutions (open symbols), measured resolutions (filled symbols); synchrotron source (circle symbol) and lab sources (square symbol) (reproduced after Withers [94])*

#### **4.1.2 Application to sintering**

As a non-destructive 3D characterization technique, X-ray CT has superior capabilities over traditional optical microscopy, SEM, and other tomography techniques. It has been applied in different domains of material sciences recently [103, 104]. With advanced detectors and optics at the synchrotron, high-resolution, in-situ, high temperature real-time observation of microstructure evolutions becomes available and routine. In-situ X-ray  $\mu$ CT has been utilized in the studies on the solidification of alloys [105-108]. In the domain of particulate materials, It covers packing and rearrangement of particles in granular materials [109, 110] (also coupled with DEM) and porous media [111].

X-ray CT was first used for the study on the sintering of glass beads by Bernard and coworkers in 2001 [112]. The technique was then used by Lame[113, 114], Vagnon [115], [116], and Olmos [117, 118] to study the sintering of metallic powder under atmosphere. Xu [119] and Niu [120] studied the sintering of ceramic particles with in-situ X-ray CT. Bernard and Guillon investigated the constrained sintering of glass films on rigid substrates [121]. Co-sintering of multilayered systems, i.e., SOFCs, was extensively studied using X-ray CT [122-127].

## 4.2 Experiment procedure

### 4.2.1 Set-up: Transmission X-ray Microscope

As a direct analog to the visible light microscope or transmission electron microscope (TEM), a Transmission X-ray Microscope (TXM) consists of a capillary condenser lens, an objective lens (Fresnel zone plate) and detector system (Fig. 4.4).

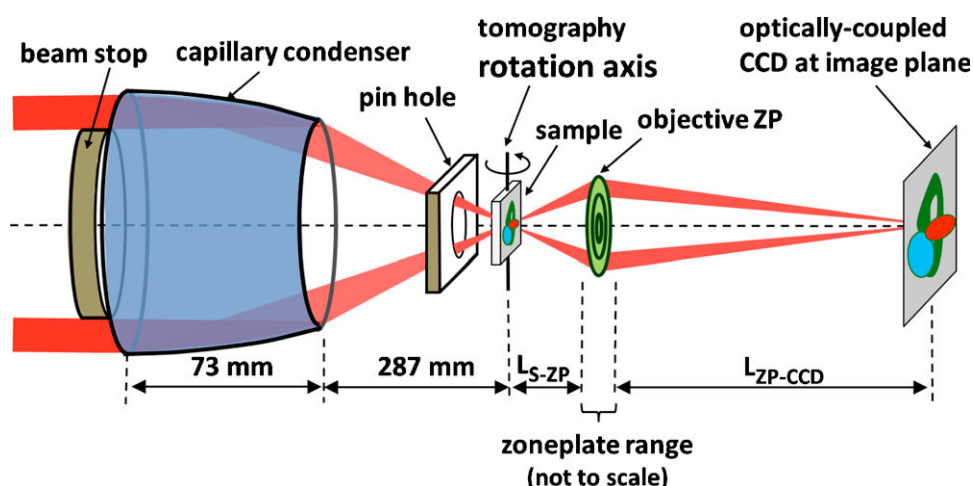


Figure 4. 4 A schematic illustration of a TXM imaging system consisting of a condenser lens, objective lens, and detector system. Beamstop and pinhole block out the unfocused x-rays (After Nelson [128])

The capillary condenser lens is to focus the X-ray beam generated by the X-ray source onto the sample and the objective lens is to magnify the X-ray image passing through the sample to form an image on the detector plane. The detector is typically a scintillated camera consisting of scintillator screen that converts X-ray beam into visible light, and a fiber-optics taper or visible light microscope objective to relay the visible light to a high-resolution Charge-Coupled Device (CCD) sensor or a Complementary Metal-Oxide-Semiconductor (CMOS) detector. The unique properties of synchrotron radiation lie in its continuous spectrum, high flux and brightness, as well as high coherence, which make it an indispensable tool in the exploration of matter. Figure 4.4 shows the TXM system setup at the Sector 32-IDC at the APS synchrotron (Advanced Photon Source, Argonne National Lab, USA), which was used in this work. The X-ray lens typically provides 10-50 times magnification while the visible light system in the detector assembly provides an additional factor of 2-20 times magnification. That gives a typical total magnification of between 200-1000 times. For example, the TXM at the APS [129, 130] has an X-ray magnification of 80 times while the visible light magnification is 10, resulting in an overall 800 times

magnification. Thus, to a typical detector pixel size of 10  $\mu\text{m}$  corresponds an effective pixel size of 12.5 nm in the sample.

Figure 4.5 shows the experimental set up for the X-ray CT data acquisition. The heating unit is designed for the in-situ real time X-ray imaging.

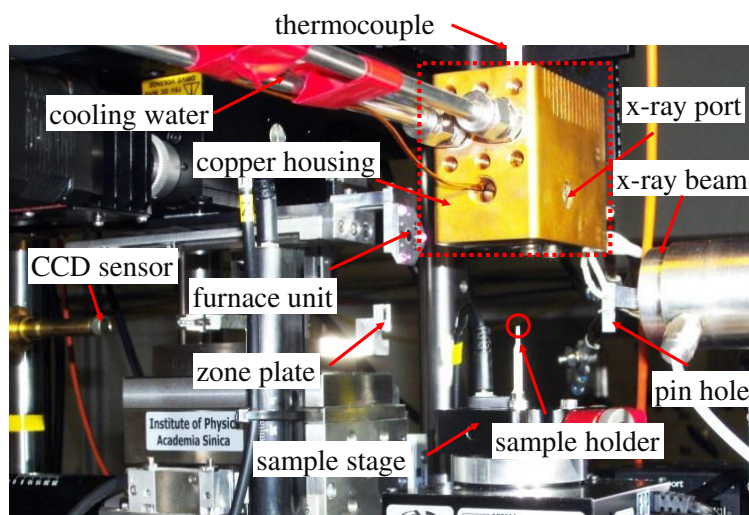


Figure 4. 5 A schematic for the setup of the TXM at Sector 32-IDC of APS Synchrotron

### 4.2.2 Sample preparation using FIB milling

In order to maximize the quality of the reconstruction, the sample should be contained within the field of view (FOV = 26  $\mu\text{m}$ ) of the TXM at the required magnification during rotation. If the region of interest (ROI) is not maintained within the FOV for the full rotation, the algorithm must essentially reconstruct an incomplete data set. Ultimately, this increases the noise observed in the reconstruction. Furthermore, in tomographic studies of composite materials (including porous ones) phase identification is typically achieved by observation of the spatial distribution of X-ray absorption. However, if the sample is not maintained within the X-ray FOV throughout the rotation, the attenuation due to sample geometry and that due to material composition cannot be separated, leading to challenges in reconstructing the difference phases within large specimens. Banhart [131] provides further discussion of this limitation due to “missing data”.

Commercial 0603 size ( $1.6 \times 0.8 \times 0.8 \text{ mm}^3$ ) Ni-MLCC chips and 01005 size ( $0.4 \times 0.2 \times 0.2 \text{ mm}^3$ ) Pd-MLCC chips (Samsung Electro-Mechanics, Suwon, South Korea) were used in our study. These green chips were first roughly machined into 60  $\mu\text{m}$  cone shape with a special

micro drill (see Fig. 4.6). The tip was then milled by a Quanta 3D FEG FIB-SEM (FEI, USA) into a 20  $\mu\text{m}$ -diameter cylinder of 20  $\mu\text{m}$  height (Fig. 4.7).

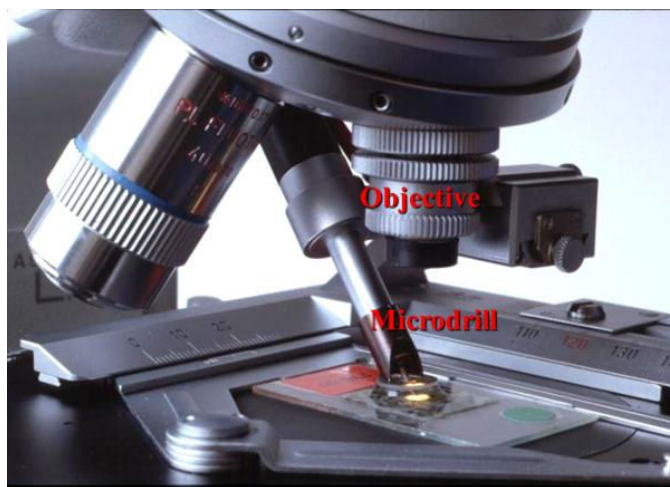


Figure 4. 6 Photograph of a microscope adapted drill

After organics were burnt out between 120 and 230  $^{\circ}\text{C}$  for 30 hrs in air, the Ni-MLCC sample was imaged with TXM operating at 8.9 keV before and after sintering (in 5%  $\text{H}_2+\text{Ar}$  atmosphere at 1100  $^{\circ}\text{C}$  for 2 hrs, heating/cooling at 15  $^{\circ}\text{C}/\text{min}$ ).

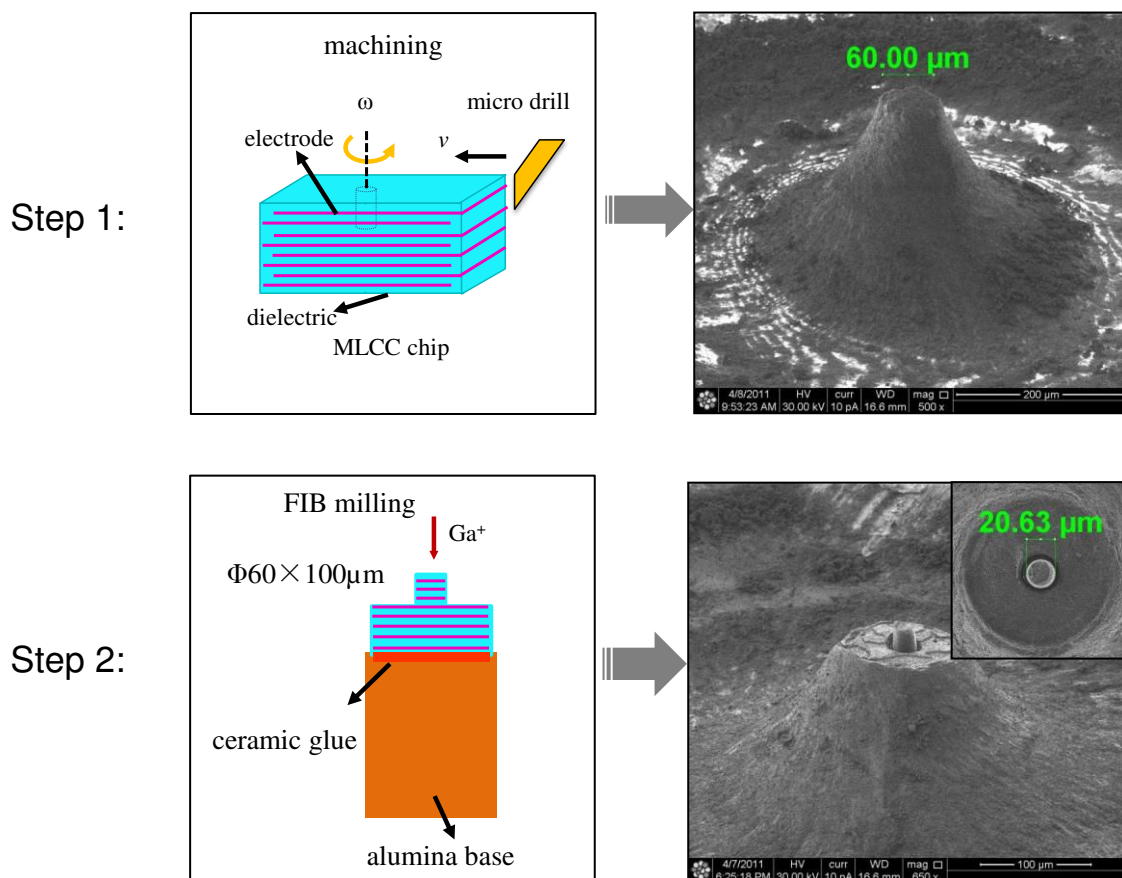


Figure 4. 7 Two-step preparation of sample for X-ray nCT

### **4.2.3 Image acquisition and 3D reconstruction**

An attempt was made to image in-situ the sintering of a cylindrical Ni-MLCC sample on beam-line. To simulate the reducing sintering atmosphere, 2% $\text{H}_2$ - $\text{N}_2$  gas was introduced from the top opening, before the heating up of the furnace. The sample was heated from room temperature at a heating rate of 15 °C/min until 1150 °C and was sintered for 1 hr at 1150 °C. During the sintering, 2D X-ray radiographs were taken every 20 °C increment and every 5 min during the dwelling time. However, no shrinkage was noticed during this standard sintering cycle. This is because with the current facility, the furnace is open for the insertion of the sample, which means that the reducing atmosphere ( $p\text{O}_2 = 10^{-11}$ - $10^{-9}$  atom) normally required for the successful sintering of nickel electrodes cannot be guaranteed. It showed that the sintering of Ni electrode was significantly modified due to the oxidation of the metal particles and no obvious densification was observed during the thermal cycle. A compromise is to characterize the sintered Ni-MLCC sample ex-situ. To explore the missing gap during the thermal cycle, the sintering of Pd-MLCC chip in air was used to simulate the sintering of Ni-MLCC in a reducing atmosphere. Pd exhibits excellent oxidation resistance. Hence, the sintering behavior of the Ni electrode in reducing atmosphere is assumed similar to the sintering of Pd electrode in the air. Note that the nano-sized ceramic inclusions were not used in the Pd electrode.

For the Ni-MLCC sample, an ex-situ experiment was carried out. A cylindrical Ni-MLCC sample was imaged before and after sintering. When the X-ray imaging was being conducted, the sample was rotated every 0.25°, each 2D projection image was collected in 2 s from a CCD camera with 2048 × 2048 pixels, which corresponds to the FOV of 26 μm. The sintering was conducted in a tube furnace in 2% $\text{H}_2$ - $\text{N}_2$  reducing atmosphere with heating/cooling rates of 15 °C/min and dwelling time of 1 hr.

For Pd-MLCCs, no specific atmosphere was used during the sintering. In-situ observation of sintering of Pd-MLCC was carried out as a reference. The sample was mounted onto a movable stage. A FibHeat200-XRD furnace (MHI, OH, USA) with an Ø 6 mm heating chamber was driven by a 1693-model DC power supply (BK Precision, CA, USA). The input current of the furnace was controlled to obtain the required temperature ramps. A type S thermocouple was introduced from the top port. Its tip was located approximately 1 mm away from the sample (position controlled by microscopy). The temperature measurement was calibrated with Au particles located upon the sample. The melting of Au particles (indicated

by the flowing of the material) was observed between the recorded temperatures of 1050 °C and 1070 °C (melting point of Au is 1064 °C). The heating unit was water-cooled so that it could operate for a long period of time at high temperature (1200 °C) without disturbing the alignment of the pin hole and zone plate. The sample was inserted through the opening at the bottom of the chamber and the region of interest was positioned in the center of the X-ray microscope window. The sample was heated up to 1200 °C at 10 °C/min, held for 60 min at this temperature and cooled down to room temperature at 15 °C/min. The sample was aligned in rotation and its position was kept all along the experiment to ensure 2D projections quality. 2D projections were recorded every 50 °C during the heating ramp below 900 °C, and every 20 °C between 900 and 1200 °C.

3D data acquisition was not possible during sintering because such a measurement takes 20-30 min (360-720 projections). During that period of time, the microstructure changes rapidly, which does not allow any reliable reconstruction with the filtered back projection algorithm. Thus, 3D data acquisition was only conducted on the green sample at room temperature. Additionally, 3D X-ray data acquisitions were carried out on additional samples that were partially sintered at 900 °C and 1100 °C, respectively. These acquisitions allow 2D projection data to be re-interpreted more accurately.

3D microstructures were reconstructed using the classical filtered back-projection algorithm from the series of 2D projection images with TXMReconstructor software package (Xradia, Inc., Pleasanton, CA, USA).

## **4.3 Results and discussion**

### **4.3.1 Ex-situ X-ray CT on Ni-MLCC sample**

Figure 4.8(b) and (c) are typical 2D projection images collected directly from the CCD camera before and after sintering, respectively. Figure 4.8(d) and (e) show the reconstructed microstructure from 2D images.

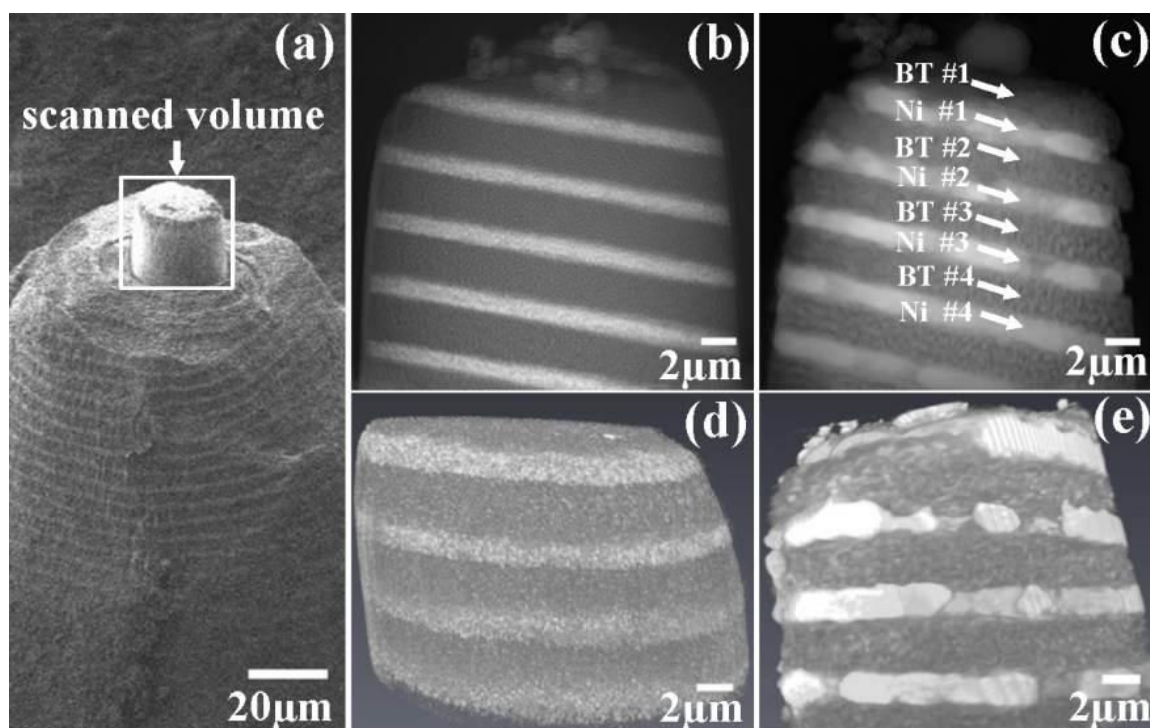


Figure 4. 8 (a) MLCC sample for X-ray tomography; (b), (c) 2D projection images before and after sintering, respectively (the layers are indexed for later use); and (d), (e) Reconstructed 3D microstructure before and after sintering, respectively.

The bright areas correspond to the Ni phase and the dark areas correspond to the BT phase (as the photon energy was 8.9 keV, above the Ni absorption edge [128]), please see the attenuation length<sup>4</sup> of Ni and BT as a function of beam energy (Fig. 4.9).

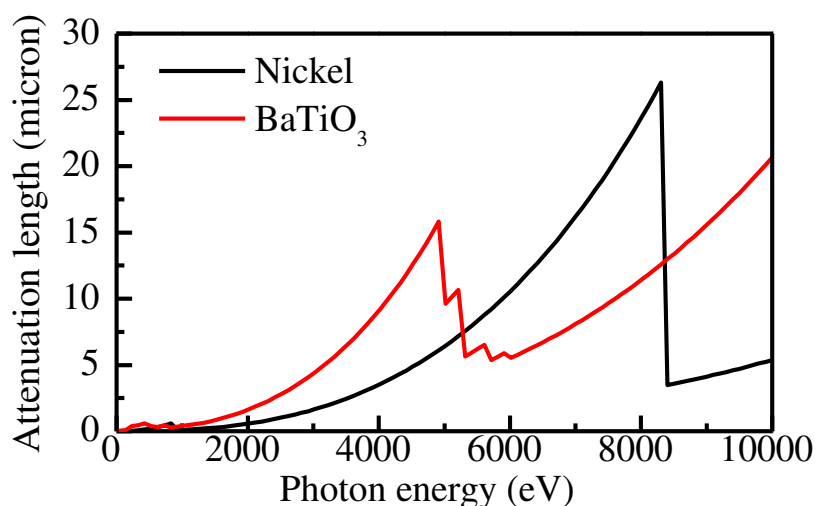
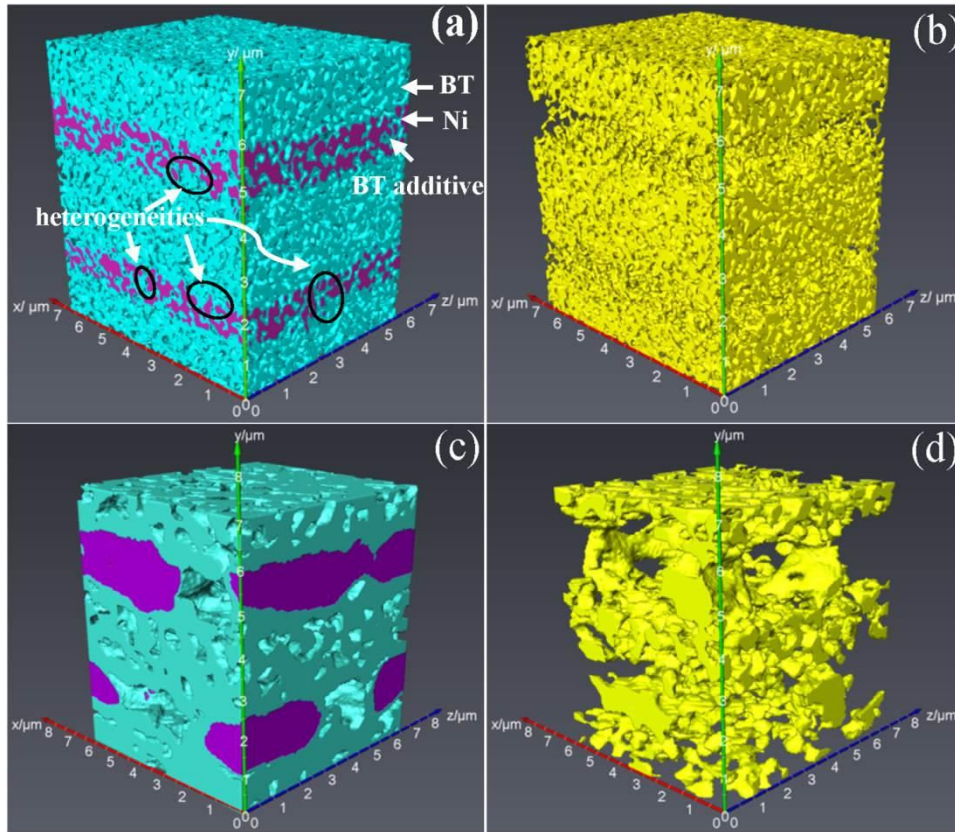


Figure 4. 9 BT and Ni absorption edge

<sup>4</sup> The depth into the material measured along the surface normal where the intensity of x-rays falls to 1/e of its value at the surface.

3D raw data was filtered using the Edge-Preserving Smoothing Filter, segmented and rendered using Avizo software (VGS, France). Figure 4.10 shows 3D rendering of a representative volume extracted from reconstructed microstructures. Note that the volumes are from the same spot of the same sample before (Fig. 4.10 (a) and (b)) and after (Fig. 4.10 (c) and (d)) sintering.



*Figure 4. 10 Microstructural changes of MLCC sample (Ni in purple, BT in green and pores in yellow): (a) multilayer before sintering, (b) pore network before sintering, (c) multilayer after sintering, and (d) pores after sintering*

In Figure 4.10(a), BT particles in the dielectrics and Ni particles in the electrodes are distinguishable. Nano-sized BT additives dispersed in Ni matrix cannot be discriminated into individual particles as the size of the contact areas is below the spatial resolution. Heterogeneous zones are found in the electrodes, with Ni particles having lower contact number and with smaller local density. Figure 4.10(b) shows the pore network in the green MLCC chip. Clear discontinuities are found in Ni layers after sintering (Fig. 4.10(c)). These discontinuities correspond to very large pores (Fig. 4.10(d)) that reduce the effective electrode overlapping area and hence the total capacitance of the capacitor. Isolated pores are present within the partially densified BT layer.



With benefit of the X-ray nanotomography technique, we have been able to observe the 3D morphology of discontinuities in electrodes in an ex-situ test. The exact orientation of layers can be tracked and we can correlate the displacement of matter within the sample induced by sintering. Figure 4.11 shows the morphology of the inner electrode #2 before and after sintering from the top view. The disconnected areas correspond well to the initial heterogeneities (#1-8) where Ni particles are less densely packed and have lower coordination number. However, the larger porosity in Ni layers near the edge does not result in any discontinuity probably due to the proximity of the free boundary.

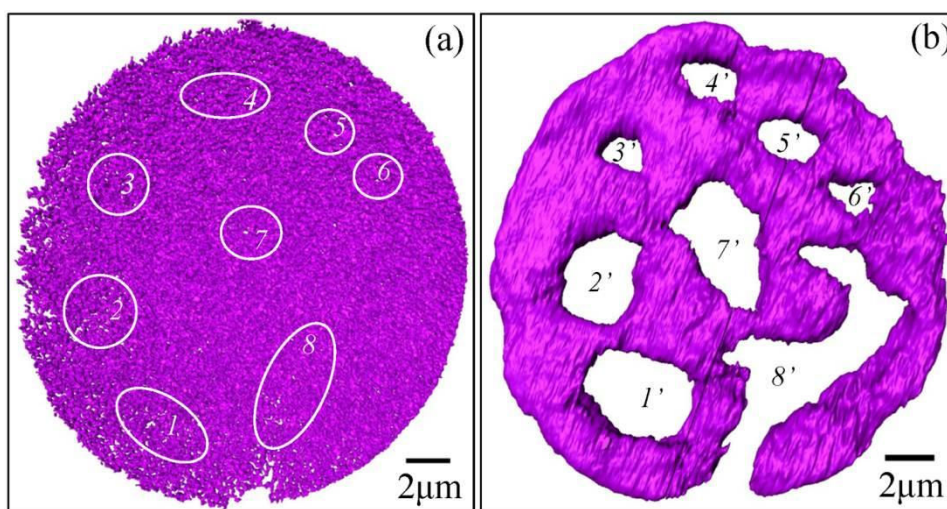


*Figure 4. 11 Morphology of inner electrode #2: (a) initial microstructure and (b) final microstructures after sintering, respectively. Microstructures of electrodes #3-4 (not present) are similar to that of electrode #2.*

Thanks to the 3D tomographic data that is saved as a stack with voxel size of  $26 \times 26 \times 26$  nm<sup>3</sup>, quantifications of the microstructure and its changes can be implemented using ImageJ (NIH, USA) together with specific plugins. For example, the discontinuity rate of the electrodes, strains and the density in the BT layers are of great interest for understanding the co-sintering of the multilayer system.

Take the electrode #2 for example; its areal (2D) discontinuity is defined as the ratio of the discontinuous areas ( $a_1, a_2, \dots, a_n$ ) to the entire area ( $A_0$ ):

$$Discontinuity_{2D} = \frac{a_1 + a_2 + \dots + a_n}{A_0} \quad (4.4)$$

The radial and axial strains in the BT layers are calculated as

$$\begin{aligned}\varepsilon^r &= \ln(l^r / l_0^r) \\ \varepsilon^a &= \ln(l^a / l_0^a)\end{aligned}\quad (4.5)$$

Where  $l^r$  and  $l^a$  denotes the radial and the axial dimensions of the BT layers images and  $l_0^r$  and  $l_0^a$  the reference dimension of the layer measured from the 3D microstructure.

The relative density of the sintered BT layers is defined as the solid volume ( $V_{solid}$ ) fraction over the total volume ( $V_{total}$ ):

$$D_{BT} = \frac{V_{solid}}{V_{total}} \quad (4.6)$$

Figure 4.12(a) shows that the top electrode layer has smaller discontinuity (6%) than inner layers (14-16%). Figure 4.12(b) shows the true axial and radial strains of dielectric layers after co-sintering. Axial strains (11-14%) are larger than radial strains (5-7%), as it is expected from geometrically constrained systems [75]. A smaller anisotropy is observed for BT layer #2, which is closer to the top free surface of the specimen. Under free sintering conditions shrinkage is expected to be almost isotropic, although structural anisotropy may be brought by tape casting and lamination. It is also interesting to observe that the swelling of electrodes is about 16% on average along the thickness direction. Figure 4.12(c) presents the relative density of the different BT layers, showing a decrease in achieved density as function of layer position in the multilayer.

In view of these microstructures and considering the relatively small thermal expansion mismatch between Ni and BT ( $\alpha_{Ni}=16.3 \times 10^{-6} / ^\circ C$ ,  $\alpha_{BT}=11 \times 10^{-6} / ^\circ C$  [132] ), we propose that the electrode discontinuities originate predominantly from the sintering strain mismatch. Ni powders sinter at a lower temperature (400-450 °C) than BT powders (950-1000 °C) [29]. Due to their larger densification rate at low temperature (<1050-1100 °C), the Ni layers are under tensile stresses while the BT layers are almost rigid. The more constraint imposed on the Ni layer, the larger the discontinuities. This explains the presence of a smaller discontinuity for the top electrode layer, which can almost sinter freely, as compared to the inner ones which are under more constraint from adjacent layers. At higher temperature (1100 °C) already densified Ni layers are under compressive stress, and they may deform by creep [133]. Due to poor wettability between Ni and BT layer [134], the viscous Ni layer tends to contract laterally, finally resulting in swelling of the electrodes. Contrasting with Ni

layers, dielectric BT layers are under tensile stress, which explains that the shrinkage along the thickness direction is larger than in-plane. The top BT layer is only constrained by the bottom Ni layer, i.e., to a less degree than other inner BT layers during sintering. This explains the higher relative density of the top BT layer in comparison with inner ones.

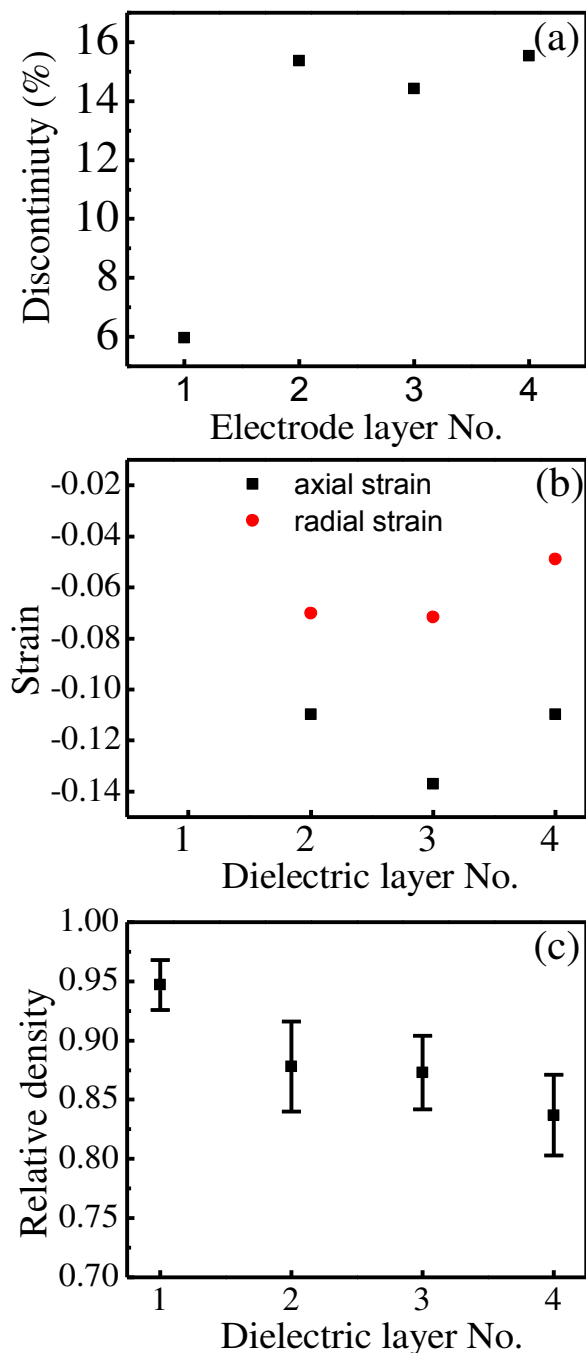


*Figure 4. 12 (a) Discontinuity of electrodes; (b) Axial and radial strains in different BT layers, irregular top BT layer (#1) was not considered and (c) Relative densities of BT layers (The layers are indexed as in Fig. 4.8(c)).*

### 4.3.2 In situ X-ray imaging of Pd-MLCC

Figure 4.13 shows the selected images of the region of interest obtained during the sintering cycle. The light grey phase corresponds to the BNT dielectrics while stronger X-ray absorption of Pd electrode leads to a dark grey phase. It should be noted that the elliptical shape of the projected electrode is due to the incident angle between the X-ray beam and the electrode plane. The initial microstructure of the electrodes exhibits some heterogeneities as implied by the grey level distribution in the electrode layers shown in Figure 4.13(a). The darker grey regions are the high density regions, while the lighter grey regions are the low density regions where particles have smaller coordination numbers. Such heterogeneities are common in green thin layers, especially when layers are composed of only a few particles piled on top of each other.

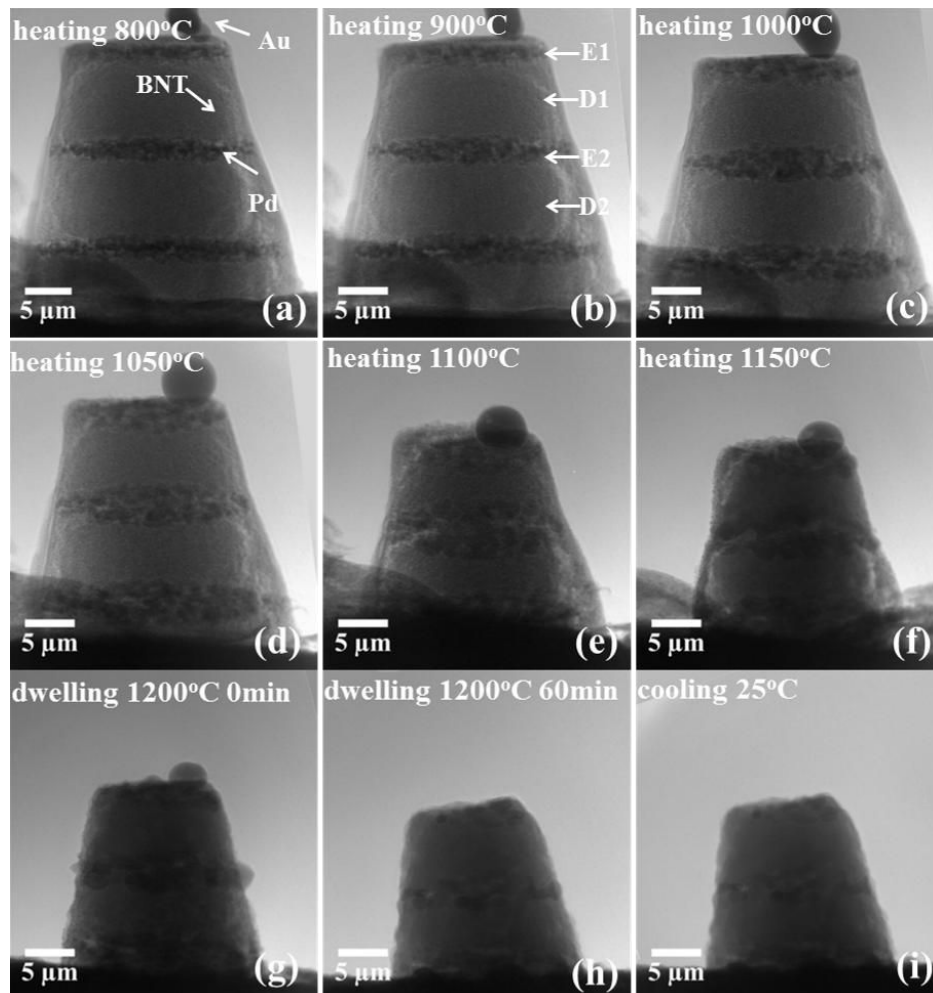
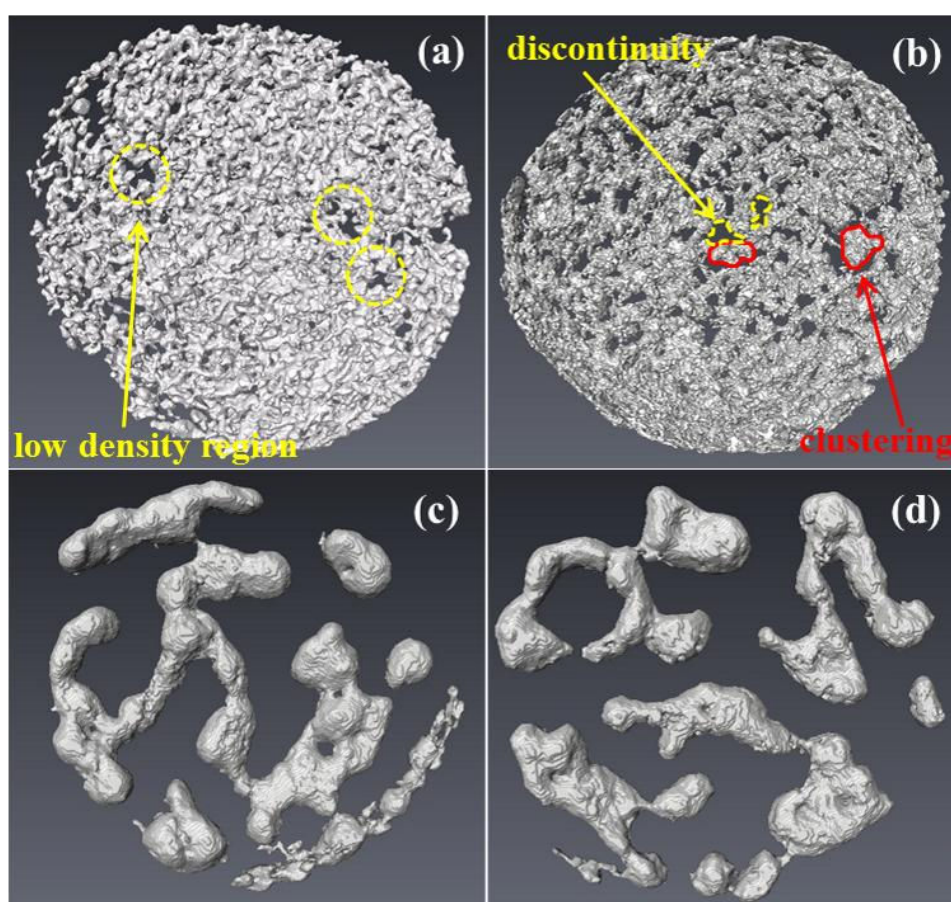


Figure 4. 13 Microstructural evolutions during sintering of a Pd-MLCC sample. Note that Au particles were used both for image alignment in the reconstruction and for calibrating the temperature in the furnace.

Neither clear microstructural evolution nor densification could be observed below 800 °C. At 900 °C (Fig. 4.13(b)), the Pd electrode layers appear more inhomogeneous. As Pd particles densify, the contrast with neighboring pores is getting stronger due to increased x-ray attenuation differences. The darkened regions indicating densified Pd suggest that sintering of Pd particles has started already at 900 °C. As sintering proceeds (Fig. 4.13(c-g)), the pores evolve into a number of discontinuities in the electrode layer. Fig. 4.13(h-i) indicate that no obvious microstructure change occur during the cooling ramp.

Figure 4.14 illustrates the morphology evolution of the electrodes at the different stages by 3D X-ray nCT.



*Figure 4. 14 3D reconstruction and rendering of the electrodes in the Pd-MLCC sample (top view): (a) green state; (b) partially sintered at 900 °C; (c) partially sintered at 1100 °C (E1); and (d) partially sintered at 1100 °C (E2)*

Figure 4.14 (a) shows the morphology of an electrode from the sample tested in situ. Circled areas point to the low-density regions. Differential densification takes place in powder

compacts of heterogeneous nature [43]. Particles in high-density regions sinter faster than those in low-density regions and form clusters. Some particles in the low-density regions desinter and large pores appear (Fig. 4.14 (b)). Finally, pores enlarge and lead to discontinuous areas in electrode layers (Figs. 4.14(c) and 4.14(d)). These discontinuities result in capacitance loss.

Continuous recording of the 2D radiographs allows radial and axial strains of the electrode and dielectrics layers to be calculated directly from dimensional changes. However, the axial strain in the electrode is not measured due to the uncertainty in thickness correlated to the elliptical projection (due to the incident angle between the X-ray beam and the electrode plane). Anisotropic sintering behavior of different layers is shown in Figure 4.15.

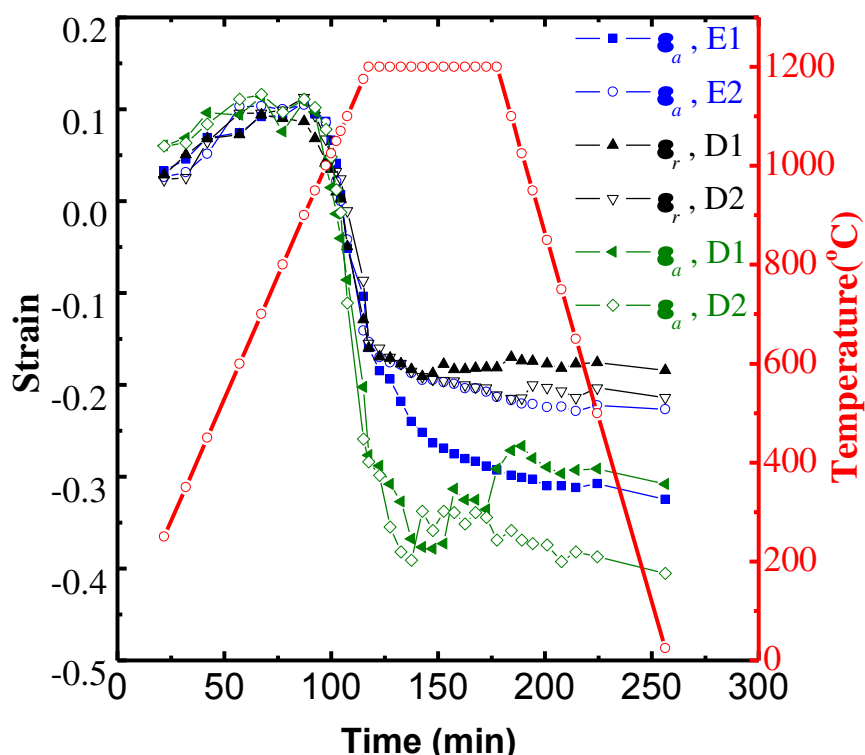


Figure 4. 15 Radial and axial strains in dielectrics layers, radial strains in electrodes as function of time (E1 stands for 1<sup>st</sup> electrode, E2 for 2<sup>nd</sup> electrode, D1 for 1<sup>st</sup> dielectric, and D2 for 2<sup>nd</sup> dielectric).

It is found that the radial shrinkage of the top electrode layer (E1, Fig. 4.13(b)) is smaller than that of the second layer (E2). This difference cannot be attributed to the initial conditions since the two layers should be very much similar. It must be related to differences in constraint levels during sintering as already observed on Ni-MLCCs. The top electrode layer has only one adjacent dielectric layer on the bottom. This layer acts as a rigid substrate and

imposes a geometrical constraint. In contrast, the second electrode is constrained by both adjacent layers. This difference has consequences on the radial shrinkage but also more significantly on the degree of discontinuity. The discontinuity, defined as percentage of uncovered areas over the total electrode area, is smaller in the top electrode layer (~56.1%) than in the second electrode layer (~60.4%) as shown in Figure. 4.14(c) and (d). These electrode discontinuities are much larger than those in commercial Pd-MLCCs. The reason is that in our experiment design the electrodes are not encapsulated in ceramics, thus easily swell and expand during sintering (Fig. 4.13). This swelling of electrodes (creep deformation without any volume change) leads to a further increase in electrode discontinuity.

In a single dielectric layer, the strain anisotropy is initially negligible. However, as the temperature reaches approximately 1000 °C, the axial strain exceeds the radial strain. As temperature increases, it is also observed that the dielectric layers sinter faster than the electrode layers. This sintering strain-rate mismatch results in in-plane tensile stresses in the dielectrics layers. These stresses accelerate the axial shrinkage of the dielectric materials through Poisson's coupling. A difference of ~0.1 between axial and radial strains is measured after the sintering cycle. Both radial and axial strains are nearly equal in the first and second dielectric layers, which are sintered under the same constraining conditions.

From the strain measurement and microstructure evolution in the 2D projections, it can be concluded that the cooling process does not affect much MLCCs. The thermal contraction during cooling has thus a negligible effect on microstructure compared to the sintering shrinkage and rules out a possible creep deformation of Pd induced by differential thermal contraction. This indicates that discontinuities in the electrodes are primarily linked to the sintering strain mismatch during the heating ramp.

We finally propose a possible mechanism for electrode microstructure changes during sintering of Ni-MLCCs as schematized in Figure 4.16. After lamination of BT sheets, there are heterogeneous regions in the electrodes. Below 950-1000 °C the Ni powder densifies except in heterogeneous zones (Fig. 4.16(a)) where de-sintering is observed [71] (Fig. 4.16(b)). As discussed earlier, at this stage the Ni layers are under tensile stress. The tensile stress in the thinner sections induces matter flow towards the thicker sections [76] (Fig. 4.16(c)) until the thinner sections are disrupted and discontinuities form. Once nickel is fully

dense, electrodes are subjected to compressive stress at high temperature (1100 °C) due to BT densification (Fig. 4.16(d)). The compressive stress causes contraction of the viscous Ni, resulting in swelling of electrodes and hence a further increase in electrode discontinuity (Fig. 4.16(e)). Meanwhile, the nano-sized BT additives are discarded by Ni due to their unwettability with Ni at high temperature. They aggregate and sinter, possibly forming percolation between two adjacent BT layers and enhancing the mechanical adhesion between Ni and BT layers in the MLCCs.

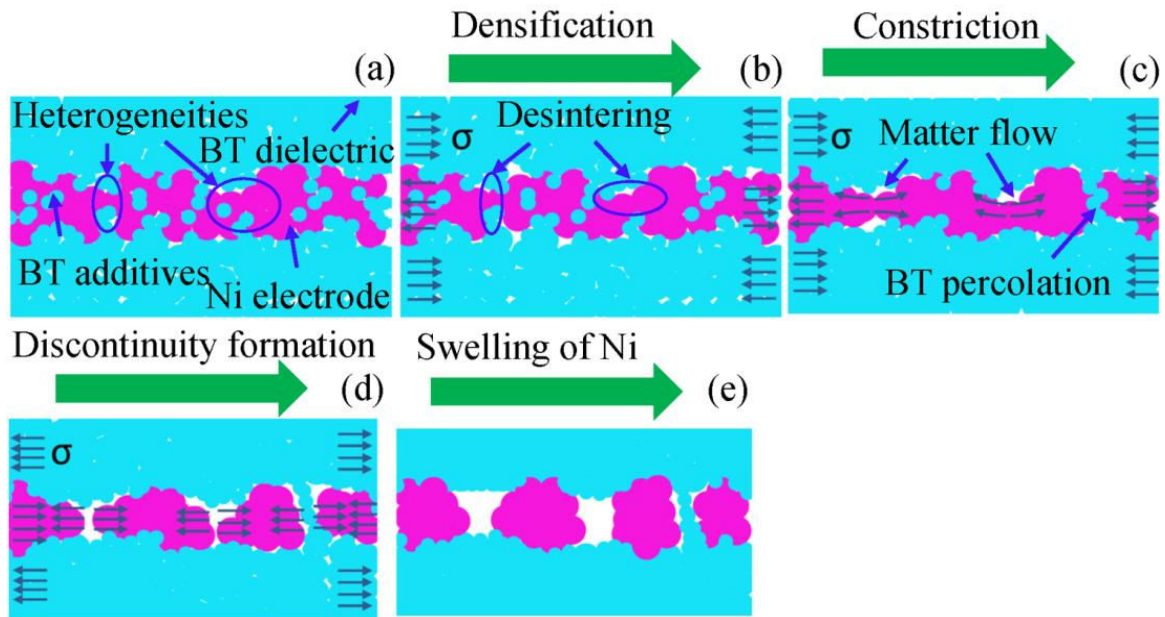


*Figure 4. 16 A schematic of the defect evolution mechanism during sintering*

#### 4.4 Conclusion

- (1) Synchrotron X-ray nano-tomography was for the first time used to study the microstructural changes during sintering of single MLCCs. As shown here, this unique technique enables 3D visualization of the internal microstructure as well as the quantification of features such as strains in three directions for each layer, defect size and morphology.
- (2) In-situ X-ray imaging of sintering of Pd-MLCC chips confirmed that the final electrode discontinuities originate from the initial heterogeneities through a differential densification process. The formation of discontinuity occurs at the early stage of sintering of MLCC when the dielectric layers serve as constraining substrates.



- (3) However, we show that care must be taken in interpreting results. The sintering behavior of the extracted small sample may deviate from that of a real several-hundred-layer chip. In a sample with very few layers, as used in these nanotomographic experiments, external and internal layers are not submitted to the same constraints, thus resulting in different discontinuity levels.

## **Chapter 5**

# **Correlative studies using FIB-SEM nanotomography**

It has been demonstrated in Chapter 4 that the X-ray nano computed tomography (nCT) enables the comparison of the microstructure change before and after sintering. However, its resolution is not sufficient to resolve the submicrometric particle packing or identify the nano BT additives. Characterization of this green microstructure at the particle length scale is however necessary, because: (i) the initial contact configuration between particles determines their sintering behavior and final microstructure; (ii) it provides us with realistic input for the DEM numerical simulations. We make use here of the excellent resolution of Focused Ion Beam (FIB)/SEM nanotomography (FIB-nT), which is rapidly emerging as a powerful tool to characterize the 3D microstructure, grain orientations, and chemical compositions in micrometric devices or materials. FIB-nT is utilized here to image green and sintered MLCCs, including the very MLCC sample characterized using X-ray nCT. Comparison between the two techniques is the scope of the present chapter.

### **5.1 Introduction**

Compared with other tomography techniques (see Fig. 5.1), FIB tomography is currently of great technological importance because of its high resolution and capability of analyzing a comparatively large volume of the material. The typical resolutions (lateral pixels and slicing steps) which can be reached by the FIB tomography are from tens of nm down to a few nm, depending on the quality of the equipment available. The FIB tomography technique can reach better resolution than X-ray tomography and mechanical serial sectioning. Although TEM tomography and 3D Atomic Probe have achieved higher resolutions, but the volume that these two techniques can probe is limited to 0.1-1  $\mu\text{m}^3$ . Hence, the small volume investigated may not be representative of the whole sample.

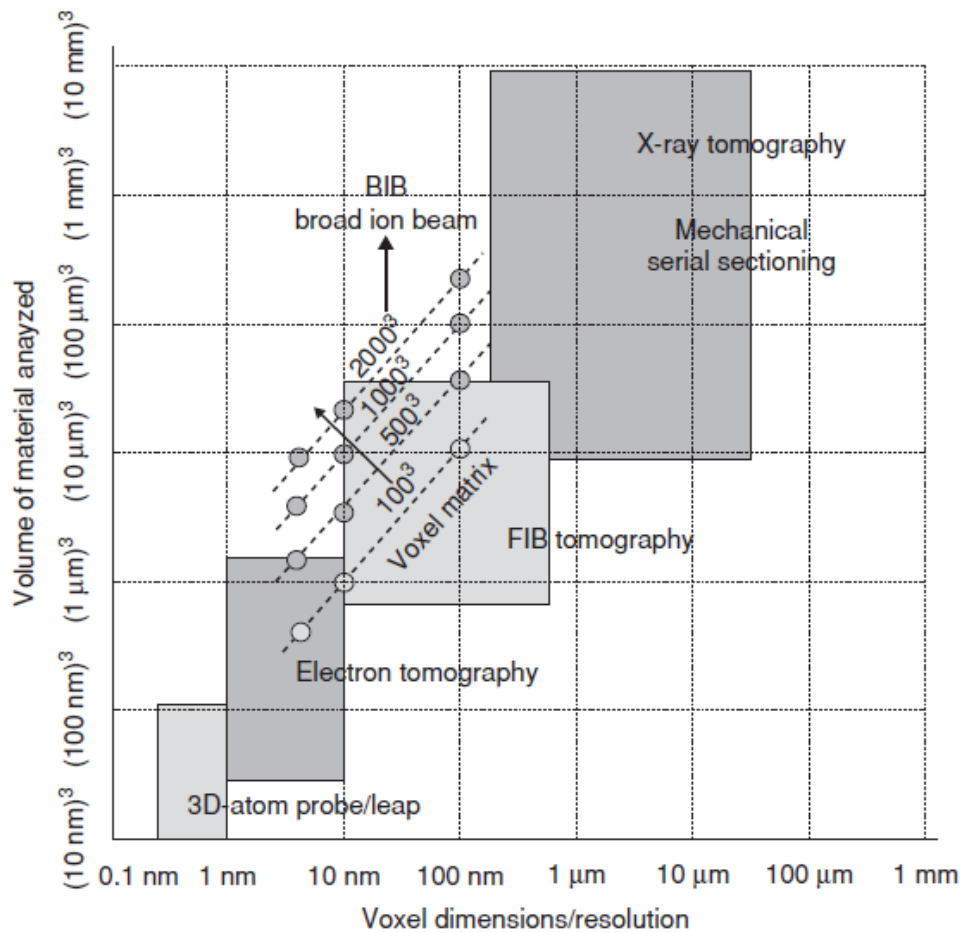


Figure 5.1 Resolution of different tomography techniques (after Holzer [135])

Nowadays, the automated acquisition of large image stacks of fine resolutions (below 10 nm) using FIB serial sectioning can be accomplished by following standard routines. The latest FIB/SEM system is capable of performing multi-channel acquisitions of microstructural (BSE, SE), chemical (EDX) [136-138] and crystallographic (EBSD) [139] information with different detectors from the same sample. FIB tomography is becoming a versatile method and widely applied in materials [137, 138, 140, 141], life [142-144], and geosciences [145, 146]. A good example of application of FIB tomography is 3D characterization of particulate media [140, 147, 148]. This unique technique is still young but developing rapidly. The advances in FIB tomography and its applications have recently been reviewed by Kubis [149], Munroe [141] and Holzer [135].

- **Working principle**

Modern FIB/SEM machines are equipped with ion and electron optical columns. These dual-beam systems are integrated with high precision MEMS (Microelectromechanical Systems)

which make them perfect tools for high precision serial sectioning and/or high-resolution imaging. As Figure 5.2 shows in a dual-beam FIB-SEM, separated ion gun and electron gun integrated in one chamber typically by an angle of  $52^\circ$  (FEI series) or  $54^\circ$  (Carl Zeiss series). They can work both independently and synergistically. The ion gun can be utilized in nano-machining and nano-fabrication. An example of this application is the TEM lamella preparation with a lift-out technique [150]. It also may serve as a SEM with the electron beam working solely.

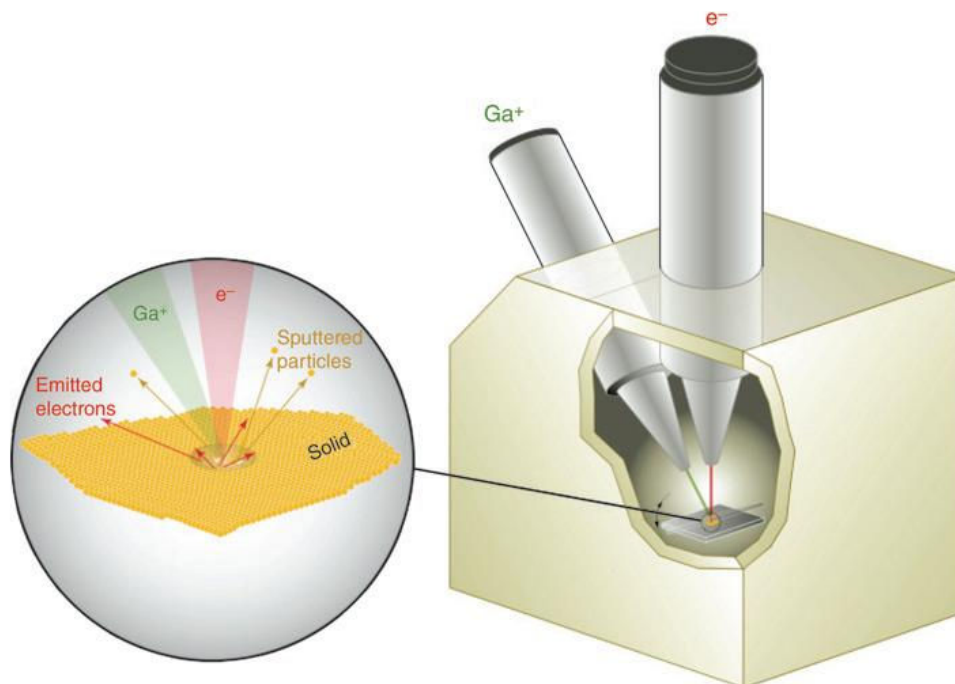


*Figure 5. 2 Dual beam FIB-SEM system (after Volkert [151])*

Anyhow, definite advantages of dual-beam FIB-SEM lie in in-situ sectioning and imaging. This allows users to conduct fine milling with the ion beam normal to the specimen surface and simultaneously image using the electron beam.

As depicted in Figure 5.3, in a dual-beam FIB-SEM system, the ion beam ( $y$ -direction) can etch (mill) away material with close to nanometric (within the range of 10 nm) precision and the sample can be rotated with a numerically controlled stage; the electron beam interact with the ion beam treated surface ( $x$ - and  $y$ -directions), and signals are collected by different detectors. Alternating performance of sectioning and imaging is secured without disturbing the sample. The sample is placed at the eucentric point, so that the electron beam that interacts with the surface can be scanned with a constant angle without changing sample position. During the acquisition of the image stack, the imaging plane is moving in the  $z$ -

direction at a prescribed interval that is either equal or non-equal to the lateral pixels, resulting in a stack with isotropic or anisotropic voxels. This sequential sectioning process can be automated.

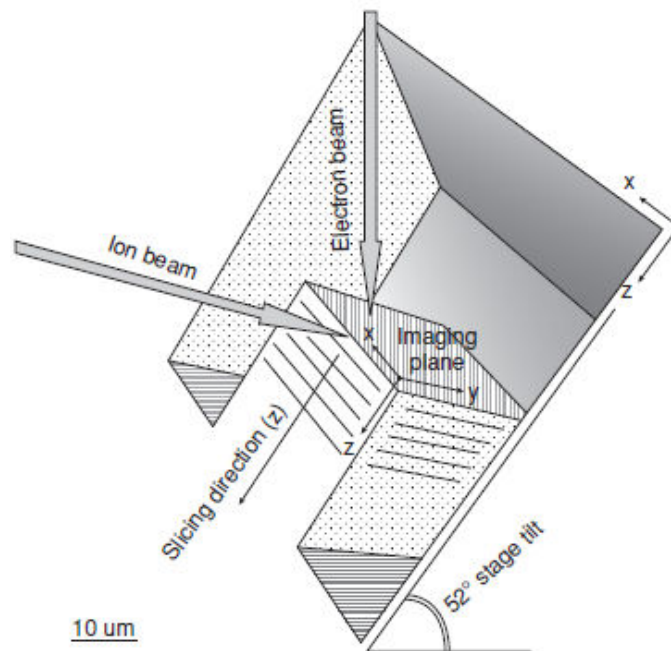


*Figure 5. 3 A schematic for the FIB serial sectioning (after Holzer [135] )*

The entire serial sectioning procedure includes three phases that are described below: (1) cube preparation and optimization of parameters, (2) serial sectioning, and (3) data processing.

### **(1) Sample preparation**

Before starting the FIB serial sectioning routine, several sectioning and imaging parameters that are dependent on each other have to be optimized such as, beam energy, magnification, slicing step. Resolution is determined by the scale that should be sufficient for evaluating microstructural, chemical, or crystallographic features in the sample. The magnification and volume relate to the resolution. Definition of an optimum magnification, the relationship between depth penetration of the electron beam and excitation volume of BSE and X-rays also must be taken into account. This relationship is illustrated in Figure 5.4 with SiO<sub>2</sub> as reference materials.

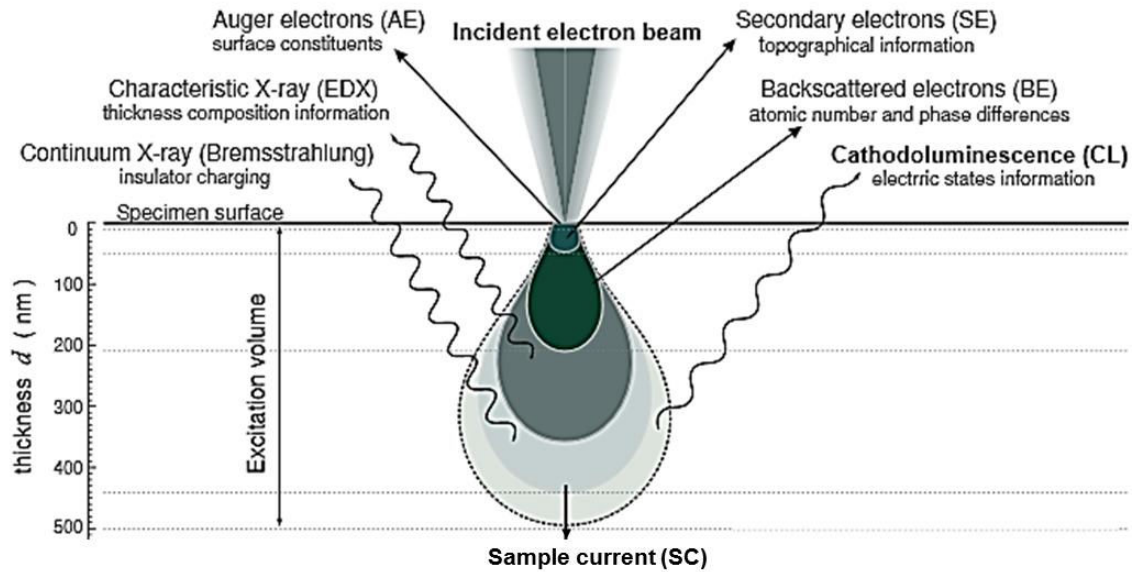


Figure 5. 4 Electron material ( $\text{SiO}_2$ ) interaction diagram (adapted from Salh [152])

Depending on the beam energy, the size of the BSE interaction volume can influence the effective resolution of FIB tomography. For instance, the depth of the BSE excitation at 5 kV is larger than 100 nm, which is too large for nano scale investigations. In contrast, at 1 kV the BSE excitation depth is in the range of a few nm which makes it a suitable parameter for nano scale analysis. By the same reasoning, slicing step size should be in line with this scale. For example, serial sectioning at  $\geq 5$  kV (SEM) with a step size in the 10 nm range will lead to a strong oversampling.

In addition, for non-conductive samples a thick conductive coating (carbon, platinum) should be deposited beforehand to secure images of good quality by avoiding charging effects. Trenches are created to prepare a cube as the volume of interest.

## (2) Data acquisition

In this step, the major concern is the drifting correction in  $z$ - direction and  $xy$  plane. In order to produce a regular stack of images which can directly be transformed into a voxel-based data volume,  $z$ -step size of milling should have similar scales to the  $xy$  pixels (i.e., approximately 10 nm). Because the acquisition of hundreds of images can last for 20 hours or even longer, drifting can become significant. Without correction, the drifting in  $z$ - direction causes  $z$ - distortions (nonevent  $z$ - step size) in the reconstructed 3D microstructure. The drifting can be compensated by pattern recognition by tracking fiduciary markers [140].

However, in modern FIB/SEM systems have become much more stable, and usually after a period of stabilization and thermal equilibration drifting becomes very small or even negligible. In contrast, drift components in  $x$ - and  $y$ - directions can be compensated during the post processing with image alignment and registration.

In practice, the  $z$ -drift correction can be verified by measuring the distance between two lines which form a certain angle (Fig. 5.5(a) and (b)). According to geometry, the average  $z$ -step size is:

$$\Delta z = \frac{z_0}{d_0} \frac{d_n - d_0}{n} \quad (5.1)$$

Where  $n$  is the number of slices,  $d_n$  is the distance between the two crossing lines,  $d_0$  is the initial distance,  $z_0$  is the distance from the intersect to the edge.

The  $x$ - and  $y$ - direction drift causes the images to move out of the field of view. For those images within the field of view, due to slight  $xy$ - drift, structure in  $z$ - direction is not continuous. This type of drift can be corrected offline. As shown in Fig. 5.5(a), before slicing, two fine paralleled lines that are perpendicular to the surface were made with FIB milling, these two points at a constant distance can be used as alignment references. After the alignment, two straight lines should be reconstructed.

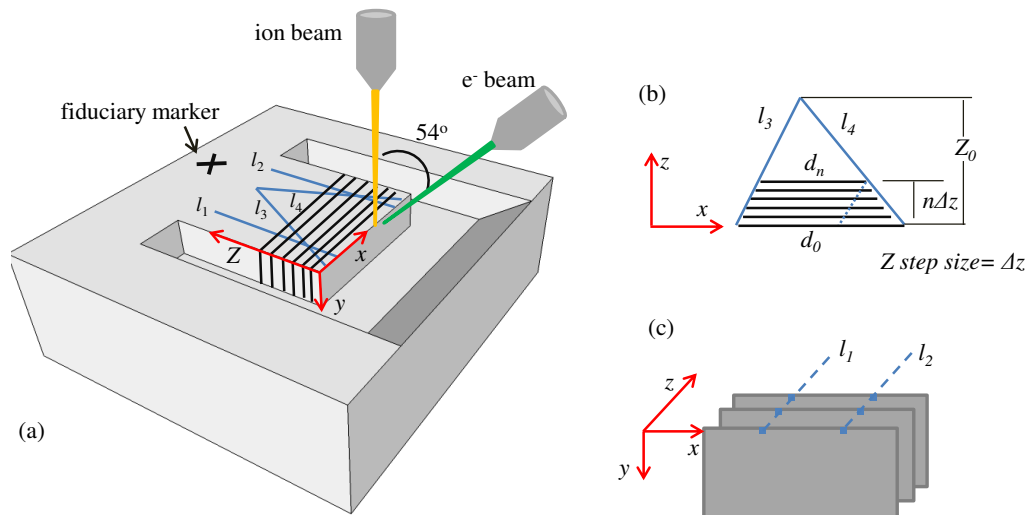


*Figure 5. 5 The schematic of drift correction*

In addition to the drift compensation, further corrections are needed because of the tilting angle ( $52^\circ$  for FEI system,  $54^\circ$  for Zeiss system) in dual beam systems.

*Focus correction:* during the serial sectioning, the imaging plane is shifted in  $z$ -direction and therefore focus tracking is required in order to correct for the increasing working distances. When shifting the working distance and imaging under oblique angle, the region of interest is shifted out of the field of view. This has to be compensated with automated region tracking.

*Fore-shortening correction:* When imaging is conducted at an angle incident to the surface, the images are not taken from front view. A tilt-correction must be applied to remove the fore-shortening effects of imaging.

In modern dual beam FIB/SEM systems, all these phenomena are compensated with the automated sectioning procedure. In this way, image stacks of high quality can be acquired.

### **(3) Data processing**

Care should be taken to obtain usable and valuable data from the 3D stacks. Usually, depending on the material system to be dealt with, specific treatments should be employed correspondingly. Nevertheless, some general procedures of image processing can be described as follows:

- Image alignment registration for 3D-reconstruction
- Removal of noises and spikes using filters (e.g., median filter)
- Segmentation of different phases (different materials, pores, etc.)
- Separation of individual objects for subsequent statistical analysis
- Visualization of volume, surface or orthotic sections based in 3D grey-scale data
- Quantitative analysis and statistical measurement of features (i.e., particle/pore size distributions, surface area, shape factors)

For interested reader, a standard FIB tomography wizard is available at (<http://www.vsg3d.com/webinar-3d-fib-tomography-and-reconstruction-materials>).

## **5.2 Experiments**

### **5.2.1 Experiment setup**

In this work, a nVision 40 (Figure 5.6) and a AURIGA 60 FIB-SEM (Carl Zeiss, Germany) were used to conduct the serial sectional data acquisitions. SE, BSE detectors were used to obtain the microstructure features and EDX detector was used to determine the composition.



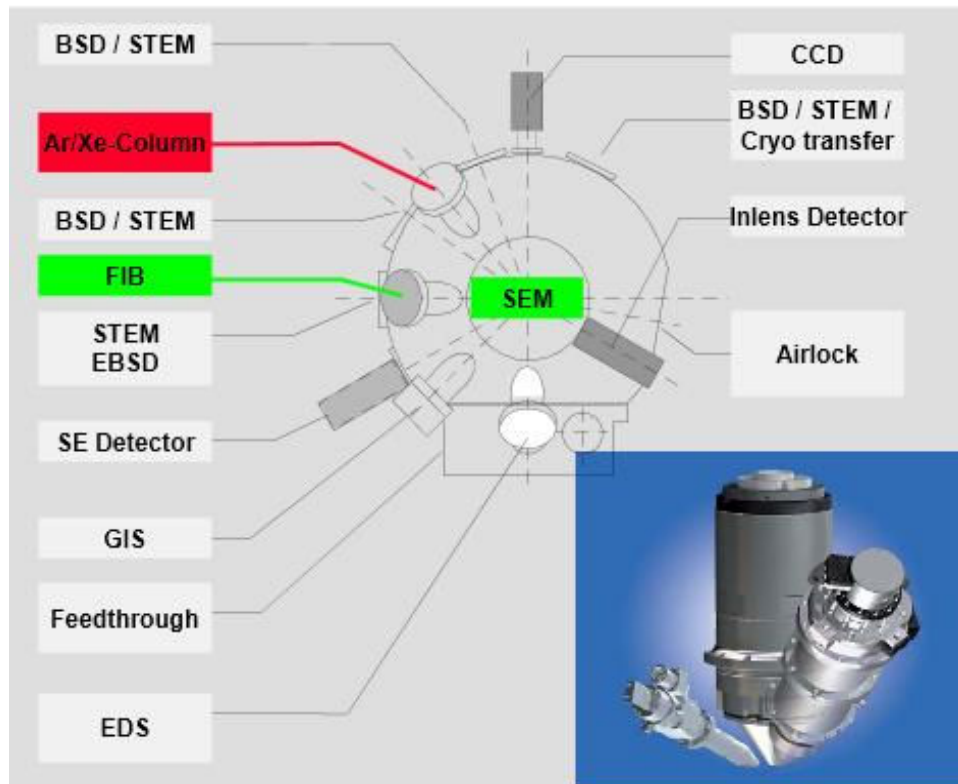


*Figure 5. 6 Configuration of the Nvision 40 FIB/SEM [153]*

## 5.2.2 Materials and procedures

- **Materials**

Commercial 0603 case size Ni-MLCC chips fabricated at Samsung (See section 3.1) were used in this work. The cylindrical Ni-MLCC sample (#1), in the green (g) state (#1-g) and after sintering (#1-s) are detailed in Chapter 4. Cross-sections of a green (#2-g) Ni-MLCC chip (binder removed) and a sintered (#3) MLCC chip were prepared by traditional metallography procedures. Sample #1-s-ct that was saved from the non-destructive X-ray nCT characterization was mounted onto conductive paste glued on the sample holder. Details of the samples examined are listed in Table 5.1.

The thickness step ( $z$  pixel) for ion beam milling was adjusted to be equal to the  $xy$  pixels to obtain an isotropic voxel. Sample #1-g and sample #2 are for comparison of microstructures in the green state between with X-ray nCT and FIB-nT. Sample #1-s and sample #1-s-ct are for comparison in the sintered state. Sample #3 is extracted from an entire 0603 MLCC chip sintered under the same conditions as the cylindrical sample (#1-g, #1-s-ct) to investigate the representativity of the cylindrical sample and possible size effect. The data acquisition on

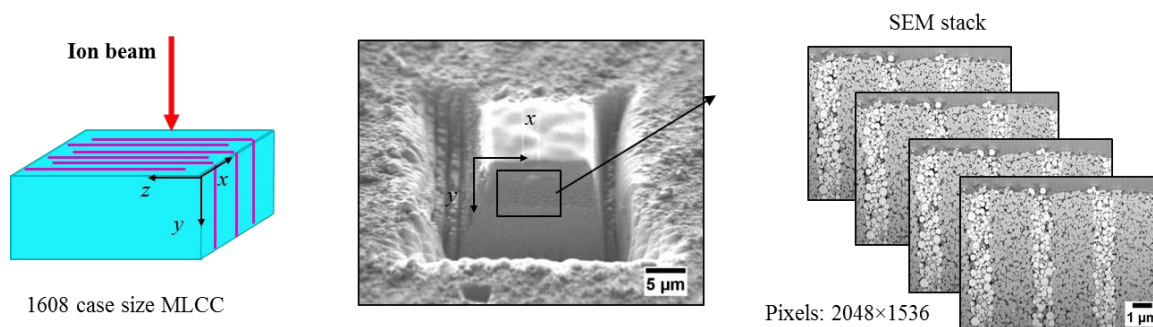
sample #3 was conducted with a larger voxel size ( $30 \times 30 \times 30 \text{ nm}^3$ ) so that a larger volume can be obtained.

Sample ID	Heat treatments	Methods	Slice number	Voxel size (x,y,z nm)	Analyzed volume( $\mu\text{m}^3$ )
# 1-g	@230 °C, 2 hours, air	X-ray nCT	-	26× 26 × 26	Ø 20 × 20
# 1-s	Heating/cooling:15 °C/min, 1150 °C, 1hr, N <sub>2</sub> +2%H <sub>2</sub>	X-ray nCT	-	26× 26 × 26	Ø 20 × 20
# 2	@230 °C, 2 hours, air	FIB-SEM (SE,BSE)	473	5 × 5× 5	9.8 × 6.6 × 2.3
# 1-s-ct	Heating/cooling:15 °C/min, @1150 °C, 1hr, N <sub>2</sub> +2%H <sub>2</sub>	FIB-SEM (SE,BSE)	578	5× 5× 5	6.5 × 5.1× 3.4
# 3	@1150 °C, 1hr, N <sub>2</sub> +2%H <sub>2</sub>	FIB-SEM (SE,BSE)	400	30 × 30 × 30	15.3× 12.0 × 7.6

*Table 5.1 The details of the samples that were analyzed*

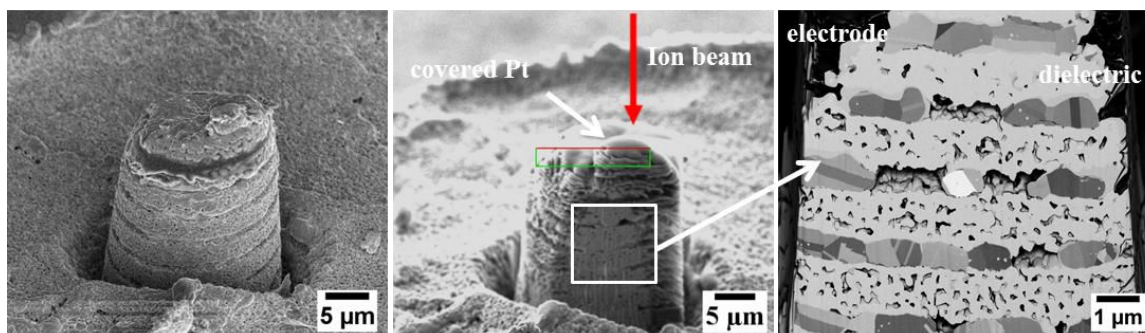
• **Procedure**

Data acquisition on a green 0603 Ni-MLCC (sample #2) was conducted using the nVision 40 FIB-SEM at the CMTC, Grenoble INP (Fig. 5.7).



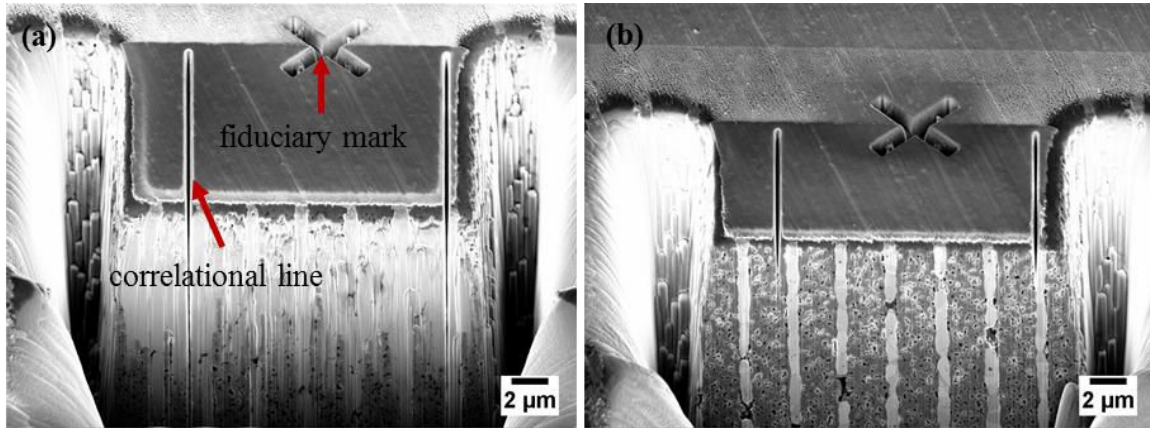
*Figure 5. 7 Serial sectioning on the sample #2*

Figure 5.8 shows the serial sectioning of the sample #1-s-ct. Note that the fiduciary marker was not used because the pattern recognition feature has not been integrated into this system at this moment.



*Figure 5. 8 Serial sectioning on the sample # 1-s-ct*

Data acquisition on sample #3 (Fig. 5.9) was conducted using AURIGA 60 FIB-SEM at IMT, University of Jena. The etched cross served as the fiduciary mark for the pattern tacking. Two correctional lines were made to verify the final reconstructed microstructure.



*Figure 5. 9 Serial sectioning on the sample # 3*

### 5.2.3 Image processing

The goal of image processing is: (1) to separate the pores, Ni and BT particles in the green and sintered samples and extract the microstructural parameters such as pore size, orientations, particle size distribution of Ni and BT particles; (2) to quantify the discontinuity and roundness of the electrode.

For this, the following steps have to be followed:

- **Slice alignment**

This pretreatment can be done manually or automated. It consists of image registration and shearing correction.

Image registration: each slice is used as the template with respect to which the next slice is aligned, so that the alignment proceeds by propagation [154]. In this work, the mapping of coordinates takes into consideration of translation and rotation. The new coordinate  $\mathbf{u}$  is given by:

$$\begin{pmatrix} \cos \theta & -\sin \theta \\ \sin \theta & \cos \theta \end{pmatrix} \times \mathbf{u} + \Delta \mathbf{u} \quad (5.2)$$

Registration can be done using an ImageJ plugin called StackReg [154] or using registration module in Avizo. After registration, the stack is as shown in Figure 5.10(d).

Shearing correction: a shearing by  $\theta$  in  $-y$  direction would be found, this could be corrected by a pre-alignment with the two correlational lines Figure 5.10(c) before the registration, or shearing a certain angle  $-\theta$  using the shearing module under Avizo.

Finally, the stack was cropped into a cube as shown in Figure 5.10(f). It is noted that the pre-designed straight lines on the surface are kept straight as they should. This means that the reconstructed 3D microstructure is quite reliable.

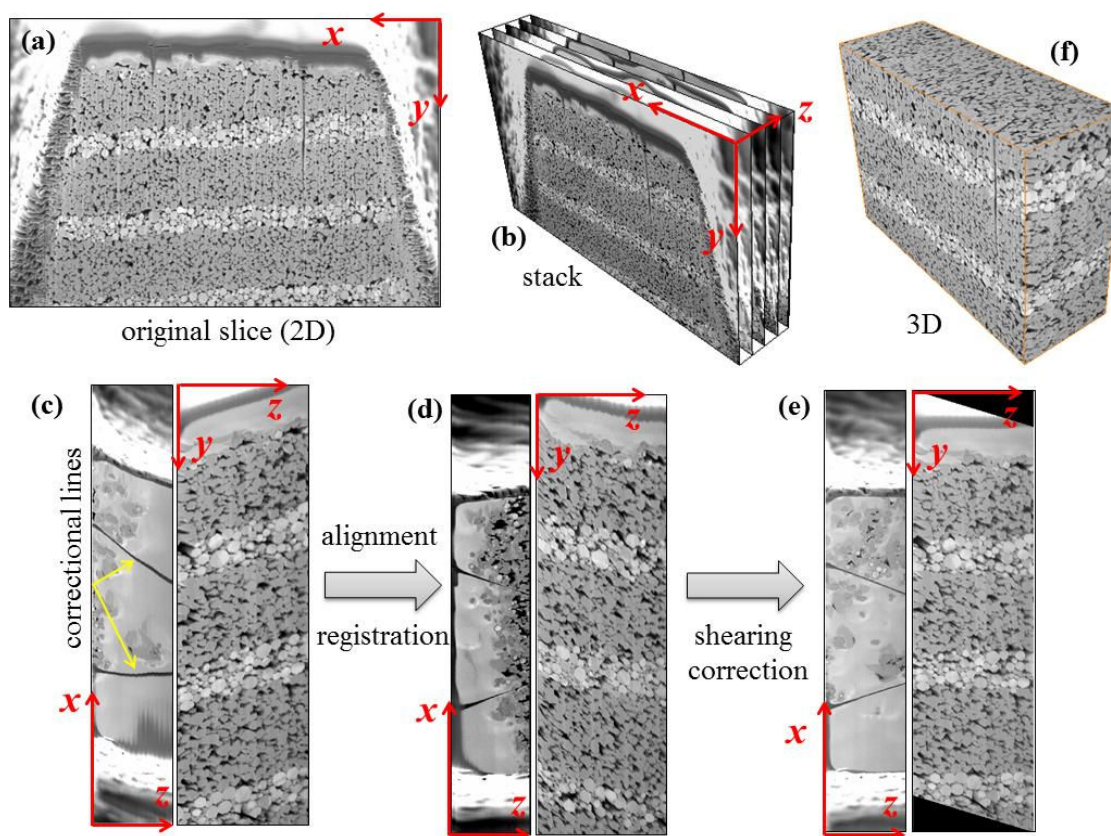


*Figure 5. 10 Image pretreatment flow chart*

- **Filtering**

- (1) Removal of noise

A 3D median filter was used to remove the noise [155]. Figure 5.11(a) shows the principle of the median filter. Pixel with high value (which is assumed as a noise) is replaced by the median value in its local neighborhood. In doing this, it preserves edges while removing noise. Figure 5.11(b) and (c) show the one slice of the FIB-BSE stack before and after the application of the 3D median filter.

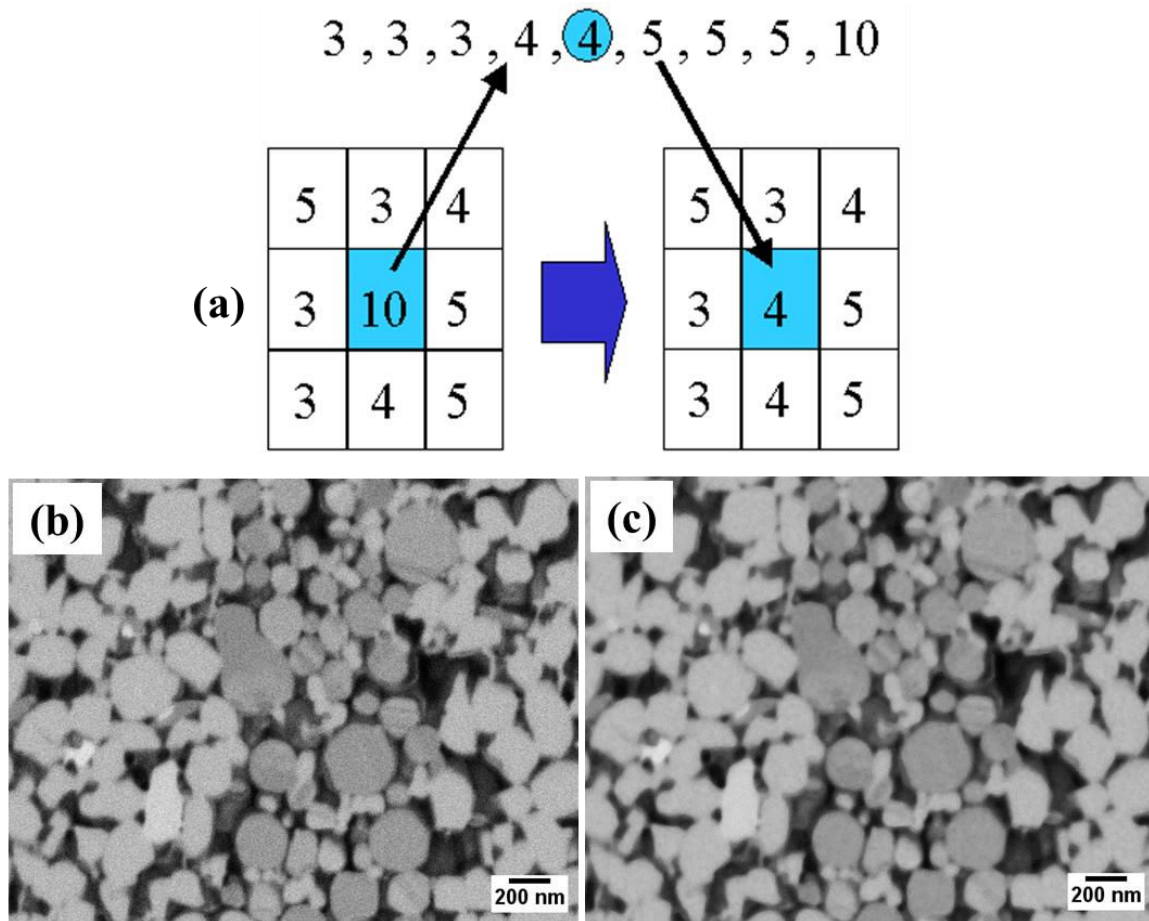


Figure 5. 11 Removal of noise using 3D median filter: (a) principle of the median filter,(b) a slice of FIB BSE stack of green MLCC (sample #2), and (c)after filtering using 3D median filter.

## (2) Removal of shadowing

Due to the incident angle between the electron beam and the sample surface, the bottom part of the images appears darker. This shadow can be problematic when segmenting images. However it can be removed by subtracting the gray gradient. This procedure can be done by using an ImageJ filter plugin “fit polynomial”. As shown in Figure 5.12 after this correction, there are two sharp peaks in the gray value histogram. The first peak corresponds to the dark-gray phase BT, while the second one the light-gray phase Ni.

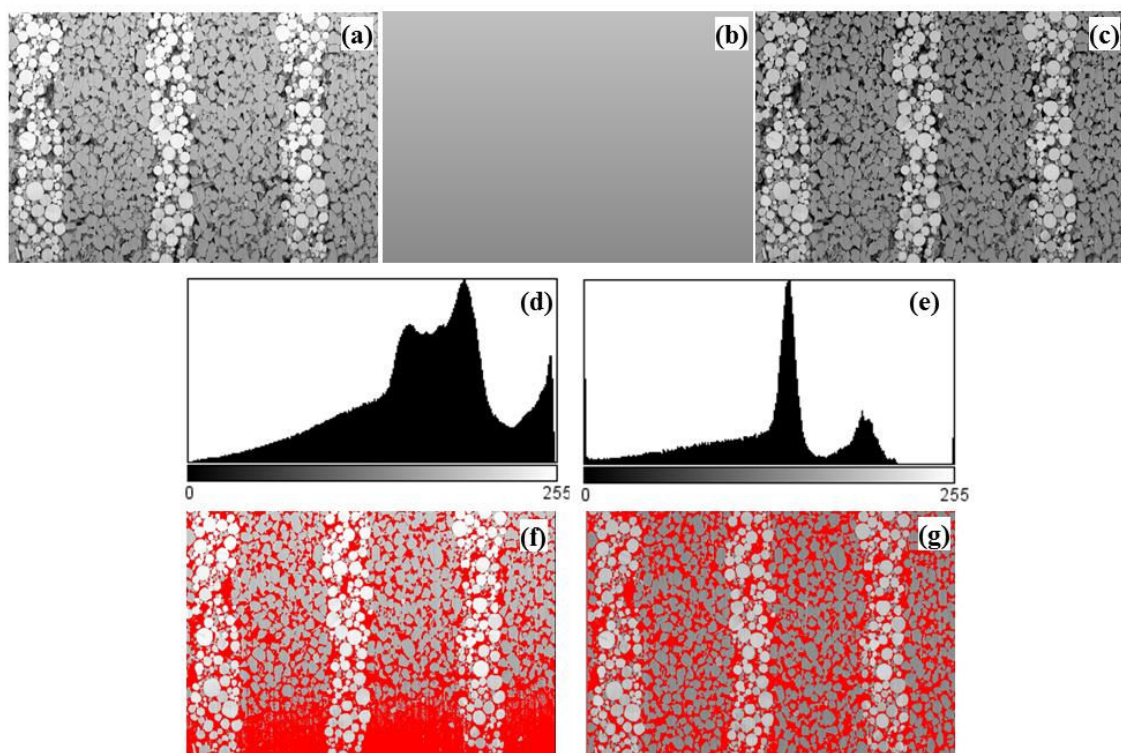


Figure 5. 12 (a) an original slice (b) the gray gradient of the slice, (c) resulting image after subtraction of the gradient image, (d) histogram of the original image a, (e) histogram of the filtered image c, (f) the pore phase separated from the original image, and (g) the pores in the image after the filtering

Figure 5.13 shows the pretreated and corrected processed stacks for samples #2, #1-s-ct and #3.

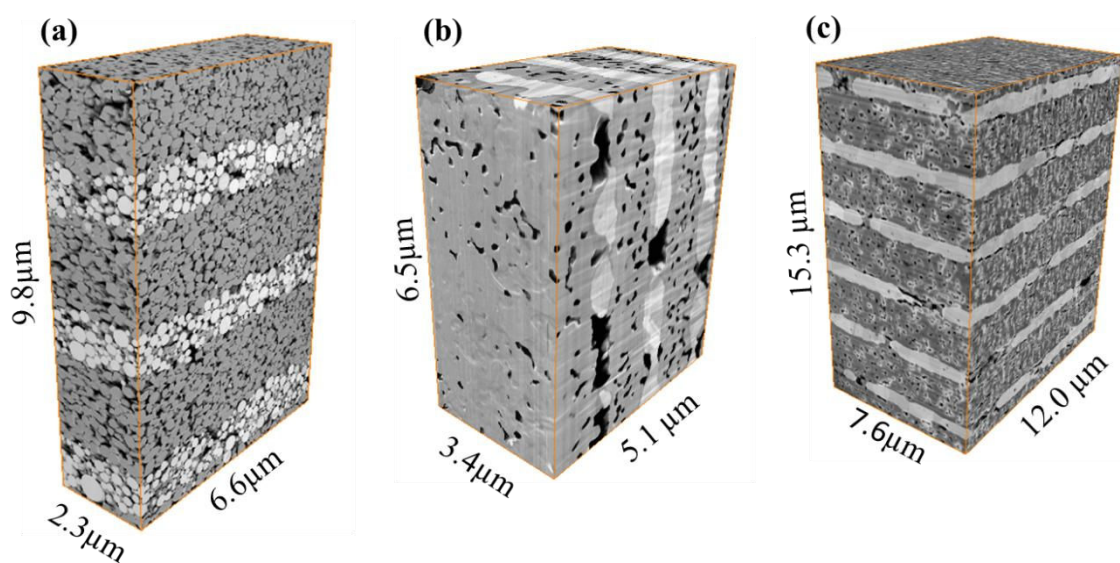


Figure 5. 13 3D reconstructed volume for (a) #2, (b) #1-s-ct and (c) #3

### 5.3 Comparison of FIB-nT with X-ray nCT

#### 5.3.1 Characterization of green microstructures

Figure 5.14 shows the microstructure of representative volume of 0603 MLCC obtained by X-ray nCT (#1-g) (Figure 5.14(a)) and FIB-nT (#2) (Fig. 5.14(b)). As for the microstructure obtained with the FIB-nT, the Ni and all BT particles, even the nano scale BT additives in the electrode, are discernible. Hence, the FIB-nT is an ideal tool to finely characterize the microstructure of the present MLCCs. Conversely, when using X-ray nCT, pore structure is distinguishable, but particles cannot be decomposed as the size of their contacting area is under resolution. We have demonstrated in Chapter 4 that the porous regions or the heterogeneities are associated with the final discontinuities of electrode. In this sense, the quality offered by X-ray nCT is sufficient to study the formation of discontinuities.

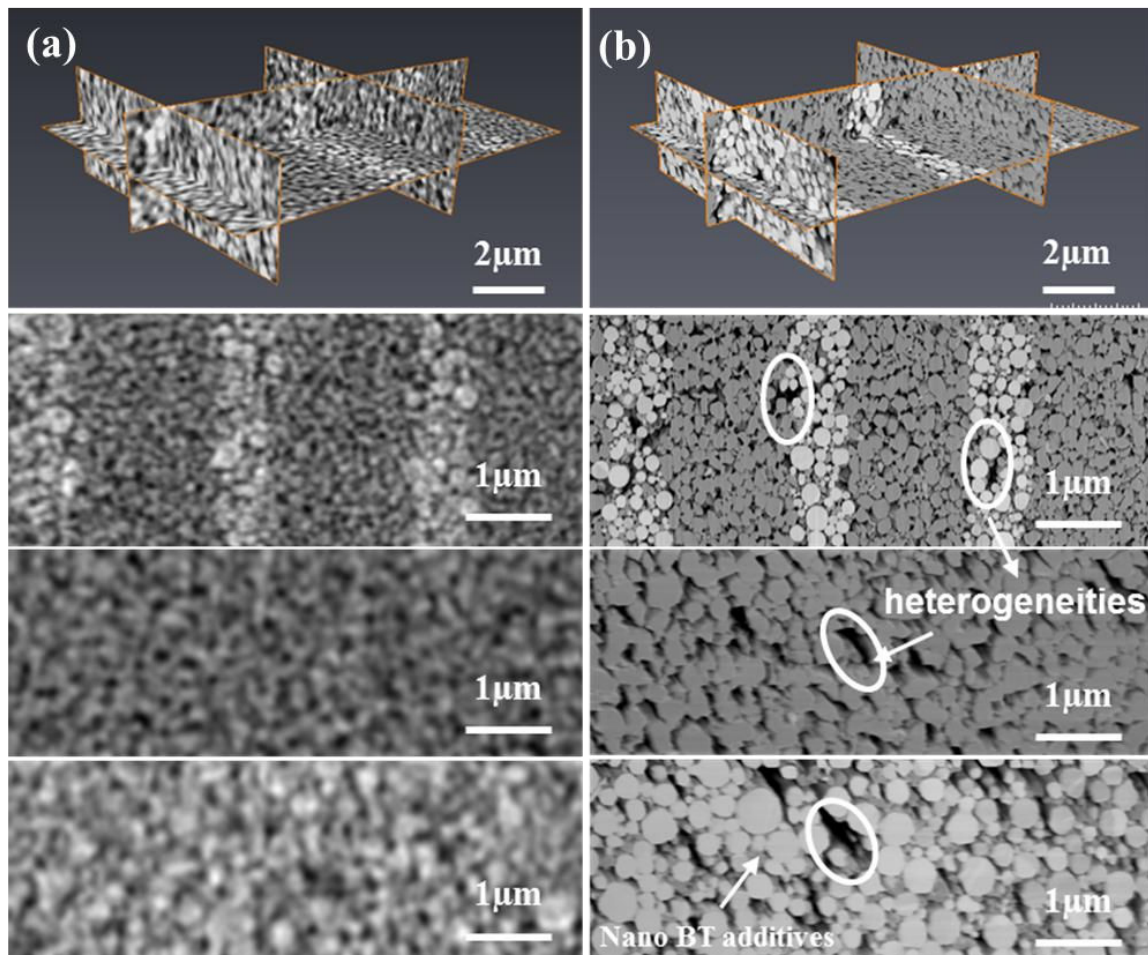


Figure 5. 14 Microstructures of the green MLCC with X-ray nCT (column a: sample #1-g) and FIB-nT (column b: sample #2)

### 5.3.2 Characterization of sintered microstructures

Figure 5.15 shows the comparison of the microstructures of the final microstructure (sintered) with X-ray nCT and FIB-nT. Note that the microstructures originate from the same location of the same sample. It can be noticed that the morphology of the discontinuities and of the pores are quite consistent with each other. Although X-ray nCT image has good Ni/BT phase contrast, pores are still blurry. This X-ray nCT image is preferable for evaluation of the electrode morphology. The FIB-SE image exhibits good solid/pore phase contrast. Thus it is preferable for pore quantification. The FIB-BSE image has good Ni/BT phase contrast, and the Ni grains, entrapped BT additives are discernible.

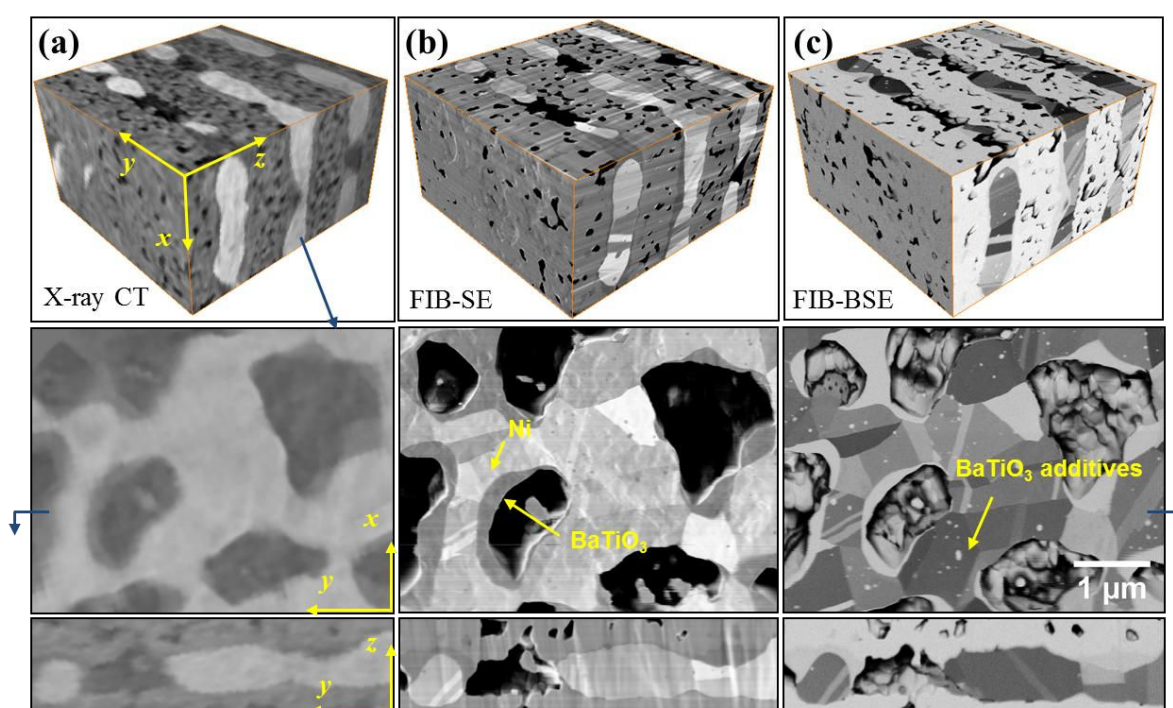


Figure 5. 15 X-ray nCT (column a) and FIB tomography (SE mode: column b), (BSE mode: column c) on the final microstructure

Through these qualitative comparisons, we conclude that X-ray nCT is efficient to characterize defects in the MLCCs, while the better resolution of FIB-nT provides more information on pore characteristic, grains, and additives. Combining the strengths of the non-destructive X-ray nCT and the high resolution FIB-nT, correlative studies can be carried out. In the following section, the quantitative correlative studies are presented.



### 5.3.3 Evaluation of pore size

Figure 5.16 shows the pore percolation in the BT layers before and after sintering. In both the green and sintered microstructures, the 3D pores are highly percolated, making it inappropriate to separate the pores.

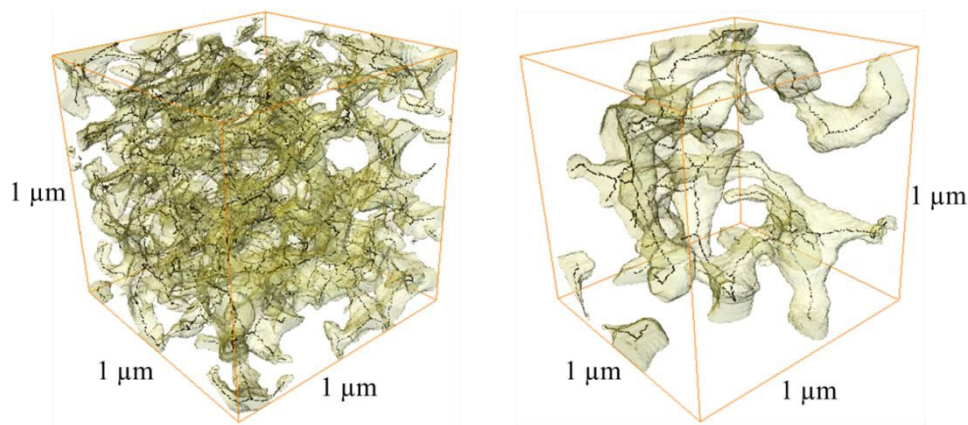


*Figure 5. 16 Percolation of pores and skeletons: (a) before sintering; (b) after sintering*

In 2D, individual pores in sections are generally easy to isolate before characterization. Separating the continuous 3D pore space into individual pores is technically feasible; however, this depends on the definition of a pore. As Bernard et al. [121] argued, there is no intrinsic partition of the 3D pore space and the definition of pore must be related to a physical phenomenon.

In this work, the pore size distribution is statistically analyzed from the 2D sections using line intercepts (in practice, 1-pixel thick). The segmentation of the pore phases is very decisive to the accuracy of the pore size measurement. With the high resolution FIB-nT, the pore/solid phase contrast is excellent. We use the porosity measured with FIB tomographic data as a benchmark (refer to Table 5.2). When we segment the pores in the microstructure obtained by X-ray nCT, first we need to ensure that the porosity is the same as that obtained from the FIB tomographic data. Figure 5.17 compares the pore size distributions in the Ni layers and BT layers in both green and sintered MLCC chips.

The pore size distribution measurements with X-ray CT and FIB-nT are reasonably in agreement with each other in terms of the mode, median, mean and frequency (i.e., they are in the same size bin). However, distribution curve for the X-ray nCT is not as smooth as that

for the FIB-nT. This is probably due to the differences in dataset quality. The voxel size for the CT microstructure is indeed 26 nm, while for FIB tomography microstructure, it is 5 nm.

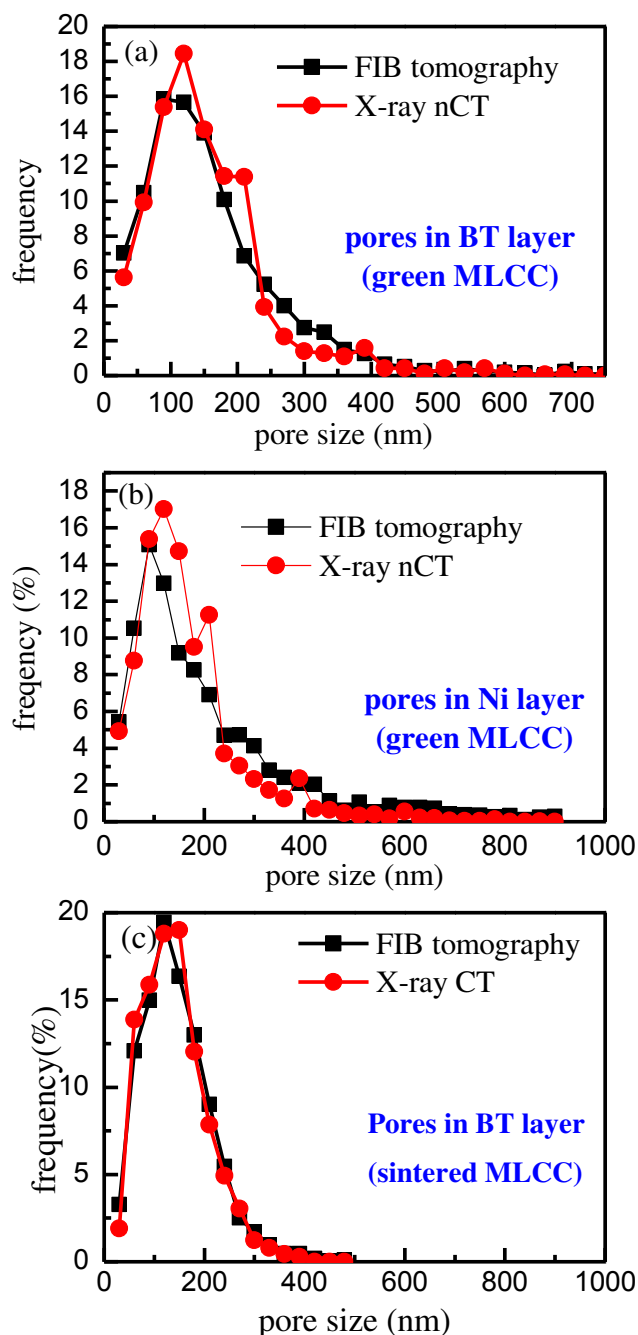


Figure 5. 17 Pore size distribution in the BT (a) and Ni (b) layer obtained with X-ray nCT and FIB-nT

Given the same volume in voxels, the size of the dataset for X-ray -nCT is 1/5 of that for the FIB-nT. Nevertheless, we can conclude that the X-ray nCT, as a pore scale analysis tool, is sufficient to study pore evolution.

In addition, note that the average pore size (160 nm, Ni layer Figure 5.17(b)) is close to the average particle size (180 nm, see Figure 3.3(b) in Chapter 3). Most of the pores can be referred to as intrinsic pores, which have the same scale of the particles. The fraction of larger pores (~800 nm, that is 4-5 times large the particles) remains small. These large pores are extrinsic pores, which are considered at the origin of electrode discontinuity (Chapter 4). The pores (extrinsic and intrinsic pores) in the sintered BT layers (Fig. 5.17(c)) do not contribute to the formation of discontinuities in the BT layer, because the BT layer is thicker. During sintering, both types of pores disappear.

## **5.4 Particle size distribution (PSD)**

The geometry and packing of the particles are key factors for the final microstructures; hence, the evaluation of the particle size distribution (PSD) is of much interest to this study. The initial particulate characteristics will be used both to identify possible initial defects and to provide input parameters for the DEM simulations. We take the advantage of the high-resolution FIB tomography to implement this task.

Segmentation and separation are required to quantify the microstructure.

### **5.4.1 Segmentation**

Ni and BT particles (including the nano sized BT additives) as well as pores have sharp contrast as shown in Figure 5.18(a-b). Following the de-shadowing processing, thresholding process was applied to the stack to separate different phases by choosing corresponding threshold value (Fig. 5.18(c)). However, due to edge effect, some sharp corners of the BT particles were recognized as Ni particles (Fig. 5.18(d)). The median filter is capable of eliminating these errors, but as a consequence of this filter some pixels in the real Ni particles disappear. In this work, the noise with volume under 150 voxels (an approximate size of 30 nm) is firstly labeled and eliminated (Fig. 5.18(e)). Some artifacts that were recognized as Ni (above 150 voxels) can be removed manually by filling the selected volume with background color (Fig. 5.18(f)). The original image is then superimposed with Ni phase (Fig. 5.18(g)) to obtain sharper contrast. The BT particles in the dielectric layers and the BT additives in the electrode are identified (Fig. 5.18(h)). The remaining phase corresponds to pores (Fig. 5.18(i)).

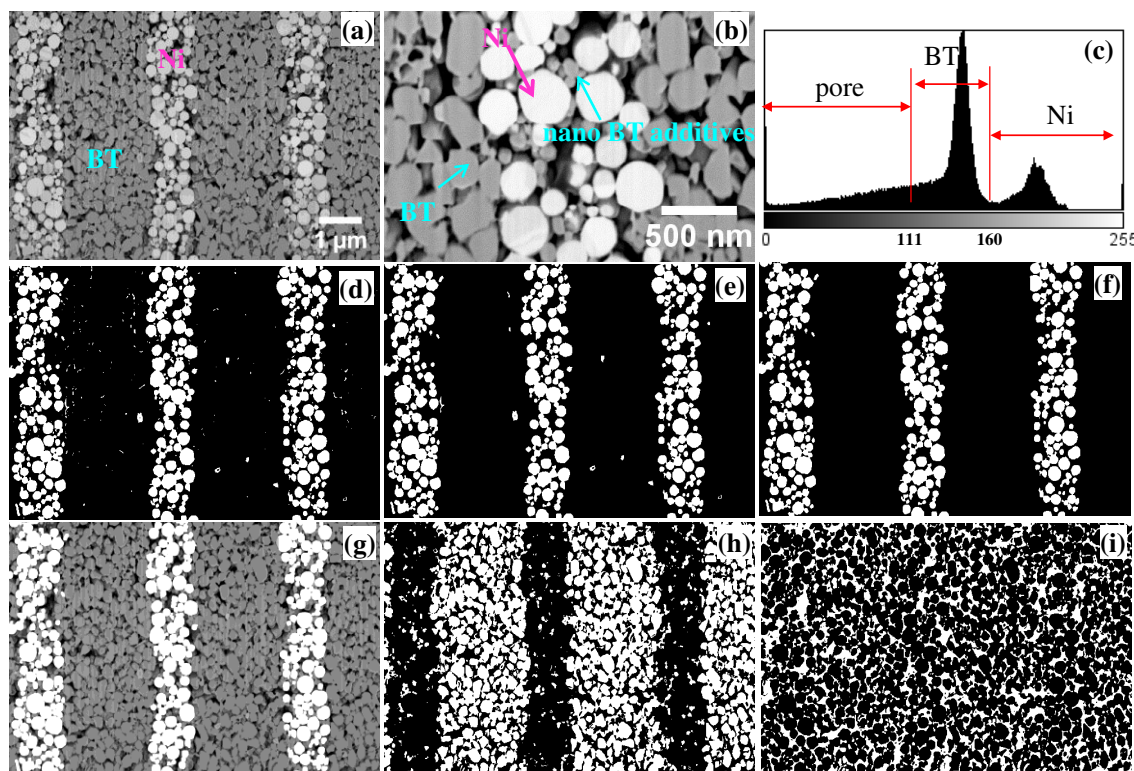


Figure 5. 18 (a) an original slice, (b) a zoomed in area of the original image, (c) histogram of the slice, (d) identification of Ni phase, (e) removal of noises from image d, (f) manual removal of the artifacts, (g) imposition of the electrode on the original image, (h) identification of the BT phase, and (i) the remaining pore phase

#### 5.4.2 3D watershed segmentation

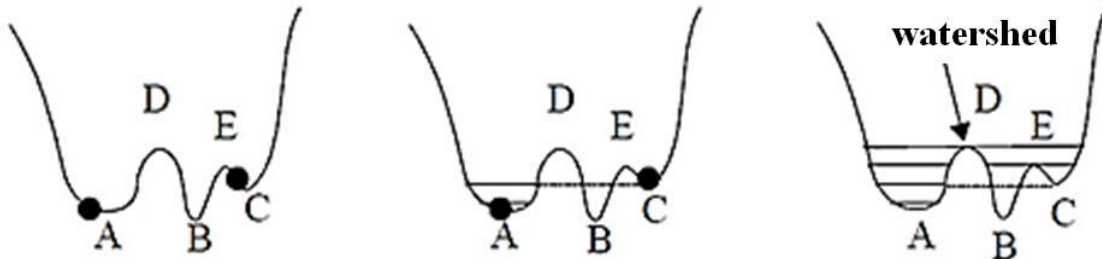
Watershed segmentation [156] is usually preferred for separating touching features in an image that are mostly convex.

This algorithm simulates the flooding from a set of labeled regions in a 2D or 3D image. It expands the regions according to a priority map, until the regions reach the watershed lines. The process can be understood as progressive immersion in a landscape (Fig. 5.19).

This algorithm depends on two inputs:

- I. Definition of the ultimate points (or, maxima): these maxima are labeled as different marker regions that are used as seeds for the flooding. It is like the water trying to retrieve the catchment areas. In doing this, there will be as many separated objects as markers.

II. Definition of Euclidean distance map: a grey image representing the landscape height field that controls the flood progression and finally the location of watershed separations. These separations are located on the crest lines between valleys of landscape, so called watershed (Fig. 5.19).



The curve represents three minima, A, B and C and two maxima D and E. The set of markers contains only A and C

A is flooded at the levels 1 and 2, but not B. Then it reaches point C.

C: From the next level

A and C are flooded until reaching point D. D belongs to the watershed. But not E

*Figure 5. 19 Definition of watershed in a watershed segmentation algorithm from [157]*

### 5.4.3 Particle size distribution

Figure 5.20 shows the separation of the Ni particle using the 3D watershed segmentation routine in the Avizo Fire packages.

Once the particles are separated, particulate characteristics, such as volume, surface area, equivalent diameter, sphericity and centroid can be calculated.

An equivalent diameter is used to describe the particle size. It is defined as:

$$d = (6V / \pi)^{1/3} \quad (5.3)$$

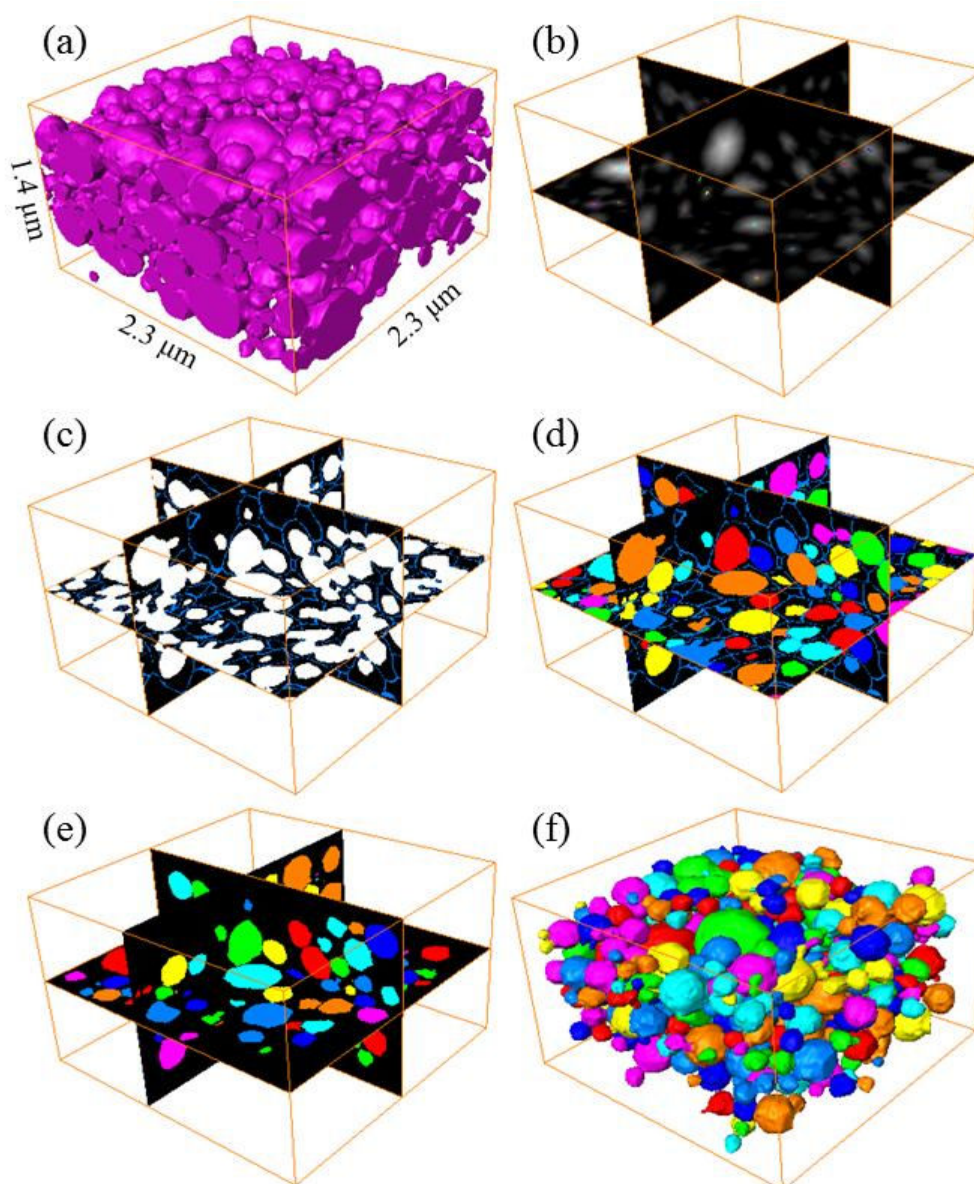
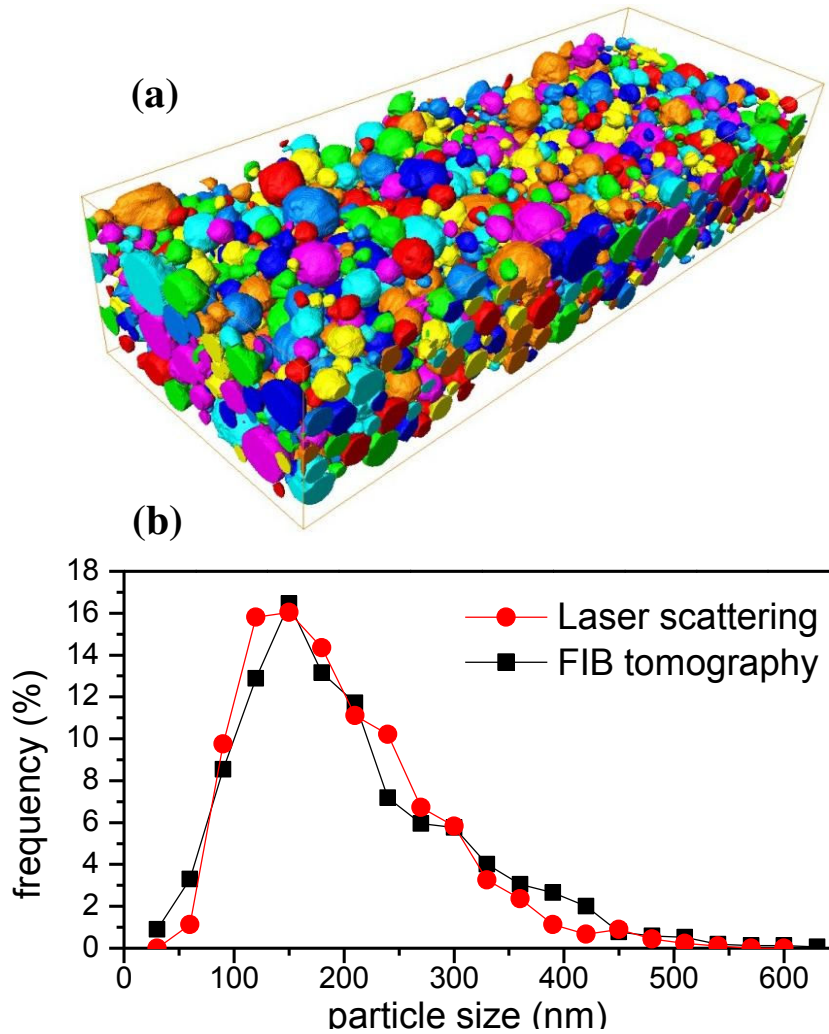


Figure 5. 20 Separation of Ni particles using 3D watershed segmentation (Avizo Fire): (a) binary stack consisting of connected nickel particles; (b) the Euclidean distance map of the binary stack; (c) binary image and watershed lines; (d) separation by subtracting the watershed lines from the binary image; (e) deletion of sectioned particles on the borders; (f) rendering of the randomly colored particles

Figure 5.21 shows the 3D visualization of the separated Ni packing of the electrode (Fig. 5.21(a)) and the corresponding PSD for the Ni particles measured by FIB-nT and laser scattering (LS)(Fig. 5.21(b)). Figure 5.21(b) demonstrates that the PSDs with laser scattering (based on 2D projection) and the FIB-nT are consistent with each other. Because the Ni particles are almost spherical, the 2D projection size (LS) is identical to the 3D size (FIB). The slight variation may be attributed to the sampling size. For the laser scattering data

collection, the sample size is approximately 1000 particles, while for the FIB tomography volume, there were about 1500 particles segmented in total.



*Figure 5. 21 Result of the 3D watershed segmentation of Ni particles in the electrode: (a) 3D view of separated Ni particles, colors are randomly assigned (BT inclusions not considered); (b) PSD measured with FIB-nT and laser scattering.*

The same 3D watershed algorithm was applied to separate the BT particles in the dielectrics layer as shown in Figure 5.22.

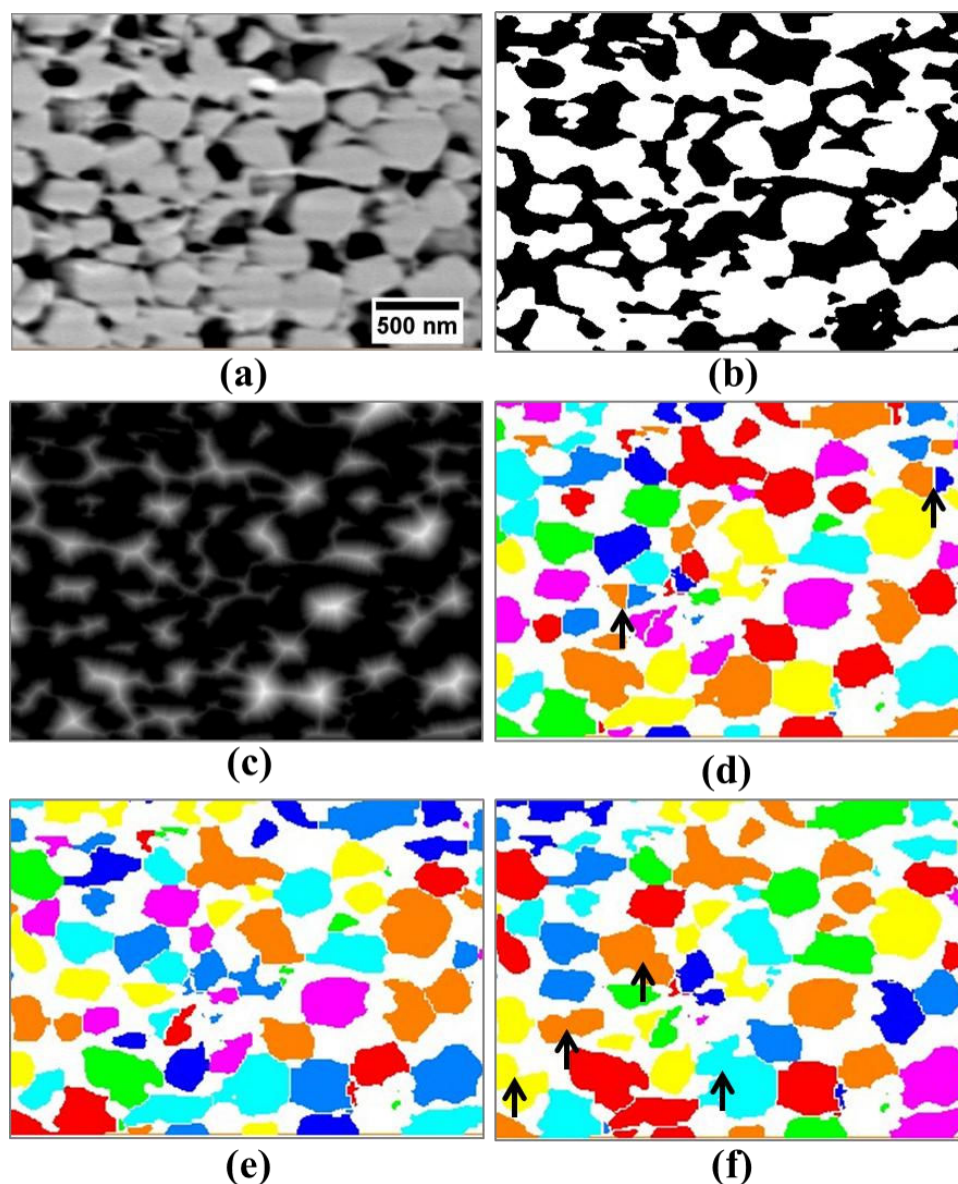


Figure 5.22 3D watershed segmentation for the BT particles in a representative dielectric layer: (a) gray level image, (b) binary image, (c) Euclidean distance map, (d) result at maxima size= 1 pixel, (e) result at maxima size = 2 pixels, (f) result at maxima size =3 pixels

We have shown here that care should be taken when applying the 3D watershed segmentation to the irregular particle systems. As detailed in the principles of the watershed, the maximum (ultimate point, calculated from a binary image) acts as a seed that will be used to retrieve the catchments. Thus, the number of maxima dictates the final number of separated objects. An overestimation of the number of maxima leads to an over segmented image (as shown by the arrows in Figure 5.22(d)). This happens when the object exhibits a concave feature. In that case, more than one maxima will be found in the volume of object (3D watershed). In another extreme case, if the maxima size is too large, contacting particles will be treated as one



(under segmentation shown in Figure 5.22(f)). So the option of the maxima size should be examined for each segmentation until an acceptable error is found. The ultimate decision for minimizing this error is made visually. In this work, the maximum size for the BT particle segmentation has been set to 2 pixels. Figure 5.23 shows the separated BT particles and the PSD with different maxima size.

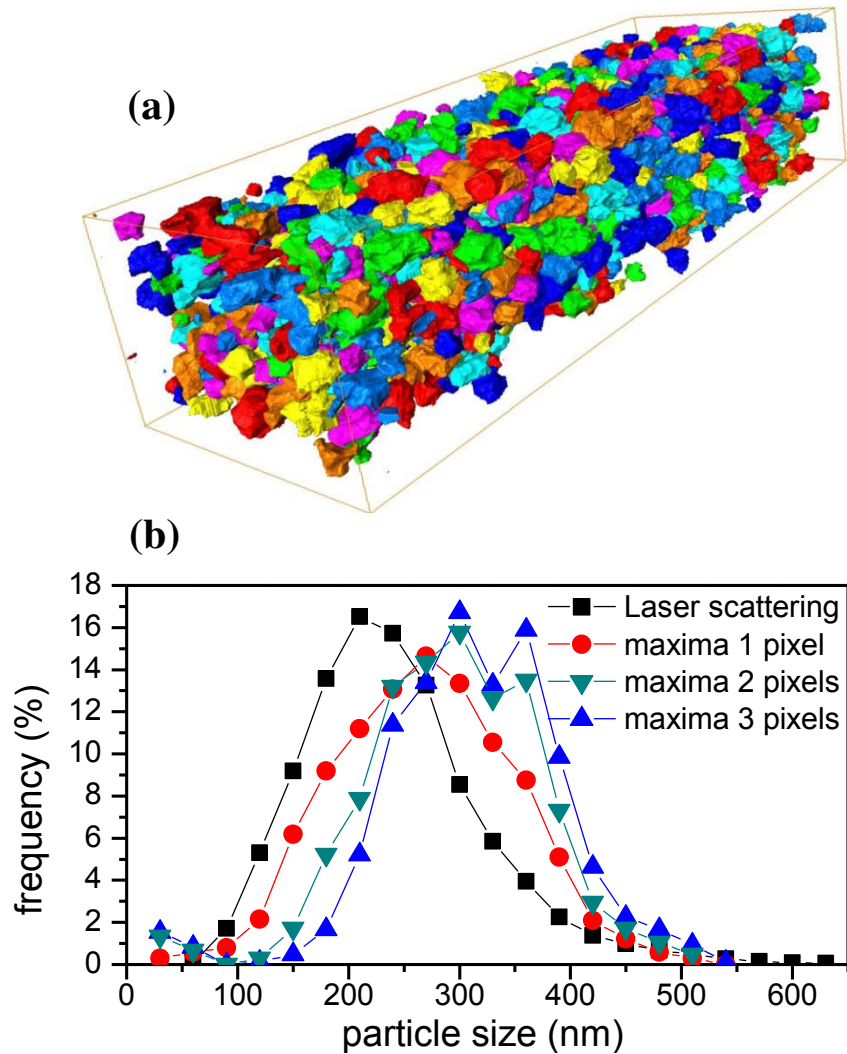


Figure 5. 23 Result of the 3D watershed segmentation of BT particles in the BT layer: (a) 3D view of separated BT particles, colors are assigned randomly;(b) PSD measured with laser scattering and FIB-nT (maxima size = 1, 2, 3 pixels)

Figure 5.23 indicates that the 2D projection based on LSA method predicts smaller particles size than the FIB-nT method. This is consistent with Kelly et al's [158] argument which states that, for nonspherical particles, image analysis leads to much larger particle sizes compared to laser diffraction. This is because laser diffraction undercounts events generated

by larger dimensions (major chord) or rather overestimates the contribution of minor chord data.

#### 5.4.4 Particle size distribution in 2D and 3D

Characterization of particles using FIB-nT is not simple. It cannot be accessed as easily as optical microscopy or SEM. In this section, an attempt is to establish the correlation between a traditional 2D sectioning measurements (SEM, OM) and 3D measurements (FIB tomography). By virtue of the 3D data, cross-sections can be attained by re-slicing the volume at an arbitrary angle. So the 2D measurement can be performed very easily by following a similar routine.

In this work, the model for unfolding cross-sections of spherical particle as described by classical stereology (see Russ' book [155]) is employed. The scheme dates back to Wicksell's work in 1925 [159] and has been refined by Schwartz [160] and Saltykov [161]. The simple idea is to use a thin plane to section the mono-size particles to obtain a mapping relation between 2D and 3D statistics as depicted in Figure 5.24.

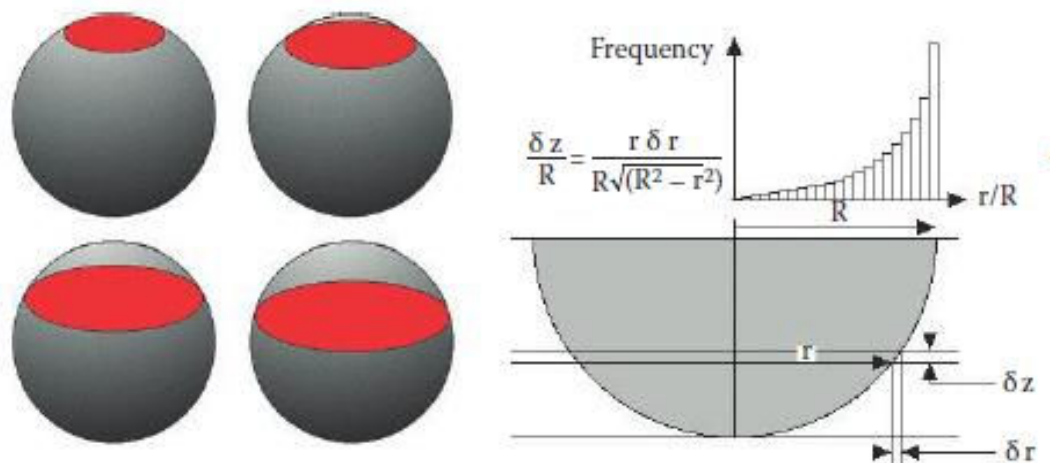


*Figure 5. 24 Sectioning a sphere randomly produce a distribution of circle sizes, which can be calculated from analytical geometry (after [155])*

The particles are distributed in a certain fashion (e.g., log-normal). We assume that each class of particles is mono-sized and can be unfolded using the classical stereology. For a 3D measurement,  $F_i$  stands for the frequency of the particle falling in the  $i$ -th bin. By multiplying the unfolding matrix, a  $f_i$  is obtained for the corresponding frequency of the sectioned size that falls in the same bin. In this work, a  $24 \times 24$  ( $n=24$ ) system matrix is used.

$$\begin{bmatrix} f_1 \\ f_2 \\ f_3 \\ f_4 \\ \vdots \\ f_n \end{bmatrix} = \begin{bmatrix} 1 & 1-\sqrt{1-\left(\frac{1}{2}\right)^2} & 1-\sqrt{1-\left(\frac{1}{3}\right)^2} & 1-\sqrt{1-\left(\frac{1}{4}\right)^2} & \dots & 1-\sqrt{1-\left(\frac{1}{n}\right)^2} \\ 0 & \sqrt{1-\left(\frac{1}{2}\right)^2} & \sqrt{1-\left(\frac{1}{3}\right)^2}-\sqrt{1-\left(\frac{2}{3}\right)^2} & \sqrt{1-\left(\frac{1}{4}\right)^2}-\sqrt{1-\left(\frac{2}{4}\right)^2} & \dots & \sqrt{1-\left(\frac{1}{n}\right)^2}-\sqrt{1-\left(\frac{2}{n}\right)^2} \\ 0 & 0 & \sqrt{1-\left(\frac{2}{3}\right)^2} & \sqrt{1-\left(\frac{2}{4}\right)^2}-\sqrt{1-\left(\frac{3}{4}\right)^2} & \dots & \sqrt{1-\left(\frac{2}{n}\right)^2}-\sqrt{1-\left(\frac{3}{n}\right)^2} \\ 0 & 0 & 0 & \sqrt{1-\left(\frac{3}{4}\right)^2} & \dots & \sqrt{1-\left(\frac{3}{n}\right)^2}-\sqrt{1-\left(\frac{4}{n}\right)^2} \\ \vdots & \vdots & \vdots & \vdots & \ddots & \vdots \\ 0 & 0 & 0 & 0 & \dots & \sqrt{1-\left(\frac{n-1}{n}\right)^2} \end{bmatrix} \times \begin{bmatrix} F_1 \\ F_2 \\ F_3 \\ F_4 \\ \vdots \\ F_n \end{bmatrix} \quad (5.3)$$

Figure 5.25 shows the correlations between the PSD of nickel particles in 2D and 3D. The 2D sectioning method underestimates the true size. After being corrected with the  $24 \times 24$  system matrix, the results are shown as the blue curve in Figure 5.25.

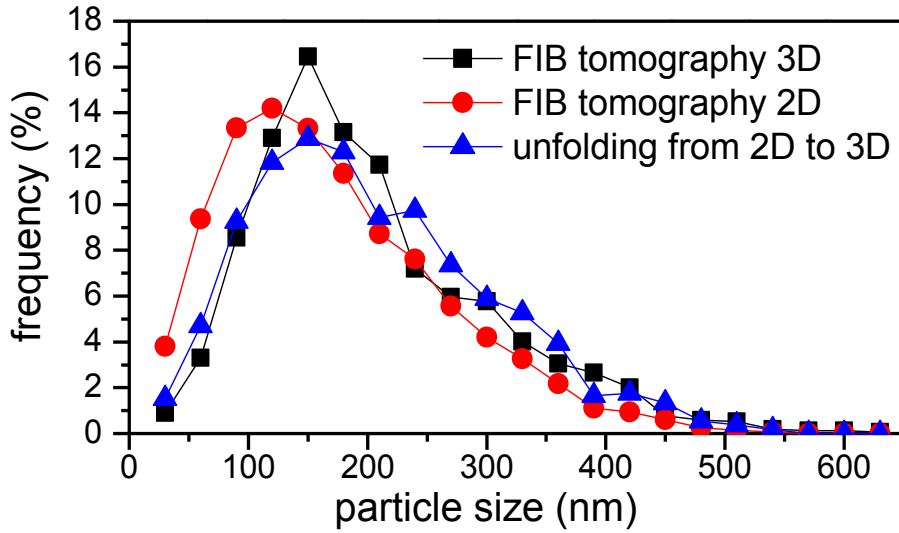


Figure 5. 25 Correlation between PSDs in 2D and 3D using the unfolding scheme

### 5.5 Heterogeneities in the green electrode

Figure 5.26(a) shows the 3D microstructures rendered with Avizo. Figure 5.26(b-d) shows the cross-sections of the Ni green electrode in three orthogonal planes. The average relative density is  $D = 0.50$ . However, local densities deviate from this average volume very much. This is because the Ni particles are not homogeneously arranged. As can be seen from the cross sections (Fig. 5.26(b-d)), they are either separated by pores or BT additives (not displayed in the image). In addition to these heterogeneities, the thickness of the electrode is not constant (Fig. 5.26(b)).

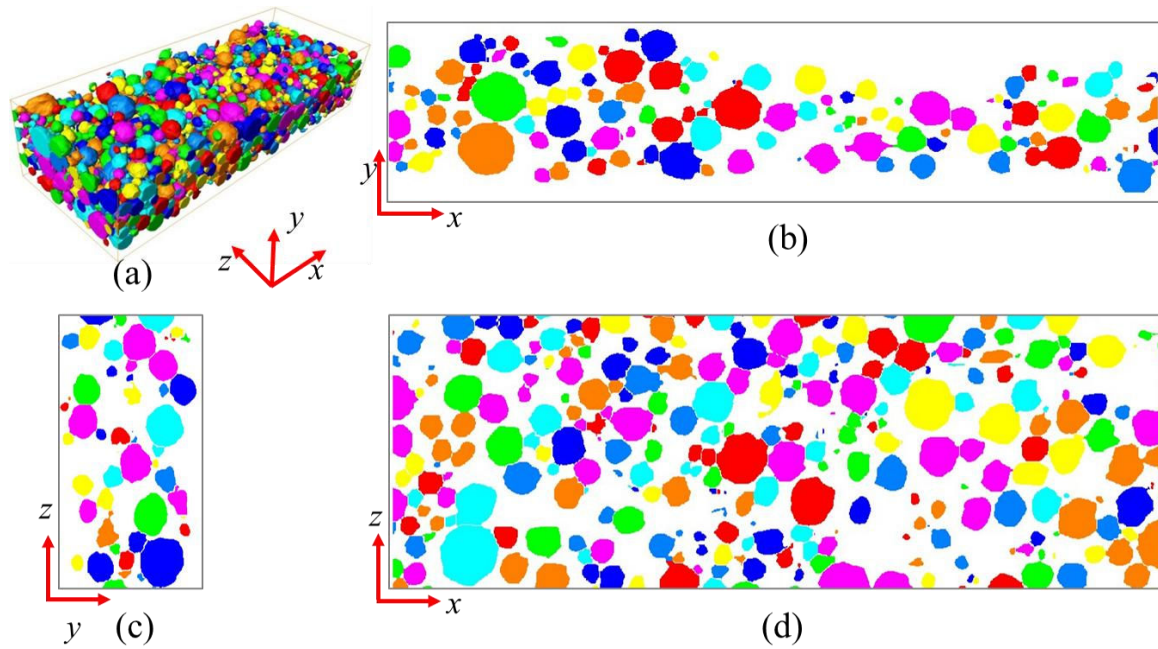


Figure 5. 26 (a) 3D rendering of the electrode (the electrode plane is  $xz$ ); (b)  $xy$  middle plane cross-section; (c)  $zy$  middle plane cross-section; (d)  $xz$  middle plane cross-section

Figure 5.27 plots the density (areal density in the serial slices) profile probed in  $x$  (Fig. 5.27(a)),  $y$  (Fig. 5.27(b)),  $z$  (Fig. 5.27(c)) direction. The peaks and valleys imply respectively the high density regions and low density regions, which can be referred to as heterogeneities. The heterogeneities can be located easily by the peaks and valleys' coordinates (in pixel). The discrepancy in the local relative density reaches up to 0.25 as shown in Figure 5.27(a).

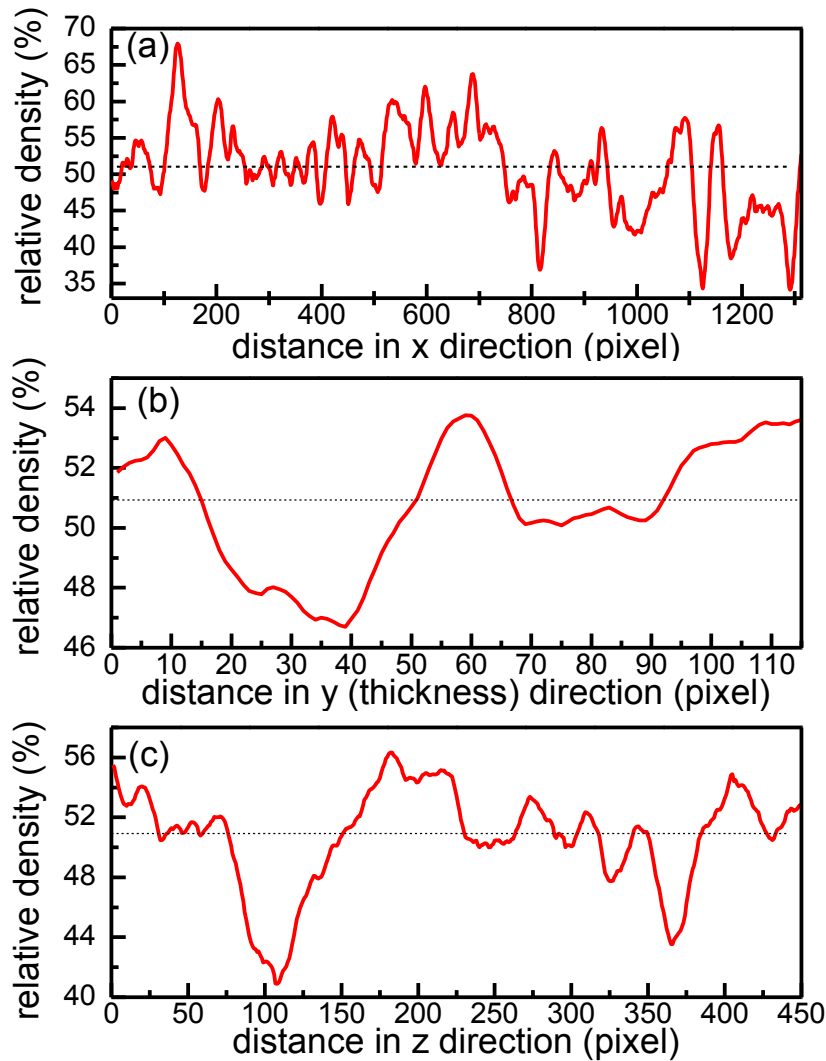


Figure 5.27 Density profile in  $x$ ,  $y$ ,  $z$  direction (1 pixel represents 5 nm)

Figure 5.28 shows the particle coordination number map at two representative heterogeneities. Slice #40 ( $xy$  slice in  $z$  direction) has the lowest density while the slice #60 has the highest density. The average coordination number in the high density regions is larger than that in the low density regions. Consider now the thickness of the electrode that sometimes consists only of a few particles. The coordination numbers are computed from 2D cross-sections. Since the step size is only 5 nm (1 pixel), we think the 2D coordination map is sufficient to signify the spatial heterogeneity.

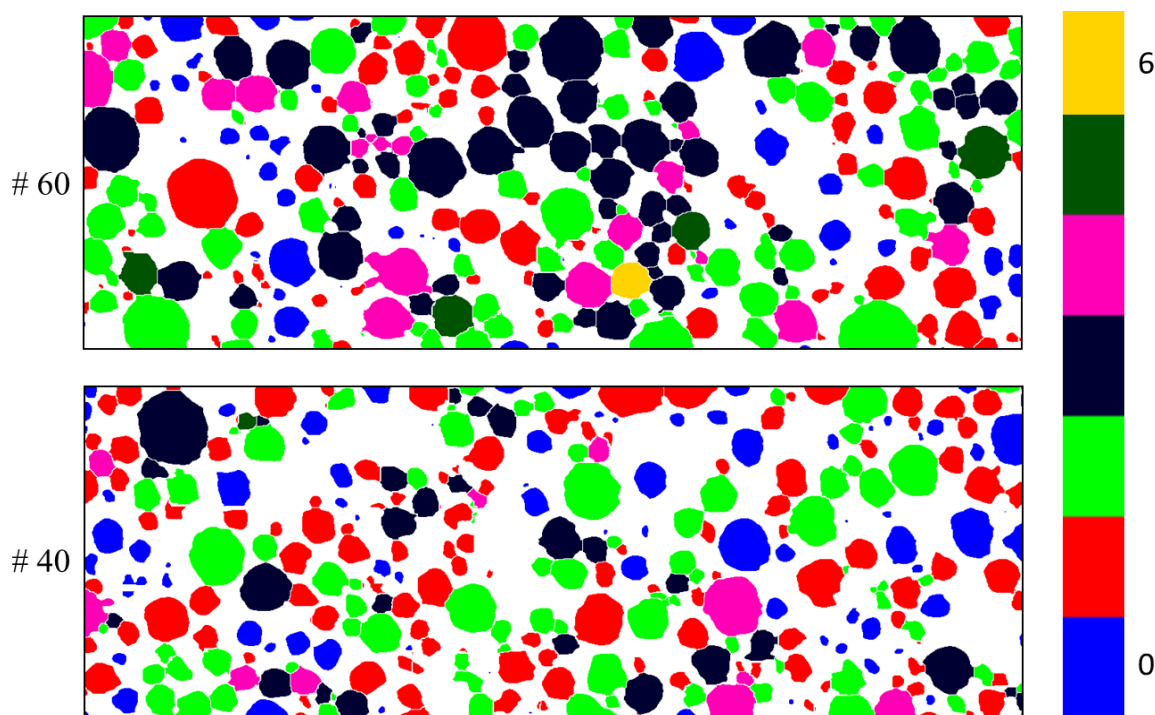


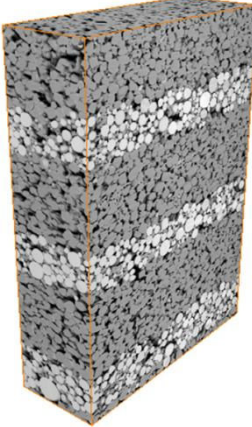
Figure 5.28 Coordination number map for the  $xz$  plane cross-sections

## 5.6 Porosity

As reviewed in Chapter 2, size and morphology of pores evolve as sintering proceeds. The pores can further play a role in physical and mechanical properties of the functional materials. Anisotropic pore development can also give valuable information on the sintering conditions (e.g., pressure-assisted, constrained sintering).

In the binary image, solid and pore phase are represented by 1 (black) and 0 (white). By counting the white pixels or voxels, pore area (2D) or pore volume (3D) is obtained. The ratio of the pore area (volume) to the envelope area (volume) represents the 2D and 3D porosity. Table 5.2 presents the 2D and 3D relative density in the three BT layers.

Green density in the BT layers is ~61%; while it is 56% for the electrode (including the 5.4% of BT additives). For porous media, in absence of heterogeneities, the 2D density (porosity) should be equal to the 3D measurement [162]. Density discrepancy in 2D and 3D for the Ni layers is larger than that for the BT layers. This echoes the significant heterogeneities in the electrode layers as previously shown in Figure 5.26.



	Layer	Density(2D)	Density(3D)	Porosity(3D)
Electrode	E1	52.9	51.9	43.6
	E2	54.8	52.7	41.5
	E3	53.7	50.9	43.2
	Avg.	53.8	51.8	42.8
Additives	E1	6.2	4.5	-
	E2	6.2	5.8	-
	E3	4.5	5.9	-
	Avg.	5.6	5.4	-
Dielectrics	D1	62.4	63.5	36.5
	D2	61.1	59.7	40.3
	D3	59.9	60.8	39.2
	Avg.	61.1	61.3	38.7

*Table 5.2 Average 2D and 3D density in different layers*

## 5.7 Anisotropy

### 5.7.1 Pore orientation in BT layer

Understanding the effect of geometrical constraint during the co-sintering of multilayers should help to manage the control of the microstructure. Anisotropy development has been reported both in experiments and in numerical simulations on constrained sintering thin films on rigid substrates [121, 163]. For the same reason, we evaluate pore orientation based on 2D cross-sections. As Figure 5.29(a) and (b) show, pores in the cross-section of the sintered sample are well isolated. These pores can be fitted as ellipses that have the same area and moments (first and the secondary moment) as the original pores (Fig. 5.29(c)). The major and minor axes define the shape of the ellipse. The orientation of pores is defined as the anti-clockwise angle between the major axis and the  $x$  axis. (Fig. 5.29(d)).

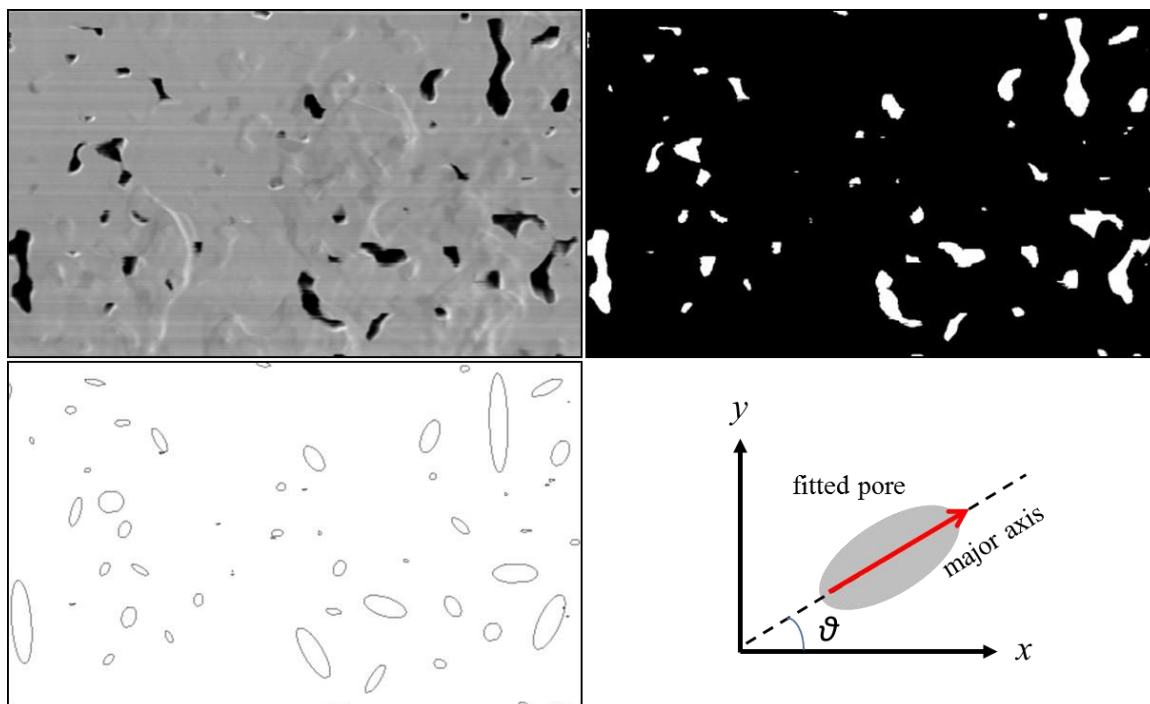


Figure 5.29 Pore orientations in the 2D cross-section

By using the particle analyzer in ImageJ, a best-fitting algorithm [164] is performed to generate equivalent ellipses and to obtain the orientation angle information.

The circularity  $C$  is defined as the ratio of  $A$  the area of a circle having a perimeter equal to  $P$ :

$$C = \frac{4\pi A}{P^2} \quad (5.3)$$

In practice, particles whose circularity is 1 and aspect ratio is less than 1.05 are not taken into account when the statistics is carried out.

Figure 5.30(a) shows the polar plot of the angular frequency as a function of the angle ( $0-180^\circ$ ). Note that, the curves for the other half ( $180-360^\circ$ ) is duplicated symmetrically for demonstration.

In the green state (black curve), most of the pores are elongated along  $\theta = 140-160^\circ$ . In tape casting, it has been observed that textured pores elongate along the tape casting direction [165] due to the fact that the particles are preferentially orientated along the tape casting direction during the die-slot tape casting procedure. It indicates that the tape casting direction is along  $\theta = 150^\circ$  in the selected coordinate system (Fig. 5.30(b)). After sintering, the fraction of pores that are oriented along the original tape casting direction increases (red curve). This means that pores further elongate along their original orientation during sintering. During



sintering, smaller intra-agglomerate pores may pinch off and disappear while larger inter-agglomerate pores, which are elongated in the tape casting direction, remain.

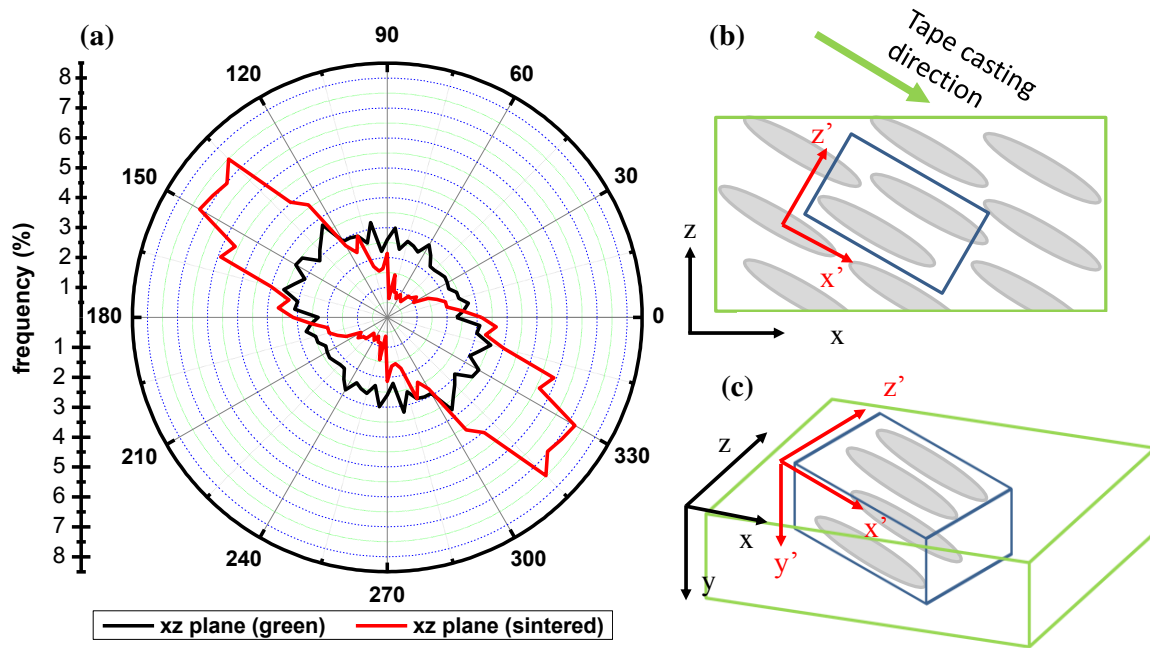


Figure 5.30 Pore orientation in the xz- plane before and after sintering

To examine the role of initial anisotropy induced by tape casting during sintering, new planes were created as shown in Figure 5.30(b).  $x'y'$  plane is considered parallel to the tape casting direction;  $y'z'$  plane is perpendicular to the tape casting direction.

Figure 5.31 shows pore orientation statistics in the vertical plane  $x'y'$  before (black curve) and after (red curve) sintering. The frequency of the pores that orient along the tape casting is initially about 3%. After sintering, the frequency of the pores that orient in the tape casting direction increased to 11%. The change is probably caused by the in-plane ( $x'z'$ ) compressive stresses developed during co-sintering of multilayers, on top of the contribution due to the disappearance of the intra-agglomerate pores. Before the BT starts to sinter (1000-1050 °C), the rapid sintering of Ni layers imposes compressive stresses, which facilitate the rearrangement and further sintering of the BT particles. Pores preferentially elongate along the direction of the compressive load. This stress induced anisotropy can be analogous to that produced during sinter forging, that is, pores preferentially orient along the direction of the external load [166]. However, once the dielectric layer really starts to densify, an in-plane tensile stress develops, which should lead to pores oriented along the thickness direction as observed in alumina films [167]. But co-sintering of YSZ layers [168] revealed that possible

large pores may evolve as the macroscopic shrinkage of the sintering body (which means perpendicular to the compressive loading direction) as evidenced by additional sinter-forging experiments on porous bodies containing artificial large pores [82].

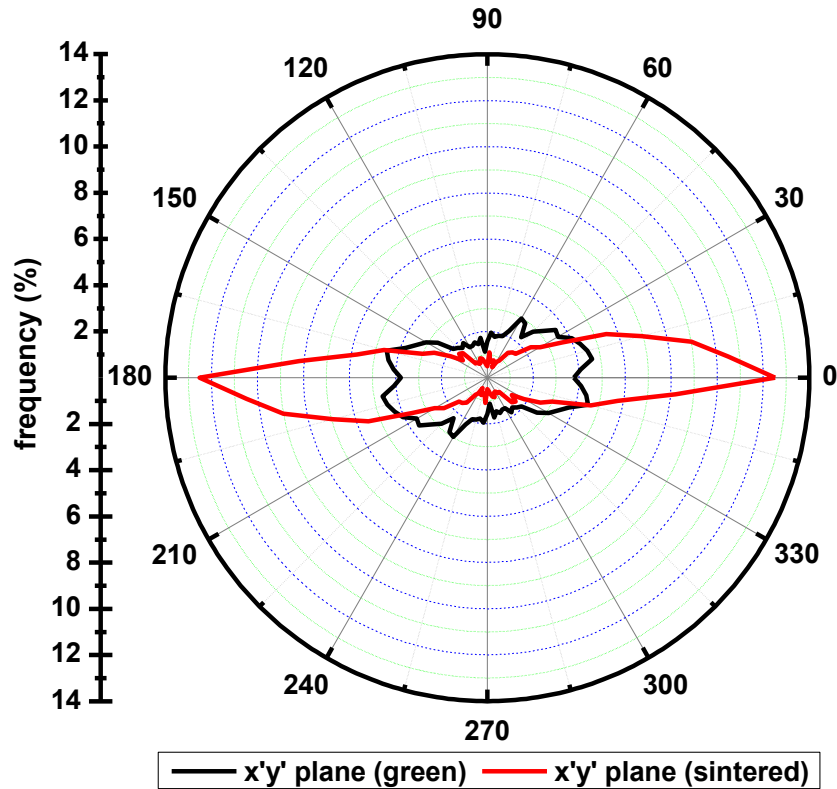


Figure 5. 31 Pore orientation in the  $x'y'$  plane before and after sintering

Figure 5. 32 shows the orientation statistics of the pore 2D sections in the  $y'z'$  plane, which is also through the thickness but perpendicular to the casting direction. The initial 2D sections of the pores are randomly orientated. It is interesting to observe that after sintering this initial random distribution tends to orientate along the horizontal direction (parallel to the in-plane stresses). The frequency of the 2D pore sections that orient at  $\theta = 0$  in  $y'z'$  plane does not increase as significantly as that in  $x'y'$  plane (Fig. 5.31). This is supportive evidence that the disappearance of the intra-agglomerate pores also contribute to the increase in the pores that orient in the stress loading direction.

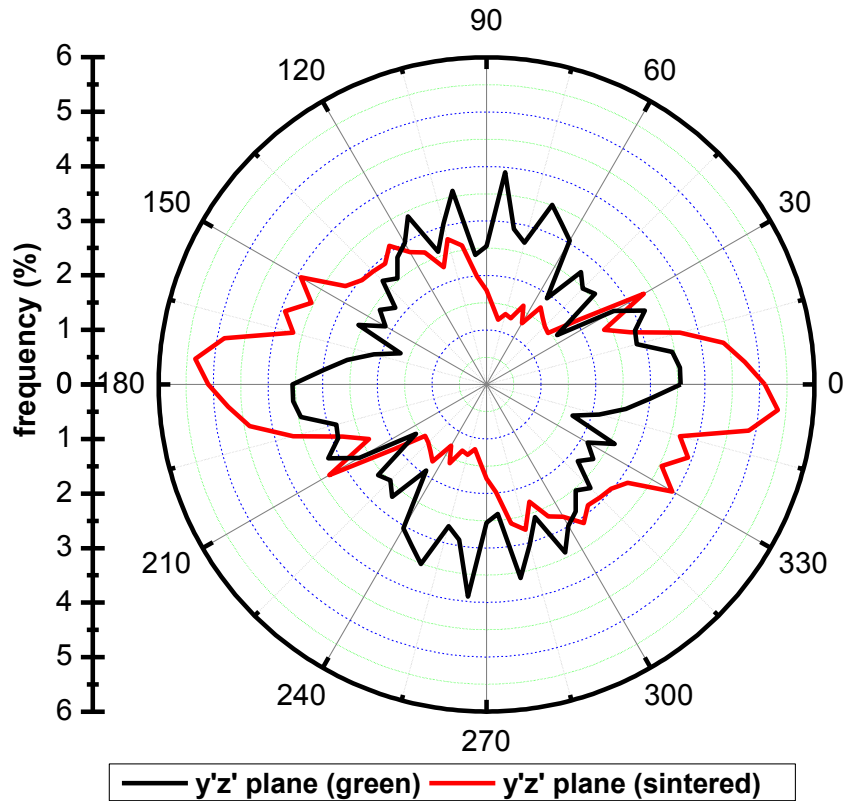


Figure 5.32 pore orientation in the  $y'z'$  plane before and after sintering

### 5.7.2 Density gradient

Figure 5.33 shows the relative density in the thickness direction. The density is calculated as the solid area fraction in the cross section plane. Two obvious findings are presented:

(1) In each single BT layer (D1, D2, and D3), the surface region (interface) is much denser than the middle region. It has been observed experimentally by Guillon [73] and Bernard [121] and in discrete simulations by Martin and Bordia [163] that in a sintered thin film on a rigid substrate, the density at the interface is lower than the inner region of the film. These studies also show that pores near the interface are elongated perpendicular to the thickness direction.

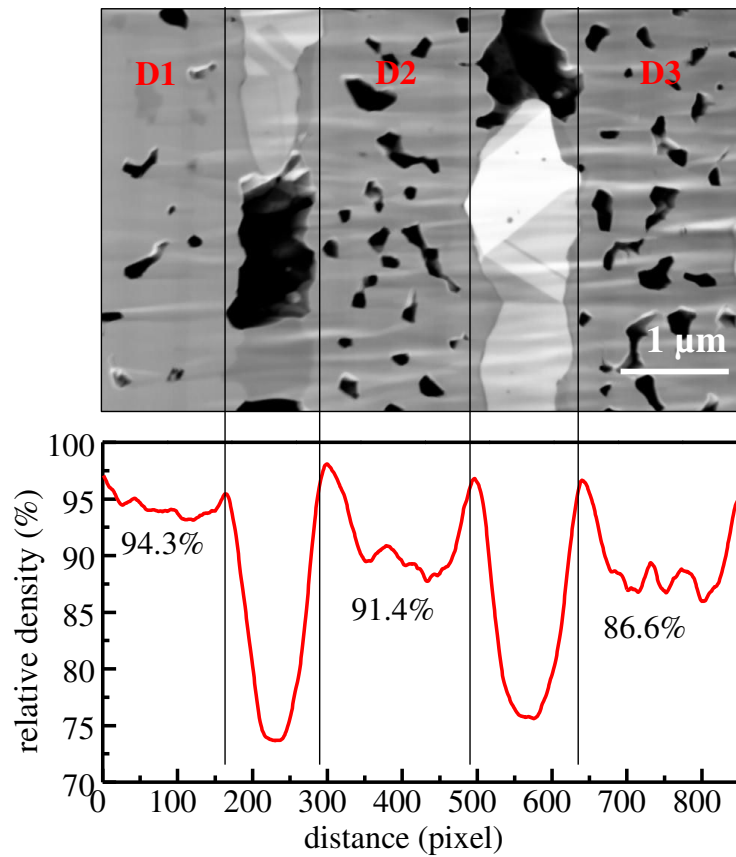
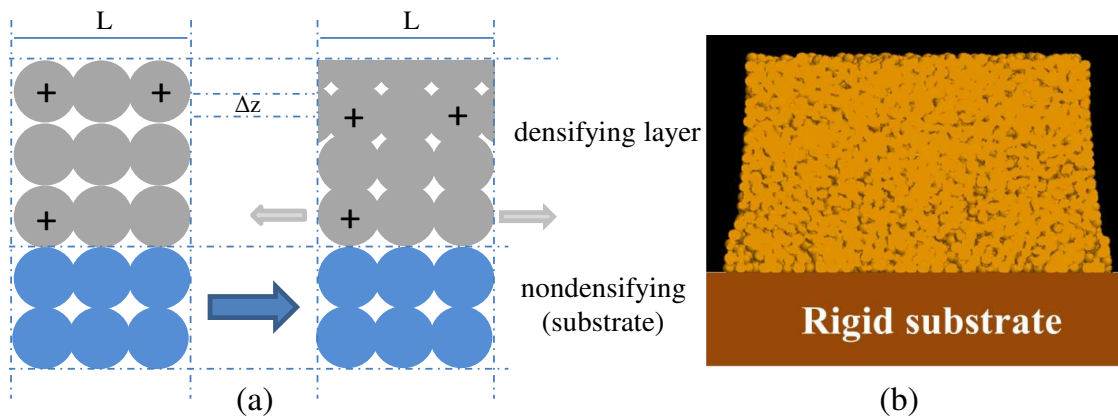


Figure 5.33 Density profile in the thickness direction (from the surface to the bottom #1-s-ct).  
The density is measured from the 2D slices along the thickness

The mechanism for the anisotropy development is depicted in Figure 5.34(a). Due to the restraining effect of the substrate, tensile stresses develop in the thin film, especially near the interface. These tensile stresses hinder the sintering of the film near the interface, thus resulting in a lower final density close to the interface. In the meanwhile, due to the restraint of the substrate, grain grows preferentially in the thickness direction, resulting in vertical oriented pores at the interface.



*Figure 5. 34 Anisotropy in thin film on substrate: (a) Bordia’s model for the constrained sintering of thin film ([169]); (b) numerical simulations by Martin and Bordia [163]*

In the current study on the co-sintering of BT/Ni/BT multilayers, both Ni and BT layers densify but at different densification rates as shown in Figure 5.35. At the early stage of the sintering of Ni/BT multilayers (400-1050 °C), the BT layer is placed under compression, as the nickel sinters earlier and faster than the BT layers. Thus, compressive stresses may facilitate particle rearrangement at the interface. The interface regions sinter faster than the inner regions in the BT layers, resulting in a higher density near the interface. Meanwhile, these compressive stresses facilitate the necks grow in the load direction, that is, in parallel to the BT planes, resulting in horizontally elongated pores. Note that when the temperature reaches 1050 °C, the stress state reverses in both layers. However, the anisotropy that initially developed at the early stage (before the temperature reaches 1050 °C) plays a decisive role in the entire sintering.

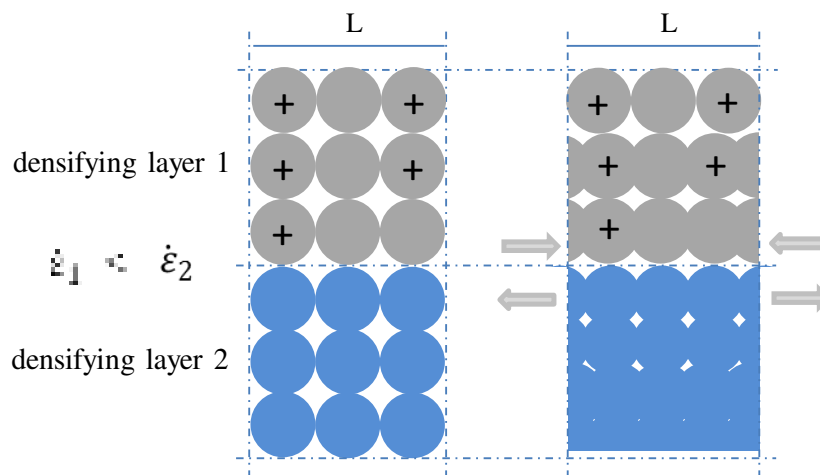


*Figure 5. 35 A model for the co-sintering of multilayers*

(2) Average relative density in the BT layers decreases from the top layer (D1) to the bottom layer (D3), as explained in Chapter 4; this is due to different constraint levels in different layers.

## 5.8 Microstructure evolution of the electrode

### 5.8.1 Discontinuity of electrode

Figure 5.36 shows the FIB reconstructed electrode of the sintered MLCC sample (#1-s-ct) that was imaged by X-ray nCT (Chapter 4). In this discontinuous electrode, only the solid area can contribute to the capacitance of MLCC. With FIB tomography (BSE), plenty of BT particles are observed in the electrode.

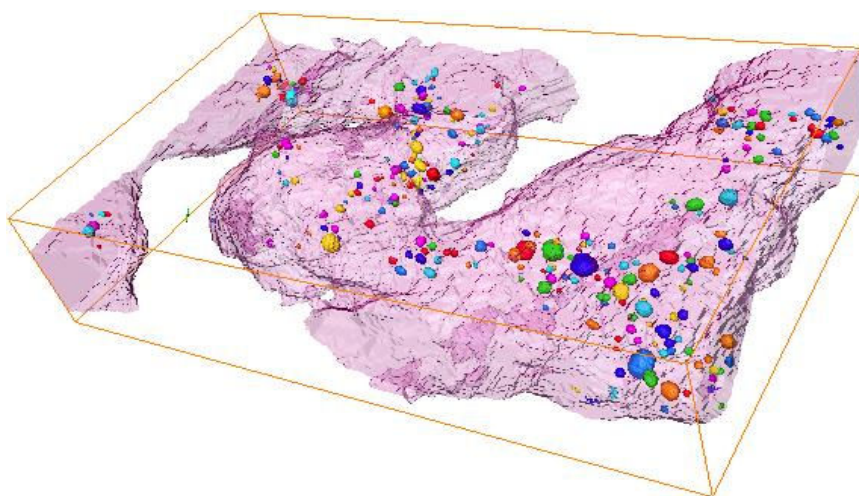


*Figure 5. 36 An electrode (#2) from the sample #1-s-ct*

A further EDX chemical analysis was carried out to confirm the phase of these entrapped particles. Figure 5.37 shows the EDX mapping of the cross-section of sample #3. The darker spots, entrapped particles (spots 1 and 2) are analyzed with EDX quantitative spot analyses.

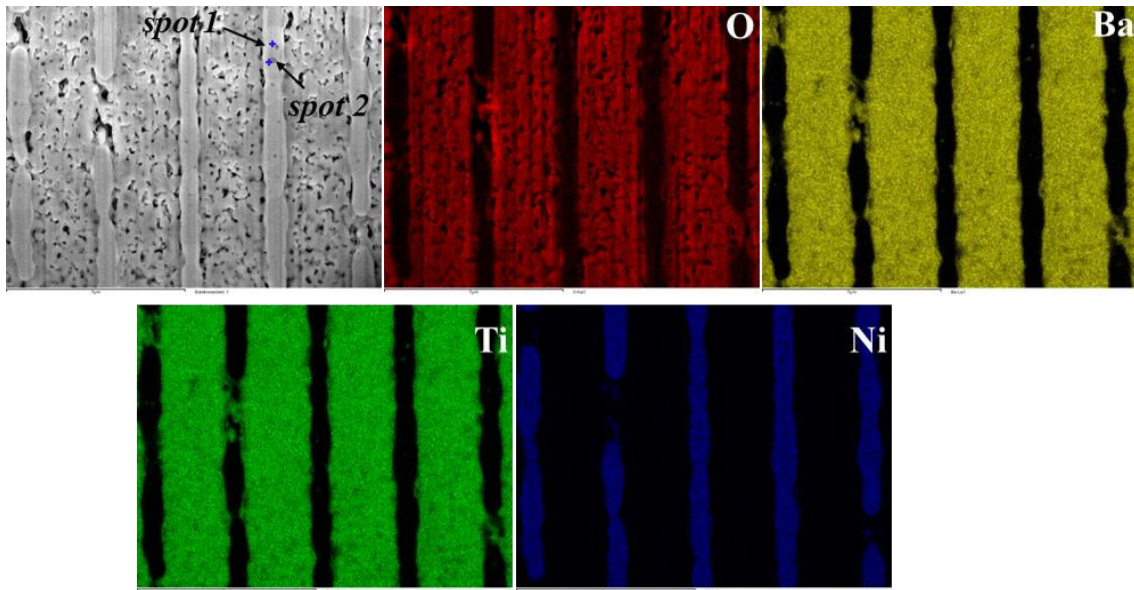


Figure 5.37 EDX mapping of the cross-section of the sintered chips (sample #3)

From the EDX mapping, the darker particles are rich in Ba, Ti and O chemicals, the same as compositions of BT. Qualitative EDX analysis (Table 5.4) indicates that these darker phases are actually entrapped BT additives in the initial Ni matrix. Most of the BT additives are excluded by the nickel matrix due to their incompatibility with Ni. These excluded BT particles sinter with adjacent BT layers to form percolating bridges. The percolation of BT (bridges between electrode layers) can improve the union of the neighboring dielectrics layers and the overall mechanical properties of the chips. From the O map, oxygen elements could be found in the electrodes. It indicates that the nickel particles absorbed the residual oxygen in the Ar+2%H<sub>2</sub> mixture. In industry, (0.1-0.01%) H<sub>2</sub>-Ar-H<sub>2</sub>O wet gas is utilized so that the content of the partial oxygen pressure is controlled within 10<sup>-9</sup>-10<sup>-11</sup> atm. This residual oxygen modifies the sintering kinetics of the electrodes and dielectrics. That may also explain why the dielectrics are not fully densified. This may alter the final dielectric properties, which are, however, not considered in our study.

Element	spot 1				spot 2			
	Ba	Ti	O	Ni	Ba	Ti	O	Ni
Atom%	31.12	33.6	36.28	0	38.09	36.93	24.98	0

Table 5.4 EDX spot analysis on sample #3

Figure 5.38 shows the BT inclusion particle size change before and after sintering in the electrode #2 in sample (#1-2-ct). The PSD distribution usually shifts towards larger particle size due to grain coarsening which consumes smaller particles. In our case, while a portion of

coarsened particles have been found, the portion of small particles increases and the average particle size does not change significantly. This is because the nano BT additive inclusions are dispersed in the electrode. Isolated single BT particles are not modified. Only aggregated BT particles sinter and form a single larger particle finally.

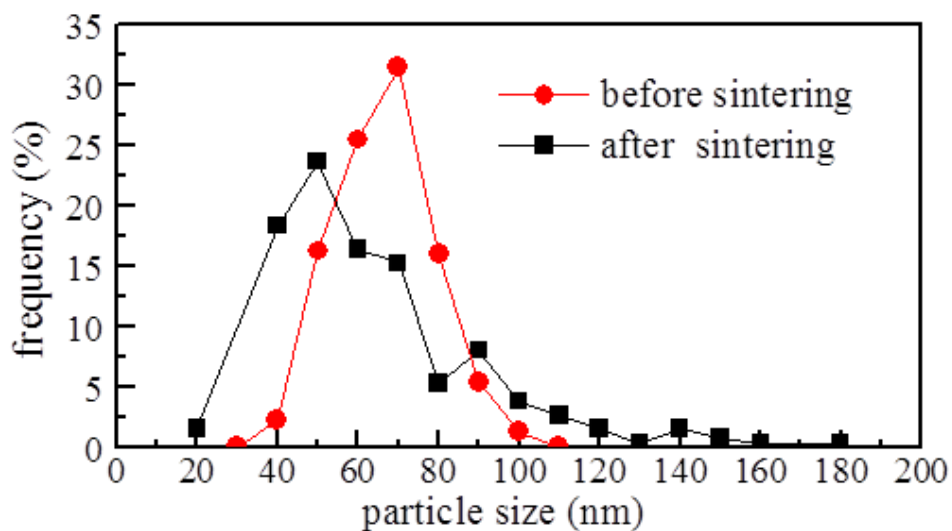


Figure 5.38 The PSD evolutions of BT inclusion particles entrapped in the electrode (#2) in sample #1-s-ct

### 5.8.2 Correlation between discontinuity and capacitance

Figure 5.39 shows two neighboring electrodes, which comprises a unit capacitor. The capacitance of a multilayer capacitor as given by Eq.(1.1) is directly proportional to the total effective electrode area.

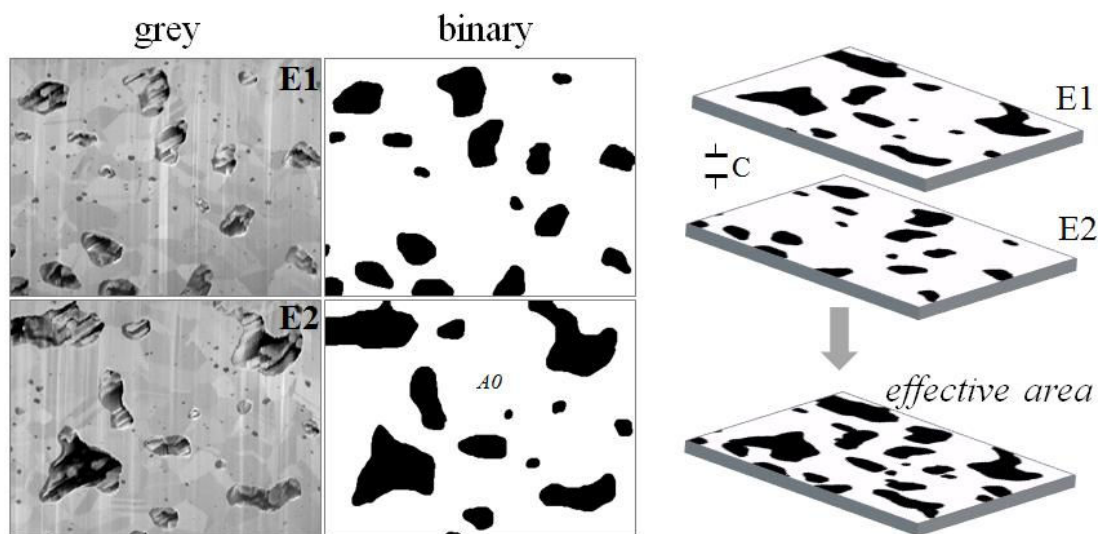


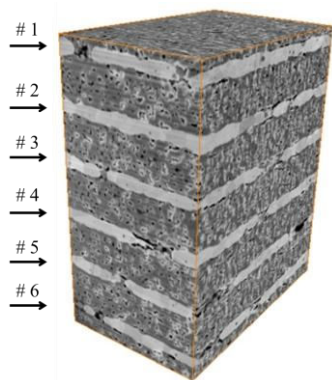
Figure 5.39 Two reconstructed electrodes and a unit capacitor



The discontinuous areas (black areas) in the electrodes lead to a decrease in the effective overlapping area, and thus in the capacitance. The effective overlapping area  $A$  (white area) in the Eq.(1.1) can be calculated by a Boolean ORing operation of the areas of the two electrodes. The relative capacitance  $C$  is

$$C/C_0 = A/A_0 \quad (5.6)$$

Table 5.5 presents the areal (2D) discontinuities of the six electrodes and the relative capacitances of the five unit capacitors in the FIB-SEM reconstructed representative volume extracted from the sintered MLCC sample (#3).



No.	discontinuity <sub>2D</sub> (%)	Relative capacitance (%)
<b>1</b>	16.3	
<b>2</b>	22.3	63.6
<b>3</b>	16.4	66.3
<b>4</b>	12.3	75.0
<b>5</b>	9.4	79.8
<b>6</b>	10.9	81.1
<b>average</b>	16.3	73.4

*Table 5.5 Discontinuity of electrodes (#1-6) measured in 2D and the relative capacitances of the five unit capacitors, which are comprised of the neighboring electrodes*

Average discontinuity is 16.3%. Notice that the average discontinuity for the electrodes that sintered with a smaller cylindrical sample is 12.5%. This size and geometry effect on the final electrode discontinuity is detailed in Chapter 4. The average relative capacitance is 26.6% compared to a capacitor with continuous electrodes. That means that theoretically, by getting rid of these electrode discontinuity, the chips could be downsized by a quarter of their size and still have the same capacitance.

## 5.9 Conclusion

High resolution FIB-nT has been utilized to characterize the green MLCC chips (#2-g) and sintered MLCC samples. The analysis also included the sample imaged with X-ray nCT (#1-s-ct) and a sintered MLCC with a real size (#3). It is concluded that:

(1) Qualitative and quantitative correlative studies on the microstructures of both the green and sintered Ni-MLCC sample have proved that the X-ray nCT spatial resolution is sufficient for the current work dealing with heterogeneity evolutions.

(2) FIB-nT enables 3D evaluation of the particulate characteristic including the particle and pore size and their distribution. This provides accurate particulate parameters for the discrete element simulations.

(3) Heterogeneities in the electrodes have been quantified. Because particles are not homogeneously arranged, there are density variations through the electrode layers. In the high density regions, the average particle coordination numbers are larger than in the low density regions.

(4) Anisotropy has been observed for both pore orientation and density in the BT layers. These anisotropic effects are considered to be caused by the compressive stress that develops during the heating stage when the Ni electrode sinters faster than the BT layers. The compressive stresses near the interface facilitate the sintering of the BT particles, leading to a denser region at the interface than in the inner regions. Under this in-plane compressive stresses, the BT particles grow preferentially in the loading direction leading to pores that orient preferentially parallel to the layers.



## **Chapter 6**

# **Discrete element simulations of the sintering of electrode material**

This chapter presents a numerical approach to simulate the sintering of powders. The Discrete Element Method (DEM) is used here specifically to simulate the sintering of a powder in the presence of inclusions as this represents well the actual process in MLCCs where Ni powders are sintered with BT particles. We take advantage of the fact that DEM simulations work explicitly at the particle length scale, which continuum techniques such as Finite Element Method cannot. This allows the retarding effect of inclusions to be taken into account, together with important effects such as inclusion size and inclusion dispersion. We first review the modeling efforts concerning sintering with rigid inclusions. Literature on DEM of sintering is reviewed. The general principles of DEM are then briefly described. Finally, the modeling of the sintering of composite materials with dp3D code is described.

### **6.1 Introduction**

The discrete (or distinct) element method (DEM), was first proposed by Cundall and Strack [170] in 1979 to study the micromechanics of geomaterials. The DEM simulates the behavior of granular materials at the particle-length scale. Over the last decades, with advances in computing power and numerical algorithms for nearest neighbor sorting, it has become possible to numerically simulate hundreds of thousands of particles with a single processor. Today DEM is becoming widely accepted as an effective method for addressing engineering problems in granular materials, especially in granular flows [171-174], micromechanics [175-177], environmental sciences [178], rock mechanics [179-181], pharmaceuticals [182, 183], and powder metallurgy [52, 163, 184-194].

#### **6.1.1 DEM simulation of sintering**

Jagota and Scherer [195, 196] were the first researchers to study sintering with DEM. Sintering of mono-sized composites was modeled with DEM simulations by assuming that all contacts follow a linear viscous law. Vergina [197] proposed a 3D DEM model that is based

on two-particle interactions. This model considered the grain-boundary and lattice diffusion. It predicted rationally the structural reorganization effects which occur during the early stage of sintering of random and of some crystalline-type packings in which various initial defects have been created. Parhami and Mc Meeking [198] used a discrete element model to predict the densification of initial stage of sintering through computer simulations, in which every particle center is represented by a node and every contact between neighboring particles by a discrete element. The velocity of each node is related to external and sintering forces governed by grain boundary and surface diffusion, derived from Bouvard and Mc Meeking's work [199]. Then the motion of each discrete element was determined and was assembled to present the behavior of a powder system with 266 particles.

The Parhami-McMeeking model has been taken and practiced by many authors [163, 189, 200, 201] to consider macroscopic behavior and/or microstructural evolutions aided with computer power and numerical schemes. Among these authors, Martin and his co-workers investigated the sintering kinetics of metal powder [187], the effect of local heterogeneities arising from non-sintering inclusions [52, 117], defects development in film/layers with complex geometry [163, 189].

Riedel and Kraft [202, 203] considered the pore evolution's influence on the sintering force. The sintering force, taking into account the pores characteristics (i.e., coordination number, volume fraction), enables prediction of the immediate and final stage of sintering. By incorporating Riedel and Kraft model, DEM simulations have been implemented to study the rearrangement of particles [188], anisotropy [204] during the sinter-forging by Wonisch et al. Wonisch et al.'s DEM study confirmed that intergranular pores are preferentially orientated along the compressive loading axis in accordance with their experimental observations. Taps et al. predicted [205] distortion of film due to constrained sintering by a rigid substrate using DEM simulations.

### **6.1.2 Principle of DEM**

The general principle of DEM is based on the writing of the mechanical equilibrium of a set of discrete objects that interact with each other through their contacts. A large majority of the simulations based on DEM uses disc-shaped and spherical elements in 2D and 3D simulations, respectively. This simplification allows to include as few geometrical parameters as possible, i.e., only the relative position of particle centers are tracked to determine particle

contacts. The greatest advantage of this assumption is computational simplicity. As a result, the computer storage and processing time are significantly reduced and a large-scale simulation within a reasonable time becomes possible. However, it should be noted that disks and spheres tend to roll or rotate easily, which does not reflect the behavior of real materials in case of large shear processes. In the remaining, we will only consider spherical particles. Also, we specialize the description of DEM by referring essentially to the dp3D code, which has been developed at SIMaP, Université de Grenoble and which be used to simulate sintering.

Particles are described by their number  $i$  ( $i = 1, N$ ), their position  $\mathbf{X}_i$ , velocity  $\mathbf{V}_i$ , angular velocity  $\boldsymbol{\omega}_i$ , radius  $\mathbf{R}_i$ , mass  $m_i$  and moment of inertia  $I_i$ .

In each simulation time step  $\Delta t$ , first the neighbors of every particle are determined. This neighborhood is defined by a previously specified interaction radius  $R_c$ . Then forces between neighboring particles are calculated, depending on a given force law, as described later in Section 6.2. The time evolution of the particle positions is governed by Newton's equations of motion:

$$\frac{d}{dt} \mathbf{X}_i = \mathbf{V}_i, m_i \frac{d}{dt} \mathbf{V}_i = \mathbf{F}_i^{tot} = \sum_{j \neq i} \mathbf{F}_{ij} + m_i \mathbf{g} \quad (6.1)$$

$$I \frac{d}{dt} \boldsymbol{\omega}_i = M_i^{tot} = \sum_{j \neq i} M_{ij} \quad (6.2)$$

Here,  $\mathbf{F}_{ij}$  and  $M_{ij}$  denote the inter-particle force and moment from the  $j$ -th particle on the  $i$ -th one (see Fig. 6.1). The first term  $\mathbf{F}_{ij}$  includes the contributions of normal force  $N$ , tangential force  $T$  and gravitational force  $m_i \mathbf{g}$ .  $\mathbf{F}_i^{tot}$  denotes the total force acting on the  $i$ -th particle and  $M_i^{tot}$  the total torque acting on the  $i$ -th particle, calculated from the particle-particle torques:

$$\mathbf{T}_{ij} = -\frac{1}{2} (\mathbf{X}_i - \mathbf{X}_j) \times \mathbf{F}_{ij} \quad (6.3)$$

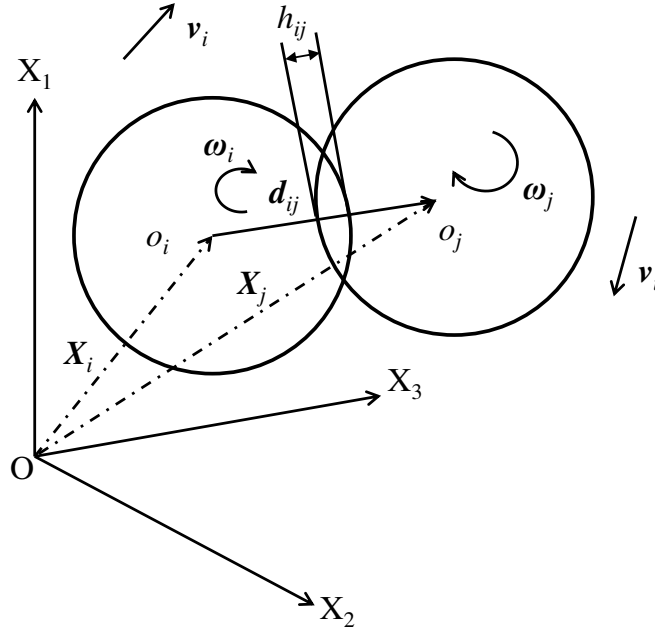


*Figure 6. 1 Two-particle contact model*

The most widely used method for integrating the equations of motion is the algorithm initially adopted by Verlet [206]. Swope et al. [207] proposed a Verlet-equivalent algorithm, which stores positions, velocities and accelerations all at the same time  $t$ . This velocity-Verlet-algorithm uses a group of equations:

$$\mathbf{X}_i(t + \Delta t) = \mathbf{X}_i(t) + \Delta t \mathbf{V}_i(t) + \frac{1}{2m_i} (\Delta t)^2 \mathbf{F}_i^{tot} \quad (6.4)$$

$$\mathbf{V}_i(t + \Delta t) = \mathbf{V}_i(t) + \frac{1}{2m_i} \Delta t (\mathbf{F}_i^{tot}(t) + \mathbf{F}_i^{tot}(t + \Delta t)) \quad (6.5)$$

$$\boldsymbol{\omega}_i(t + \Delta t) = \boldsymbol{\omega}_i(t) + \frac{1}{2I_i} \Delta t (M_i^{tot}(t) + M_i^{tot}(t + \Delta t)) \quad (6.6)$$

This method, which is the standard integrating method in dp3D, has the advantages of numerical stability, convenience and simplicity [208].

To obtain a proper integration of the particle movement, the time step must be chosen carefully. The time step is determined using the method proposed by Cundall and Strack [170] as:

$$\Delta t = 2f_i \sqrt{\frac{m_0}{K_0}} \quad (6.7)$$

In analogy with a contact with stiffness  $K_0$  and an oscillating mass  $m_0$ . The safety factor  $f_t$  is less than unity to ensure stability of the calculation,  $m_0$  is the smallest particle mass and  $K_0$  is the maximum contact stiffness, defined by contact equations. The simulation for quasi-static deformation can be carried out either using a so-called non viscous damping method [170] or by scaling the density of the particles by a factor of  $\beta$  with a typical value of  $\beta = 10^{12}$  [209].

- **Boundary conditions**

Three types of boundary conditions are typically available in DEM. Note that they can be mixed together depending on the application.

*I. Rigid Walls*

Rigid walls can be constructed using objects such as planes, spheres, or cylinders. These objects have an infinite mass, so their motion is not dictated by the second law of Newton (6.1) but only by the imposed conditions set by the user. Walls may represent real process conditions such as a die wall in uniaxial close-die compaction.

*II. Free surface*

Particles on surface of the sample only interact with other particles.

*III. Periodic boundary*

Periodic conditions are imposed by stating that when a particle protrudes outside the periodic cell through a given face, a mirror particle is generated on the opposite face of the periodic cell. The mirror particle interacts with other particles on that face (Fig. 6.2). Similarly, when the center of a particle lies outside the periodic cell, the particle is translated to the opposite face of the cell by a distance equal to the length between the two opposite faces. The relative density of the sample is defined as the ratio between the particles volume and the volume of the cell. Periodic conditions are well adapted for simulating a Representative Volume Element (RVE) far away from any rigid walls. Typically, it may represent a volume of powder inside a matrix far from the perturbation of the rigid die wall.



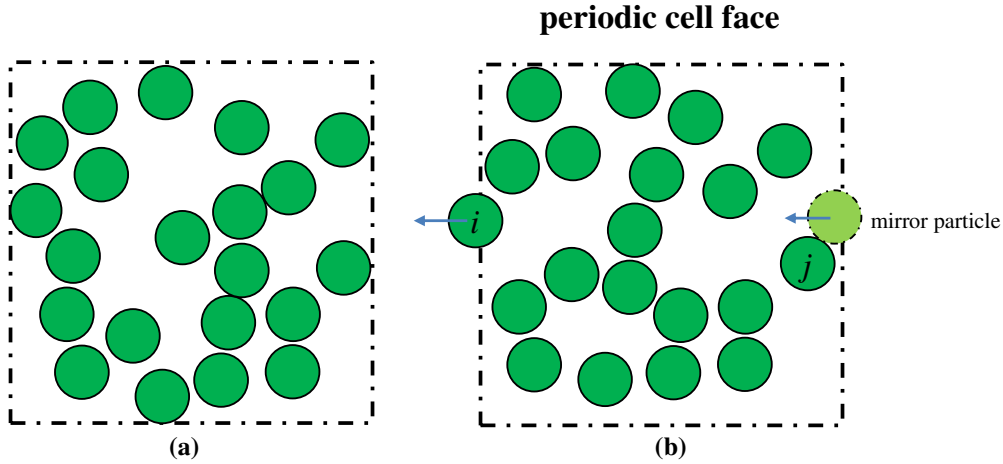


Figure 6. 2 Schematics of (a) wall conditions; (b) periodic conditions

In a typical DEM simulation, macroscopic strains are imposed. Depending on the boundary conditions that have been chosen, strains are imposed by moving the objects or by moving the boundaries of the periodic cell by the following equation:

$$\Delta x_j = \dot{\varepsilon}_{ij} x_i \Delta t \quad (6.8)$$

Where  $x_i$  is the location of the object centroid or of the periodic cell, and  $\dot{\varepsilon}_{ij}$  is the imposed strain rate. The centers may also be moved according to the same equation (as if they are points in a continuum) at the beginning of each time step. This, in general, facilitates the convergence toward force equilibrium.

The imposed strains in the simulation result in contacting particles generating contact forces. These contact forces produce stresses at the macroscopic scale. The macroscopic stress tensor  $\Sigma_{ij}$  may be computed from contact forces by considering a set of particles inside a volume  $V$ :

$$\Sigma_{ij} = \frac{1}{V} \sum_{contacts} (T_i + N_i) l_j \quad (6.9)$$

Where  $l_j$  is the branch vector between particles  $i$  and  $j$  centers.

In DEM of sintering, stress is imposed, instead of strain. This is done by calculating the strain rate of the simulation box which needs to be imposed to minimize the error between the calculated stress and the required stress. To simulate free sintering a zero (or very small compressive stress) should be imposed.

## 6.2 Model description

In this section, we describe the contact forces, which model particle interactions in an electrode layer (Ni and nano BT). In Chapter 3, experiments have shown that electrode powders containing both nickel and nano BT particles sinter earlier (400-800 °C) than BT powders (950-1050 °C). Using X-ray tomography, we have demonstrated that the discontinuities of electrode form at the early stage of sintering while the BT has not started to sinter yet. To simulate the sintering process of Ni/BT composite powders below 950°C, we make the following simplifying assumptions:

- All particles are spherical.
- Particles cannot rotate (we assume that sufficiently large contacts grow fast enough to counteract rotations).
- BT-BT contacts are elastic.
- Ni-Ni contacts are sintering contacts.
- Ni-BT contacts are viscous contacts.
- Coarsening is neglected.
- Sintering is isothermal.
- Gravitation is neglected.

To keep some generality to the model description, we define Ni as the matrix particle, and BT as the inclusion. Spherical matrix and inclusions particles interact through specific contact laws. In such a case, three types of contacts coexist: inclusion-inclusion (*ii*), matrix-matrix (*mm*), and inclusion-matrix (*im*) contacts. We define an equivalent radius  $R^* = R_1 R_2 / (R_1 + R_2)$ , for two particles of radius  $R_1$  and  $R_2$ .

For (*ii*) contacts between particles with Young's modulus  $E$  and Poisson's ratio  $\nu$ , the normal contact force is elastic with an additional adhesive term given by the Derjaguin-Muller-Toporov model [210]:

$$N_{ii} = \frac{8}{3} \frac{E}{1-\nu^2} \frac{a_{ii}^3}{R} - 2\pi w R^* \quad (6.10)$$

Where  $a_{ii}$  is the elastic contact radius and  $w$  is the work of adhesion (twice the surface energy). The second term denotes the driving force for agglomeration between small particles. Frictional forces  $T_{ii} = \mu N_{ii}$  between inclusion particles are also included using Coulomb law

(with a friction coefficient set to  $\mu = 0.1$ ). For inclusions, we set  $E = 130$  GPa,  $\nu = 0.25$  and  $w = 0.05$  J m<sup>-2</sup>, typical values for BT polycrystalline ceramics [211].

We use the model of Parhami and McMeeking for sintering (*mm*) contacts [198]. It assumes that grain boundary and surface diffusion are the major mechanisms of mass transport [163, 187]. Particles approach each other due to the flux of vacancies from the inner of the grain boundary to the triple point (pore). The normal contact force is given by:

$$N_{mm} = \frac{\pi a_{mm}^4}{8\Delta_b} \frac{dh}{dt} - \pi\gamma_s \left[ 8R^* \left( 1 - \cos \frac{\varphi}{2} \right) + a_{mm} \sin \frac{\varphi}{2} \right] \quad (6.11)$$

Where  $a_{mm}$  (Fig. 6.3(a)) is the sintering contact radius,  $h$  the indentation,  $\varphi$  the dihedral angle,  $\gamma_s$  the surface energy and  $\Delta_b$  a diffusion parameter related to the grain boundary diffusion coefficient:

$$\Delta_b = \frac{\Omega}{kT} \delta_b D_{0b} \exp(-Q_b / RT) \quad (6.12)$$

with  $\delta_b$  the grain boundary thickness,  $D_{0b}$  a material constant,  $Q_b$  the activation energy,  $\Omega$  the atomic volume,  $R$  the gas constant and  $T$  the temperature. The first term on the right-hand side of Eq (6.11) may be considered as a normal viscosity, whereas the second term relates to surface tension effects. The same viscosity term was used by Kraft et al. [202] in the normal force expression but their tensile term was slightly different. The tangential force  $T_{mm}$  at a (*mm*) contact opposes the tangential component of the relative velocity at the contact,  $du/dt$ , and is given by:

$$T_{mm} = -\eta \frac{\pi a_{mm}^2 R^{*2}}{2\Delta_b} \frac{du}{dt} \quad (6.13)$$

where  $\eta$  is a dimensionless viscous parameter [212]. A value of  $\eta = 0.1$  was used in this study. Note that Eq. (6.13) also applies to (*im*) contacts. The contact radius  $a_{mm}$  which appears in Eq. (6.11) and (6.13) is given by a generalization of Coble's law [213] for contacts between non-monomodal particles, as proposed by Parhami and McMeeking [198] and confirmed numerically by Pan [214]:

$$a_{mm}^2 = 4R^*h \quad (6.14)$$

For (*im*) contacts, we assume that a nearly flat surface, instead of a sintering neck, forms on the matrix side at the (*im*) contact (Fig. 6.3(b)). In support of this assumption, clear interfaces between matrix and inclusions are observed in some sintered polycrystalline ceramic or metal matrix composites [31, 215]. The normal force is given solely by the viscosity term of Eq.

(6.11) and the contact radius  $a_{im}$  is derived by conservation of matter (the derivation is available in the supplementary material online):

$$a_{im}^2 = 4R_m h \quad (6.15)$$

Where  $R_m$  is the radius of the matrix particle.

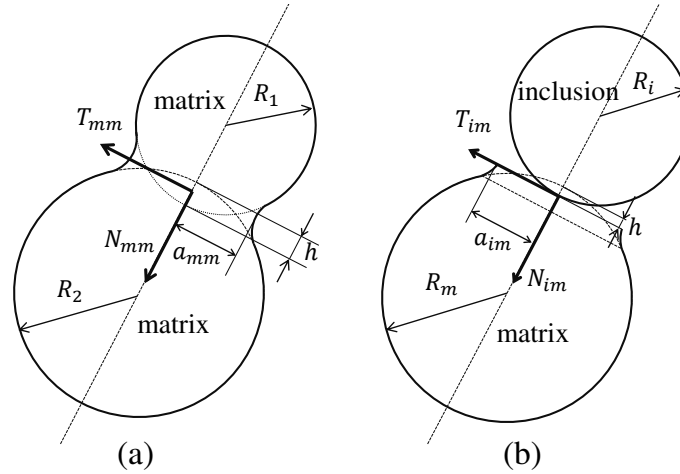


*Figure 6. 3 Contact models: (a) matrix-matrix contact (matrix can be metal or ceramic); and (b) inclusion-matrix contact*

Note that the inclusion/matrix contact model we propose here is comparable to the case of particles sintering on a rigid substrate. In accordance with Ref. [163], Eq.(6.15) is equivalent to Eq.(6.14) if the inclusion particle is treated as a flat constraining substrate (when the radius of inclusion  $R_i = \infty$ ). This would indicate that Eq.(6.15) may also apply to polyhedron inclusions. Inclusion shape may affect the sintering behavior of the composite, as shown by Sudre and Lange et al. [216] although Nakada et al. [217] experimentally found that the shape of the inclusions had little effect on the macroscopic densification behavior of ZnO matrix with 10 vol% of ZrO<sub>2</sub> inclusions.

### 6.3 Simulation procedure

- **Generation of packing**

The preparation method consists of several steps:

- (1) Making of a gas of randomly distributed non-overlapping spheres in a periodic simulation box. Before a new particle is generated, a potential position will be checked. If this particle is not intersecting with any other existing particles, it is accepted, otherwise, a new attempt is performed. This routine is repeated until all

particles are accommodated. This process takes tolerable time to result in a low packing fraction of approximately 0.32, with no contact between particles.

- (2) Jamming under isostatic equilibrium. In this stage, the loose gas is submitted to a slow stress-controlled hydrostatic densification to ensure force equilibration. During this preparation stage, friction is not introduced and only elastic contacts appear between particles [190]. This preparation stage is stopped when the relative density in the simulation box is equal to 0.55. A large external pressure can also be imposed to simulate close-die compaction and attain larger green density.
- (3) Sintering. In this stage, normal and tangential forces are activated depending on the contact (Eqs. (6.10) to (6.13)). Densification is stopped when the macroscopic density is 0.85 to ensure that interactions between neighboring contacts remains negligible.

- **Generating of composites with inclusions**

Generation of composites with inclusions can be realized in a similar way; however, matrix and inclusion particles will be labeled as different materials. In presence of aggregated inclusions, adhesion between inclusions is treated with specific bonding forces, thus ensuring the aggregate survival during jamming (Fig. 6.4).

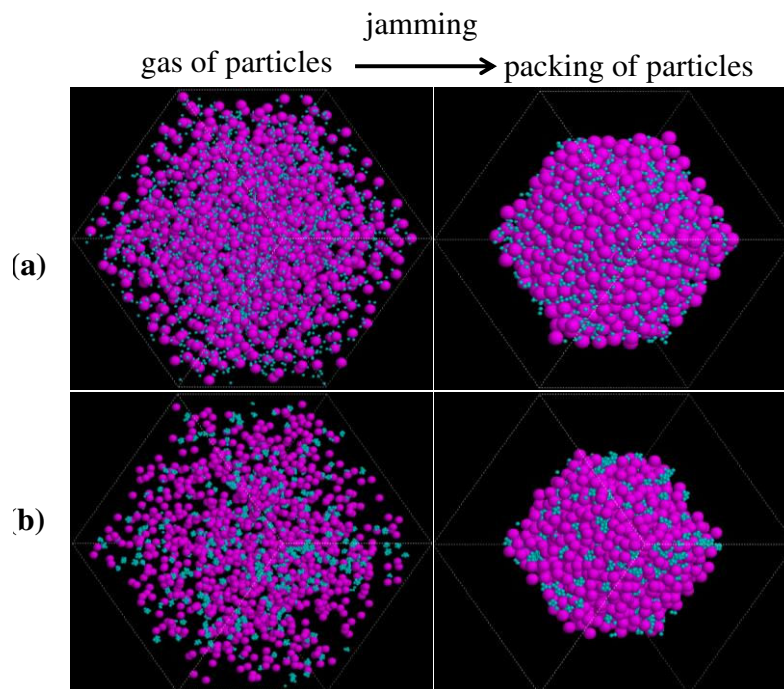


*Figure 6. 4 Generating of the numerical samples: (a) randomly dispersed; (b) aggregated inclusions*

A series of composite samples consisting of 1000 spherical monosized matrix particles of 180 nm and various volume fractions of inclusions (5%, 10%, 15% and 20%) were generated. For 20% volume fraction, the inclusion size was varied (60, 100, 180 and 300 nm, see Fig. 6.5 (a, b and c)). Periodic conditions are kept all along the sintering stage.

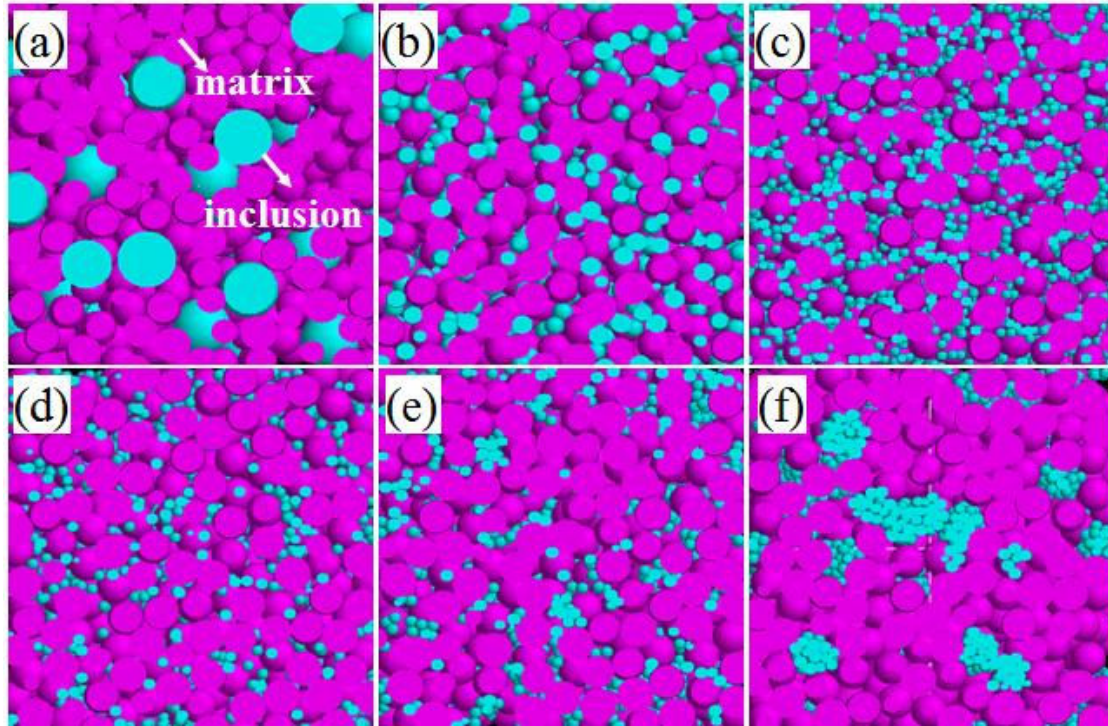


*Figure 6. 5 Numerical microstructure of composites with: 20% of randomly dispersed 300 nm (a), 100 nm (b), 60 nm (c) inclusions; 10% of randomly dispersed 60 nm inclusions (d); and 10% of agglomerated 60 nm inclusions (agglomerate sizes are ~ 120 nm (e) and ~300 nm (f)).*

In standard homogeneous samples (Fig. 6.5 (a, b, c and d)), inclusions are randomly dispersed in the matrix. In contrast, two other types of samples, with 10% and 20% of 60 nm inclusions were also generated to test the effect of an heterogeneous packing of inclusions. These samples are initially made of matrix particles randomly mixed with inclusions that are clustered together as agglomerates with average diameters of ~120 nm (Fig. 6.5(e)) and ~300 nm (Fig. 6.5(f)), respectively. All these samples were sintered isothermally at 800 °C. The material parameters needed for the Nickel material of the matrix are listed in Table 6.1.

$\delta_b D_{0b} \text{ (m}^3 \text{ s}^{-1}\text{)}$	$Q_b \text{ (kJ mol}^{-1}\text{)}$	$\Omega \text{ (m}^3\text{)}$	$\gamma_s \text{ (J m}^{-2}\text{)}$	$\varphi \text{ (}^\circ\text{)}$
$3.5 \times 10^{-15}$	232	$1.09 \times 10^{-29}$	2.0	146

Table 6.1 Material constants of Ni used in Eqs. (6.11), (6.12), and (6.13) [218]. Activation energy of Ni is regarded as a fitting parameter.

### 6.4 Result and Discussion

The most obvious effect of introducing inclusions into the matrix is to substitute (*mm*) contacts, which are bound to sinter, by (*im*) contacts. This effect is stronger as the number of inclusions increases. Also, since the inclusion number scales inversely with the cube of particle size, smaller inclusions will lead to a larger number of substitutions between (*mm*) and (*im*) contacts. This effect is demonstrated in Figure 6.6, which shows that starting from an average contact number between matrix particles  $Z_{mm} = 4.4$ , the green powder loses on average one to two (*mm*) contacts when the inclusion volume fraction increases to 20%. The size effect is also clear: while the gain of (*im*) contacts is only moderate for 180 nm inclusions, it is much larger for 60 nm inclusions. This is because smaller inclusion particles are much more efficient in decorating the surface of large matrix particles.

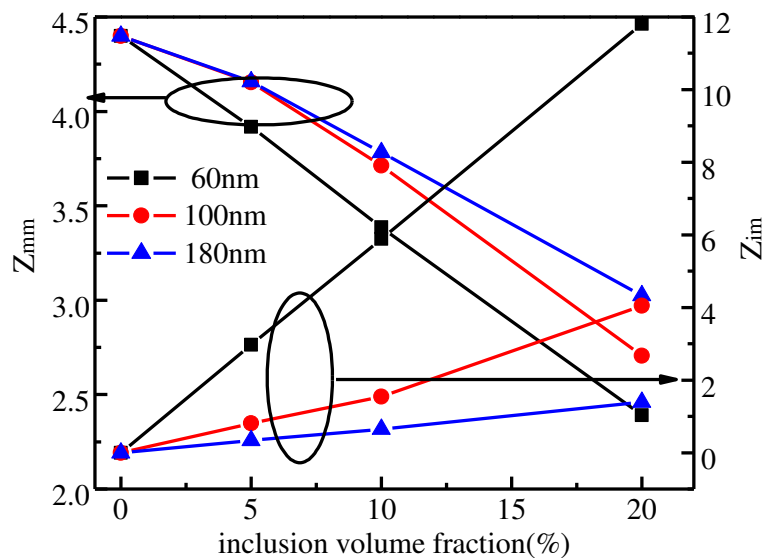


Figure 6. 6 (*mm*) and (*im*) contact numbers in the green packing for various amounts and size of inclusions.

Although all packings exhibit a net gain in contacts due to densification and rearrangement, the initial loss of (*mm*) contacts due to the presence of inclusions is not recovered during sintering. The (*mm*) contact number depends almost linearly on the relative density, once the rearrangement stage is completed (Fig. 6.7(a, b and c)). Figure 6.7(c) demonstrates that when

inclusions are introduced as larger agglomerates, their effect on the decrease in ( $mm$ ) contact number is less pronounced.

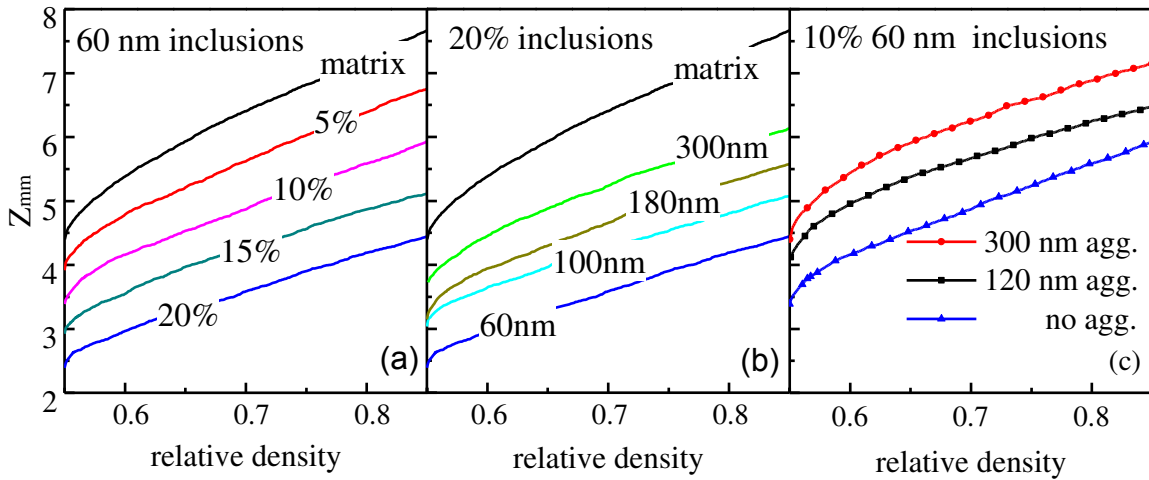


Figure 6. 7 Evolution of ( $mm$ ) contacts upon densification: (a) effect of inclusion amount, (b) of inclusion size, and (c) of the inclusions as agglomerates (agg.) or well dispersed (no agg.)

Figure 6.8 shows the typical evolutions of the relative indentation for the three types of contact in the composite. In accordance with Eqs.(6.(10-15)), the ( $ii$ ) elastic contact growth is negligible, while the ( $mm$ ) contacts grow faster than the ( $im$ ) contacts due to the surface energy term (Eq. (6.11)) which drives densification.

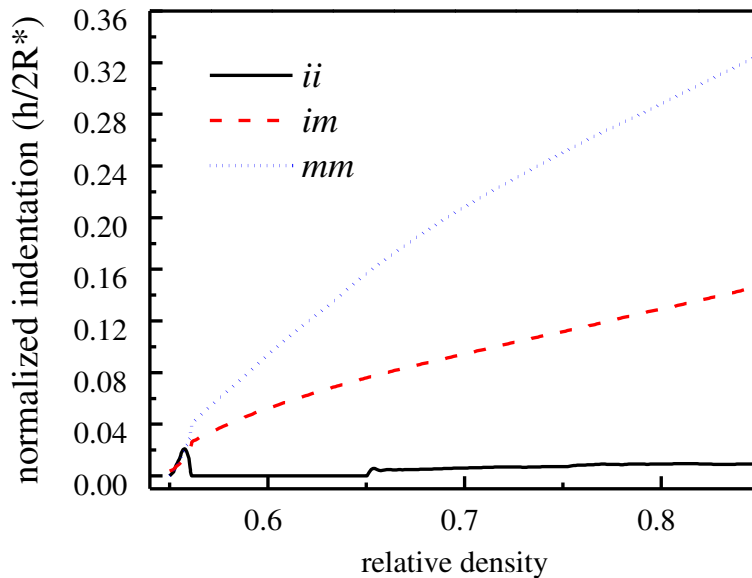


Figure 6. 8 Contact indentation evolution of three types of contacts.

The reduction in ( $mm$ ) contact number due to the substitution by ( $im$ ) contacts results in a retardation effect on the macroscopic shrinkage of the composites. This is demonstrated by



Figure 6.9(a) which shows the densification rate ( $\frac{1}{D} \frac{dD}{dt}$ ) against relative density for the various packings. As expected, the sintering of the pure matrix is the fastest. The densification rate of composites is decreasing with increasing amount of inclusions for a given size. We define the retarding factor as the ratio of the matrix and composite densification rates for a given relative density  $D$ . This factor is approximately 7 at  $D = 0.70$  when 20% of 60 nm inclusions are introduced. It also shows that a small amount (5%) of (small) inclusions is sufficient to have a noticeable retarding effect. Figure 6.9(b) demonstrates that densification rates decrease as inclusion size decreases for a given volume fraction. For instance, when the particle size ratio of the inclusion to matrix decreases from 5/3 ( $R_i = 300$  nm) to 1/3 ( $R_i = 60$  nm), the retarding factor increases from 2 to 7 at  $D = 0.70$ .

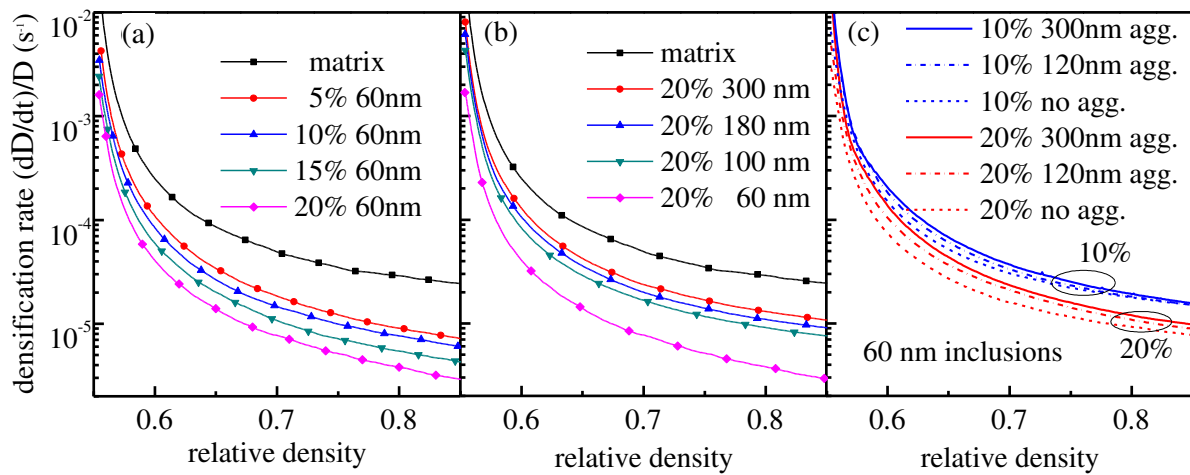


Figure 6. 9 Densification rate evolution with relative density: (a) effect of inclusion amount, (b) effect of inclusion size, and (c) of inclusions as agglomerates (agg.) or well dispersed (no agg.).

Figure 6.9(c) shows that, for a given volume amount and size of inclusions, the spatial distribution homogeneity of the inclusions can also influence the magnitude of the retardation. It indicates that the more the inclusions agglomerate, the weaker the retarding effect. This may be understood by considering these agglomerates of fine inclusions as larger (and more deformable) particles of equivalent size (the same reasoning applies for Fig. 6.9(c)). Note that the effect of agglomerates is only discernible when the volume fraction is large (20%). Still, the effect of homogeneity is of second order as compared to the effect of volume fraction and size in our simulations for which aggregates are very large.

Experimental data on the retarding effect of inclusions deals essentially with large inclusions [50, 215, 217, 219]. For example, Weiser et al. [50] studied the sintering of ZnO/SiC

composites containing 0-20% inclusions with size ratio (inclusion to matrix) value of 1-150 and found a retarding factor of ~2.5 for 20% inclusions. This number compares satisfactorily with our simulations, which predict a factor of 2 for 20% of 300 nm inclusions. Still, one should be careful when comparing these experimental data for which the inclusion to matrix size ratio is much larger than in our simulations. For composites with small inclusions, there is a lack of experimental data to quantitatively compare with our simulations. However, literature on Ni/BT composites indicates some interesting general trends. Ueyama et al. [220] found possible to suppress sintering of the Ni electrode paste film by adding 10 mass % of BT particles of 30 nm size while 50 nm particles had a less retarding effect. This result was obtained only when the 30 nm particles were well dispersed. On the opposite, Sugimara et al.[31], while demonstrating the retarding effect of BT (30-100 nm) on the sintering of Ni powder (200 nm), found that agglomerated 30 nm inclusions had a smaller retarding effect than well dispersed larger inclusions. These results are in broad agreement with our simulations which point to the following general rule: smaller inclusions have a greater retarding effect if they are well dispersed.

## **6.5 Conclusions**

- (1) A matrix/rigid inclusion contact model has been proposed which take size effect into account .
- (2) The effects of volume fraction, size and homogeneity of rigid non-sintering inclusions on the densification behavior of the matrix have been investigated using discrete element simulations at the particle length scale. It is found that the densification rate of the matrix decreases with increasing amount of inclusions and with decreasing size of inclusions. For a given amount and size of inclusions, a better dispersion of the inclusions results in a stronger retardation of densification.
- (3) By controlling the size, volume fraction and dispersion degree of the BT additives in the nickel paste, the sintering kinetics can be tailored to reduce the sintering mismatch between nickel and BT



## Chapter 7

# DEM simulation of Ni/BaTiO<sub>3</sub> multilayers

The previous chapter dealt with the simulation, using the DEM codes dp3D, of the sintering of a composite electrode material. The sintering of the representative volume element of the mixture was conducted under idealistic boundary conditions (periodic conditions), which do not reflect the firing conditions of a real MLCC. In this chapter, we seek to implement conditions that take into account more realistically the geometry of an MLCC, the constraining conditions that characterize MLCC sintering, and the particle size distribution obtained from experimental observations. The aim of these simulations is to provide information on the evolution of the microstructure in the electrode. In particular, we study the initiation and the evolution of discontinuities at the length scale of particles.

### 7.1 Model description

As detailed in Chapter 3, significant discontinuities of electrode (Ni or Pd) have formed already at the early stage of co-sintering, before the onset of densification of the dielectric layers. When the dielectric material starts to sinter, the electrode layers are almost dense (Fig. 3.7(f)). At this final stage, it is not possible anymore to consider the Ni (or Pd) layer as a collection of individual particles with the characteristics of a particulate system. The DEM model is inappropriate to simulate the final stage of electrode sintering. Thus, this chapter mainly focuses on the early stage of the co-sintering of Ni/BT multilayers (i.e. temperature range of 700-1050 °C). We note that only a small amount (~3%) of shrinkage is observed in the BT material at this stage. The BT-BT contacts in the dielectric layers are modeled as sintering contacts. That is to say, like Ni-Ni contacts, BT particles also sinter but at a negligible rate. This allows to model two different materials which co-sinter at significantly different rates. To implement these simulations for Ni-Ni and Ni-BT contacts, the normal forces and tangential forces are calculated using the same contact models as in Chapter 6.2. For both Ni-Ni contacts and the BT-BT contacts, Eq.(6.11) is used to calculate the normal force and Eq.(6.13) for the tangential force. In the presence of nano-sized BT inclusions in the electrodes, BT-BT contacts between these nano BT particles are modeled as elastic.

## 7.2 Simulation procedures

### 7.2.1 Sample preparation

- **Particle size distributions (PSDs)**

As in the preceding chapter, BT and Ni particles are ideally treated as spheres. The PSDs of the BT particles in the dielectric layers and of the Ni particles in the electrode layers are fitted as log-normal functions directly from the FIB nano-tomography data (see Chapter 5.3.2). The log-normalized particle size  $\ln d$  is distributed according to a log-normal function:

$$f(d) = f_0 + \frac{A}{\sigma_{\ln} \sqrt{2\pi} d} \exp \left[ -\frac{\left[ \ln \frac{d}{d_c} \right]^2}{2\sigma_{\ln}^2} \right] \quad (7.1)$$

Where  $f_0$  is the offset, A is the area,  $\mu_{\ln}$  and  $\sigma_{\ln}^2$  are the expected (or mean) value and variance for the log-normal distribution, respectively. The real mean value of particles  $\mu$  can be calculated as  $\mu = \exp(\mu_{\ln} + \sigma_{\ln}^2 / 2)$  and the variance is calculated as  $\sigma^2 = (\exp(\mu_{\ln})^2 - 1) \cdot \exp(2\mu_{\ln} + (\sigma_{\ln})^2)$  [221].

Representing all particle sizes given by Eq.(7.1) would result in a very large number of particles. This would be CPU prohibitive. Instead, we cut off the PSD for small particles by simulating only particles larger than  $d_{min}$ .

For the Ni powder in the electrode and BT powder in the dielectrics, the parameters for the fitted PSD functions are listed in Table 7.1:

Powder	$f_0$	A	$\sigma_{\ln}$	$d_c$ (nm)	$d_{min}$ (nm)
Ni	0.276	2836.645	0.473	182.96	27
BT	-0.074	3086.47	0.325	274.38	60

Table 7.1 Fitted parameters of the PSD functions

For the nano scale BT additives, the exact PSD is not known but the mean additive particle size is 50 nm. This value is used in the simulations.

- **Cylindrical samples**

To reduce the CPU simulation time to a tolerable duration, a representative BT/Ni/BT sandwich multilayered cylinder with a diameter of  $\varnothing = 10 \mu\text{m}$  was created (Fig.7.1). This geometry is close to that of the sample used for the synchrotron nanotomography. BT and Ni

particles with lognormal distribution (Eq.(7.2) and Eq.(7.3) respectively) were randomly generated using Box-Muller transform [222] and using the parameter given in Table 7.1. Green packings with density range of 0.3-0.5 (depending on the green density to be achieved) were first generated (see Chapter 6.3 for the routine description). In that initial packing stage, interactions between particles are solely elastic. Figure 7.1(a) shows a BT layer. Figure 7.1(b) shows a nickel electrode without any BT inclusions. Figure 7.1(c) shows a Ni electrode with 10 vol. % mono-sized BT inclusions ( $d = 50$  nm) which are homogeneously dispersed (no agglomeration). The cylindrical BT and Ni discs were aligned and stacked (Fig. 7.1(d)). These stacked multilayers were then hydrostatically jammed together to achieve a green density equal to that observed in real MLCC samples.

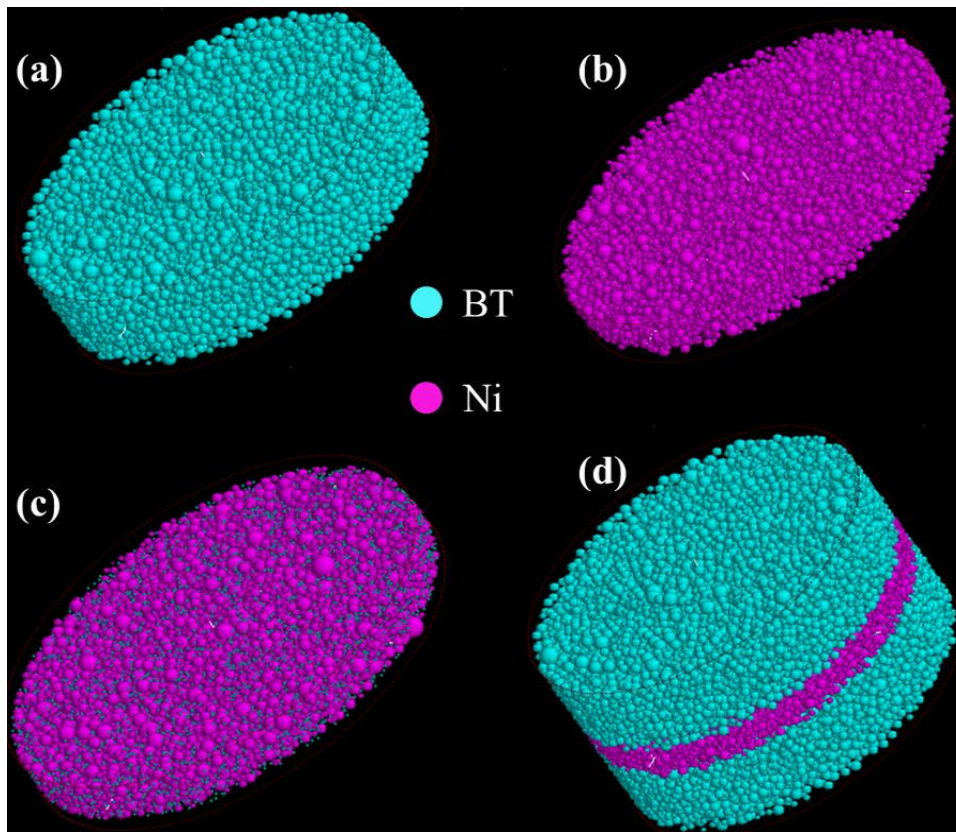


*Figure 7. 1 Numerical samples: (a) BT dielectric layer (b) Ni electrode layer without BT additives (c)Ni electrode with 10 vol.% BT additives (d) BT/Ni/BT multilayers*

Table 7.2 lists the initial conditions of the BT dielectric layers and electrode layers including the pure Ni electrode and the Ni/BT composite electrode. Except mentioned otherwise, these are the standard parameters used in the simulations.

Layer	Thickness (μm)	Particle number	Green density
BT	2.4	9375	0.61
Ni	1.0	6500	0.50
Ni/BT	1.0	6500 (Ni):1300(BT)	0.55

*Table 7.2 Standard sample properties for the numerical samples*

### 7.2.2 Sintering conditions

All surfaces (top, bottom and lateral) of the cylindrical sample are considered as free surfaces. The physical properties of Ni are detailed in Chapter 6.2. In the absence of diffusion data specific to Barium Titanate (BT), the sintering properties in the dielectric layer were assumed to be the same as those of Alumina (Al<sub>2</sub>O<sub>3</sub>) except for the sintering activation energy  $Q_b$ . Specific surface energy  $\gamma_s$  is known to vary moderately from one oxide to the other, and remains close to 1.0 J/m<sup>2</sup>. The volume of the diffusing particles is  $8.47 \times 10^{-30}$ . The properties used are listed in Table 7.2. Note that, for a given microstructure, it can be shown that time in dp3D may be advantageously normalized to  $\tau = k_B TR^4 / \gamma_s \Omega \delta D_b$  [187]. Thus, sintering kinetics obtained from one DEM simulation for a given set of material ( $\delta_b D_{0b}$ ,  $Q_b$ ,  $\gamma_s$ ,  $\Omega$ ,  $R$ ) and process ( $T$ ) parameters can be used to retrieve the sintering kinetics of another set. By correlating sintering kinetics of a BT disc sample (Chapter 3) with DEM simulations of the sintering of BT under the same conditions (i.e., PSD, green density and heating ramp and temperature), we may fit a suitable activation energy ( $Q_b = 480$  KJ/mol). By using the material properties of  $\alpha$ -Al<sub>2</sub>O<sub>3</sub> in Table 7.2 for all material parameters except the activation energy, no physical meaning can be ascribed to the activation energy. It only represents a practical manner to model the slow BT sintering kinetics at low temperature.

$\delta_b D_{0b}$ (m <sup>3</sup> /s)	$\gamma_s$ (J/m <sup>2</sup> )	$\Omega$ (m <sup>3</sup> )	$\eta_{Ni-BT}$	$\eta_{BT-BT}$
$1.3 \times 10^{-8}$	1.1	$8.47 \times 10^{-30}$	0.1	1

*Table 7.2 Material properties of BT (adopted from  $\alpha$ -Al<sub>2</sub>O<sub>3</sub> [204])*

Table 7.3 lists the values of the viscous parameter  $\eta$  used in the simulations. Except mentioned otherwise (see Chapter 7.6 on the effect of  $\eta$ ), these are the values used in all simulations. A BT-BT contact viscosity value of  $\eta_{BT-BT} = 1$  is believed acceptable, since the irregular shape of BT particles resist significantly the rotations and slides of the BT particles, hence the rearrangement of the BT particles can be neglected.

### 7.2.3 Post processing

- **Voxelisation**

The output of a dp3D simulation is a set of pheres defined simply by their coordinates and radii. These spheres are truncated due to the densification process which has taken place during sintering (Fig. 7.2(a)). To visualize in a more realistic manner the simulated microstructures of the sintered samples, necks and grain boundaries need to be taken into account. In accordance with Eq. (6.14), the neck size is estimated using Coble's law as Figure 7.2(b) shows.

$$a_c^2 = 4R^* (h_1 + h_2) \quad (7.2)$$

Where the  $a_c$  is the contact radius,  $R^*$  is the reduced radius, defined as  $R^* = R_1 R_2 / (R_1 + R_2)$ ,  $h$  ( $= h_1 + h_2$ ) is the indentation. The volume redistributed in the triangular torus is equal to the overlapped volume. The out surface of the neck is tangential to the two particles with curvatures of  $\rho_1$  and  $\rho_2$ . The geometry lengths are given by Eqs. (7.(3-6)). The derivation of these values is detailed in Appendix B.

$$\rho_1 = \frac{a^2 - 2R_1 h_2 + h_2^2}{2R_1 - 2a} \quad (7.3)$$

$$\rho_2 = \frac{a^2 - 2R_2 h_1 + h_1^2}{2R_2 - 2a} \quad (7.4)$$

$$y_1 = \frac{(R_1 - h_2)\rho_1}{R_1 + \rho_1} \quad (7.5)$$

$$y_2 = \frac{(R_2 - h_1)\rho_2}{R_2 + \rho_2} \quad (7.6)$$

To voxelise the sample, the entire sample including the solid volume and porous volume was subdivided in voxels with values 1 (solid) and 0 (porosity). The routine is detailed in Ref. [193]. This routine assumes that contacts do not interfere with their neighbors. Hence, when the sample reaches a high densisty (>0.85-0.90), many triple contacts (or higher coordination contacts) exist and the validity of this post-processing process is not any more ensured.

- **Visualization**

The voxelized microstructures can be resliced and visualised using ImageJ or Avizo software packages as shown in Figure 7.2(b). Quantification of the real microsturtures can be made



from the 3D microstructures. In this study, we focus on the discontinuity of the electrode, defined as the percentage of uncovered area over the enveloping area.

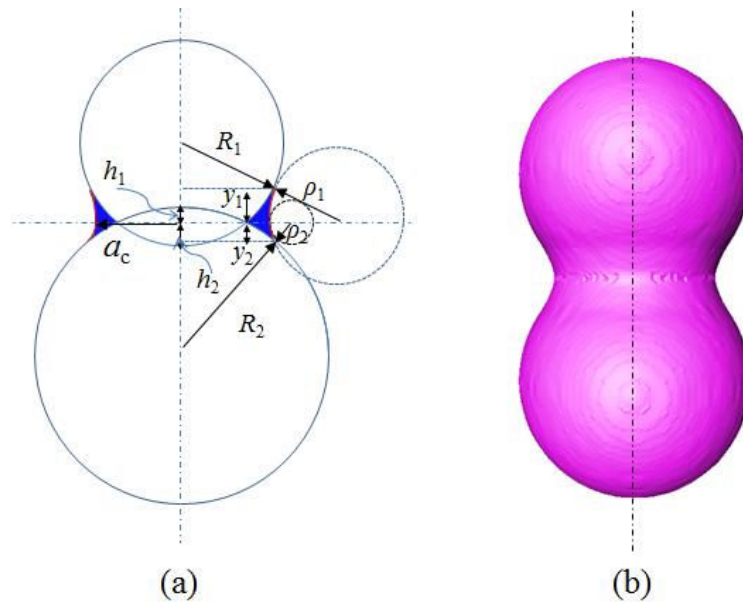


*Figure 7. 2 (a) Definition of Coble Contact radius  $a_c$ ; (b) visualization of two sintered particles after the voxelization procedures*

### **7.3 Free sintering and constrained sintering**

The simulation results of the sintering of a single Ni layer were compared with those of BT/Ni/BT layers under the same conditions to understand the main consequences of constrained sintering. The DEM simulations started at an initial temperature of 700 °C with a heating rate of 1 °C/min. The Ni layer has a 0.50 green density. The sintering was terminated at 1050 °C (total time = 21 000 s, approximately 6 hrs). The viscous parameter  $\eta_{Ni-Ni}$  was set to 0.1.

Figure 7.3 shows the microstructure (Fig. 7.3(a)) of the green electrode together with the microstructures of the electrodes that have been freely sintered (Fig. 7.3(c)) and constrained sintered (Fig. 7.3(d)) in the presence of BT layers. For clarity, in that last case the BT layers are not shown. Close inspection of Figure 7.3(a) indicates that there are numerous heterogeneous zones which exhibit rather large pores. These zones, previously mentioned as inter-agglomerate pores (Chapter 3.3), are shown in circled areas in Figure 7.3(a). These porous zones are typically larger than the average size of the particles. The packing can be subdivided into well packed agglomerates separated by these extrinsic pores. The particles in

these well packed agglomerates have higher coordination numbers than the average value. Pores between particles within these agglomerates are defined as intra-agglomerate pores.

After sintering, the Ni electrode sintered freely has densified homogeneously with nearly no discernable discontinuity. Conversely, the Ni electrode which has been sintered under constraints imposed by the BT layers clearly breaks into discontinuous areas (discontinuity content is about 14.5%). Constraints play an important role in the formation of discontinuous electrode, and we shall examine in more details in the following sections the mechanisms that lead to these discontinuities.

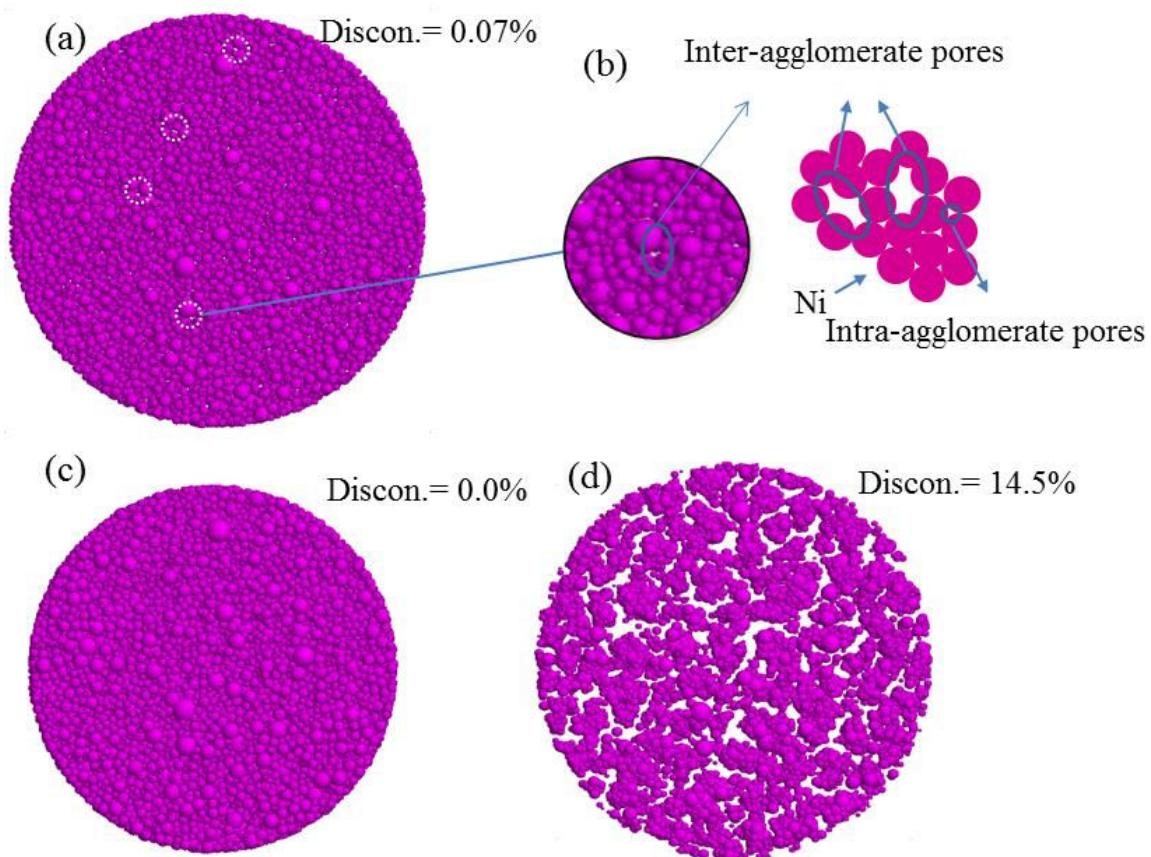


*Figure 7. 3 Microstructure evolution of electrode: (a) green microstructure; (b) definition of the inter/intra- agglomerate pores; (c) freely sintered electrode; and (d) constrained sintered electrode*

- ***Defect evolution mechanisms***

To understand how these defects initiate and evolve, a representative area was selected and followed in detail. Particles in the final continuous area were colored differently to easily

trace them at different phases of the sintering. As Figure 7.4 demonstrates, particles that pertain to these continuous areas were initially closely packed (see the agglomerates in Figure 7.4(a)). The pores that bound these agglomerates are mostly inter-agglomerate pores and may be considered as initial heterogeneities, as shown in the circled areas. In the close packed agglomerates (colored areas) which are mainly formed of intra-agglomerate pores, particles sinter faster while the initial inter-agglomerate pores enlarge due to the shrinkage of agglomerates.

As sintering proceeds, the contacting particles at the boundaries are detached due to local sintering shrinkage mismatch. This contact loss is referred to as de-sintering. The de-sintering indicated by the arrows in the Figure 7.4(c) results in the growth of pores (discontinuities). On the other hand, intra-agglomerate pores shrink and gradually pinch off and finally disappear as shown in the Figure 7.4(d-f).

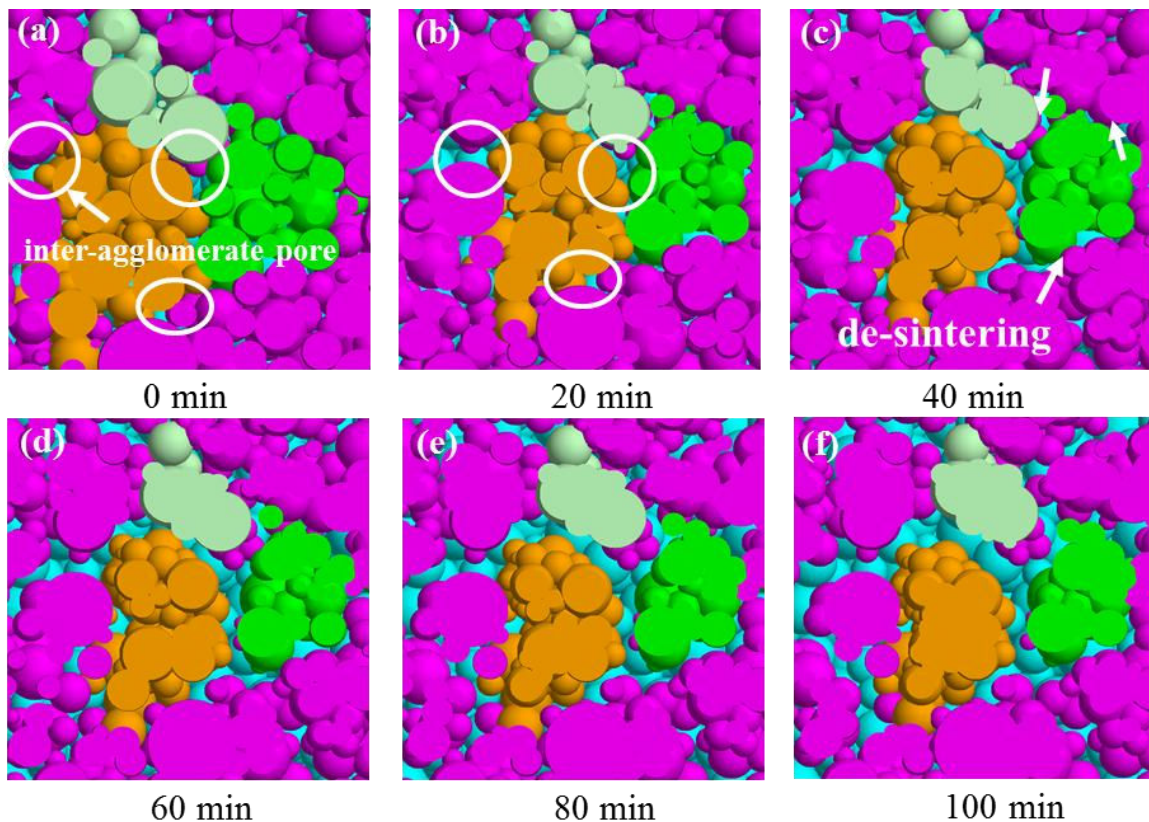


*Figure 7. 4 The microstructure evolution in the magnified area as function of sintering time during the heating ramp*

## 7.4 Effect of heating ramp

A standard sample (BT layer and Ni layer see Table 7.2) was sintered at different heating rates: 1, 5, 10, 15, 30 and 50 °C/min, starting from 700 °C until 1050 °C.

Figure 7.5 plots the electrode discontinuity as a function of temperature with different heating rates. As sintering proceeds during the heating ramp, the discontinuity increases as sintering temperature increases. It is concluded that a fast heating rate results in lower discontinuity. For instance, with heating rate increasing from 1 °C/min to 50 °C/min the discontinuity decreases from 15.44% to 1.73%. However, it should be clear that according to the simulation, the density reached at a given temperature is also lower for a faster heating ramp. This is because the value of the heating rate impacts the duration of the ramp during which the Ni layer may be considered to sinter under constraint.

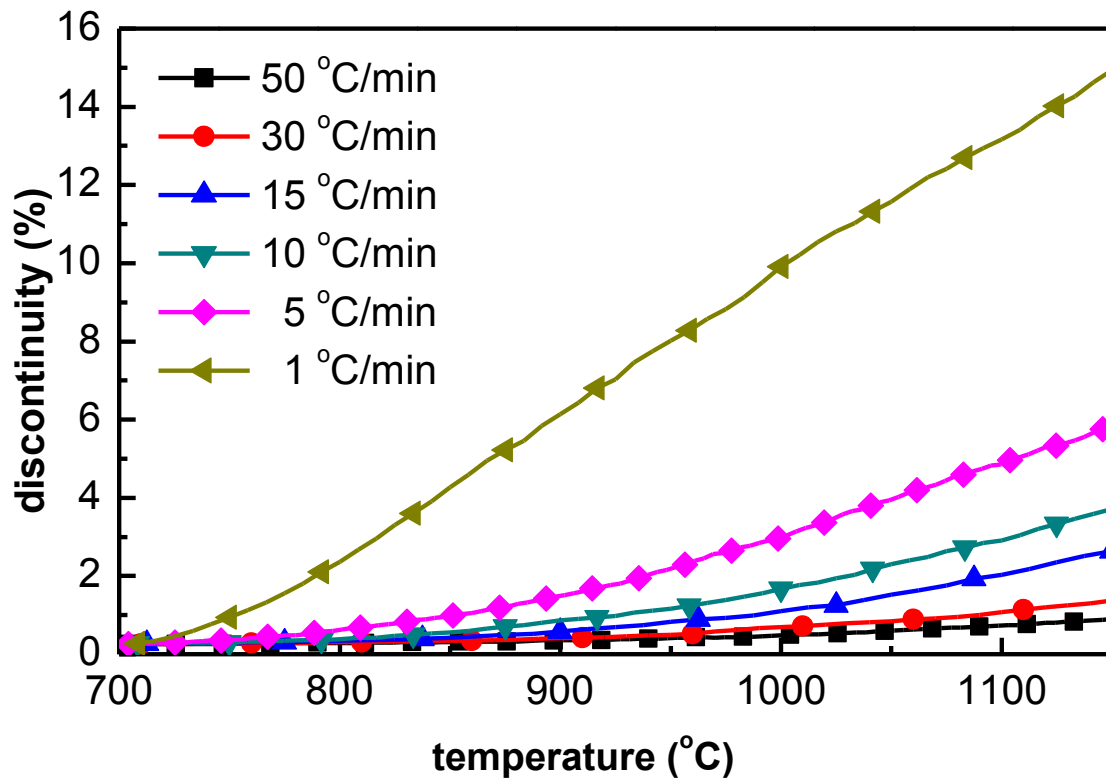
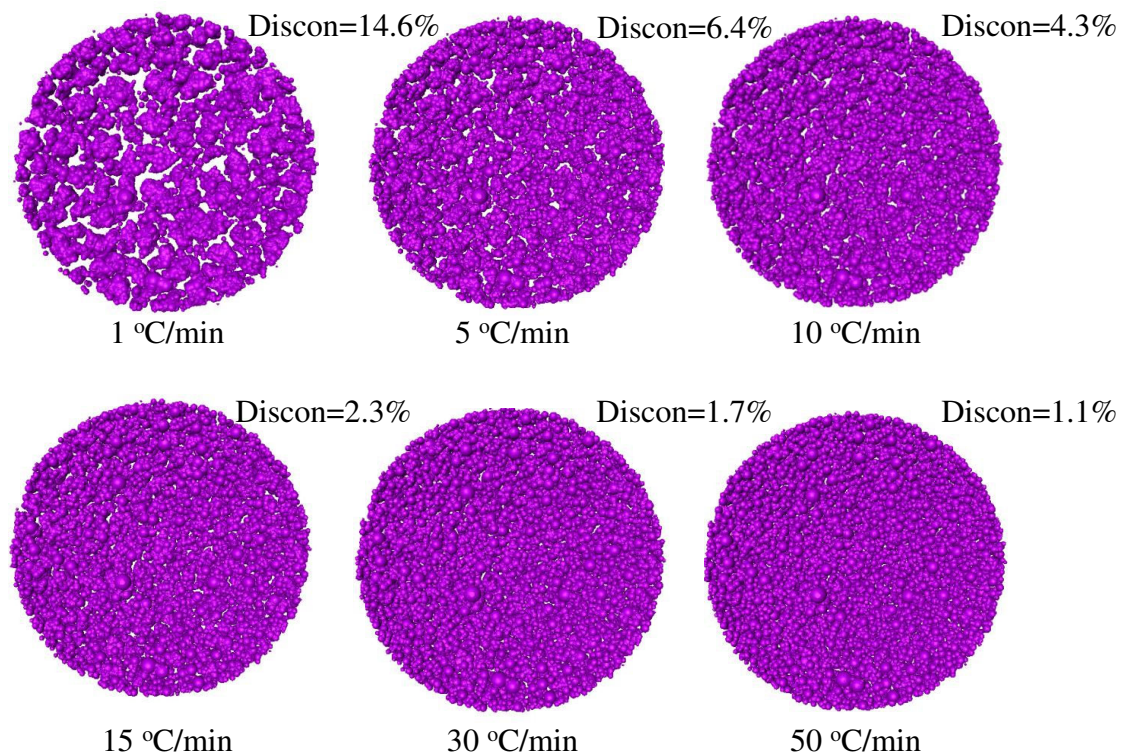


Figure 7.5 Electrode discontinuity against the temperature

As Figure 3.5 shows, the Ni electrode (with 10 vol. % BT inclusions) sinters sooner and faster than the BT dielectric layer during the heating stage. The sintering shrinkage mismatch between electrode and dielectrics, which is built up in this stage, directly contributes to the electrode discontinuity. Experimental observations indicate that below the critical temperature (1050 °C, @15 °C/min), the electrode is always under tensile stresses. Above this

critical temperature, BT layers sinter faster than electrode layers and compressive stresses are generated. Using fast heating rate allows the Ni to be only slightly sintered when reaching the high temperature domain (above the critical temperature and the dwelling temperature 1150 °C). In that case, the compressive stresses experienced at higher temperature should facilitate the final densification of Ni, resulting in slower growth of discontinuities, or even some recovery of the discontinuities. When the Ni approaches completion of sintering, it is still viscous and highly deformable. In this stage, compressive stresses will cause lateral contraction and a further increase in the discontinuity through a swelling mechanism already discussed in Chapter 5. It is not possible to simulate with DEM this last stage. This is because DEM operates with interacting particles, which are not suited to simulate a continuum. In any case, the discontinuity initiation and development, which is well predicted by DEM during the heating stage, will contribute to the final discontinuity.

Figure 7.6 shows the microstructures (*z*- axis view.) at the end of the different heating ramps running from 700 to 1050 °C.



*Figure 7.6 Microstructure and the discontinuity of the electrode sintered at different heating rates. The discontinuities of the electrode are 14.55% (at 1 °C/min), 6.44% (at 5 °C/min), 4.33% (at 10 °C/min), 2.27% (at 15 °C/min), 1.7% (30 °C/min), and 1.13 % ( at 50 °C/min).*

The results of these simulations indicate that the shorter the sample is exposed to sintering during the heating stage, the less discontinuity is built up. In the industrial firing process, there is a second binder bake-out (BBO) step. For example, the Ni-MLCC chips are held at 800 °C for 1 hr to remove the organic completely. During this BBO process, the electrode has already sintered to some extent (Fig. 3.7). This seems to be detrimental according to the simulations. To solve this problem, one possibility would be to apply a fast heating schedule. An alternative solution is to adapt the organic system such that it can be burnt out at a lower temperature (<400 °C for example) before nickel starts to sinter.

### 7.5 Effect of green density

DEM simulations allow particulate microstructures to be generated at various green densities. We take advantage of this feature to study the effect of green density on the evolution of discontinuity. The sintering of BT/Ni/BT multilayers consisting of the same two BT layers ( $D = 0.60$ ) and constant thickness electrode with different packing density ( $D = 0.40, 0.45, 0.50, 0.55, \text{ and } 0.60$ , pure nickel) was simulated at a heating rate of 15 °C/min from 700 to 1050 °C.

Figure 7.7 plots the electrode discontinuity as a function of heating time for samples with different green densities.

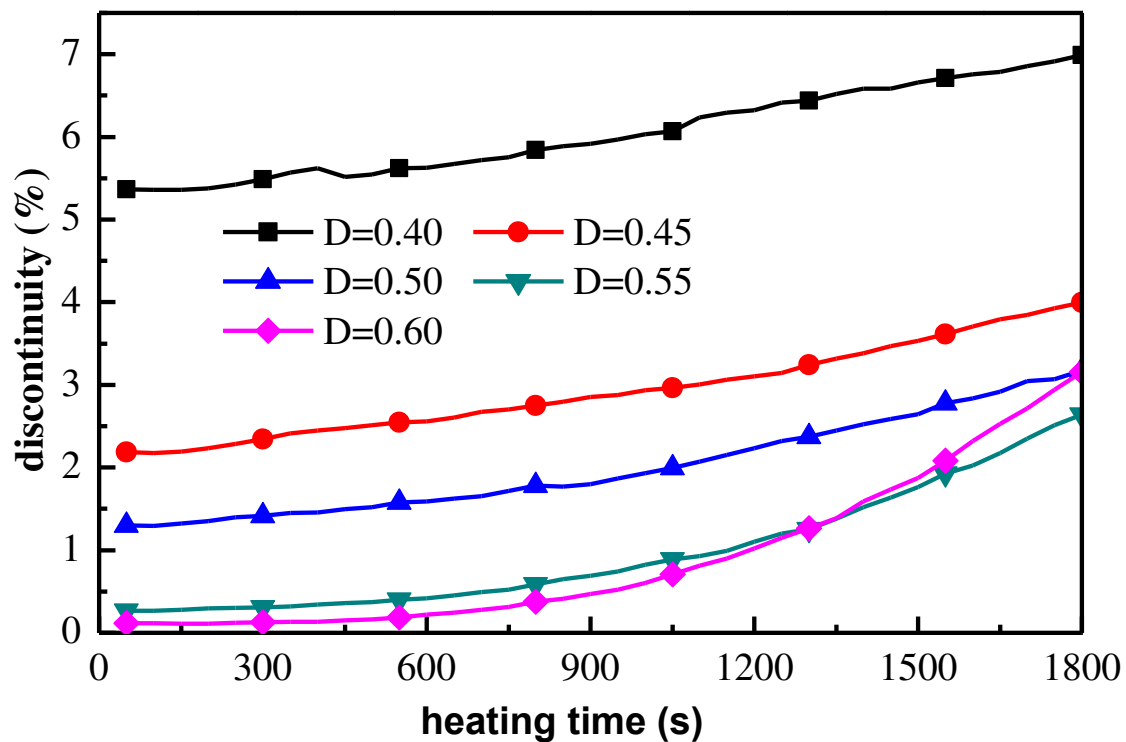
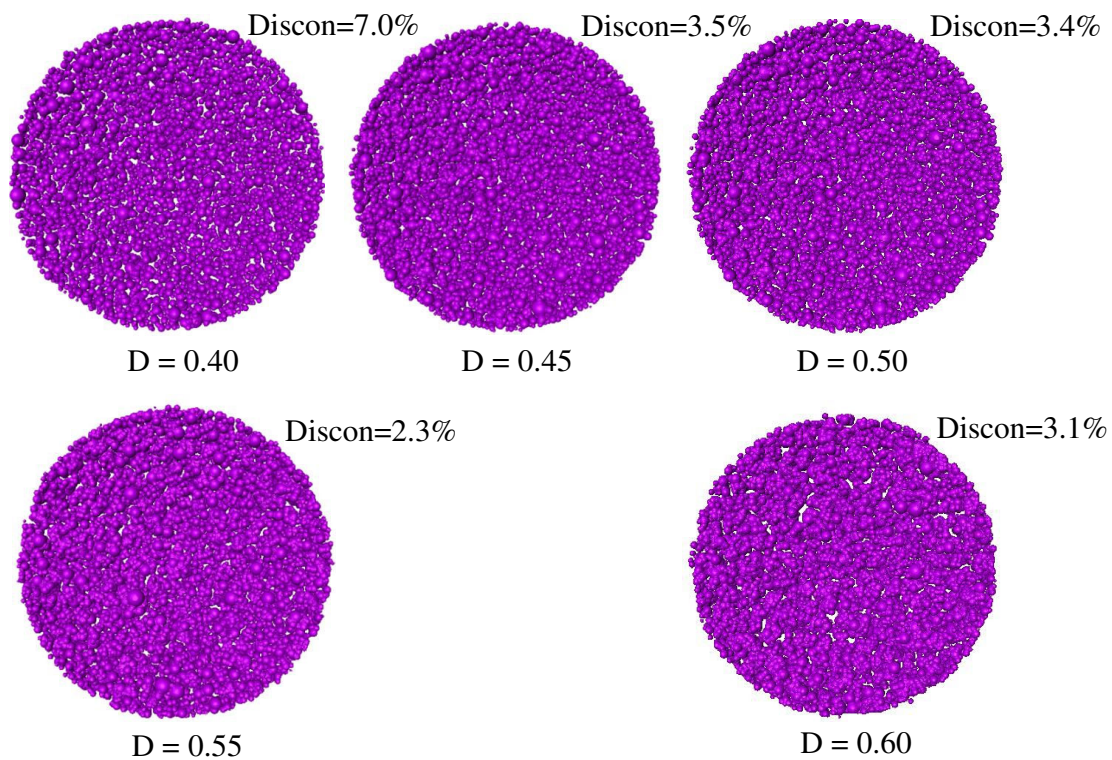


Figure 7.7 Discontinuity of electrode as functions of heating time

Owing to our definition of discontinuity (see Eq.(4.4)), it is found that the initial discontinuity is related to the initial green density. Lower green density results in more initial pores or heterogeneities. For all green densities, the effect of constrained sintering is to increase discontinuity.

Figure 7.8 shows the sintered microstructure of these samples after the heating ramp. It is found that within the range of  $D = 0.40-0.55$ , the lower the green density, the higher the final discontinuity. This is supportive of our early argument: the final discontinuity of electrode originates from initial heterogeneity (pores).



*Figure 7. 8 Microstructure of electrode with different green density (at 15 °C/min)*

We also note that when the green density of the Ni layer is large ( $D_0 = 0.60$ ), the discontinuity growth rate is somewhat larger than that of more porous green layers although they have fewer initial pores (heterogeneities). This is because a denser green body sinters faster, owing to the larger number of contacts between particles that increase the total driving force for sintering. For the same given heating time, the faster the sintering, the larger the shrinkage mismatch, thus leading to a larger discontinuity.

### 7.6 Effect of contact viscosity

We have seen that the BT layer constrains the sintering of the Ni layer. It is thus important to understand the consequence of the interactions at the interfaces between Ni and BT particles. The tangential force partly dictates the amplitude of particle rearrangement at the interface between Ni and BT. However, we shall see that particle rearrangement in the Ni layers is also critical. The following simulations attempt to decouple the effect of rearrangements by varying the values of  $\eta_{\text{Ni-Ni}}$  and  $\eta_{\text{Ni-BT}}$  that dictate the amplitude of viscous tangential forces at the contact in Eq.(6.13). The exact value of  $\eta$  is very difficult to ascertain. Parhami and McMeeking [198] and Henrich et al. [188] using the same tangential law, used 0.003 and 0.3 values, respectively. In any case, the value of  $\eta$  should be less than unity. The rationale for this is that the normal viscosity term in Eq. (6.11) should be of the same order or larger than the tangential viscosity term (Eq. (6.13) when the normal and tangential relative velocities are of the same order.

In order to mimic the behavior of the real irregular shaped BT particles, a large viscosity coefficient  $\eta_{\text{BT-BT}} = 1$  is used in all simulations [163]. For Ni-Ni and Ni-BT contacts, extreme values (0 and 1) are used to decouple clearly the effect. A 0.01 value has also been tested for  $\eta_{\text{Ni-Ni}}$  to approach more realistic values given in the literature [198].

$\eta_{\text{Ni-Ni}}$	$\eta_{\text{Ni-BT}}$	$\eta_{\text{BT-BT}}$
0	0	1
1	0	1
1	1	1
0.01	1	1
0	1	1

*Table 7.3 Contact viscosity between Ni-Ni, Ni-BT, and BT-BT contacts (dimensionless)*

Figure 7.9 plots electrode discontinuity evolution against the sintering time during the heating ramps for multilayers with various material viscosities. Both the viscosity between Ni-Ni and that between Ni-BT (interface) influence the electrode discontinuity. For a given Ni-BT viscosity value ( $\eta_{\text{Ni-BT}} = 1$ ), the larger the Ni-Ni viscosity, the larger the electrode discontinuity. It is because the viscosity between sintering particles plays an important role in the rearrangement of the sintering particles. When particle rearrangement is limited, it is not possible for particles to compensate for the BT layer constraint, leading to local tensile stresses. Thus, at the location of a local heterogeneity, contacts are broken and the heterogeneity is able to grow.



More generally, viscosity hinders the rearrangement of sintering particles, while the rearrangement of particles has been proved in experiments by Kieback et al. [223] and DEM simulations [188, 189] to be able to facilitate the homogeneous sintering of powder. Additionally, the viscosity between Ni and BT hinders the interface rearrangement, such that a relative rigid interface is maintained during sintering, thus allowing the in-built stresses near the interface to be transmitted. This is in accordance with previous DEM simulations on the development of cracks in constrained sintering systems [189].

The variation of  $\eta_{Ni-BT}$  does not seem to have as much impact on discontinuity as the variation of  $\eta_{Ni-Ni}$ . This is not intuitive since section 7.3, which compared free sintering and constrained sintering conditions, demonstrated the importance of the existence of the Ni-BT interface. In fact, the interaction that affects mostly the rearrangement of Ni particles at the Ni-BT interface is the normal contact force (Eq.(6.11)) that exists between Ni and BT particles. Since the interface is not smooth (BT particles are spherical), any tangential or normal motion of Ni particles result in a counteracting viscous force opposite to  $dh/dt$ .

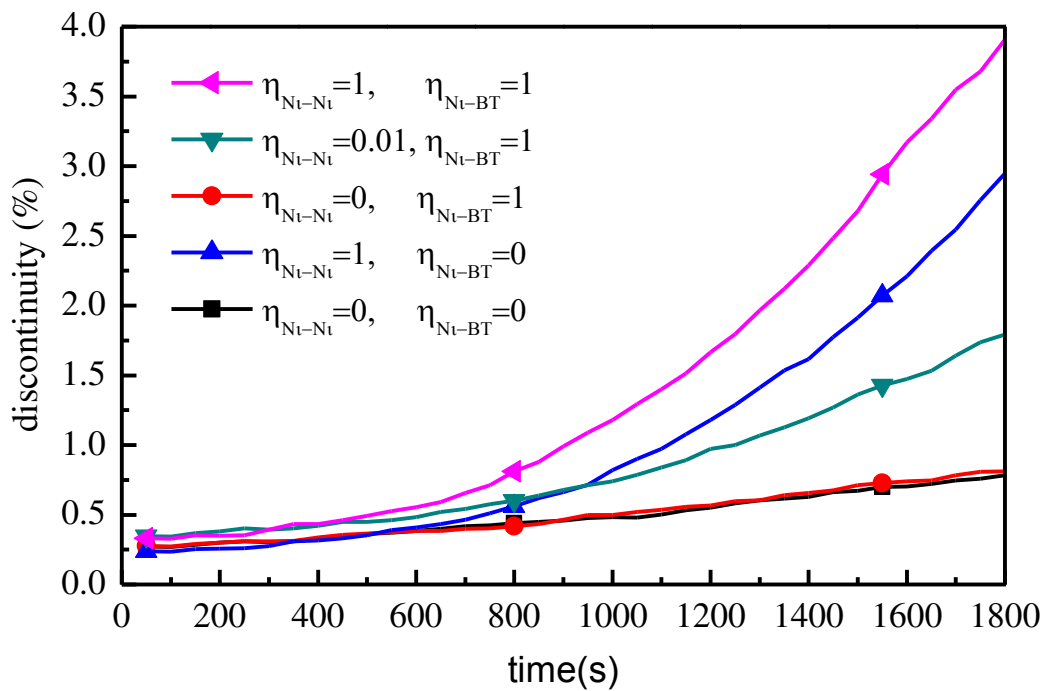
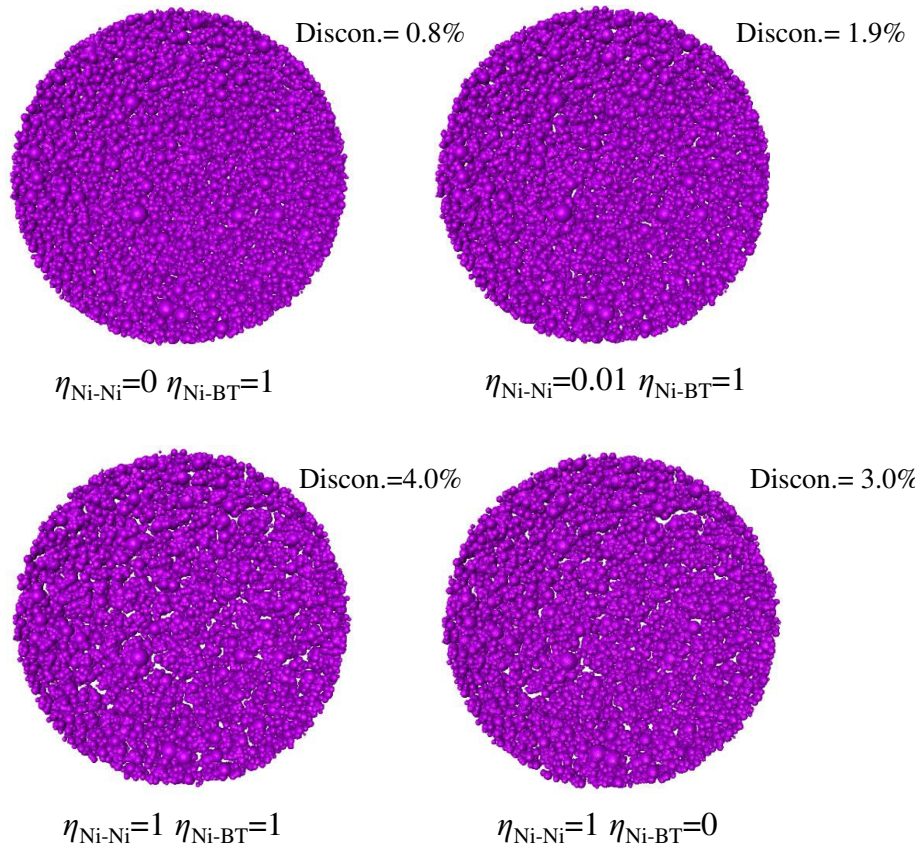


Figure 7. 9 Discontinuity of electrode as functions of heating time for different values of the viscous parameter.

From Figure 7.10 showing the microstructures at the end of the heating stage, it is observed that on top of the difference in discontinuity in percentage, the pores form at different locations in the electrode. This difference is due to the rearrangement of the particles.

It has been observed that rearrangement of particles should accelerate the sintering kinetics [188]. Thus, the shrinkage mismatch between the electrode and dielectrics should increase and a larger discontinuity of electrode could be expected. However, in these simulations, we observed the reverse. This is because a constraint is a more crucial requirement for the formation of discontinuities and easy rearrangement of the particles at the interface lowers the constraint at the interface.



*Figure 7. 10 Microstructure of electrode with different viscosities (at 15 °C/min)*

### **7.7 Effect of electrode thickness**

The electrode thickness is an important functional parameter. It has decreased over the years in the MLCC industry. Here we investigate its effect on the sintering process. To investigate the effect of the electrode thickness on the electrode discontinuity, BT/Ni/BT multilayers with electrode having different average thickness were sintered at 15 °C/min from 700 to 1050 °C. The samples are shown in Figure 7.11. The BT layers have a constant thickness (2.4 μm) while the thickness of electrode varies:  $H = 0.2 \mu\text{m}$ ,  $0.4 \mu\text{m}$ ,  $0.6 \mu\text{m}$ ,  $1.0 \mu\text{m}$ . These serial thicknesses correspond to on average 1, 2, 3 and 5 layers of particles packed in the electrode layer.

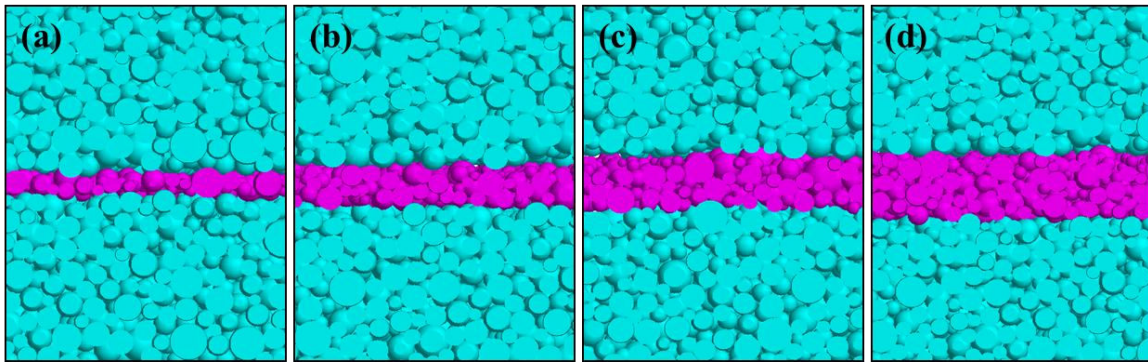


Figure 7.11 Green microstructures of different samples with (a) 0.2  $\mu\text{m}$  (b) 0.4  $\mu\text{m}$  (c) 0.6  $\mu\text{m}$  (d) 0.8  $\mu\text{m}$  thick electrode (pure nickel)

Figure 7.12 shows the effect of the initial thickness of the electrode on its final discontinuity after sintering.

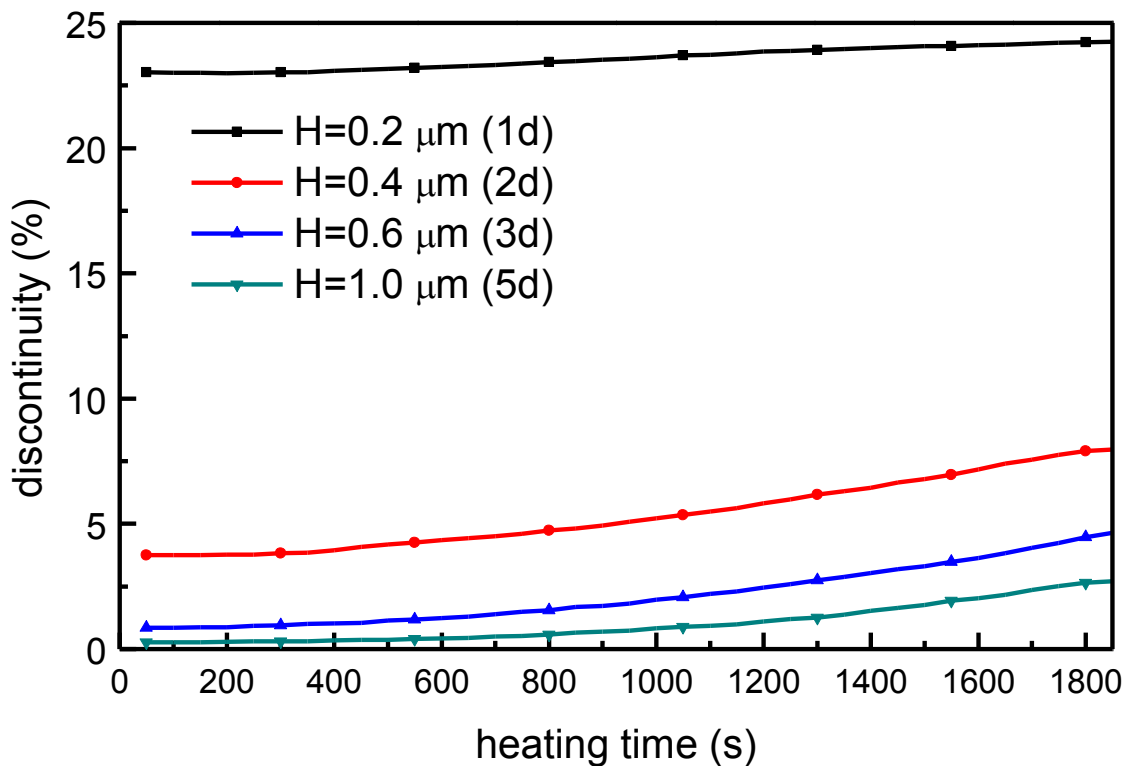
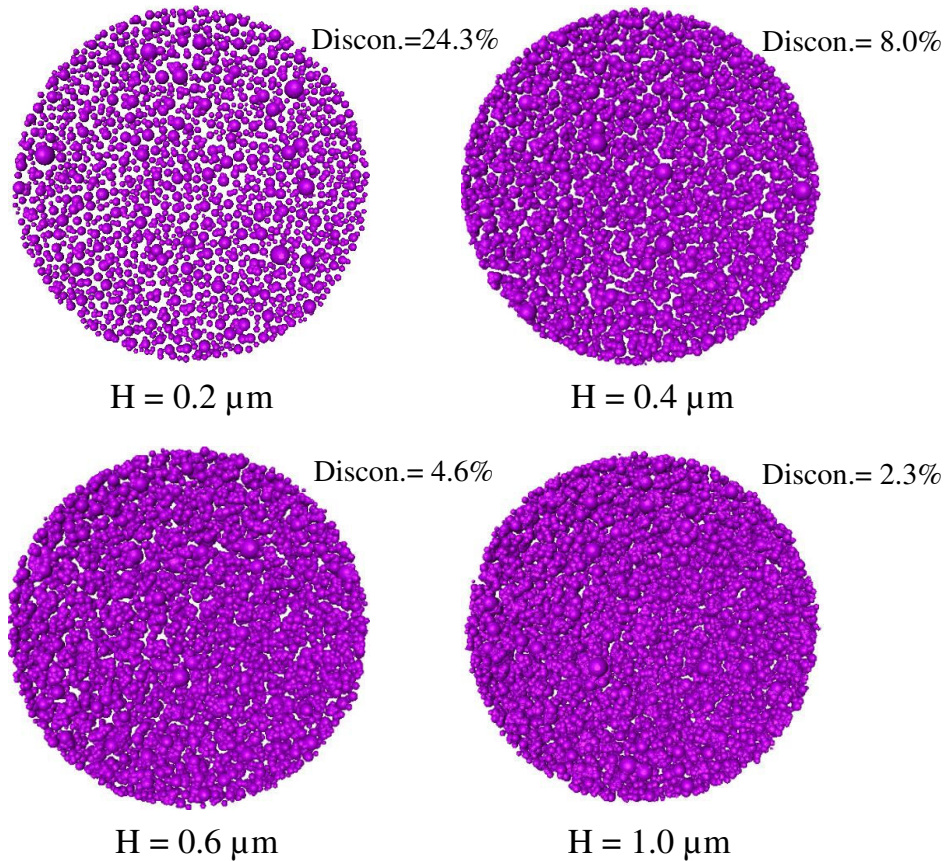


Figure 7.12 Electrode discontinuity as functions of heating time for various electrode thickness

It is observed that the thinner the electrode thickness, the larger the electrode discontinuity. However, the layer thickness has mostly an effect on the initial heterogeneity value. For example, when the electrode consists of a monolayer of particles ( $H = 0.2 \mu\text{m}$ ), a large initial discontinuity content (22.8%) is calculated.

Figure 7.13 shows the sintered microstructures at the end of the heating ramps. As sintering proceeds, the discontinuity content only increases slightly. It is found that the continuous areas are formed by the bonding and sintering of several particles (Fig. 7.13(a)). They do not connect with the neighboring continuous areas. In a thin electrode, almost each single particle is constrained by the top and bottom layers simultaneously. Hence, the rearrangement of particles is almost impossible.



*Figure 7. 13 Microstructure of electrode with different electrode thickness (at 15 °C/min)*

It is concluded that by increasing the electrode thickness the connectivity of the electrode can be enhanced. However, increase in electrode thickness leads to an increase in the overall size of the MLCC chips and consumption of electrode materials. This is clearly not an option that the MLCC industry can adopt. Still, the electrode thickness should be carefully designed to obtain acceptable level of electrode discontinuities.

### **7.8 Retarding effect of the inclusions**

To investigate the effect of the inclusions on the electrode discontinuity, sintering of the multilayers with pure Ni electrode and Ni/BT composite electrode were compared. Figure

7.14(b) shows the composite electrode ( $D = 0.55$ ) containing 10 vol. % 50 nm mono sized BT inclusions. Figure 7.3(a) shows the pure electrode obtained by taking out the BT inclusions ( $D = 0.50$ ). Thus, the two electrodes have the same packing of Ni particles. The sintering was conducted from 700 to 1050 °C at a heating rate of 15 °C/min.

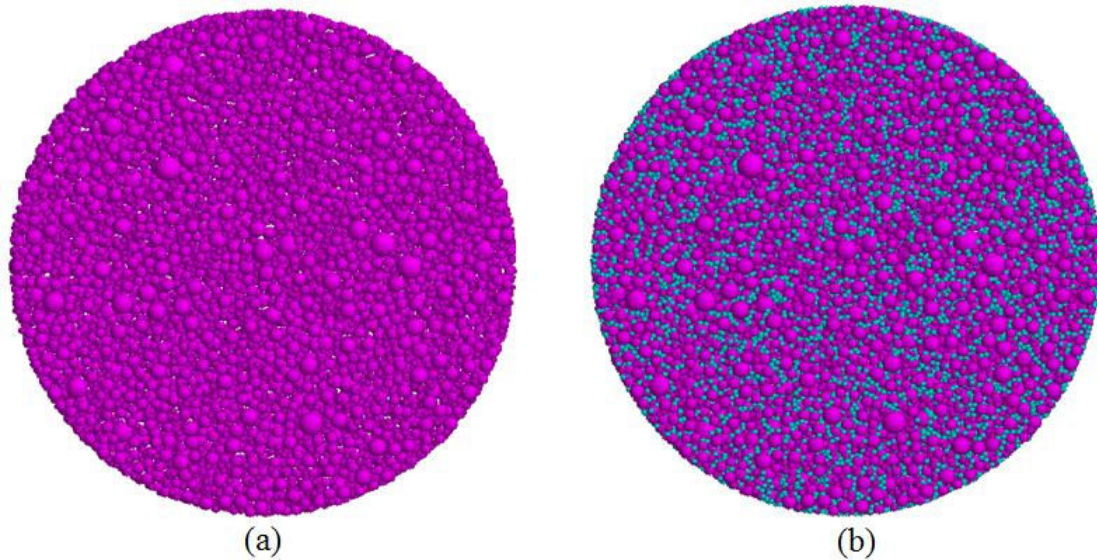


*Figure 7. 14 Green microstructures of pure Ni electrode (a) and Ni/BT composite electrode with 10 vol. % of 50 nm BT inclusions (b)*

Figure 7.15 compares microstructures of electrodes after 10 000 s of isothermal sintering at 1150 °C. Figure 7.15(a) shows the microstructures of the sintered pure Ni electrode with 4.37% of discontinuity. Figure 7.15(b) shows the microstructures of the composite electrode with a discontinuity of 2.75%. Note that the BT inclusions in composite electrode are not represented as part of the electrode, because the inclusions are equivalent to the discontinuities which cannot accommodate charges when a MLCC is operating.

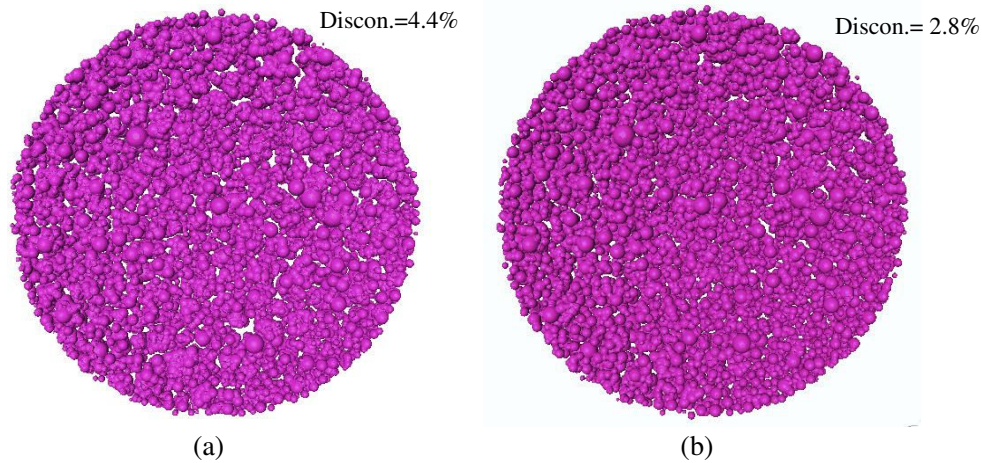


Figure 7. 15 Microstructures of the sintered pure Ni electrode (a) and the composite electrode excluding the BT inclusions

Figure 7.16 plots the discontinuities in the pure Ni and composite electrodes increasing as sintering proceeds.

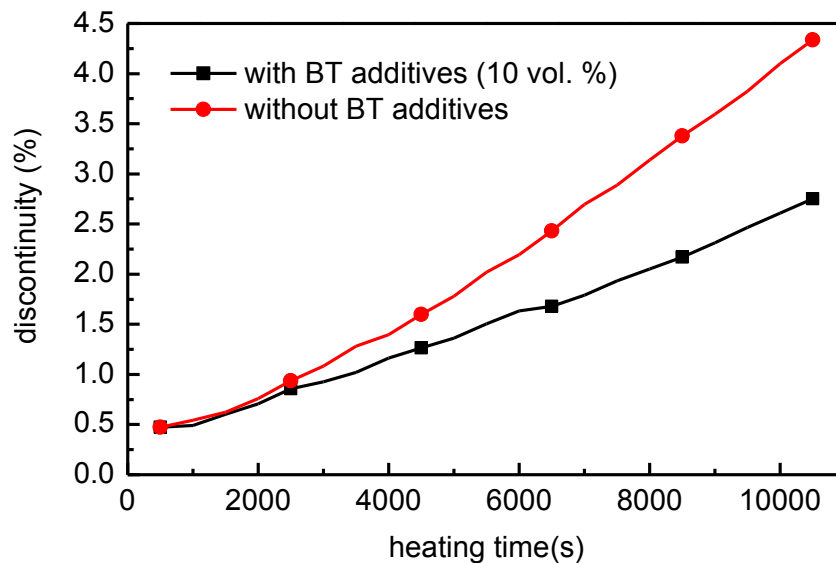


Figure 7. 16 Discontinuity as function of sintering time

The two electrodes start from the same initial discontinuity percentage but then the discontinuity growth in the composite electrode is slower than that in the pure nickel electrode. The discontinuity is attributed to the shrinkage mismatch. The presence of inclusions leads to a decrease of the sintering mismatch between electrode and dielectrics, by retarding the sintering of Ni particles (while the sintering kinetics of BT layer is not changed).

## 7.9 Co-sintering induced anisotropy

As detailed in Chapter 5, anisotropic shrinkage behavior was observed in the co-sintering of multilayers. In this section, a simplified and perfectly packed multilayer system was sintered using DEM to validate the basics of microstructure evolution before considering complex multilayers with heterogeneous microstructures. As Figure 7.17 shows BT/Ni/BT multilayers consist of symmetrically and crystalline-like packed mono size BT and Ni particles.

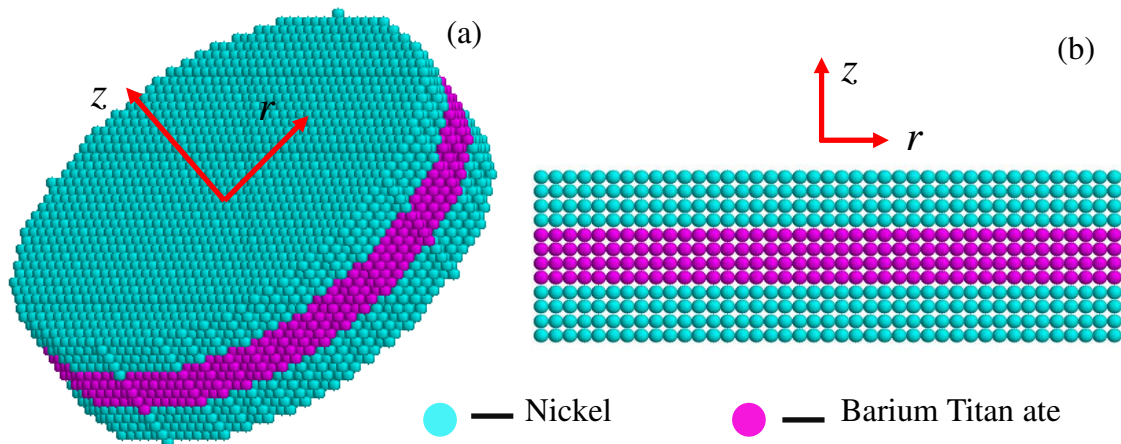


Figure 7. 17 Crystalline-like packed BT/Ni/BT multilayers

The initial contact size is 0.1 (normalized by  $2R$ ). Initial average green density is  $D = 0.55$  (Fig. 7.18(a)). Contact laws developed previously for sintering are further used without modifications. Several significant results can be highlighted (see Fig. 7.18(b)):

First, the electrode is continuous and seems to be able to achieve a full densification. This is due to the homogenous initial microstructures. This again indicates that initial heterogeneity is one of the conditions that lead to electrode discontinuity.

Second, an obvious anisotropy is found in different layers. The pores in BT layers are orientated in parallel to the layer plane while the pores in the Ni layers are orientated perpendicular to the layer plane. In the BT layers, the interface regions are denser than the inner regions; conversely, in the Ni layers, the interface regions are less dense than the inner regions (in Fig. 7.18(b)). Note that density was measured in the middle of the sample as indicated by the selected volume in the dashed lined rectangular volume. This anisotropy is in qualitative agreement with experimental data (see Chapter 5.3.2) and the same arguments can be used to explain this anisotropy. That is, the compressive stresses facilitate the growth of

vertical BT-BT contacts; while the tensile stresses hinder the growth of the vertical Ni-Ni contacts. Figure 7.19(a) shows the evolution of typical horizontal and vertical Ni-Ni and BT-BT contacts evolve as a function of time.

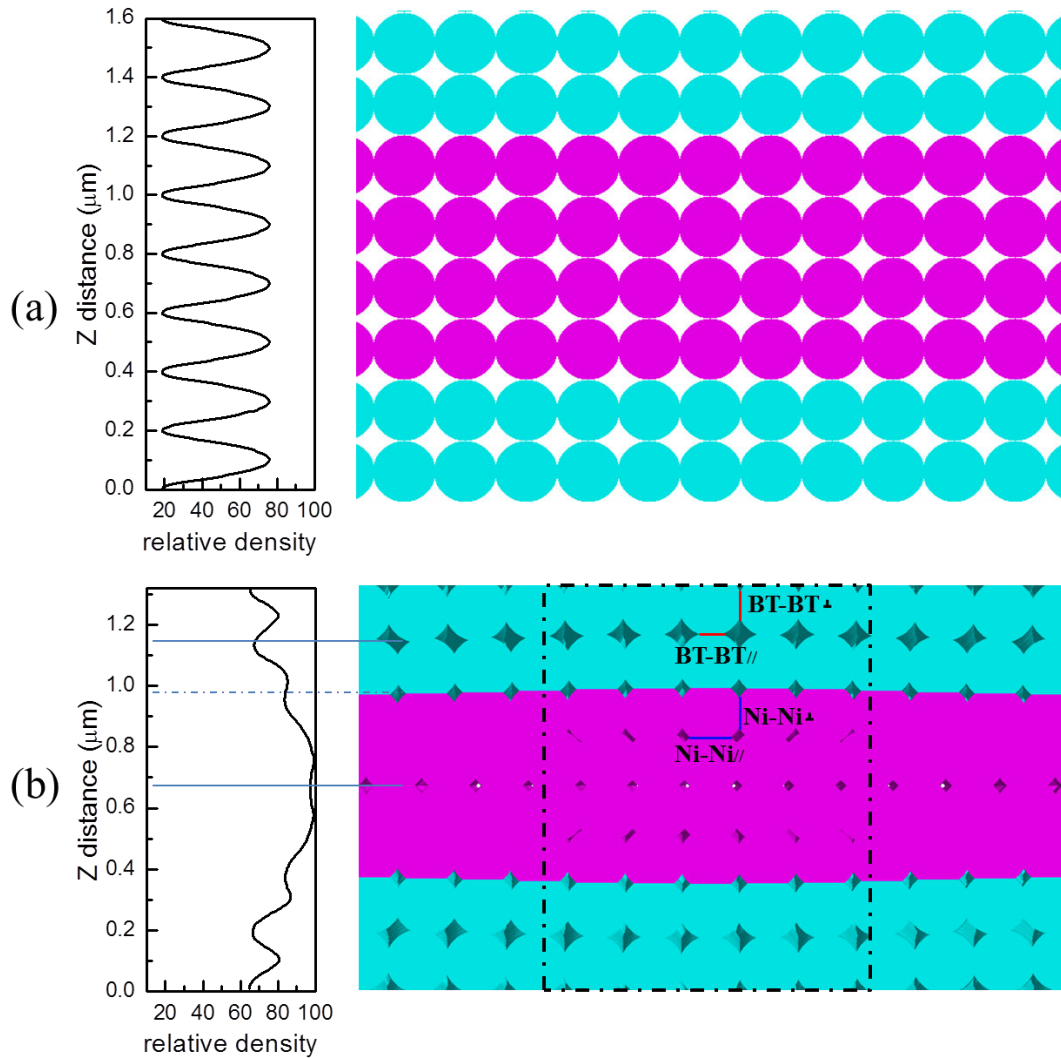


Figure 7. 18 Microstructure and density profile: (a) before sintering (b) after sintering



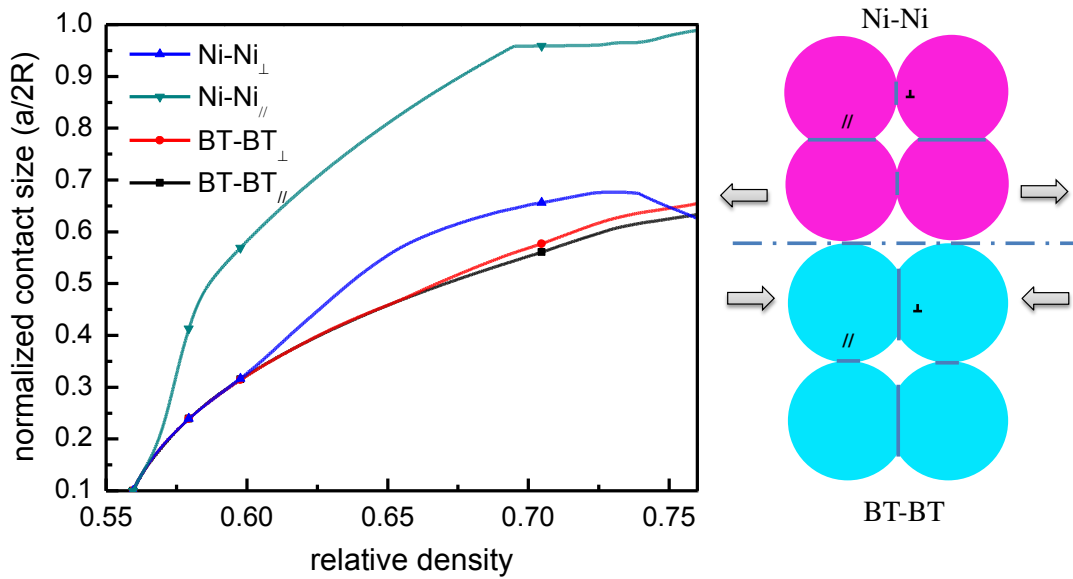


Figure 7. 19 The normalized vertical and horizontal contact sizes of the Ni-Ni contacts and BT-BT contacts evolve as function of density

It is found that the anisotropy is more pronounced for the Ni-Ni contacts than for BT-BT contacts because the Ni sinters earlier and faster.

Figure 7.20 shows contact size distributions (regardless of the orientation of the contacts) of the Ni-Ni contacts and the BT-BT contacts after having achieved different densities. Generally, all the distributions are bimodal. The two modes indicate the horizontal and vertical ( $z$ - direction) contacts. As sintering proceeds, both the vertical and the horizontal contacts grow, resulting in the two peaks' shift to the right. By referring to the average contact size with Figure 7.19(a), the major peak for the Ni-Ni contact distribution indicates the horizontal contacts. Also, it is interesting to notice that the population of the horizontal contacts increases compared with the population of the vertical contacts. this might be because some vertical contacts size decrease at some point ( $D = 0.73-0.74$ ), due to the desintering of the Ni-Ni under tensile stresses (refer to the blue curve in Fig.7.19(a)). For the BT-BT contacts, the major peak represents the horizontal contacts while the minor peak represents the vertical contacts. The population of vertical contacts is comparatively smaller than that of the horizontal contacts. This is because only a small population of particles, which are near the interface (1-2 layers of particles) might be influenced. Note that the absolute number of vertical and horizontal contacts is almost unchanged in Ni and BT layers.

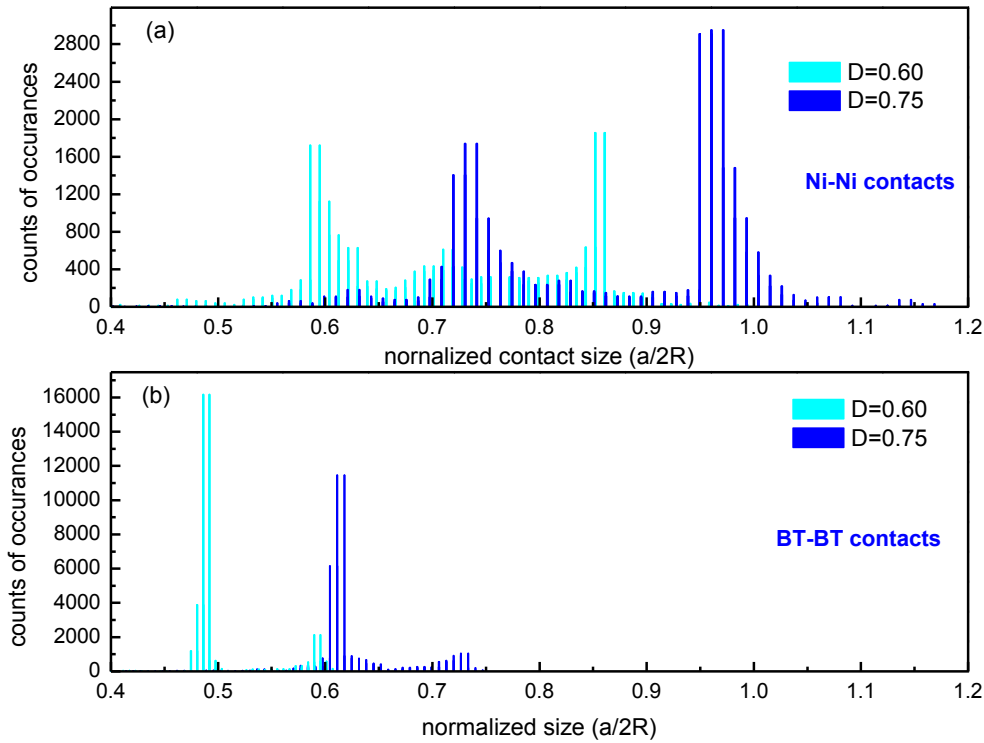


Figure 7.20 Contact size evolution during sintering

## 7.10 Towards more realistic microstructure: coupling with experiments

In the aforementioned simulations, the PSDs of BT and Ni simulated particles were those of experimental data. The packings were randomly generated and then were isostatically compacted to obtain the same green density as measured from experiments. However, we have demonstrated that some inter-agglomerate pores which size are several times the average particle size, exist before sintering. These inter-agglomerate pores are considered to form from the inhomogeneous dispersion of nickel particles and/or the release of the gas due to the burning of the binders at the binder burn out process. It may thus be interesting to be able to generate numerical microstructures from even more realistic conditions.

Thanks to the high-resolution FIB-nT, all single particles, even the nano sized BT additives, can be separated using marker controlled 3D watershed segmentation (see Chapter 5). Assuming that particles can be approximated to spheres, a corresponding numerical sample can be reproduced by locating particles of equivalent radius (see Eq.(5.3)) at the same positions of their centroid.

Figure 7.21 shows how the representative cylindrical BT/Ni/BT sandwiched sample (Fig. 7.21(b)) is duplicated from its real microstructure (Fig. 7.21(a)).

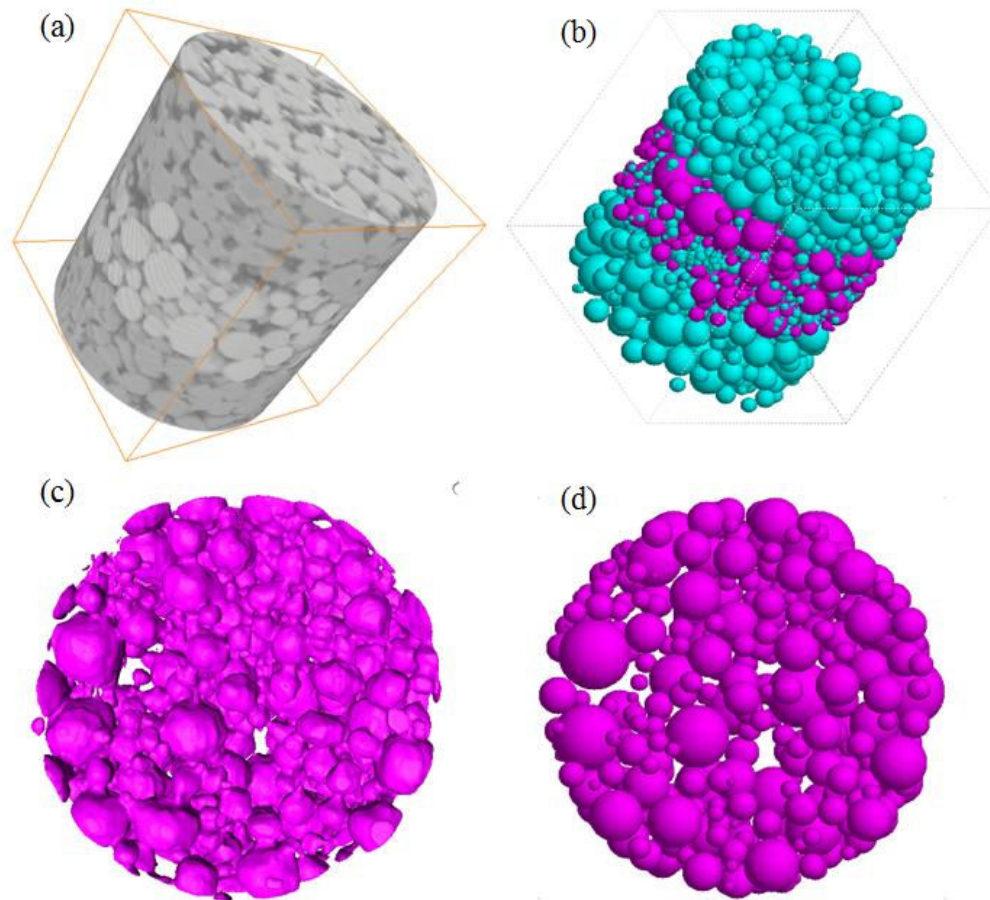


*Figure 7. 21 (a) Cylinder sample extracted from FIB-nT; (b) equivalent numerical model; (c) initial microstructures of the Ni electrode; (d) equivalent numerical model*

Note that the direct processing of nanotomography images into numerical microstructures causes abnormal initial inter-particle contacts as shown in the ellipses in Figure 7.22(a). This is because real particles have irregular shape. Simple intersecting spheres overestimate the size of these contacts. Conversely, some contacts that existed in the real sample disappear from the numerical sample.

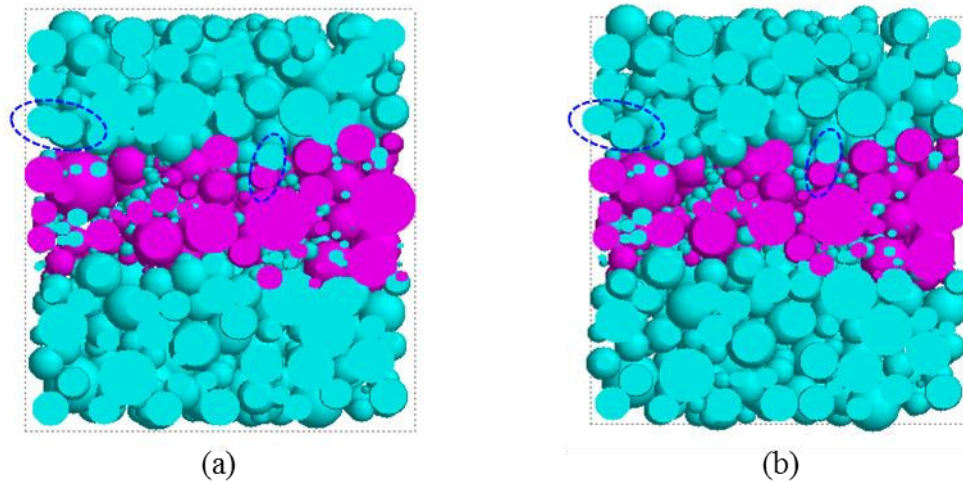
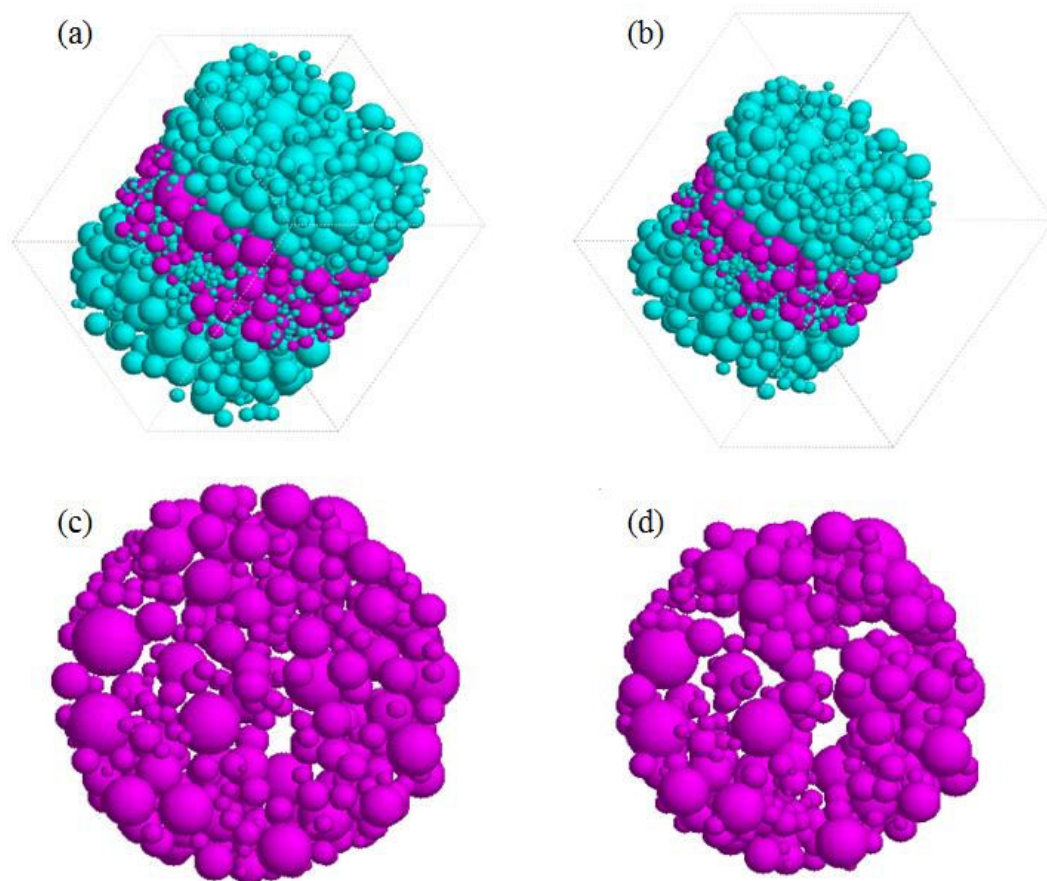


Figure 7.22 Rearrangement of particles after relaxation process

The sintering behavior of these direct fitted green microstructures with abnormal initial contacts can be quite different from the real situation. Thus, an unloading process was simulated to release the stresses originating from the abnormal overlapping of particles. After a relaxation, reasonable initial relative contact size (0.1) was obtained (Fig. 7.22(b)). Ni packing was not rearranged so much due to the almost spherical nature of the Ni particles. In that case, the numerical Ni packing replicates correctly the real packing and initial inter-agglomerate pores. On the other hand, in the BT layers, significant rearrangement of BT particles was observed in the BT layers during the relaxation treatment. Since the BT particles act primarily as a constraining substrate and do not densify much, we consider that the proposed method leads to a realistic microstructure.

Figure 7.23 shows microstructures before and after sintering during the standard heating stage. Discontinuous areas in the sintered electrode clearly originate from the initial inter-agglomerate pores, which can be considered as initial defects. It may also be observed that large initial defects lead to significant discontinuities (Fig. 7.23(d)). In any case, the findings from these simulations that use numerical microstructures originating from experimental data confirm those from the fully numerical processed microstructures.



*Figure 7. 23 Microstructures of electrode before and after sintering (nano additives of BT have been removed for clarity)*

## **7.11 Conclusions**

We have described in this chapter DEM simulations of co-sintering of BT/Ni/BT multilayers during the heating stage. This stage is believed to be critical for the initiation of discontinuities. The effects of inclusions, heating rate, green density, electrode thickness and of the rearrangement of particles have been investigated. The following conclusions can be made:

(1) Intrinsic heterogeneities (inter-agglomerate pores) are the origins of discontinuities in the electrode. It was shown that a theoretically perfectly homogenous electrode can develop a continuous and dense microstructure, even in the presence of the adjacent constraining BT layers. However, a heterogeneous electrode can also achieve full densification in the absence of external constraints. Therefore, the existence of heterogeneities and the presence of

constraining conditions are the necessary conditions for the formation of large electrode discontinuities.

(2) Electrode discontinuities can be lessened by the introduction of inclusions, which retard the densification of electrode materials.

(3) A fast heating can reduce the formation of the discontinuities as the sintering mismatch between electrode and dielectric is reduced.

(4) The electrode thickness should be carefully designed to obtain continuous, homogenous layer. A maximal particle size of 1/10 of the average layer thickness seems to be a good compromise.

(5) The green density of electrode should be optimized. In general, it is always disadvantageous to start with a too porous electrode, since more pores lead to more heterogeneities. The electrode should not be too dense so that a fast densification of electrode materials is avoided. It is likely that the condition of a too dense green electrode is hardly met in real industrial settings.

(6) Particle rearrangement of electrode powders should improve the connectivity of the electrode.



## Chapter 8

# Conclusion and perspectives

### 8.1 General conclusions

Multilayer ceramic capacitors (MLCCs), as the most widely used passive components in the electronics devices, face the problem of electrode discontinuity (uncovered ratio of sintered electrode) which forms during the co-firing process. This challenge becomes more important as the size of the MLCCs steadily decrease due to miniaturization. Ni-electrode BT based MLCCs, which account for 95% of the MLCC market, have been considered in this work.

In comparison with conventional post-sintering 2D sectioning methods, nondestructive X-ray nano computed tomography (X-ray nCT) was utilized to comprehend the evolution mechanism of the electrode discontinuity. Synchrotron X-ray nCT characterization was conducted at the Beamline 32-IDC of the Synchrotron Advanced Photon Source (Argonne National Laboratory, USA). X-ray nCT characterizations of initial and sintered microstructures of a representative cylindrical volume ( $\text{\O}20 \mu\text{m} \times 20 \mu\text{m}$ ) extracted from a Ni-MLCC chip using FIB machining indicate that the final discontinuities are linked to the initial heterogeneities already present in the green state. In-situ X-ray imaging of the sintering of a cylindrical Pd-MLCC sample prepared by the same routine, was carried out to refine the missing data taken during in the ex-situ observation of the sintering of the Ni-MLCC sample. It is confirmed that the discontinuities of the electrode originate from the initial existing heterogeneities, represented by the inter-agglomerate porous and low density regions. These discontinuities form during the heating ramp due to the sintering shrinkage mismatch between electrodes and dielectrics.

Correlative studies on green and sintered MLCCs (including the one imaged by X-ray nCT) were carried out using high resolution ( $5 \times 5 \times 5 \text{ nm}^3$ ) FIB-nT.

These comparisons are very informative and show that:

- (1) The current spatial resolution (30 nm) of the X-ray nCT is sufficient to study pore evolution and the formation of electrode discontinuities.



- (2) Particulate characteristics, such as particle (pore) size, particle (pore) size distribution can be quantitatively analyzed, providing realistic input for the DEM simulations.

These multi-scale characterizations using X-ray nCT and FIB-nT have shed light on comprehension of the anisotropic sintering behavior and microstructure evolutions during the co-sintering of multilayered systems. This knowledge is not limited to the MLCCs, and can be extended to SOFCs, H/LTTCs, and gas separation membranes, etc. General conclusions are:

- (1) Due to the sintering kinetics mismatch, compressive stresses developed near the interfacial region on the slowly densifying layer side and facilitate the sintering of particles preferentially in the layer plane, resulting in preferential growth of the vertical contacts.
- (2) Conversely, on the fast-densifying side, the tensile stresses can hinder the sintering in the layer plane, resulting in preferential growth of the horizontal contacts.
- (3) Density gradient was observed due to this anisotropic sintering behavior. In the slowly densifying layer, the interface is denser than the inner regions; in the fast-densifying layer, the interface is less dense than the inner regions.

As it has been revealed in experiments (Chapter 3 and 4), discontinuities have formed already during the heating stage. The Discrete Element Method (DEM) is a powerful tool to study the microstructure evolution during this stage. We consider that in the early stage of sintering of Ni/BT MLCCs, Ni sinters earlier and faster than BT, and that BT shows negligible shrinkage by the end of the heating ramp.

The proposed model was first tested on the Ni/BT composite material. The effects of the size, the volume fraction and the dispersion degree (aggregates) of BT additives were investigated. The retardation effect of the inclusions on the sintering of a nickel matrix has been documented:

- (1) The retardation effect increases as the inclusion size decreases;
- (2) The retardation effect increases as the inclusion volume fraction increases;
- (3) For a given size and a given volume fraction of inclusions, a good dispersion of the inclusions can enhance the retardation effect.

Sintering kinetics is tuned by controlling the size, the volume fraction (which fits to micromechanical previously established) and dispersion degree of the inclusions.

The DEM simulations were also applied to the sintering of BT/Ni/BT multilayers. Particle size and size distribution measured from the experiments were used as inputs for the particle properties. The comparison of the free sintering of a mono electrode layer with the constrained sintering of a sandwiched Ni electrode shows that the presence of constraints is a necessary condition for the appearance of discontinuities. However, a second necessary condition is the existence of an initial heterogeneity. In a real particulate system, this second condition is always met.

The qualitative conclusions that are found from experimental observations and from detailed simulations at the particle length scale agree with each other.

It has been demonstrated that the introduction of 10 vol.% BT inclusions into the Ni electrode leads to a reduction of electrode discontinuity. A series of DEM simulations on different samples and conditions have been carried out to suggest possible ways to optimize parameters for producing MLCC chips with lower electrode discontinuity. The following conclusions have been achieved:

- (1) Fast heating rates are beneficial to obtain lower electrode discontinuity. During the heating stage, the electrodes sinter significantly while the dielectrics hardly densify. The shorter the heating ramp, the less sintering mismatch is accumulated and hence less discontinuity.
- (2) An optimum green density should be targeted in the electrode. Loose green packing of the electrode must be avoided since it can lead to high discontinuity due to higher probability of having initial heterogeneity. A too high green density may also lead to a larger sintering mismatch, as the coordination number and sintering potential are increased.
- (3) The electrode thickness should be carefully designed to obtain electrode with acceptable discontinuity level. The constraints are transmitted via the interfaces through a few layers of particles. So the thinner the electrode layers are in comparison with the particle size, the stronger the effect of the constraint is.

- (4) The presence of initial heterogeneity contributes significantly on the final discontinuity in the electrode.

### **8.2 Recommendations**

Based on our findings from both experiments and numerical simulations, we may propose some suggestions to manufacturers to improve the MLCC fabrication process.

- **To produce MLCC green chips with homogenous packing in electrode.**

- (1) Use of electrode metal powders with narrow particle size distributions should help to achieve a homogenous packing in electrode.
- (2) Good dispersion of metal powders and ceramic inclusions should reduce the amount of initial heterogeneities.
- (3) Green density of electrode should be optimized. Balance between sintering kinetics and initial heterogeneity should be achieved.
- (4) Electrode thickness should be optimized to balance electrode discontinuity and the MLCC chip's size and consumption of metal.
- (5) Smoothness of the dielectric sheets is important for printing smooth electrodes.
- (6) Binder burn out process should be carefully conducted to release the gas slowly and avoid residual pores.

- **To optimize the firing temperature profile**

- (1) Reducing the temperature and dwelling time at the second BBO process should reduce the discontinuity formation. Binders with lower decomposition temperature need to be developed.
- (2) Fast heating rates can be utilized but may lead to potential thermal cracks.
- (3) Dwelling time should be minimized to let the material obtain sufficient mechanical and physical properties but not allow the electrode to deform and swell.

### **8.3 Research Perspectives**

- **2D X-ray imaging and 3D tomography**

X-ray imaging as a non-destructive method is an excellent technique to study the microstructure evolutions during sintering. Currently, time-resolved 2D X-ray imaging

(radiography) is available at most synchrotron beam lines equipped with CCD (scanning time few seconds) or CMOS (scanning time *ms*) detectors. However, the projected images are insufficient for accurate quantification in space. Fast X-ray micro Computed Tomography ( $\mu$ CT) with CMOS detectors allows for fast 3D data acquisition with  $512 \times 512$  pixels (ESRF) within 10s. This ultrafast X-ray  $\mu$ CT should be qualified as a time resolved tool to study sintering at micro-scale. In the current study, nanotomography is required to investigate submicron and nano scale powders. However, to date, the only available synchrotron X-ray nCT (Sector 32-IDC) with high-temperature measurement capability is located at APS and takes 20-30 min for each 3D data acquisition scanning with a CCD detector.

Thus, combination of in-situ 2D imaging and ex-situ X-ray nCT is a compromise. In addition, high resolution FIB-nT can be used as a correlative method.

- **Coupling of tomography and DEM simulations**

In the case of a direct coupling, MLCC samples should consist of micro-scale particles, which are decomposable with current ultrafast X-ray  $\mu$ CT. The initial microstructure is fitted for DEM simulation input. DEM simulations are performed using the same experimental conditions and the same materials properties. Finally, the in-situ reconstructed 3D microstructure and DEM simulated microstructure can be directly compared and correlated.

In the case of an indirect coupling, in the presence of nano scale particles, the destructive FIB-nT is used to obtain the 3D green microstructure and then is transformed to the DEM model. The simulation results can be compared with additional sintered MLCC sample.

In both case, the DEM simulations face transformation issue. That is the fitted packing has different contact statistics. One ultimate solution is to use irregular shape elements that are duplicated from the tomographic data. Another compromise is to introduce an unloading and arrangement process. In this sense, the direct comparison is in fact an indirect one.

One possible use of DEM simulation, which does not require extensive experimental input, is the optimization of the particle size distribution in the Ni layer (both for Ni and BT additives). Simulations may provide an optimum for green density and initial heterogeneity content.

- **Multi-scale modeling**

### *Conclusion and perspectives*

---

In this DEM simulation study, only sintering during the heating stage was modeled. As experiment shows, once the sintering temperature of dielectric is reached, the ceramic particles start to sinter while the metal electrodes are almost fully dense. At this point, it is inappropriate to simulate the continuum electrode materials using DEM simulation. At this point, simulations using coupling between FEM (for the Ni layer) and DEM (for the BT layer) may lead to new insight in the MLCC process.

# Appendix A

Based on clear interfaces at inclusion-matrix contacts observed in sintered metal or ceramic matrix composites [52, 215], we assume that unlike the sintering neck formed at the matrix-matrix contact, a nearly flat surface is formed at the inclusion-matrix contact on the matrix particle side (Fig. A1). The outer surface of this plateau is of axial length  $\rho$ , which is also assumed to be the radius of curvature in the axial direction. The axial length  $\rho$  is assumed to approximate to indentation  $h$  [213].

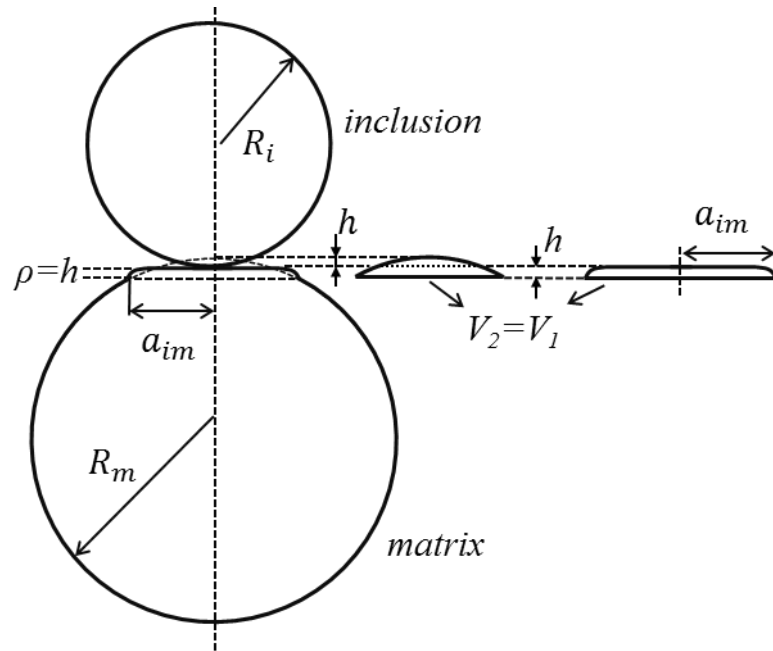


Figure A.1 inclusion-matrix contact model

The cylindrical plateau  $V_1$  and spherical cap  $V_2$  with height of  $2h$  ( $= h+\rho$ ) are calculated as:

$$V_1 = \pi a_{im}^2 h \quad (\text{A.1})$$

$$V_2 = \pi(2h)^2 \left( R_m - \frac{1}{3} \cdot 2h \right) \quad (\text{A.2})$$

Using mass conservation, the volumes  $V_1$  and  $V_2$  are equal, which leads to:

$$a_{im}^2 = 4R_m h - \frac{8}{3} h^2, \quad (\text{A.3})$$

Neglecting the  $h^2$  term ( $h \ll a_{im}$ ) leads to Eq. (6.14).



## Appendix B

For sintering contacts, the contact radius  $a$  can be estimated using Coble's law [213] (see Figure B.1). The outer surface of the neck is tangent to the two spheres with radius of  $\rho_1$  and  $\rho_2$ . The contact radius is given by:

$$a^2 = 4 \frac{R_1 R_2}{R_1 + R_2} (h_1 + h_2) \quad (\text{B.1})$$

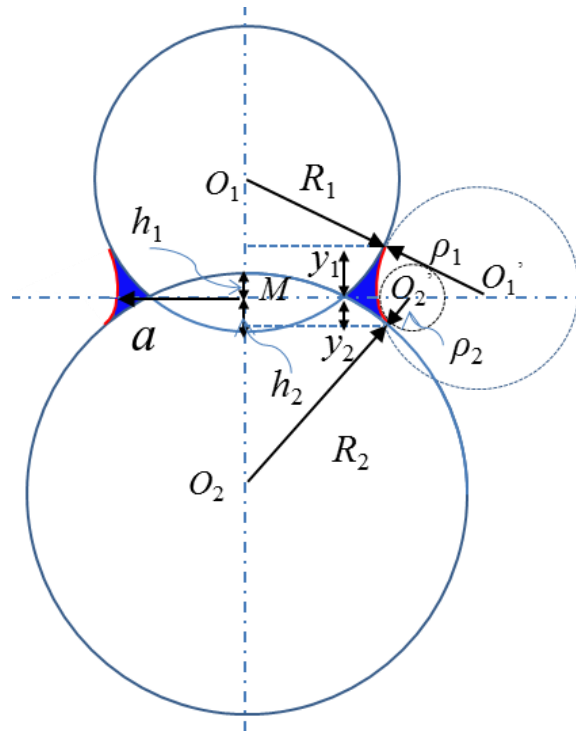


Figure B.1 Contact model by Coble's Law

Using simple geometric relations in triangles  $\Delta O_1 M O_1'$  and  $\Delta O_2 M O_2'$ :

$$(R_1 - h_2)^2 + (a + \rho_1)^2 = (R_1 + \rho_1)^2 \quad (\text{B.2})$$

$$(R_2 - h_1)^2 + (a + \rho_2)^2 = (R_2 + \rho_2)^2 \quad (\text{B.3})$$

Solving Eq. (B.2) and Eq. (B.3) leads to;

$$\rho_1 = \frac{a^2 - 2R_1 h_2 + h_2^2}{2R_1 - 2a} \quad (\text{B.4})$$

$$\rho_2 = \frac{a^2 - 2R_2 h_1 + h_1^2}{2R_2 - 2a} \quad (\text{B.5})$$

Using the Similar Triangles Theorem, we obtain:



$$y_1 = \frac{(R_1 - h_2)\rho_1}{R_1 + \rho_1} \text{ (B.6)}$$

$$y_2 = \frac{(R_2 - h_1)\rho_2}{R_2 + \rho_2} \text{ (B.7)}$$

Which is used to obtain the final expression of the neck radius.

# Appendix C

According to the Wicksell's classic work in 1925 [159], the frequency of particle size from the 2D section of mono-sized partilce sample (Fig. C.1) follows:

$$f(r) = \frac{r \delta r}{R \sqrt{(R^2 - r^2)}} \quad (C.1)$$

Hence, the accumulative frequency is given by:

$$G(r) = \int_0^r f(r) dr = \int_0^r \frac{r dr}{R \sqrt{(R^2 - r^2)}} = 1 - \sqrt{1 - \left(\frac{r}{R}\right)^2} \quad (C.2)$$

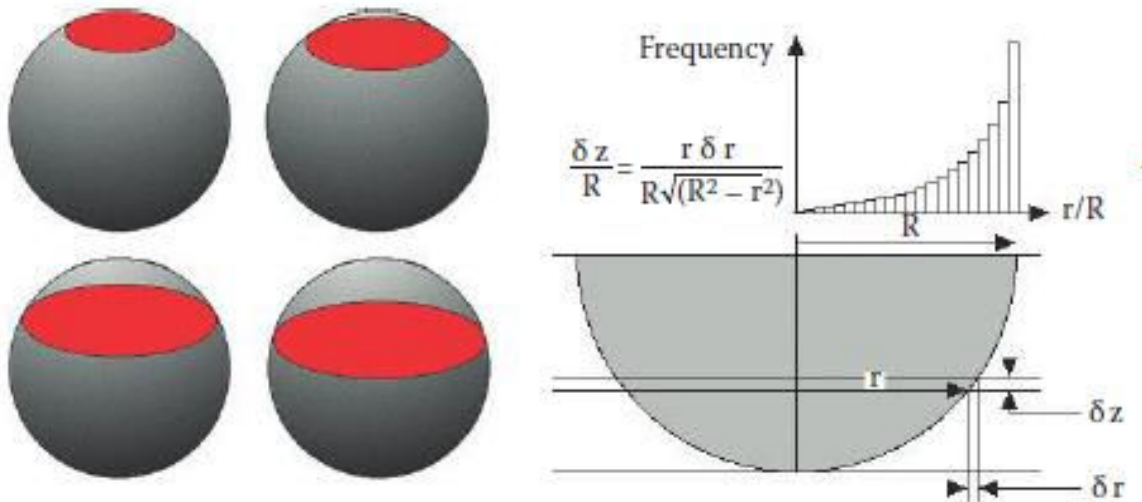


Figure C.1 Sectioning a sphere randomly produce a distribution of circle sizes, which can be calculated from analytical geometry

For the actual size (3D) distribution of spheres (Fig. C.2(a)), we can assume that spheres which are in the same bin size (i.e., Class  $N_i$ ) are mono sized. The corresponding cross-sectioned 2D circle size of these spheres belonging to Class  $N_i$  will distribute according to Eq. (C.1). And the frequency is distributed as Figure C.2(b).

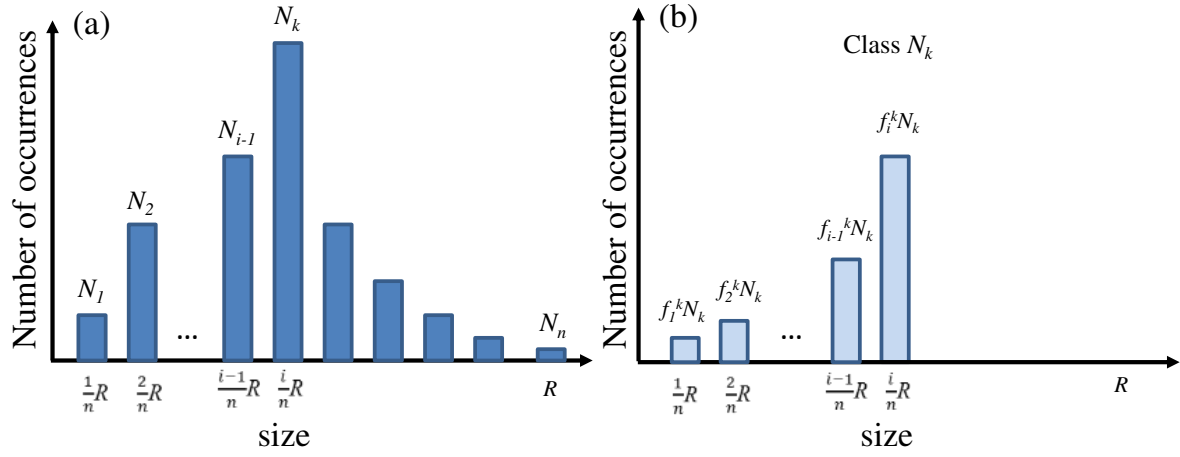


Figure C.2 Practice of the sectioning of each class of the spheres

$$\sum_{i=1}^k f_i^k = f_1^k + f_2^k + \dots + f_{i-1}^k + f_i^k = 1 \quad (C.3)$$

$$f_i^k = 1 - G\left(\frac{i-1}{k}R\right) = \sqrt{1 - \left(\frac{i-1}{i}\right)^2} \quad (C.4)$$

$$f_{i-1}^k = G\left(\frac{i-1}{k}R\right) - G\left(\frac{i-2}{k}R\right) = \sqrt{1 - \left(\frac{i-2}{i}\right)^2} - \sqrt{1 - \left(\frac{i-1}{i}\right)^2} \quad (C.5)$$

$$f_1^k = G\left(\frac{1}{k}R\right) = 1 - \sqrt{1 - \left(\frac{1}{k}\right)^2} \quad (C.6)$$

This scheme applies to all other classes of particles. Finally, for the 2D sphere size distribution that has the same size range and bin size:

$$N'_k = f_i^k N_k + f_i^{k+1} N_{k+1} + \dots + f_i^{n-1} N_{n-1} + f_i^n N_n \quad (C.7)$$

For the final frequency distribution of the 2D sectioned size is the sum of  $N$  sets of the classic distributions:

$$\begin{bmatrix} N'_1 \\ N'_2 \\ N'_3 \\ N'_4 \\ \vdots \\ N'_n \end{bmatrix} = \begin{bmatrix} 1 & 1 - \sqrt{1 - \left(\frac{1}{2}\right)^2} & 1 - \sqrt{1 - \left(\frac{1}{3}\right)^2} & 1 - \sqrt{1 - \left(\frac{1}{4}\right)^2} & \dots & 1 - \sqrt{1 - \left(\frac{1}{n}\right)^2} \\ 0 & \sqrt{1 - \left(\frac{1}{2}\right)^2} & \sqrt{1 - \left(\frac{1}{3}\right)^2} - \sqrt{1 - \left(\frac{2}{3}\right)^2} & \sqrt{1 - \left(\frac{1}{4}\right)^2} - \sqrt{1 - \left(\frac{2}{4}\right)^2} & \dots & \sqrt{1 - \left(\frac{1}{n}\right)^2} - \sqrt{1 - \left(\frac{2}{n}\right)^2} \\ 0 & 0 & \sqrt{1 - \left(\frac{2}{3}\right)^2} & \sqrt{1 - \left(\frac{2}{4}\right)^2} - \sqrt{1 - \left(\frac{3}{4}\right)^2} & \dots & \sqrt{1 - \left(\frac{2}{n}\right)^2} - \sqrt{1 - \left(\frac{3}{n}\right)^2} \\ 0 & 0 & 0 & \sqrt{1 - \left(\frac{3}{4}\right)^2} & \dots & \sqrt{1 - \left(\frac{n-1}{n}\right)^2} \\ \vdots & \vdots & \vdots & \vdots & \ddots & \vdots \\ 0 & 0 & 0 & 0 & \dots & \sqrt{1 - \left(\frac{n-1}{n}\right)^2} \end{bmatrix} \times \begin{bmatrix} N_1 \\ N_2 \\ N_3 \\ N_4 \\ \vdots \\ N_n \end{bmatrix} \quad (C.8)$$

# Author's contribution

## Peer-reviewed articles

- [1]. Z. Yan, O. Guillon, S. Wang, C.L. Martin, C-S. Lee, D. Bouvard, Synchrotron x-ray nano-tomography characterization of the sintering of multilayered systems. *Appl. Phys. Lett.* 100(2012)263107.
- [2]. Z. Yan, C.L. Martin, O. Guillon, D. Bouvard, Effect of size and homogeneity of rigid inclusions on the sintering of composites, *Scripta Mater.* 69 (2013) 327-330
- [3]. Z. Yan, O. Guillon, C.L. Martin, S. Wang, C-S. Lee, D. Bouvard, In-situ synchrotron x-ray microscopy of sintering of multilayers. *Appl. Phys. Lett.* 102(2013)223107
- [4]. Z. Yan, O. Guillon, C.L. Martin, S. Wang, C-S. Lee, D. Bouvard, correlative studies on constrained sintering of Multilayer Ceramic Capacitors using X-ray and FIB-SEM. *Acta Mater.* 2013 (to be submitted)
- [5]. Z. Yan, C.L. Martin, O. Guillon, D. Bouvard, Discrete element simulations on constrained sintering of Multilayer Ceramic Capacitors. *J. Am. Ceram. Soc.* 2013 (to be submitted)

## Conferences

- [1]. Z. Yan, C.L. Martin, O. Guillon, R.K. Bordia, Discrete element simulation: a tool to model sintering at the particle length scale, 12<sup>th</sup> International Conference on Ceramic Processing Science. 4-7 Aug, 2013, Portland, USA (Invited plenary talk, presented by C.L. Martin)
- [2]. Z. Yan, O. Guillon, S. Wang, C.L. Martin, C-S. Lee, D. Bouvard. Sintering of Ni-based electrode in multilayer ceramic capacitors: numerical simulations and experiments, 2012 Powder Metallurgy World Congress & Exhibition. 14-18 Oct, 2012, Yokohama, Japan (Oral)
- [3]. Z. Yan, O. Guillon, S. Wang, C.L. Martin, C. Lee, D. Bouvard. Microstructural evolution during co-sintering of multi-layer ceramic capacitors: coupling of simulation and experiment. International Conference on Sintering, 28 Aug-1 Sept, 2011, Jeju, South Korea (Poster)
- [4]. X. Liu, Z. Yan, C.L. Martin. Discrete Element Simulation of sintering: Towards more

*Author's contributions*

---

realistic microstructures, International Conference Sintering 2011, 28 Aug-1 Sept, 2011, Jeju, South Korea (Oral)

# References

- [1] A Moulson, J. M. Herbert, *Electroceramics: Materials, properties, applications*, John Wiley & Sons, Chichester, 2003.
- [2] D. M. Zogbi, *Capacitors: World Markets, Technologies & Opportunities: 2012-2017(2012)*, Paumanok Publications
- [3] Technavio, *Global Multilayer Ceramic Capacitor Market 2010-2014*, 2011
- [4] H. Kishi, Y. Mizuno, H. Chazono, Base-Metal Electrode-Multilayer Ceramic Capacitors: Past, Present and Future Perspectives, *Jpn. J. Appl. Phys.*, 42 (2003) 1-15.
- [5] M.-J. Pan, C. A. Randall, A brief introduction to ceramic capacitors. *Electrical Insulation Magazine*, IEEE 26 (2010) 44-50.
- [6] H. Takagi, History and Future Prospect of Electro-ceramics in Japan and Asia, in: *IMAPS/ACerS 8th International CICMT Conference and Exhibition*, Erfurt, Germany, 2012.
- [7] M. Randall, D. Skamser, T. Kinard, J. Qazi, A. Tajuddin, S. Troler-McKinstry, C. Randall, S. W. Ko, T. Decbakupt, *Thin Film MLCC, CARTS 2007 Symposium Proceedings*, Albuquerque, NM, 2007
- [8] <http://www.murata.com>, accessed 13.05.2013
- [9] D. D. Liu, M. J. Sampson, Reliability evaluation of base-metal-electrode multilayer ceramic capacitors for potential space applications, *CARTS proceed.*, (2011) 45-63.
- [10] [http://commons.wikimedia.org/wiki/File:BaTiO3\\_oxygen\\_coordination.png](http://commons.wikimedia.org/wiki/File:BaTiO3_oxygen_coordination.png), accessed 24.05.2013
- [11] <http://www.avx.com/docs/techinfo/mlcmt.pdf>, accessed 01.05.2013
- [12] K. Kinoshita, A. Yamaji, Grain-size effects on dielectric properties in barium titanate ceramics, *J. Appl. Phys.*, 47 (1976) 371-373.
- [13] G. Arlt, D. Hennings, G. De With, Dielectric properties of fine-grained barium titanate ceramics, *J. Appl. Phys.*, 58 (1985) 1619-1626.
- [14] M. H. Frey, D. A. Payne, Grain-size effect on structure and phase transformations for barium titanate, *Phys. Rev. B*, 54 (1996) 3158-3168
- [15] D. McCauley, R. E. Newnham, C. A. Randall, Intrinsic Size Effects in a Barium Titanate Glass-Ceramic, *J. Am. Ceram. Soc.*, 81 (1998) 979-987.
- [16] Y. Mizuno, T. Hagiwara, H. Kishi, Microstructural Design of Dielectrics for Ni-MLCC with Ultra-thin Active Layers, *J. Ceram. Soc. Jpn.*, 115 (2007) 360-364.

## References

---

- [17] C.-H. Kim, K.-J. Park, Y.-J. Yoon, M.-H. Hong, J.-O. Hong, K.-H. Hur, Role of yttrium and magnesium in the formation of core-shell structure of BaTiO<sub>3</sub> grains in MLCC, *J. Eu. Ceram. Soc.*, 28 (2008) 1213-1219.
- [18] H. Kishi, Y. Okino, M. Honda, Y. Iguchi, M. Imaeda, Y. Takahashi, H. Ohsato, T. Okuda, The effect of MgO and rare-earth oxide on formation behavior of core-shell structure in BaTiO<sub>3</sub>, *Jpn. J. Appl. Phys.*, 36 (1997) 5954-5957.
- [19] H. Chazono, M. Fujimoto, Sintering characteristics and formation mechanisms of core-shell structure in BaTiO<sub>3</sub>-Nb<sub>2</sub>O<sub>5</sub>-Co<sub>3</sub>O<sub>5</sub> ternary system, *Jpn. J. Appl. Phys.*, 34 (1995) 5354-5359.
- [20] Y. Fujikawa, Y. Umeda, F. Yamane, Analysis on the sintering process of X7R MLCC materials, *J. Jpn. Soc. Powder Powder Metall.*, 51 (2004) 839-844.
- [21] C. S. Chen, C. C. Chou, I. N. Lin, Microstructure of X7R type basemetal-electroded BaTiO<sub>3</sub> capacitor materials co-doped with MgO/Y<sub>2</sub>O<sub>3</sub> additives, *J. Electroceram.*, 13 (2004) 567-571.
- [22] D. Hennings, G. Rosenstein, Temperature-stable dielectrics based on chemically inhomogeneous BaTiO<sub>3</sub>, *J. Am. Ceram. Soc.*, 67 (1984) 249-254.
- [23] C. A. Randall, S. F. Wang, D. Laubscher, J. P. Dougherty, W. Huebner, Structure property relationships in core-shell BaTiO<sub>3</sub>-LiF ceramics, *J. Mater. Res.*, 8 (1993) 871-879.
- [24] S. H. Yoon, J. H. Lee, D. Y. Kim, N. M. Hwang, Core-shell structure of acceptor-rich, coarse barium titanate grains, *J. Am. Ceram. Soc.*, 85 (2002) 3111-3113.
- [25] M. Cannon, Focus on Power: Advancements in Ceramic Capacitors, APEC 2011: Applied Energy and Conversion Conference, 2011
- [26] J. R. Yoon, D. S. Shin, D. Y. Jeong, H. Y. Lee, Control of Connectivity of Ni Electrode with Heating Rates During Sintering and Electrical Properties in BaTiO<sub>3</sub> Based Multilayer Ceramic Capacitors, *Trans. Electr. Electron. Mater.*, 13 (2012) 181-184.
- [27] M. M. Samantaray, A. Gurav, E. C. Dickey, C. A. Randall, Electrode Defects in Multilayer Capacitors Part I: Modeling the Effect of Electrode Roughness and Porosity on Electric Field Enhancement and Leakage Current, *J Am Ceram Soc*, 95 (2012) 257-263
- [28] A. V. Polotai, I. Fujii, D. P. Shay, G.-Y. Yang, E. C. Dickey, C. A. Randall, Effect of Heating Rates during Sintering on the Electrical Properties of Ultra-Thin Ni-BaTiO<sub>3</sub> Multilayer Ceramic Capacitors, *J. Am. Ceram. Soc.*, 91 (2008) 2540-2544.
- [29] A. V. Polotai, G.-Y. Yang, E. C. Dickey, C. A. Randall, Utilization of Multiple-Stage Sintering to Control Ni Electrode Continuity in Ultrathin Ni-BaTiO<sub>3</sub> Multilayer Capacitors, *J. Am. Ceram. Soc.*, 90 (2007) 3811-3817

- [30] J. G. Pepin, W. Borland, P. O'Callaghan, R. J. S. Young, Electrode-Based Causes of Delaminations in Multilayer Ceramic Capacitors, *J. Am. Ceram. Soc.*, 72 (1989) 2287-2291.
- [31] K. Sugimura, K. Hirao, Effect of a BaTiO<sub>3</sub> nanoparticle additive on the quality of thin-film Ni electrodes in MLCC, *J. Ceram. Soc. Jpn.*, 117 (2009) 1039-1043.
- [32] Y. Kinemuchi, S. Uchimura, K. Watari, Centrifugal sintering of BaTiO<sub>3</sub>/Ni layered ceramics, *J. Eu. Ceram. Soc.*, 25 (2005) 2223-2226.
- [33] Y.-I. Shin, K.-M. Kang, Y.-G. Jung, J.-G. Yeo, S.-G. Lee, U. Paik, Internal stresses in BaTiO<sub>3</sub>/Ni MLCCs, *J. Eu. Ceram. Soc.*, 23 (2003) 1427-1434.
- [34] S.-H. Wang, Y.-L. Chai, W.-H. Lee, A novel approach to sintering (Ba,Ca)(Ti,Zr)O<sub>3</sub> multilayer ceramic capacitors with Ni electrodes, *J. Eu. Ceram. Soc.*, 32 (2012) 1711-1723
- [35] J. G. Pepin, High fire multilayer ceramic capacitor electrode technology, *Electronic Components and Technology Conference*, 1991, Atlanta, GA, USA,
- [36] T. Takahashi, Y. Nakano, H. Shoji, H. Matsushita, H. Ogawa, A. Onoe, H. Kanai, Y. Yamashita, Effects of additives on the sintering behavior of the Ni internal electrode of BaTiO<sub>3</sub>-based multilayer ceramic capacitors *Applications of Ferroelectrics: Proceedings of the 11th IEEE International Symposium*, 1998
- [37] Ji-Hun Kang, Dongwon Joo, Hyun-Min Cha, Yeon-Gil Jung, Ungyu Paik, Shrinkage behavior and interfacial diffusion in Ni-based internal electrodes with BaTiO<sub>3</sub> additive, *Ceram. Int.*, 34 (2008) 1487-1494.
- [38] K.S. Weil, E.S. Mast, V.L. Sprenkle, Agglomeration behavior of solid nickel on polycrystalline barium titanate, *Mater. Lett.*, 61 (2007) 4993-4996.
- [39] A. V. Polotai, T.-H. Jeong, G.-Y. Yang, E. C. Dickey, C. A. Randall, Pascal Pinceloup, Abhijit S. Gurav, Effect of Cr additions on the microstructural stability of Ni electrodes in ultra-thin BaTiO<sub>3</sub> multilayer capacitors, *J. Electroceram.* 18 (2007).
- [40] A.V. Polotai, D. P. Shay, G.-Y. Yang, E. C. Dickey, C. A. Randall, in. *Applications of Ferroelectrics*, 17th IEEE International Symposium on the. IEEE, 1 (2008)1-2.
- [41] J.-H. Jean, C.-R. Chang, Effect of Densification Mismatch on Camber Development during Cofiring of Nickel-Based Multilayer Ceramic Capacitors, *J. Am. Ceram. Soc.*, 80 (1997) 2401-2406.
- [42] B.-Y. Yu, W.-C. J. Wei, Defects of Base Metal Electrode Layers in Multi-Layer Ceramic Capacitor, *J. Am. Ceram. Soc.*, 88 (2005) 2328-2331.
- [43] M. N. Rahaman, *Ceramic Processing and Sintering*, 2nd ed, New York, 2003.
- [44] S.-J. L. Kang, *Sintering Densification Grain Growth and Microstructure*, 1st ed, Elsevier Butterworth-Heinemann, Burlington, 2005.



## References

---

- [45] H. Tanaka, A. Yamamoto, J. Shimoyama, H. Ogino, K. Kishio, Strongly connected ex situ MgB<sub>2</sub> polycrystalline bulks fabricated by solid-state self-sintering, *Supercond. Sci. Technol.*, 25 (2012) 115022.
- [46] D. Ravi, D. J. Green, Sintering stresses and distortion produced by density differences in bi-layer structures, *J. Eu. Ceram. Soc.*, 26 (2006) 17-25.
- [47] D. J. Green, O. Guillon, J. Rödel, Constrained sintering: A delicate balance of scales, *J. Eu. Ceram. Soc.*, 28 (2008) 1451-1466.
- [48] R. Raj, R. K. Bordia, Sintering behavior of bi-modal powder compacts, *ACTA METALLURGICA*, 32 (1984) 1003-1019.
- [49] L. C. De Jonghe, M. N. Rahaman, C. H. Hsueh, Transient stresses in bimodal compacts during sintering, *Acta Metall.*, 34 (1986) 1467-1471.
- [50] M. W. Weiser, L. C. D. Jonghe, Inclusion Size and Sintering of Composite Powders, *J. Am. Ceram. Soc.*, 71 (1988) C125-C127.
- [51] W. H. Tuan, E. Gilbert, R. J. Brook, Sintering of heterogeneous ceramic compacts, *J. Mater. Sci.*, 24 (1989) 1062-1068.
- [52] L. Olmos, C. L. Martin, D. Bouvard, Sintering of mixtures of powders: Experiments and modelling, *Powder Technol.*, 190 (2009) 134-140.
- [53] K. Shinagawa, Sintering Stress and Viscosity of Ni/Al<sub>2</sub>O<sub>3</sub> Powder Mixtures, *AIP Conf. Proceed.*, 973 (2008) 22-27.
- [54] R. K. Bordia, G. W. Scherer, On constrained sintering-I: Constitutive model for a sintering body, *Acta Metall.*, 36 (1988) 2393-2397.
- [55] R. K. Bordia, G. W. Scherer, On constrained sintering-III: Rigid inclusions, *Acta Metall.*, 36 (1988) 2411-2416.
- [56] R. K. Bordia, G. W. Scherer, On constrained sintering-II: Comparison of constitutive models, *Acta Metall.*, 36 (1988) 2399-2409.
- [57] G. W. Scherera, Sintering with Rigid Inclusions, *J. Am. Ceram. Soc.*, 70 (1987) 719-725.
- [58] W. Hong, L. R. Dharani, Pressureless Sintering of a Ceramic Matrix with Multiple Rigid Inclusions: Finite Element Model, *J. Am. Ceram. Soc.*, 78 (1995) 1593-1600.
- [59] J. W. Choe, J. N. Calata, G.-Q. Lu, Constrained-film sintering of a gold circuit paste, *J. Mater. Res.*, 10 (1995) 986-995.
- [60] R. K. Bordia, R. Raj, Sintering behavior of ceramic films constrained by a rigid substrate, *J. Am. Ceram. Soc.*, 68 (1985) 287-292.
- [61] G. W. Scherer, T. Garino, Viscous sintering on a rigid substrate, *J. Am. Ceram. Soc.*, 68 (1985) 216-220.

- [62] C. H. Hsueh, Sintering of a ceramic film on a rigid substrate, *Scripta Metall.*, 19 (1985) 1213-1217.
- [63] P. Z. Cai, D. J. Green, G. L. Messing, Constrained densification of alumina/zirconia hybrid laminates, II: viscoelastic stress computation, *J. Am. Ceram. Soc.*, 80 (1997) 1940-1948.
- [64] S.-H. Lee, G. L. Messing, D. J. Green, Warpage Evolution of Screen Printed Multilayer Ceramics During Co-firing, *Key Eng. Mater.*, 264-268 (2004) 321-330.
- [65] J.-C. Chang, J.-H. Jeanw, Camber Development During the Cofiring of Bi-Layer Glass-Based Dielectric Laminate, *J. Am. Ceram. Soc.*, 88 (2005) 1165-1170.
- [66] C. S. Kim, S. J. Lombardow, R. A. Winholtz, Strain-Induced Deformation in Magnesia-Alumina Layered Composites, *J. Am. Ceram. Soc.*, 88 (2005) 2064-2070.
- [67] C. S. Kim, S. J. Lombardow, Effect of Processing on the Microstructure and Induced-Strain Mismatch in Magnesia-Alumina-Layered Composites, *J. Am. Ceram. Soc.*, 89 (2006) 2718-2725.
- [68] O. Guillon, Partial Constrained Sintering of Ceramic Layers on Metallic Substrates: A Comparison Between Modeling and Experiments, *J. Am. Ceram. Soc.*, 94 (2011) 1040-1045.
- [69] J. Chang, O. Guillon, J. Rödel, S.-J. L. Kang, Characterization of warpage behaviour of Gd-doped ceria/NiO-yttria stabilized zirconia bi-layer samples for solid oxide fuel cell application, *J. Power Sources*, 185 (2008) 759-764.
- [70] C. S. Kim, S. J. Lombardo, Curvature and bifurcation of MgO-Al<sub>2</sub>O<sub>3</sub> bilayer ceramic structures, *J. Ceram. Process. Res.*, 9 (2008) 93-96.
- [71] J. M. Heintz, O. Sudre, F. F. Lange, Instability of Polycrystalline Bridges that Span Cracks in Powder Films Densified on a Substrate, *J. Am. Ceram. Soc.*, 77 (1994) 787-791.
- [72] L. E. Khoong, Y. M. Tan, Y. C. Lam, Study of deformation and porosity evolution of low temperature co-fired ceramic for embedded structures fabrication, *J. Eu. Ceram. Soc.*, 29 (2009) 2737-2745.
- [73] O. Guillon, S. Krauß, J. Rödel, Influence of thickness on the constrained sintering of alumina films, *J. Eu. Ceram. Soc.*, 27 (2007) 2623-2627.
- [74] O. Guillon, Microstructural Characterization of Alumina Films During Constrained Sintering, *J. Am. Ceram. Soc.*, 93 (2010) 627-629.
- [75] O. Guillon, R. K. Bordia, C. L. Martin, Constrained Sintering of Ceramic Films and Coatings, in: Z.Z. Fang (Ed.) *Sintering of Advanced Materials*, Woodhead Publishing Ltd., 2011.

## References

---

- [76] A. C. Lewis, D. Josell, T. P. Weihs, Stability in thin film multilayers and microlaminates: the role of free energy, structure, and orientation at interfaces and grain boundaries, *Scripta Mater.*, 48 (2003) 1079-1085.
- [77] K.T. Miller, F. F. Lange, D. B. Marshall, The instability of polycrystalline thin films: Experiment and theory, *J. Mater. Res.*, 5 (1990) 151-160.
- [78] <http://www.horiba.com>, accessed 4.5.2013
- [79] H. P. Myers, *Introductory Solid State Physics*, Taylor & Francis, 2002.
- [80] <http://www.microscopy.ethz.ch/bragg.htm>, accessed 11.09.2013
- [81] [http://www.isc.fraunhofer.de/uploads/media/TOM-AC\\_english\\_01.pdf](http://www.isc.fraunhofer.de/uploads/media/TOM-AC_english_01.pdf), accessed 8.25.2013
- [82] D. M. Frame, *Microstructural development and the evolution of defects in constrained and sinter-forged ceramics*, University of Washington, PhD, 2006
- [83] F. Mees, *Applications of X-ray computed tomography in the geosciences*, Geological Society of London, London, 2003.
- [84] S. Bugani, M. Camaiti, L. Morselli, E. V. Castele, P. Cloetens, K. Janssens, x-ray computed tomography as a non-destructive tool for stone conservation, in: *9th International Conference on NDT of Art*, Jerusalem Israel, 2008.
- [85] P. A. Midgley, E. P. W. Ward, A. B. Hungria, J. M. Thomas, *Nanotomography in the chemical, biological and materials sciences*, *Chem. Soc. Rev.*, 36 (2007) 1477-1494.
- [86] S. Vasic, B. Grob ty, J. Kuebler, T. Graule, L. Baumgartner, X-ray computed micro tomography as complementary method for the characterization of activated porous ceramic preforms, *J. Mater. Res.*, 22 (2007) 1414-1424.
- [87] J. Chen, C. Wu, J. Tian, W. Li, S. Yu, Three-dimensional imaging of a complex concaved cuboctahedron copper sulfide crystal by x-ray nanotomography, *Appl. Phys. Lett.*, 92 (2008) 233104
- [88] A. Kaestner, E. Lehmann, M. Stampanoni, Imaging and image processing in porous media research, *Adv. Water Resour.*, 31 (2008) 1174-1187.
- [89] W. Li, N. Wang, J. Chen, G. Liu, Z. Pan, Y. Guan, Y. Yang, W. Wu, J. Tian, S. Wei, Z. Wu, Y. Tian, L. Guo, Quantitative study of interior nanostructure in hollow zinc oxide particles on the basis of nondestructive x-ray nanotomography, *Appl. Phys. Lett.*, 95 (2009) 053108
- [90] J.-Y. Buffiere, E. Maire, J. Adrien, J.-P. Masse, E. Boller, In-situ Experiments with X ray Tomography: An Attractive Tool for Experimental Mechanics, *Exp. Mechan.*, 50 (2010) 289-305.

- [91] Y. K. Chen, Y. S. Chu, J. Yi, I. McNulty, Q. Shen, P. W. Voorhees, D. C. Dunand, Morphological and topological analysis of coarsened nanoporous gold by X-ray nanotomography, *Appl. Phys. Lett.*, 96 (2010) 043122.
- [92] A. Schropp, P. Boye, A. Goldschmidt, S. Hönig, R. Hoppe, J. Patommel, C. Rakete, D. Samberg, S. Stephan, S. Schöder, M. Burghammer, C. G. Schroer, Non-destructive and quantitative imaging of a nano-structured microchip by ptychographic hard X-ray scanning microscopy, *J. Microscopy*, 241 (2010) 9-12.
- [93] A. Diaz, P. Trtik, M. Guizar-Sicairos, A. Menzel, P. Thibault, O. Bunk, Quantitative x-ray phase nanotomography, *Phys. Rev. B*, 85 (2012) 020104.
- [94] P. J. Withers, X-ray nanotomography, *Material today*, 10 (2007) 26-34.
- [95] W. A. Kalender, Review: X-ray computed tomography, *Phys. Med. Biol.*, 51 (2006) R29-R43.
- [96][http://www.ndt-ed.org/EducationResources/HighSchool/Radiography/hs\\_rad\\_index.htm](http://www.ndt-ed.org/EducationResources/HighSchool/Radiography/hs_rad_index.htm), accessed 06.07.2013
- [97] A. C. Kak, M. Slaney, Principles of Computerized Tomographic Imaging, The Institute of Electrical and Electronics Engineers, Inc., New York, 1987.
- [98] A. Tkachuk, F. Duewer, H. Cui, M. Feser, S. Wang, W. Yun, X-ray computed tomography in Zernike phase contrast mode at 8 keV with 50-nm resolution using Cu rotating anode X-ray source, *Zeitschrift für Kristallographie* 222 (2007) 650-655.
- [99] Y. S. Chu, M. Yi, F. De Carlo, Q. Shen, W.-K. Lee, H. J. Wu, C. L. Wang, J. Y. Wang, C. J. Liu, C. H. Wang, S. R. Wu, C. C. Chien, Y. Hwu, A. Tkachuk, W. Yun, M. Feser, K. S. Liang, C. S. Yang, J. H. Je, G. Margaritondo, Hard-x-ray microscopy with Fresnel zone plates reaches 40 nm Rayleigh resolution, *Appl. Phys. Lett.*, 92 (2008) 103119.
- [100] W. Chao, J. Kim, S. Rekawa, P. Fischer, E. H. Anderson, Demonstration of 12 nm resolution Fresnel zone plate lens based soft X-ray microscopy, *Opt. Express*, 17 (2009) 17669-17677.
- [101] J. Vila-Comamala, K. Jefimovs, J. Raabe, T. Pilvi, R. H. Fink, M. Senoner, A. Maaßdorf, M. Ritala, C. David, Advanced thin film technology for ultrahigh resolution X-ray microscopy, *Ultramicroscopy*, 109 (2009) 1360-1364.
- [102] A. Sakdinawat, D. Attwood, Nanoscale X-ray imaging, *Nature Photonics*, 14 (2010) 799-882
- [103] L. Salvo, P. Cloetens, E. Maire, S. Zabler, J. J. Blandin, J.-Y. Buffière, W. Ludwig, E. Boller, D. Bellet, C. Jossierond, X-ray micro-tomography an attractive characterisation

## References

---

technique in materials science, Nuclear instruments and methods in physics research section B: Beam interactions with materials and atoms, 200 (2003) 273-286.

[104] L. Salvo, M. Suéry, A. Marmottant, N. Limodin, D. Bernard, 3D imaging in material science: Application of X-ray tomography, *Comptes Rendus Physique*, 11 (2010) 641-649.

[105] H. N. Thi, H. Jamgotchian, J. Gastaldi, J. Härtwig, T. Schenk, H. Klein, B. Billi, J. Baruchel, Y. Dabo, Preliminary in situ and real-time study of directional solidification of metallic alloys by x-ray imaging techniques, *J. Phys. D: Appl. Phys.*, 36 (2003) A83-A86.

[106] N. Limodin, L. Salvo, E. Boller, M. Suéry, M. Felberbaum, S. Gailliègue, K. Madi, In situ and real-time 3-D microtomography investigation of dendritic solidification in an Al-10 wt.% Cu alloy, *Acta Mater.*, 57 (2009) 2300-2310.

[107] A. Bareggiw, E. Maire, A. Lasalle, S. Deville, Dynamics of the Freezing Front During the Solidification of a Colloidal Alumina Aqueous Suspension: In Situ X-Ray Radiography Tomography, and Modeling, *J. Am. Ceram. Soc.*, 94(2011) 3570-3578

[108] D. Tolnai, P. Townsend, G. Requen, L. Salvo, J. Lendvai, H.P. Degischer, In situ synchrotron tomographic investigation of the solidification of an AlMg4.7Si8 alloy, *Acta Mater.*, 60 (2012) 2568-2577.

[109] A. Marmottant, L. Salvo, C.L. Martin, A. Mortensen, Coordination measurements in compacted NaCl irregular powders using X-ray microtomography, *J. Eu. Ceram. Soc.*, 28 (2008) 2441-2449.

[110] M. Tsukahara, S. Mitrovic, V. Gajdosik, G. Margaritondo, L. Pournin, M. Ramaioli, D. Sage, Y. Hwu, M. Unser, Th. M. Liebling, Coupled tomography and distinct-element-method approach to exploring the granular media microstructure in a jamming hourglass, *Phys. Rev. E*, 77 (2008) 061306.

[111] R. Moreno-Atanasio, R. A. Williams, X. Jia, Combining X-ray microtomography with computer simulation for analysis of granular and porous materials, *Particuology*, 8 (2010) 81-99.

[112] D. Bernard, D. Gendron, S. Bordere, Proceedings of the 4th Pacific RIM International Conf. Adv. Mater. Process., PRICM4, 2001

[113] O. Lame, D. Bellet, M. D. Michiel, D. Bouvard, In situ microtomography investigation of metal powder compacts during sintering, *Nucl. Instrum. Method. Phys. Res. B*, 200 (2003) 287-294.

[114] O. Lame, D. Bellet, M. D. Michiel, D. Bouvard, Bulk observation of metal powder sintering by X-ray synchrotron microtomography, *Acta Mater.*, 52 (2004) 977-984.

- [115] A. Vagnon, O. Lame, D. Bouvard, M. D. Michiel, D. Bellet, G. Kapelski, Deformation of steel powder compacts during sintering: Correlation between macroscopic measurement and in situ microtomography analysis, *Acta Mater.*, 54 (2006) 513-522.
- [116] A. Vagnon, J. P. Rivière, J. M. Missiaen, D. Bellet, M. D. Michiel, C. Josserond, D. Bouvard, 3D statistical analysis of a copper powder sintering observed in situ by synchrotron microtomography, *Acta Mater.*, 56 (2008) 1084-1093.
- [117] L. Olmos, C. L. Martin, D. Bouvard, D. Bellet, M. D. Michiel, Investigation of the Sintering of Heterogeneous Powder Systems by Synchrotron Microtomography and Discrete Element Simulation, *J. Am. Ceram. Soc.*, 92 (2009) 1492-1499.
- [118] L. Olmos, T. Takahashi, D. Bouvard, C. L. Martin, L. Salvo, D. Bellet, M. D. Michiel, Analysing the sintering of heterogeneous powder structures by in situ microtomography, *Philosophical Magazine*, 89 (2009):2949-2965.
- [119] F. Xu, X.-F. Hu, H. Miao, J.-Hua Zhao, In situ investigation of ceramic sintering by synchrotron radiation X-ray computed tomography, *Opt. Lasers Eng.*, 48 (2010) 1082-1088.
- [120] Y. Niu, F. Xu, X. Hu, J. Zhao, H. Miao, X. Wu, Z. Zhang, In situ investigation of the silicon carbide particles sintering, *J. Nanomater.*, 2011 (2011) 26.
- [121] D. Bernard, O. Guillon, N. Combaret, E. Plougonven, Constrained sintering of glass films: Microstructure evolution assessed through synchrotron computed microtomography, *Acta Mater.*, 59 (2011) 6228-6238.
- [122] P. R. Shearing, Characterisation of Solid Oxide Fuel Cell Electrode Microstructures in Three Dimensions, Imperial College London, PhD, 2009
- [123] P. R. Shearing, J. Gelb, N. P. Brandon, X-ray nano computerised tomography of SOFC electrodes using a focused ion beam sample-preparation technique, *J. Eu. Ceram. Soc.*, 30 (2010) 1809-1814.
- [124] Y. Guan, W. Li, Y. Gong, G. Liu, X. Zhang, J. Chen, J. Gelb, W. Yun, Y. Xiong, Y. Tian, H. Wang, Analysis of the three-dimensional microstructure of a solid-oxide fuel cell anode using nano X-ray tomography, *J. Power Sources*, 196 (2011) 1915-1919.
- [125] G. J. Nelson, W. M. Harris, J. J. Lombardo, J. R. I. Jr., W. K. S. Chiu, P. Tanasini, M. Cantoni, J. V. herle, C. Comninellis, J. C. Andrews, Y. Liu, P. Pianetta, Y. S. Chu, Comparison of SOFC cathode microstructure quantified using X-ray nanotomography and focused ion beam-scanning electron microscopy, *Electrochem. Commun.*, 13 (2011) 586-589.
- [126] P. R. Shearing, R. S. Bradley, J. Gelb, S. N. Lee, A. Atkinson, P. J. Withers, N. P. Brandon, Using Synchrotron X-Ray Nano-CT to Characterize SOFC Electrode

## References

---

Microstructures in Three-Dimensions at Operating Temperature, *Electrochem. Solid-State Lett.*, 14 (2011) B117-B120

[127] G. J. Nelson, K. N. Grew, J. R. I. Jeffrey J. Lombardo, W. M. Harris, A. Faes, A. Hessler-Wyser, J. V. Herle, S. Wang, Y. S. Chu, A. V. Virkar, W. K. S. Chiu, Three-dimensional microstructural changes in the Ni-YSZ solid oxide fuel cell anode during operation, *Acta Mater.*, 60 (2012) 3491-3500.

[128] G. J. Nelson, W. M. Harris, J. R. I., K. N. Grew, W. K. S. Chiu, Y. S. Chu, J. Yi, J. C. Andrews, Y. Liu, P. Pianetta, Three-dimensional mapping of nickel oxidation states using full field x-ray absorption near edge structure nanotomography, *Appl. Phys. Lett.*, 98 (2011) 173109.

[129] Q. Shen, W.-K. Lee, K. Fezza, Y. S. Chu, F. D. Carlo, P. Jemian, J. Ilavsky, M. Erdmann, G. G. Long, Dedicated full-field X-ray imaging beamline at Advanced Photon Source, *Nuclear Instruments and Methods in Physics Research A*, 582 (2007) 77-79.

[130] Y. Wang, Y. K. Chen, W. K. S. Chiu, In Situ 3D Imaging and Characterization of Nano-Structures with X-ray Nano-CT Technique, *ECS Trans.*, (2011) 21-29.

[131] B. John, *Advanced tomographic methods in materials research and engineering*, Oxford University Press, New York, 2008.

[132] J.-S. Park, H. Shin, K. S. Hong, H. S. Jung, J.-K. Lee, K.-Y. Rhee, Effect of margin widths on the residual stress in a multi-layer ceramic capacitor, *Microelectr. Eng.*, 83 (2006) 2558-2563.

[133] M. F. Ashby, A first report on sintering diagrams, *Acta Metall.*, 22 (1974) 275-289.

[134] A. Masuda, Y. Mizuno, S. Ueda, H. Chazono, H. kishi, Development of Multilayer Ceramics Capacitors exhibiting high Q value, *Microelectronics*, 13 (1994) 37-42.

[135] L. Holzer, M. Cantoni, *Review of FIB-tomography, Nanofabrication Using Focused Ion and Electron Beams: Principles and Applications*, Oxford University Press, 2012

[136] P. G. Kotula, M. R. Keenan, J. R. Michael, Tomographic Spectral Imaging with Multivariate Statistical Analysis: Comprehensive 3D Microanalysis, *Microsc Microanal*, 12 (2006) 36-48.

[137] F. Lasagni, A. Lasagni, E. Marks, C. Holzapfel, F. Mücklich, H. P. Degischer, Three-dimensional characterization of 'as-cast' and solution-treated AlSi12(Sr) alloys by high-resolution FIB tomography, *Acta Mater.*, 55 (2007) 3875-3882.

[138] F. Lasagni, A. Lasagni, M. Engstler, H. P. Degischer, F. Mücklich, Nano-characterization of Cast Structures by FIB-Tomography, *Adv. Eng. Mater.*, 10 (2008) 62-66.

- [139] S. Zaefferer, S. I. Wright, D. Raabe, Three-dimensional orientation microscopy in a focused ion beam-scanning electron microscope: A new dimension of microstructure characterization, *Metall. Mater. Trans. A*, 39 (2008) 374-389.
- [140] L. Holzer, F. Indutnyi, P. H. Gasser, B. Münch, M. Wegmann, Three-dimensional analysis of porous BaTiO<sub>3</sub> ceramics using FIB nanotomography, *J. Microscopy*, 216 (2004) 84-95.
- [141] P. R. Munroe, The application of focused ion beam microscopy in the material sciences, *Mater. Charact.*, 60 (2009) 2-13.
- [142] J. AW. Heymann, M. Hayles, I. Gestmann, L. A Giannuzzi, B. Lich, S. Subramaniam, Site-specific 3D imaging of cells and tissues with a dual beam microscope, *J. Struct. Biol.*, 155 (2006) 63-73.
- [143] J. AW Heymann, D. Shi, S. Kim, D. Bliss, J. LS Milne, S. Subramaniam, 3D imaging of mammalian cells with ion-abrasion scanning electron microscopy, *J. Struct. Biol.*, 166 (2009) 1-7.
- [144] E. Schroeder-Reiter, F. Pérez-Willard, U. Zeile, G. Wanner, Focused ion beam (FIB) combined with high resolution scanning electron microscopy: A promising tool for 3D analysis of chromosome architecture, *J. Struct. Biol.*, 165 (2009) 97-106.
- [145] S. Zhang, R. E. Klimentidis, P. Barthelemy, Porosity and permeability analysis on nanoscale FIB-SEM 3D imaging of shale rock, in: SCA Symposium, 2011.
- [146] R. Wirth, Focused Ion Beam (FIB) combined with SEM and TEM: Advanced analytical tools for studies of chemical composition, microstructure and crystal structure in geomaterials on a nanometre scale, *Chem. Geol.*, 261 (2009) 217-229.
- [147] L. Holzer, B. Muench, M. Wegmann, P. Gasser, R. J. Flatt, FIB-Nanotomography of Particulate Systems-Part I: Particle Shape and Topology of Interfaces, *J. Am. Ceram. Soc.*, 89 (2006) 2577-2585.
- [148] B. Münch, P. Gasser, L. Holzer, R. Flatt, FIB-Nanotomography of Particulate Systems-Part II: Particle Recognition and Effect of Boundary Truncation, *J. Am. Ceram. Soc.*, 89 (2006) 2586-2595.
- [149] A. J. Kubis, G. J. Shiflet, R. Hull, D. N. Dunn, Focused ion-beam tomography, *Metall. Mater. Trans. A*, 35 (2004) 1935-1943.
- [150] L. A. Giannuzzi, B. W. Kempshall, S. M. Schwarz, J. K. Lomness, B. I. Prenitzer, F. A. Stevie, FIB lift-out specimen preparation techniques, in: *Introduction to Focused Ion Beam*, Springer US, (2005) 201-228[151]



## References

---

- [151] C. A. Volkert, A. M. Minor, Focused ion beam microscopy and micromachining, *MRS Bull.*, 32 (2007) 389-395.
- [152] R. Salh, Silicon Nanocluster in Silicon Dioxide: Cathodoluminescence, Energy Dispersive X-Ray Analysis, Infrared Spectroscopy Studies, 2011.
- [153] H. Stegmann, R. Hübner, Y. Ritz, D. Uteß, B. Volkmann, H.-J. Engelmann, In-situ Low Energy Noble Gas Ion Milling in a Three Beam Instrument, FIB-Workshop: Focused Ion Beams in Research, Science and Technology, Halle, Germany, 2009
- [154] P. Thevenaz, U. E. Ruttimann, M. Unser, A pyramid approach to subpixel registration based on intensity, *IEEE Transactions on Image Processing*, 7 (1998) 27-41.
- [155] J. C. Russ, *The image processing handbook*, CRC press, 2006.
- [156] L. Vincent, P. Soille, Watersheds in digital spaces: an efficient algorithm based on immersion simulations, *IEEE transactions on pattern analysis and machine intelligence*, 13 (1991) 583-598.
- [157] [www.vsg.com](http://www.vsg.com), accessed 2013
- [158] [http://www.donner-tech.com/whats\\_wrong\\_with\\_ld.pdf](http://www.donner-tech.com/whats_wrong_with_ld.pdf), accessed 23.05.2013
- [159] S. D. Wicksell, The corpuscle problem: a mathematical study of a biometric problem, *Biometrika*, 17 (1925) 84-99.
- [160] H. A. Schwartz., The metallographic determination of size distribution of temper carbon nodules, *Metals and Alloys*, 5 (1934) 139-141.
- [161] S. A. Saltykov, *Stereometric Metallography*, 2<sup>nd</sup> ed., Metallurgizdat, Moscow, 1958.
- [162] F. A. L. Dullien, *Porous Media. Fluid Transport and Pore Structure*, Academic Press, 1992.
- [163] C. L. Martin, R. K. Bordia, The effect of a substrate on the sintering of constrained films, *Acta Mater.*, 57 (2009) 549-558.
- [164] H. Cremér, *Mathematical Methods of Statistics (PMS-9)*, Princeton University press, 1999.
- [165] Y. Shigegaki, M. E. Brito, K. Hirao, M. Toriyama, S. Kanzaki, Strain tolerant porous silicon nitride, *J. Am. Ceram. Soc.*, 80 (1997) 495-498.
- [166] R. Zuo, E. Aulbach, R. K. Bordia, J. Rödel, Critical evaluation of hot forging experiments: Case study in alumina, *J. Am. Ceram. Soc.*, 86 (2003) 1009-1105.
- [167] O. Guillon, E. Aulbach, R. Bordia, J. Rödel, Constrained sintering of alumina thin films: Comparison between experiment and modeling, *J. Am. Ceram. Soc.*, 90 (2007) 1733-1737.
- [168] R. Mücke, N. H. Menzler, H. P. Buchkremer, D. Stöver, Cofiring of Thin Zirconia Films During SOFC Manufacturing, *J. Am. Ceram. Soc.*, 92 (2009) S95-S102.

- [169] R. K. Bordia, G. W. Scherer, *Ceram. Trans.* 1 (1988) 872-886.
- [170] P. A. Cundall, O. DL Strack, A discrete numerical model for granular assemblies, *Geotechnique*, 29 (1979) 47-65.
- [171] Y. Tsuji, T. Kawaguchi, T. Tanaka, Discrete particle simulation of two-dimensional fluidized bed, *Powder Technol.*, 77 (1993) 79-87.
- [172] P. A. Langston, U. Tüzün, D. M. Heyes, Discrete element simulation of granular flow in 2D and 3D hoppers: dependence of discharge rate and wall stress on particle interactions, *Chem. Eng. Sci.*, 50 (1995) 967-987.
- [173] B. H. Xu, A. B. Yu, Numerical simulation of the gas-solid flow in a fluidized bed by combining discrete particle method with computational fluid dynamics, *Chem. Eng. Sci.*, 52 (1997) 2785-2809.
- [174] L. Vu-Quoc, X. Zhang, O. R. Walton, A 3-D discrete-element method for dry granular flows of ellipsoidal particles, *Comput. Meth. Appl. Mech. Eng.*, 187 (2000) 483-528.
- [175] C. O'Sullivan, L. Cui, Micromechanics of granular material response during load reversals: Combined DEM and experimental study, *Powder Technol.*, 193 (2009) 289-302.
- [176] R. Garcia-Rojo, S. McNamara, H. J. Herrmann, in: *European Congress on Computational Methods in Applied Sciences and Engineering: ECCOMAS 2004*, Jyväskylä, 2004.
- [177] G. Jeffson, G. K. Haritos, R. M. McMeeking, The elastic response of a cohesive aggregate-a discrete element model with coupled particle interaction, *J. Mech. Phys. Solid.*, 50 (2002) 2539-2575.
- [178] K. Richards, M. Bithell, M. Dove, R. Hodge, Discrete-element modelling: methods and applications in the environmental sciences, *Phil. Trans. R. Soc. Lond. A*, 362 (2004) 1797-1816
- [179] G. A. D'addetta, F. Kun, E. Ramm, H. J. Herrmann, From solids to granulates-discrete element simulations of fracture and fragmentation processes in geomaterials, in: *Continuous and discontinuous modelling of cohesive-frictional materials*, Springer US, (2001) 231-258.
- [180] S. Hentz, F. V. Donzé, L. Daudeville, Discrete element modelling of concrete submitted to dynamic loading at high strain rates, *Comput. Struct.*, 82 (2004) 2509-2524.
- [181] M. Jiang, S. Leroueil, J.-M. Konrad, Yielding of microstructured geomaterial by distinct element method analysis, *J. Eng. Mech.*, 131 (2005) 1209-1213.
- [182] X. Fu, M. Dutt, A. C. Bentham, B. C. Hancock, R. E. Cameron, J. A. Elliott, Investigation of particle packing in model pharmaceutical powders using X-ray microtomography and discrete element method, *Powder Technol.*, 167 (2006) 134-140.

## References

---

- [183] W. R. Ketterhagen, M. T am Ende, B. C. Hancock, Process modeling in the pharmaceutical industry using the discrete element method, *J. Pharma. Sci.*, 98 (2009) 442-470.
- [184] C. L. Martin, D. Bouvard, Study of the cold compaction of composite powders by the discrete element method, *Acta Mater.*, 51 (2003) 373-386.
- [185] C. L. Martin, D. Bouvard, S. Shima, Study of particle rearrangement during powder compaction by the Discrete Element Method, *J. Mech. Phys. Solid.*, 51 (2003) 667-693.
- [186] S. Luding, K. Manetsberger, J. Müllers, A discrete model for long time sintering, *J. Mech. Phys. Solid.*, 53 (2005) 455-491.
- [187] C. L. Martin, L. C.R. Schneider, L. Olmos, D. Bouvard, Discrete element modeling of metallic powder sintering, *Scripta Mater.*, 55 (2006) 425-428.
- [188] B. Henrich, A. Wonisch, T. Kraft, M. Moseler, H. Riedel, Simulations of the influence of rearrangement during sintering, *Acta Mater.*, 55 (2007) 753-762.
- [189] C. L. Martin, H. Camacho-Montes, L. Olmos, D. Bouvard, R. K. Bordia, Evolution of Defects During Sintering: Discrete Element Simulations, *J. Am. Ceram. Soc.*, 92 (2009) 1435-1441.
- [190] C. L. Martin, R. K. Bordia, Influence of adhesion and friction on the geometry of packings of spherical particles, *Phys. Rev. E*, 77 (2008) 031307.
- [191] C. L. Martin, Unloading of powder compacts and their resulting tensile strength, *Acta Mater.*, 51 (2003) 4589-4602.
- [192] C. L. Martin, D. Bouvard, Discrete Element Simulations of the Compaction of Aggregated Ceramic Powders, *J. Am. Ceram. Soc.*, 89 (2006) 3379-3387.
- [193] S. M. Sweeney, C. L. Martin, Pore size distributions calculated from 3-D images of DEM-simulated powder compacts, *Acta Mater.*, 51 (2003) 3635-3649.
- [194] P. Pizette, C. L. Martin, G. Delette, P. Sornay, F. Sans, Compaction of aggregated ceramic powders: From contact laws to fracture and yield surfaces, *Powder Technol.*, 198 (2010) 240-250.
- [195] A. Jagota, G. W. Scherer, Viscosities and Sintering Rates of Composite Packings of Spheres, *J. Am. Ceram. Soc.*, 78 (1995) 521-528.
- [196] A. Jagota, G. W. Scherer, Viscosities and Sintering Rates of a Two-Dimensional Granular Composite, *J. Am. Ceram. Soc.*, 76 (1993) 3123-3135.
- [197] W. J. Soppe, G. J. M. Janssen, B. C. Bonekamp, L. A. C. Veringa, H. J. Veringa, A computer-simulation method for sintering in 3-dimensional powder compacts, *J. Mater. Sci.*, 29 (1994) 754-761.

- [198] F. Parhami, R. M. McMeeking, A network model for initial stage sintering, *Mech. Mater.*, 27 (1998) 111-124.
- [199] D. Bouvard, R. M. McMeeking, Deformation of interparticle necks by diffusion-controlled creep, *J Am Ceram Soc*, 79 (1996) 666-672.
- [200] C. Wang, S. Chen, Application of the complex network method in solid-state sintering, *Comput. Mater. Sci.*, 69 (2013) 14-21.
- [201] J. Rojek, K. Pietrzak, M. Chmielewski, D. Kaliński, S. Nosewicz, Discrete element simulation of powder sintering, *Comput. Meth. Mater. Sci.*, 11 (2011) 68-73.
- [202] T. Kraft, H. Riedel, Numerical simulation of solid state sintering, model and application, *J. Eu. Ceram. Soc.*, 24 (2004) 345-361.
- [203] H. Riedel, H. Zipse, J. Svoboda, Equilibrium pore surfaces sintering stresses and constitutive equations for the intermediate and late stages of sintering-II diffusional densification and creep, *Acta Metall. Mater.*, 42 (1994) 445-452.
- [204] A. Wonisch, O. Guillon, T. Kraft, M. Moseler, H. Riedel, J. Rödel, Stress-induced anisotropy of sintering alumina: Discrete element modelling and experiments, *Acta Mater.*, 55 (2007) 5187-5199.
- [205] T. Rasp, C. Jamin, A. Wonisch, T. Kraft, O. Guillon, Shape Distortion and Delamination During Constrained Sintering of Ceramic Stripes: Discrete Element Simulations and Experiments, *J. Am. Ceram. Soc.*, 95 (2012) 586-592.
- [206] L. Verlet, Computer experiment on classical fluids. I. Thermodynamical properties of Lennard-Jones molecules, *Phys. Rev.*, 159 (1967) 98.
- [207] W. C Swope, H. C Andersen, P. H Berens, K. R Wilson, A computer simulation method for the calculation of equilibrium constants for the formation of physical clusters of molecules: Application to small water clusters, *J. Chem. Phys.*, 76 (1982) 637.
- [208] M. P. Allen, D. J. Tildesley, *Computer simulation of liquids*, Oxford Science Press, Oxford, 1987.
- [209] C. Thornton, S. J. Antony, Quasi-static deformation of particulate media, *Phil Trans Roy. Soc. Lond. Math. Phys. Sci.*, (1998) 2763-2782.
- [210] B.V. Derjaguin, V. M. Muller, Y. P. Toporov, Effect of contact deformations on the adhesion of particles, *J. Colloid. Interface Sci.*, 53 (1975) 314-326.
- [211] S. D. Mesarovic, K. L. Johnson, Adhesive contact of elastic-plastic spheres, *J. Mech. Phys. Solid.*, 48 (2000) 2009-2033.
- [212] R. Raj, M. F. Ashby, On grain boundary sliding and diffusional creep, *J. Am. Ceram. Soc.*, 2 (1971) 1113-1127.

## References

---

- [213] R. L. Coble, Initial Sintering of Alumina and Hematite, *J. Am. Ceram. Soc.*, 41 (1958) 55-62.
- [214] J. Pan, H. Le, S. Kucherenko, J. A. Yeomans, A model for the sintering of spherical particles of different sizes by solid state diffusion, *Acta Mater.*, 46 (1998) 4671-4690.
- [215] W. H. Tuan, R. J. Brook, Sintering of heterogeneous ceramic compacts, *J. Mater. Sci.*, 24 (1989) 1953-1958.
- [216] O. Sudre, G. Bao, B. Fan, F. F. Lange, Anthony G. Evans, Effect of Inclusions on Densification: II, Numerical Model, *J. Am. Ceram. Soc.*, 75 (1992) 525-531.
- [217] Y. Nakada, T. Kimura, Effects of Shape and Size of Inclusions on the Sintering of ZnO-ZrO<sub>2</sub> Composites, *J. Am. Ceram. Soc.*, 80 (1997) 401-406.
- [218] F. B. Swinkels, M. F. Ashby, A second report on sintering diagrams, *Acta Metall.*, 29 (1980) 259-281.
- [219] R. K. Bordia, R. Raj, Sintering of TiO<sub>2</sub>-Al<sub>2</sub>O<sub>3</sub> Composites: A Model Experimental Investigation, *J. Am. Ceram. Soc.*, 71 (1988) 302-310.
- [220] R. Ueyama, K. Koumoto, K. Yubuta, T. Fujii, Influence of BaTiO<sub>3</sub> nano particle on paste and sintering properties of Ni internal electrode films by MLCC, *J. Ceram. Soc. Jpn.*, 111 (2003) 282-284.
- [221] N. L. Johnson, S. Kotz, N. Balakrishnan, *Continuous Multivariate Distributions, Volume 1, Models and Applications*, New York: John Wiley & Sons, 2002.
- [222] G. E. P. Box, M. E. Muller, A Note on the Generation of Random Normal Deviates, *Ann. Math. Statist.* 29(1958) 610-611.
- [223] B. Kieback, M. Noethe, R. Grupp, J. Banhart, T. Rasp, T. Kraft, Analysis of particle rolling and intrinsic rotations in copper powder during sintering, *J. Mater. Sci.*, 47 (2012) 7047-7055.

## RESUME

L'objectif de cette thèse est de comprendre les mécanismes d'évolution de la discontinuité dans une électrode lors du frittage de condensateurs céramiques multicouches (multilayer ceramic capacitors, MLCCs) en couplant nanotomographie et simulations discrètes. Les observations multi-échelles à l'aide de rayons X synchrotron (résolution de 30 nm) en tomodensitométrie et le couplage de la microscope électronique à balayage à un faisceau d'ions focalisé (résolution de 5 nm) sur des MLCCs commerciales de Ni- et Pd- ont révélé que les discontinuités proviennent d'hétérogénéités initiales d'empilement (zones poreuses) dans l'électrode. Les discontinuités se forment à un stade précoce du frittage de l'électrode. A ce stade le frittage de l'électrode est contraint par les couches diélectriques, qui n'ont pas encore commencé à fritter. Les simulations par éléments discrets, ont été effectuées sur le frittage d'un mélange de Ni et de BaTiO<sub>3</sub> et sur des multicouches BaTiO<sub>3</sub>/Ni/BaTiO<sub>3</sub>. Les données d'entrée de ces simulations ont été obtenues à partir des observations expérimentales en nano tomographie. En accord avec les expériences, les simulations montrent que les discontinuités proviennent des hétérogénéités initiales et qu'elles se développent à cause des contraintes engendrées par les couches adjacentes. Une étude paramétrique indique que les discontinuités d'électrodes peuvent être minimisées par l'homogénéisation de la compacité, par l'augmentation de l'épaisseur des électrodes et par l'utilisation d'un chauffage rapide.

Mots clés: frittage; condensateur céramique multicouche (MLCC); simulations discrètes; Nano-tomographie

## ABSTRACT

The aim of this thesis is to understand the electrode discontinuity evolution mechanism during the sintering of multilayer ceramic capacitors (MLCCs) by coupling nanotomography observations with discrete simulations. Multi-scale correlative studies using synchrotron X-ray nano (resolution of 30 nm) computed tomography and Focused Ion Beam nano (resolution of 5 nm) tomography on commercial Ni- and Pd-MLCCs revealed that electrode discontinuities originate from initial packing heterogeneities (porous regions) in the electrode. The discontinuities form at the early stage of the sintering of electrode under the constraints from the dielectrics layers which have not started to sinter yet. Discrete element simulations, using the particulate characteristics of the packing obtained from nano tomographic data as inputs, were carried out on the sintering of BaTiO<sub>3</sub> dispersed Ni electrode and BaTiO<sub>3</sub>/Ni/BaTiO<sub>3</sub> multilayers. In agreement with experiments, simulations show that discontinuities originate from the initial heterogeneities under constraint from adjacent layers. Parametric studies suggest that electrode discontinuities can be minimized by homogenizing the packing density and increasing the thickness of the electrodes and using a fast heating rate.

**Key Words:** Sintering; Multilayer Ceramic Capacitor (MLCC); Discrete Element Method; Nano-tomography